Joining aluminium-based composites using diffusion bonding techniques

Bushby, Roger Stanley

Award date:
1993

Awarding institution:
University of Bath

JOINING ALUMINIUM-BASED COMPOSITES USING DIFFUSION BONDING TECHNIQUES

Submitted by Roger Stanley Bushby

for the degree of PhD

of the University of Bath

1993

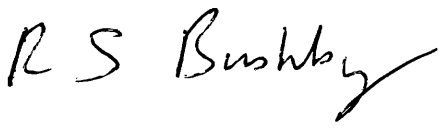

Roger S Bushby

ProQuest LLC
789 East Eisenhower Parkway
P.O. Box 1346
Ann Arbor, MI 48106-1346

ABSTRACT

The diffusion bonding of aluminium alloys, with and without ceramic reinforcement, has been investigated. The composite materials were (a) commercial-purity aluminium reinforced with Nicalon fibres and (b) Al-Cu-Mg alloy (2124) reinforced with silicon carbide particulate. Bonding experiments were carried out in air using a range of temperatures (400°C to 550°C) and pressures (3 MPa to 34 MPa) and a selection of interlayers based upon copper. The systems involved both solid-state and liquid-phase bonding processes.

The joints were evaluated using a shear test method with a jig devised to avoid the peel stresses normally associated with more conventional shear testing. Microstructures of the bonds were investigated using light microscopy and analytical electron microscopy, both scanning and transmission modes.

It was found that for commercial-purity aluminium, the optimum bonding technique involved the use of a 2124 alloy interlayer at a temperature of 500°C. The mechanism of bonding involved the magnesium present in the interlayer disrupting the surface oxide so as to produce a joint via the solid-state process. A similar approach proved to be successful for the aluminium reinforced with Nicalon fibre, although a higher pressure was required to achieve intimate contact between these stiffer materials. When the bonded aluminium, with and without reinforcement, was tested in

shear failure occurred away from the joint interface and this was attributed to a precipitation hardening reaction associated with the presence of copper diffused from the interlayer.

For 2124 alloy satisfactory bonds, close to the yield strength of the alloy, were achieved at 500°C without an interlayer and, although failure occurred at the joint interface during shear testing, the bond area was ~90%. For 2124 alloy reinforced with SiC particulate the strength of the joint was low due to restricted metal-to-metal contact at the joint interface. The use of a 2124 alloy interlayer improved the strength of the composite joint appreciably. The highest joint strength was obtained, however, by bonding the composite with a copper-silver alloy interlayer (at 510°C), due to the fact that the formation of eutectic liquid provided 'keying' with the SiC reinforcement.

ACKNOWLEDGEMENTS

I would like to thank Professor V.D. Scott, Head of School of Materials Science, for his continued supervision and guidance during this project. Much praise is given also to the Technical Staff of the School. I also take this opportunity to thank my industrial supervisor Mr R.L. Trumper, of DRA Holton Heath, for the supply of materials and for his helpful advice and discussion. The support of the SERC and MOD Procurement Executive is also acknowledged.

Finally, I would like to thank Alison for her love and encouragement over the past three years, and my parents for their continued support.

CONTENTS Page

1. INTRODUCTION TO COMPOSITE MATERIALS

1.1. Historical 1

1.2. Metal matrix composites 3

1.2.1. Composites reinforced with particulates 4

1.2.2. Composites reinforced with short fibres 5

1.2.3. Composites reinforced with long fibres 6

1.2.4. Metals used for composite matrices 8

1.2.5. Types of reinforcement used for composites 9

1.3. Primary fabrication techniques 14

1.3.1. Liquid metal infiltration 15

1.3.2. Squeeze casting 16

1.3.3. Compocasting 18

1.3.4. Spray deposition 20

1.3.5. Powder metallurgy 21

1.3.6. Diffusion bonding 22

1.4. Composite microstructure and properties 24

1.5. Secondary fabrication techniques 29

1.5.1. Forming 29

1.5.2. Machining 30

1.5.3. Joining 31

1.6. Diffusion bonding techniques 32

1.6.1. Diffusion in metals 33

1.6.2. Diffusion bonding aluminium alloys 40

1.6.3. Diffusion bonding metal matrix composites 42

1.7. Scope of the investigation 45

2. EXPERIMENTAL PROCEDURE

2.1. Materials used in the investigation 47

2.1.1. Unreinforced aluminium alloys 47

2.1.2. Commercial-purity aluminium reinforced with Nicalon fibre (Al/Nic) 47

2.1.3. Aluminium alloy (2124) reinforced with SiC particulate (2124/P) 48

2.1.4. Interlayers for bonding 48

2.2. Diffusion bonding experiments 49

2.2.1. Bonding apparatus 49

2.2.2. Prior preparation of joint surfaces 50

2.2.3. Bonding procedure 51

2.3. Mechanical evaluation of as-received and diffusion-bonded materials 52

2.3.1. Hardness testing of unreinforced alloy and metal matrices 52

2.3.2. Fibre/matrix interfacial friction stress in composite materials 53

2.3.3. Bond strength determination 54

(a) Lap-shear test method 54

(b) A modified shear test method 55

2.4. Microstructural analysis 56

2.4.1. Light microscopy 56

(a) Principle of the technique 56

(b) Preparation of specimens 58

2.4.2. Scanning electron microscopy 59

(a) Principle of the technique 59

(b) Preparation of specimens 61

2.4.3. Electron-probe microanalysis 61

(a) Principle of the technique 61

(b) Measurement of oxide film thickness 64

2.4.4. Transmission electron microscopy 66

(a) Principle of the technique 66

(b) Preparation of specimens 69

2.5. Differential scanning calorimetry 71

3. RESULTS

3.1. Comparison of the methods of shear testing 72

3.2. Commercial-purity aluminium 73
3.2.1. As-received material 73
3.2.2. Bonding without an interlayer 74
3.2.3. Bonding with a zinc interlayer 75
3.2.4. Bonding with a copper interlayer 75
3.2.5. Bonding with a nickel-coated copper interlayer 80
3.2.6. Bonding with a copper-silver alloy interlayer 81
3.2.7. Bonding with an aluminium alloy (2124) interlayer 86
3.2.8. Bonding with a copper-zinc alloy interlayer 88

3.3. Commercial-purity aluminium reinforced with Nicalon fibre (Al/Nic) 88
3.3.1. As-received material 88
3.3.2. Bonding with a copper interlayer 89
3.3.3. Bonding with a nickel-coated copper interlayer 91
3.3.4. Bonding with a copper-silver alloy interlayer 92
3.3.5. Bonding with an aluminium alloy (2124) interlayer 93

3.4. Aluminium alloy (2124) 95
3.4.1. As-received material 95
3.4.2. Bonding without an interlayer 96
3.4.3. Bonding with a zinc interlayer 100
3.4.4. Bonding with a copper-silver alloy interlayer 100

3.5. Aluminium alloy reinforced with SiC particulate (2124/P) 102
3.5.1. As-received material 102
3.5.2. Bonding without an interlayer 103
3.5.3. Bonding with a copper-silver alloy interlayer 105

3.5.4. Bonding with an aluminium alloy (2124) interlayer 107

3.6. The bonding of dissimilar materials 108

3.6.1. Aluminium bonded to 2124 alloy 108

3.6.2. Aluminium bonded to 2124/P composite 109

3.6.3. Alloy (2124) bonded to Al/Nic composite 110

3.6.4. Alloy (2124) bonded to 2124/P composite 111

3.6.5. Al/Nic bonded to 2124/P composite 111

4. DISCUSSION

4.1. Assessment of the modified shear test method 112

4.2. Fibre/matrix indentation test data as related to the shear test values 115

4.3. Solid-state bonding of aluminium and aluminium-based composites with and without alloy (2124) interlayers 117

4.3.1. Bonding unreinforced aluminium 117

4.3.2. Bonding composite materials 129

4.4. Liquid-phase bonding of aluminium and aluminium-based composite using metal and alloy interlayers 139

4.4.1. Use of a zinc interlayer 139

4.4.2. Use of an aluminium alloy (2124) interlayer 141

4.4.3. Use of a copper interlayer 143

4.4.4. Use of a nickel-coated copper interlayer 150

4.4.5. Use of a copper-silver alloy interlayer 152

4.4.6. Use of a copper-zinc alloy interlayer 160

5. CONCLUSIONS

5.1. Mechanical test techniques 162

5.2. Solid-state bonding methods 163

5.3. Liquid-phase bonding methods 165

5.4. Recommended bonding techniques 167

6. FUTURE WORK 168

7. REFERENCES 170

APPENDIX

TABLES

FIGURES

1. INTRODUCTION TO COMPOSITE MATERIALS

1.1. Historical

The idea of reinforcing a brittle material with some sort of fibre has been around for thousands of years. Ancient Egyptians added chopped straw to clay slurry when making bricks to reduce the amount of shrinkage cracks which occurred during drying [1]. The fact that the straw reinforced the clay after it had hardened was probably incidental. However, the principle was soon well established and over the years other composite systems have been developed, from concrete - a particulate reinforced composite - to more sophisticated combinations of materials.

The most notable advances have been made in the last eighty years when it was realised that is was possible to form composites from a whole range of materials with the benefit of increased mechanical properties and, usually, a weight saving. Early this century moulded Bakelite phenolic resin components, toughened by paper or asbestos fibres, were manufactured and sold successfully. This led to the development of other resin systems which used glass fibres as reinforcement. Here, not only high toughness was achieved, but also an increase in specific stiffness and strength. Early glass-reinforced plastics (GRP) found application during the war as aircraft radomes, and are

still used today for more mundane purposes. However, since the introduction of fibres and matrix materials with improved mechanical properties polymer composites have progressed rapidly, particularly in the high performance market. Examples include carbon fibre reinforced epoxy (CFRE) and polyetheretherketone (PEEK), a temperature resistant thermoplastic, used mainly for aerospace applications up to several hundred degrees Celsius.

In competition with these materials are the light alloys, in particular high performance aluminium alloys which have been developed from the original Duralumin (Al-Cu-Mg) alloys [2] to the more advanced lighter Al-Li alloys [3]. However, because these are age-hardening alloys they are limited to low temperature application and are unlikely to be further improved. It proposed that a new generation of metal matrix composites (MMCs) with superior mechanical properties will supersede these as structural materials [4], particularly in high temperature applications >300°C.

This has been reflected by the recent research on aero-engine materials with plans to increase efficiency, hence, lower running costs by raising operating temperatures. This would be achieved by replacing conventional compression and combustion chamber materials, such as titanium and nickel superalloys [5], with higher performance carbon-carbon [6], glass or ceramic matrix [7], intermetallic [8] and metal matrix composites [4,9].

A performance map [9] of these materials' operating temperatures versus strength/weight ratio is shown in Fig. 1.1; the predicted trends in jet engine materials usage [4] are illustrated in Fig. 1.2.

The present work is concerned with aluminium-based metal matrix composites, and these are described more fully in the following section.

1.2. Metal matrix composites

Research into metal matrix composites (MMCs) was first carried out over thirty years ago. Early systems included tungsten wire reinforced copper, which were relatively easy to produce. These were used in academic studies of composite behaviour throughout the 60's and early 70's, although the commercial development of MMCs was stunted by the lack of strong reinforcing fibres. Interest has been renewed in the last decade [10] by the introduction of stiff, strong ceramic fibres such as DuPont's FP alumina, ICI's Saffil (short alumina) fibre and the Japanese Nicalon (a silicon carbide-based) fibre. These are nearer to the materials required for commercial use. Areas that have been addressed include composite manufacture, processing and mechanical properties.

The majority of work has studied aluminium alloy matrix composites, although some interest has been shown more recently in magnesium, titanium and to a lesser extent copper, lead and tin [4]. Reinforcement can be of three types; particulate, such as silicon carbide; short fibres, typically alumina; and continuous fibres, carbon, alumina or silicon carbide. This reinforcement is available loose, as woven mats or as bound preforms. The metal matrix may be introduced by a variety of techniques but most commonly some form of liquid metal infiltration is used.

1.2.1. Composites reinforced with particulates

Particulate-reinforced metals have been used commercially for years, such as tungsten carbide in cobalt for machine tool tips [4]. This application has taken advantage of the excellent wear properties of the composite imparted by the presence of the hard reinforcing ceramic phase, whilst still retaining a degree of metallic toughness.

More recent research has focused on improving the mechanical properties of more conventional alloys by using ceramic reinforcement, the most common system being aluminium reinforced with particulate silicon carbide. Due to the shape and even distribution of the SiC

reinforcement within the composite isotropic properties are achieved, although there are only moderate gains in stiffness and strength with reductions in both the ductility and fracture toughness [11]. The composite is, however, relatively cheap to produce compared with other MMC systems and has excellent wear properties.

The three main manufacturing processes are (a) powder metallurgy (b) liquid metal casting and, (c) low pressure plasma co-spraying. Some degree of anisotropy may be induced using conventional secondary fabrication processes such as rolling, forging and extrusion, although high tool wear rates are encountered as a result of the hard reinforcements used.

Numerous papers have been published on particulate reinforced MMCs including reviews by Ibrahim, Mohamed and Lavernia [12], Humphreys, Basu and Djazeb [13] and Girot, Quenisset and Naslain [14]. These cover aspects from matrix and reinforcing materials through to manufacturing processes, microstructure, properties and applications.

1.2.2. Composites reinforced with short fibres

The introduction of short alumina fibres, such as Saffil, (developed and manufactured by ICI) has led to significant

advances in MMC fabrication. Here, a fibre preform is infiltrated using a liquid metal (a process described more fully in section 1.3.). Again, aluminium alloys are used almost exclusively as matrices due to their low densities and melting temperatures. The resultant composite is anisotropic, due to preferred fibre orientation which occurs during preform manufacture, and has superior mechanical properties to particulate-reinforced metals. This is attributed to the higher load transfer between fibres and matrix which is a function of fibre length and fibre/matrix bonding [15]. Other short reinforcing fibres such as carbon and silicon carbide may also be used.

Manufacture and properties of short fibre composites are covered in reviews by Girot *et al* [14] and Harris [16,17].

1.2.3. Composites reinforced with long fibres

Early work on MMCs, first carried out in the 60's, used continuous reinforcement in the form of long fibres including metallic wires of tungsten and stainless steel. These, however, were unsuitable for commercial use due to their high densities and it was not until the late 60's, with the advent of boron monofilaments, that long fibre composites were realised as potential high performance materials. Work was carried out on the manufacture of

boron fibre reinforced aluminium using diffusion bonding as a primary fabrication route [18]. These MMCs were expensive to produce and highly anisotropic as a result of the directional fibre lay-up needed for the high strength and stiffness required. This coupled with poor fibre/matrix bonding gave transverse properties below that of the aluminium matrix. Other types of fibre lay-up (0°,90°) can be used to increase the isotropy of the composite, although this reduces the longitudinal strength. The majority of long fibre composites find uses in uniaxial loading situations such as the use of stainless steel fibres to selectively reinforce aluminium connecting rods for internal combustion engines [2,9].

More recent work has focused on the newer, smaller fibres (~15 μm), such as Nicalon (SiC-based), using liquid metal infiltration as a manufacturing process for near-net shaped aluminium components. For more specialised applications plasma spray/filament winding techniques are being investigated, although these are used mainly for fabricating silicon carbide monofilament reinforced titanium composites.

1.2.4. Metals used for composite matrices

Although studies have been carried out on magnesium, titanium, copper and even lead based MMCs [4] aluminium alloys have been used almost exclusively as matrix materials. This is due to their castability and low density, and although the reinforcements are often denser than the aluminium matrices the composite has improved specific properties compared with unreinforced alloy. A wide range of aluminium alloys have been studied including casting alloys such as 357 (Al-7Si-0.5Mg) [19] and the heat-treatable wrought alloys 2xxx (Al-Cu) [20,21] and 6xxx (Al-Mg-Si) [22].

The advantage of using a precipitation hardenable alloy is that the composite strength may be increased by heat-treatment. However, the high temperature application of these composites is limited due to their susceptibility to overageing, hence weakening [23]. More stable aluminium alloys have been studied. For example, Scott, Kerry and Trumper have reported work [24] on the ageing characteristics of an Al-Cu-Mg-Ag alloy which is more stable than the conventional Duralumin alloys [2] at high temperatures; the use of this alloy in MMCs is currently being investigated [25]. The presence of the reinforcing phase, whether fibres or particulate, also affects the precipitation behaviour. Prangnell and Stobbs [26] have investigated the precipitation sequence in an Al-Cu alloy

reinforced with SiC particulate concluding that the ageing response of the alloy is accelerated as a result of the high internal stresses. This is confirmed by similar studies carried out on 2124 (Al-Cu-Mg) alloy reinforced with short SiC fibres [21].

1.2.5. Types of reinforcement used for composites

As mentioned in previous sections reinforcement can be in the form of long fibres, short fibres or particulate and are usually some type of ceramic such as silicon carbide or alumina. When used in MMCs these reinforcements are invariably woven, or bound, into some type of preform prior to the introduction of the metal matrix.

In this study, reinforcements of silicon carbide in both particulate and continuous form are used. The former is simply 'grinding grit' similar to that used on emery paper and is produced commercially by heating sand (SiO_2) with coke (C) to a temperature of ~2200°C [27]. The SiC is then ground to the appropriate size, usually within the range 1 μm to 150 μm, and graded before being used in MMCs.

The continuous SiC reinforcement is in the form of fibres manufactured commercially by Nippon Carbon Company under

the trade name 'Nicalon', and were developed by Yajima and co-workers [28] over ten years ago. These fibres are not produced by chemical vapour deposition (CVD), as used in the manufacture of SiC monofilaments [28,67,68], but by melt-spinning a polymeric precursor. This process has been well documented in a series of papers by Hasegawa and co-workers [29-34] the main points of which are outlined below, and summarised in Fig. 1.3.

The technique involves forming polydimethylsilane by reacting sodium with dichlorodimethylsilane [29] which is then heated with argon in an autoclave to ~450°C for 14 hours. This introduces Si-C bonds into the chain to give a poly-carbosilane. After condensing, fibres are formed by melt-spinning the polymer at ~350°C in inert gas atmosphere [30]. These fibres are very weak and have to be treated to prevent them from melting during subsequent stages of manufacture. This is achieved by curing the fibres at ~200°C in air, or by oxidation with ozone at room temperature, to form crosslinks thereby rendering the polymer infusible. This process, however, can introduce unwanted oxygen in the form of Si-O-Si and Si-O-C bonds which disrupt the Si-C-Si structure in later processing [34] and is difficult to remove. In the final stage fibres are slowly heated to ~1300°C, in vacuum or inert gas, which promotes the development of Si-C-Si bonds.

According to Bunsell, Simon, Abe and Akiyama [35] fibres obtained by the above route contain not only β-SiC, in the form of small crystallites ~5 nm, but also significant amounts of free carbon as well as excess silicon and oxygen probably combined as silica. This was confirmed by Sasaki, Nishina, Sato and Okamura [36] in a Raman study of similar fibres. More difficult to determine is the fibre composition, especially since three types of Nicalon are available - NLP 101, NLM 102 and NLM 202.

Simon and Bunsell [36] have analysed the first two grades of fibre using Auger spectrometry, reporting the average composition, ~65 wt% silicon carbide, ~10 wt% free carbon and ~25 wt% silica. Electron-probe microanalysis (EPMA) also revealed that the composition does not vary across the fibre, although the presence of a thin surface SiO_2 layer could not be ruled out due to the limited resolution of the technique.

More recent studies [38,39,40] have shown that the oxygen present in the fibre is in fact not combined solely with silicon but also carbon. Porte and Sartre [38] used x-ray photo-electron spectroscopy to identify this oxycarbide phase along with SiC, SiO_2 and free carbon. Bulk molar ratios were determined as $SiC:SiO_xC_y:C:SiO_2$ = 1:0.5:0.8:0.08. Laffon, Flank, Lagrarde, Laridjani, Hagege, Olry, Cotteret, Dixmier, Miguel, Hommel and Legrand [39] went one step further, proposing a structure

for the fibre which consisted of a 'continuum' of tetrahedra, SiC_4 and SiC_xO_y (where $x + y = 4$). They also identified silica in limited amounts at the fibre surface. The free carbon is thought to be distributed throughout the fibre as grouped aromatic rings, ~1 nm in size.

Bleay, Chapman, Love and Scott [40] have used quantitative EPMA to analyse the NL 227 grade Nicalon fibre, as used in the present work. By comparing the peak shapes of the soft x-ray spectra they were able to establish the nature of chemical bonding within the fibre from which the following phase compositions were calculated; ~63 wt% silicon carbide, ~22 wt% oxycarbide and ~15 wt% free carbon. An oxygen-rich layer was also detected at the fibre surface which was associated with silica.

The mechanical properties of the fibre also vary considerably. Nippon Carbon, the fibre manufacturer, claim a strength of ~2.5 GPa and a stiffness of ~200 GPa [41]. It is generally agreed that the value for stiffness is appropriate [35,43,46]. However, due to the strength being dependent on the defect population of the fibre, hence, gauge length, a variety of strengths have been published [28,29,35,37,41-48] within the range ~1 GPa to 2 GPa. This is further complicated by the variability in fibre diameter which affects pyrolysis, therefore, strength, and the grade of the Nicalon fibre tested which is not always reported with the results. The range of

diameters produced is due to the nature of the manufacturing process. Reported values are ~15 μm [35] for production fibres and ~13 μm for laboratory produced fibres [35,47]. The density of the fibres is fairly consistent at ~2.5 gcm^{-3}.

Bunsell *et al* [35] have published mechanical test data for the Nicalon grade NLM 202 fibre; the strength was 1.5 ± 0.5 GPa, and the modulus 193 ± 34 GPa, for a gauge length of 220 mm and a Weibull shape parameter, m, of 3.3. The number of samples tested is not given. A similar grade of Nicalon has also been tested by Chapman [19] who determined the strength of single fibres with a variety of pre-treatments. Measured values decreased from 1513 ± 473 MPa for as-received fibres, to 742 ± 299 MPa for fibres extracted from a 150.0 aluminium MMC, manufactured using liquid metal infiltration. Although the reported values for fibre modulus are all ~200 GPa, this is still below that for pure β-SiC, ~450 GPa. The lower modulus is due mainly to differences in structure with the SiC in the fibre being modified by the presence of the free carbon and oxycarbide phase [38,39,40].

In high temperature studies of Nicalon [35,41-48] the fibre was found to be stable up to ~1000°C, above which mechanical properties decreased. However, the majority of MMCs are aluminium-based and will therefore be limited to temperatures of ~400°C. It is only during liquid metal

processing that fibre degradation may occur although the temperatures involved are ~750°C. Nicalon fibre will only experience higher temperatures when used in glass or ceramic matrix composites [7,47].

1.3. Primary fabrication techniques

Although numerous MMC fabrication routes are available, the production of consistently sound material is still a problem with only a few MMC components being manufactured commercially. The most fundamental problem in MMC manufacture is how to combine reinforcement with the metal and achieve good dispersion. For example, in fibre composites the non-wetting phenomenon means that pressure has to be applied during casting to ensure thorough infiltration, whilst for particulate composites it is often difficult to overcome grouping of reinforcement.

A summary of MMC manufacturing techniques, for MMCs with continuous and discontinuous reinforcement is shown in Figs. 1.4a and 1.4b, respectively [16]. Other reviews include 'Fibre-reinforced MMCs' by Chou, Kelly and Okura [49], 'Solidification processing of reinforced metals' by Mortensen [50], and 'Processing of particulate MMCs' by Ibrahim [12]. The most common techniques are described below.

1.3.1. Liquid metal infiltration

The liquid metal infiltration (LMI) process is used mainly for fabricating continuous or long fibre composites. In this technique, a fibre preform is placed in a preheated die, which is then evacuated, followed by introduction of liquid metal via positive pressure, Fig. 1.5. Preforms usually consist of continuous fibres of Nicalon, carbon or Safimax (ICI alumina fibre) and are in the form of either unidirectional or woven fibre tows. It is also possible to use short fibre preforms such as Saffil (ICI alumina) although these normally find application in squeeze cast MMCs. Thin sheet or thin walled components can be made by the LMI process although intricate shapes are a problem. Well dispersed, low volume fraction composites are also difficult to produce. It is proposed that the LMI process will supply a low volume, high performance market such as the aerospace industry [4]. This is due mainly to the high cost of the fibre reinforcement. Variations of the LMI process are described in a paper by Mykura [51].

In the present work use is made of a Nicalon fibre reinforced aluminium alloy, manufactured by Cray Advanced Materials using a LMI process patented by Booth, Clifford and Parratt [52]. Here, molten aluminium, superheated to ~750°C, is introduced into the die or mould under low pressure with maximum pressure (~7 MPa) being applied only at the end of the cycle. This gives minimum preform

movement, or fibre drift, whilst maintaining maximum consolidation.

1.3.2. Squeeze casting

Essentially, squeeze casting involves compressing molten metal during solidification in order to compensate for the volume contraction. The process was first used over fifty years ago in Russia [2] and more recently has found uses in the West. Industrial applications include the production of aluminium alloy wheels, first introduced by the Toyota Motor Company in 1979.

The pressure applied during the process may vary from ~3 MPa to 200 MPa, although for commercial routes the higher pressures are usually required. The high pressures involved force entrapped gases into solution, thereby reducing closed porosity and increases mould wall contact allowing more rapid cooling and a refinement in microstructure. This gives an increased strength and ductility (up to 50%) compared with alloys cast using conventional foundry techniques [2]. Another effect of pressure which has to be considered is the increased freezing temperature of the melt which can be up to 25°C for 200 MPa [49].

Squeeze casting is also a near-net shape process, due to the absence of runners and gates, which makes it an ideal candidate for the production of MMC components since these are difficult to machine. This has been taken advantage of in the use of squeeze cast aluminium reinforced with short alumina fibres for pistons in high performance internal combustion engines [2,50,54].

Most of the squeeze cast MMC material currently under investigation is produced in academic institutions in small amounts using relatively simple equipment. One of the first studies was carried out by Bader, Clyne, Cappleman and Hubert (1985) who reported work [55] on aluminium alloy infiltrated alumina preforms. Similar studies have since been described in many other publications [14,16,17,19-22,50-60].

The fibre preform is invariably made from short alumina fibres bound together with silica and is disc shaped. This is the most common type of reinforcement although other fibres can be used [20,21]. For example, Coleman [61] has produced long fibre composites by squeeze casting using a preform made by winding fibre tows around a rectangular mandrell.

A schematic diagram of the squeeze casting technique is shown in Fig. 1.6. The fibre preform, or insert, is first desized at around 600°C and then placed in a die cavity

preheated to ~300°C. Superheated molten metal (typically aluminium) is then introduced via a launder, in excess to ensure that the preform is not crushed during 'squeezing', and pressure applied (~20 MPa) using a hydraulic ram. This is held for several minutes, forcing the liquid metal into the preform and consolidating the casting during solidification. The applied pressure is usually limited by the capacity of the hydraulics, which is obviously lower than a parallel industrial process. After the die has cooled to below ~200°C the ram is withdrawn from the die and the MMC billet is removed by means of the dovetail profile.

Above a preform volume fraction of ~0.3 (Saffil fibres) infiltration is poor often resulting in excessive fibre crushing. The volume fraction may be increased to ~0.6 by using long fibres [61,62], as these are more readily infiltrated.

1.3.3. Compocasting.

This MMC fabrication route involves combining the reinforcement (usually ceramic particulate) with a molten or semi-solid metal. In terms of commercial development, the DURAL (stir casting) process [12] is probably the most advanced, involving the mixing of ceramic particulate with

molten metal (typically an aluminium alloy). Although the exact details of the technique remain confidential it is widely known that difficulties have been encountered [12], including settling of the reinforcement, segregation of second phases, interfacial reactions and fracture of the reinforcement.

Rheocasting, a similar process, was originally developed for unreinforced alloys by Flemings, Rick and Young [63]. The principle is simple; a semi-solid metal (temperature between liquidus and solidus) is vigorously agitated so as to break up any interdendritic growth. Normally the melt would be too viscous to pour above 20% solid content [2] but, using this process fluidity can be maintained up to 60% [49]. This has obvious benefits such as lowering pouring temperatures, reducing shrinkage, as well as refining the microstructure.

It was soon realised that MMCs could be manufactured using a similar route [12,14]; reinforcement added during the agitation stage would, unlike fully liquid metals, disperse evenly and be held in place between the solid matter. The lower temperatures involved would also reduce the severity of any matrix/reinforcement interfacial reactions.

For high volume fractions of reinforcement, ~0.6, a secondary process is often required to consolidate the MMC

[14,49] such as squeeze casting, injection, gravity casting, rolling or extrusion, although the high pressures involved can damage the reinforcement particularly if short fibres are used.

1.3.4. Spray deposition

Spray deposition was developed by Osprey Metals to manufacture simple shapes from difficult to cast alloys such as steels, superalloys, copper and aluminium [12,64]. The technique involves directing a stream of atomised liquid metal (using N_2) onto a substrate, or collector, the shape and motion of which determines the form of the final product. The rapid solidification rate of the metal minimises segregation and refines the grain size with no significant increase in solute solubility.

This process has been developed further by ALCAN to manufacture MMCs using spray co-deposition [64]. Particulate reinforcement (usually SiC) is injected into the atomised liquid and subsequently co-deposited onto the substrate. The alloys used include Al-Cu-Mg (2xxx series), Al-Mg-Si (6xxx series) and Al-Zn-Mg (7xxx) series as well as casting alloys such as Al-Si. The resultant MMC ingot can be up to 150 kg [65], ~98% dense, with an even distribution of reinforcement.

Spray deposition compares favourably with more conventional powder processing routes for MMC manufacture, but avoids expensive blending operations. One drawback, however, is that the volume fraction is limited to ~15-20% with particulates rarely less than 15 μm [13]. As with other MMC fabrication techniques the co-deposited billet can be processed further using rolling, extrusion and forging [14].

1.3.5. Powder metallurgy

This technique is derived from the more conventional powder metallurgy route for manufacturing metal alloy components. The most common MMC production process is shown schematically in Fig. 1.7. [12] and involves the blending of pre-alloyed powders with the reinforcement (invariably SiC grit), pressing to ~75% density followed by degassing and consolidation using some form of hot pressing. Further processing, such as rolling or extrusion, is usually necessary to form more specific shapes as well as to break up and disperse any residual oxide present on the alloyed powders [64].

Variations on the above theme include pressing at higher temperatures, sometimes forming liquid phases, to achieve greater consolidation. This can also have the benefit of

increasing matrix-reinforcement bonding and reducing processing pressure, hence, fracture of the reinforcement [14].

The powder metallurgy (blending) route is one of the most expensive MMC manufacturing techniques, but is the easiest for producing high volume fraction (up to 50%) particulate composites. It is likely, therefore, that the process will produce components for high cost, low volume applications such as aerospace [64].

A SiC particulate-reinforced aluminium alloy (2124), manufactured by British Petroleum using the powder blending-extrusion route [10], is used in the present work.

1.3.6. Diffusion bonding

Diffusion bonding is one of the oldest MMC manufacturing techniques, developed in the 1960's for fabricating mainly aluminium-based continuous fibre composites. The process involves consolidating layers of preformed MMC, usually in sheet form, by applying heat and pressure. The preform sheet is made using techniques such as roll bonding, step pressing, plasma spraying and continuous casting [16-18,49,69]. It is very important to clean surfaces prior

to bonding because the residual oxide layer present on metals can cause problems, particularly with aluminium. This can be reduced by bonding in a vacuum, although some oxide will always be present in the consolidated composite.

Early work was carried out using boron monofilaments with aluminium alloys. Here, bonding temperatures were low (<480°C) so as to minimise fibre degradation caused by interfacial reactions [16,67,68]. However, because both bulk diffusion and surface deformation are temperature dependent bonding times were long, >30 minutes, and applied pressures high (~100 MPa) often resulting in fibre damage.

The advent of the more stable SiC monofilaments enabled liquid-phase bonding to be used. This was achieved at temperatures above 500°C and used either low melting point alloys, or interlayers between preformed MMC sheet. The lower pressures, <10 MPa, and short bonding times, ~5 minutes, used in this process also reduced fibre damage and interfacial reaction [16].

Yajima, Okamura and Tanaka [70,71] have developed a fabrication technique derived from the diffusion bonding route. Here, preformed Nicalon fibres are stacked with aluminium foils in an evacuated die and heated to ~720°C, at which point ~20 MPa is applied for 5 minutes. The

aluminium melts and is consolidated by the applied pressure, similar to LMI or squeeze casting.

The major drawback with all these fabrication processes is the expense arising from the cost of the reinforcement, tooling and the intensive labour involved.

1.4. Composite microstructure and properties

The mechanical properties of a composite material depend not only on those of the matrix and reinforcement but also on factors such as orientation, shape, volume fraction and distribution of the reinforcing phase. The matrix/ reinforcement interface is also an important feature as it transfers load and controls the fracture behaviour of the composite. In MMCs, particularly with long fibre reinforcement, the high temperatures involved during manufacture often lead to fibre/matrix interfacial reaction which lead to a low toughness and strength [49].

In this section, microstructure-property relationships are reviewed for MMCs used in this work, namely, aluminium alloy (2124) reinforced with SiC particulate produced via a powder metallurgy (PM) route, and aluminium alloy (150.0) with continuous Nicalon fibre reinforcement manufactured using LMI.

The mechanical properties of the 2124/SiC_p composite have not been widely published. Humphreys *et al* [13] reported that gains in tensile strength of up to 100 MPa may be achieved compared with base metal, measured as 450-500 MPa with T8 treatment [2,21]. The stiffness of the composite is also higher following a rule of mixtures with a volume fraction of 0.2 giving a Youngs modulus of ~100 GPa. However, fracture toughness and ductility are low, due mainly to the inhomogeneity of the reinforcement [11].

With regard to the interface numerous papers have been published on the reaction of SiC with aluminium alloys [12,13,14,19,72-77]. It is generally accepted that for solid-state processes such as PM limited interfacial reaction occurs, with matrix/reinforcement bonding being achieved mainly by mechanical keying [12,13] and interdiffusion [72].

In these composites the low aspect ratio of the SiC_p results in a small strengthening effect by load transfer from matrix to reinforcement. The major contributary effects occur in the matrix and these include internal stresses, grain size, substructures, work hardening, dispersion strengthening and, in the case of the 2124 alloy, precipitation hardening. These phenomena may be explained more fully by considering the movement of dislocations within the matrix and how they interact with the reinforcement and dispersoids [9,13,78,79].

High dislocation density is an unavoidable feature in most MMCs, created during manufacture or some other thermo-mechanical treatment. Most are generated during cooling as a result of the differences in contraction of the matrix and reinforcement. These tend to cluster near the reinforcement increasing the local flow stress of the matrix. This coupled with forest interaction of dislocations can increase the work hardening rate. Another strengthening effect is due to the refined grain size caused by increased nucleation at SiC reinforcement; recrystallisation may also be hindered leaving a dislocation structure in the form of subgrains. Both these strengthening mechanisms have been reported to follow a Hall-Petch type relationship [13]. Dispersoids also contribute to the strength of the composite by offering resistance to dislocation movement. These include not only the intentional intermetallic phases, but also residual oxides originating from the surface of the alloy powder. According to Humphreys *et al* [13] these oxides may influence grain size but appear to have little effect on mechanical properties. However, alumina levels as high as ~0.8% have been reported by Barlow [82] for an Al/SiC_w MMC produced by PM in which the whiskers had an alumina size. The yield strength was increased by ~20% and the initial work hardening rate doubled compared with a MMC using uncoated whiskers.

Peak ageing is usually difficult to attain because the precipitation sequence is accelerated by the large number of dislocations present in the matrix [13]. They also tend to be unevenly distributed clustering near to SiC particles where dislocation density is high [26]. There are few publications on the ageing of 2124/SiC_p MMCs; most work has been carried out on other systems utilising other Al-Cu alloys [79]. Studies are reported, however, for 2124 alloy reinforced with SiC whiskers [21,23,78,80-82].

The high temperature strength of most particulate composites is low since the dislocation interactions discussed above can be relieved by climb processes above ~300°C [13,79,82]. For composites with age-hardenable matrices (such as a 2xxx series aluminium alloy) an additional loss of strength may occur as a result of precipitate overageing [21,23,78-82].

The mechanical properties of long fibre MMCs depend not only on the strength and stiffness of the reinforcement but also on the microstructure of the matrix and fibre/matrix interface as these transfer load to fibres. Longitudinal and transverse strengths for aluminium unidirectionally reinforced with Nicalon fibre have been reported by Chapman [19] as 149 ± 22 MPa and ~20 MPa, respectively. The composite, manufactured using LMI, had a volume fraction of 0.44. The transverse strength was increased to 83 ± 8 MPa by using a woven fibre preform,

although the longitudinal strength was reduced to 130 ± 12 MPa. The low strength of these composites was attributed to microstructural features arising from manufacture, including large regions of porosity due to poor infiltration caused by the uneven distribution of fibres, and embrittlement by intermetallic bridging of fibres. Degradation of the fibre/matrix interface also occurred by the formation of aluminium carbide, not as a continuous layer over the surface of the fibre, but as small needles growing into the aluminium matrix. The following carbide forming reaction is the most widely published for aluminium/SiC composites produced via liquid-phase routes [12,13,20-23,49-53,72-77],

$$4Al + 3SiC \rightarrow Al_4C_3 + Si \qquad (1)$$

However, for composites involving Nicalon fibre, which also contains free carbon and an oxycarbide phase, other carbide forming reactions have been suggested [19],

$$4Al + 3C \rightarrow Al_4C_3 \qquad (2)$$

$$(2x+4y)Al + 3SiO_xC_y \rightarrow xAl_2O_3 + yAl_4C_3 + 3Si \qquad (3)$$

Studies by Chapman [19] on Nicalon fibre reinforced aluminium found Al_3C_4 and Al_2O_3 in isolation at the interface indicating that reaction (3) was not responsible for carbide formation. He concluded that the free carbon reaction (2), as reported by Yang and Scott [83] for carbon/aluminium composites, was the main Al_4C_3 forming reaction. The alumina particles were believed to have

formed by the reaction of aluminium with the silica layer present on the fibre.

1.5. Secondary fabrication techniques

Secondary fabrication is an integral part of any manufacturing route, often involving processes such as forming, machining and joining. For conventional metals and alloys these are well established and relatively easy to perform. For fabricating MMCs, however, these techniques are often unsuitable due to problems caused by the ceramic reinforcement.

1.5.1. Forming

Forming processes such as rolling, extrusion and forging have been used for MMCs, with varying degrees of success, the main problems arising from the hardwearing and brittle nature of the ceramic reinforcements which result in composite damage and excessive tool wear rates [84]. Reinforcement damage occurs as a result of the high deformations experienced during processing and long fibres are particularly unsuitable. Durrant, Scott, Trumper and Clift [85,86] have reported that simple upset forging of

Saffil/aluminium composite cylinders resulted in gross fibre breakage even at temperatures up to the melting point of the aluminium, although less damage was observed for lower fibre volume fraction composites. Particulate-reinforced composites are most suited to forming processes although high tool wear rates may still be encountered [14].

1.5.2. Machining

MMCs are notoriously difficult to machine due to the hardwearing and brittle nature of the ceramic reinforcements. The degree of difficulty can vary according to the type of reinforcement used, its volume fraction and distribution. Conventional techniques such as cutting, turning and milling may be used although high tool wear rates are often encountered as well as reinforcement damage [87]. This damage may be severe for long fibre composites, often extending some tens of μm below the surface, although machining with diamond-tipped tools reduces this markedly [88]. Other cutting techniques are reviewed by Gindy and Clegg [89] where, for almost every process, similar problems were encountered. More sophisticated techniques involve cutting the composite with an energetic beam of light (laser) or electrons. In these processes, however, melting often

occurs, which may alter the alloy microstucture or produce regions of non-wetted reinforcement. Even using a water-jet cutting technique the abrasive used may cause melting as a result of frictional heating.

1.5.3. Joining

Several techniques for joining MMCs have been investigated, ranging from the conventional mechanical fastening to more sophisticated techniques such as diffusion bonding. The main difficulties associated with these processes are the preparation of surfaces prior to joining, high tool wear rates and reinforcement damage.

Techniques which involve mechanical fastening such as bolting or riveting require substrate drilling which, as well as causing reinforment damage, gives rise to stress concentrations which may cause premature failure of the composite during service [84]. Damage during the preparation stage may be reduced by using adhesives, although these have a low strength (~40 MPa), requiring large overlap areas, and are stable only up to ~100°C. Conventional joining processes with high temperature stability, such as welding and brazing, create extensive molten regions which encourages fibre/matrix reaction and microstructural changes to the matrix, which may reduce

the mechanical strength of the composite. Furthermore, for aluminium alloys, welding often requires the use of a flux to disrupt the surface oxide and this may cause corrosion problems during service [90]. An alternative high temperature joining technique is diffusion bonding, a process used commercially for titanium, although its application to joining aluminium alloys is not yet established. The technique is also a potential candidate for bonding together MMCs since the low pressures and temperatures involved would minimise reinforcement damage and interfacial reaction.

1.6. Diffusion bonding techniques

Diffusion bonding has been extensively used to join metals to themselves [91,92] and to other metals [93], as well as to ceramics [94-96]. The process involves applying pressure to a workpiece held at high temperature, usually in an inert gas or low pressure atmosphere to limit the surface oxidation which may otherwise inhibit metal diffusion across the interface. The technique works well with titanium because oxides and contaminants are readily dissolvable in the metal at bonding temperatures of ~850°C [2,92], and is often combined with superplastic forming [97,98]. With aluminium, however, the tenacious oxide film forms a diffusion barrier which inhibits bonding

[99]. Halide fluxes may be used, although it is likely that corrosion problems would arise during service. Fragmentation of the oxide by deformation is another solution [100], although this process may cause extensive reinforcement damage when used for joining MMCs. Another approach employs a metal interlayer which reacts with the aluminium to promote diffusion but, in doing so, brittle second phases may be formed which are deleterious to joint strength [93]. If, however, the appropriate interlayer material is chosen a low melting point phase may be formed at the joint, a process usually termed diffusion brazing, transient- or liquid-phase bonding [93]. Solid-state and liquid-phase diffusion bonding techniques are summarised in Fig. 1.8.

1.6.1. Diffusion in metals

Diffusion is defined as the movement of a species through a medium in either the solid, liquid or gaseous state. In the present work, solid- and liquid-state diffusion processes are used to bond metals and MMCs. Diffusion in solids is easier to explain as much work has been published on the subject. In the next section, an outline of the main features of solid-state diffusion in metals is given along with a brief description of diffusion within liquids.

Diffusion in the solid-state

A number of mechanisms have been proposed for the movement of atoms within the interior of a metal [101],

(a) Direct interchange of atoms,

(b) Zener ring mechanism,

(c) Vacancy diffusion.

These are illustrated schematically in Fig. 1.9.

Each mechanism is dependent on the crystal structure of the metal. It is generally recognised for face-centred cubic metals that (c) is the main method for atomic movement, since it requires the least amount of thermal energy to be activated. This proposition is supported by results from experiments which trace the movement of the bond interface during the diffusion bonding of dissimilar metals where the velocity of the interdiffusing atoms is unequal, an effect which can be explained only by the vacancy theory. This phenomenon of unequal diffusion, more commonly known as the Kirkendall effect, may lead to the formation of porosity on the side of the diffusion couple which contains the more mobile species. As the vacancy distribution increases with an increase in temperature the atoms in the lower melting point metal will diffuse more rapidly. This difference in atomic flow may also create an asymmetrical stress state in the material, which may lead to structural changes normally associated with high temperatures and plastic deformation, such as recrystallisation and grain growth. The

application of pressure during diffusion bonding, however, may inhibit the the formation of porosity by reducing vacancy mobility.

Diffusion in the liquid-state

The rate of diffusion in a binary eutectic liquid (just above the melting point) is around several orders of magnitude greater than for a similar alloy in the solid-state [101]. This is surprising since metallic liquids are known to have a similar atom separation to metallic solids, as evidenced by their similar densities. There is no exact description for the structure of liquids, however, it is believed that regions of short range order exist surrounded by large numbers of defects such as dislocations. Applying the vacancy theory shows that the energy associated with diffusion in liquids is lower than in the solid-state.

Modelling solid-state diffusion bonding

Most modelling, or predictions, of diffusion in metals in the solid-state are derived from Fick's second Law,

$$\frac{\delta N_A}{\delta t} = \frac{\delta}{\delta x} \tilde{D} \frac{\delta N_A}{\delta x}$$

where, $\tilde{D}$ is the diffusion coefficient (area/sec)

N_A is the atom fraction of element A

x is the distance from a reference point

t is time of process.

Solutions of the differential equation may be used to determine the concentration of a species at a distance, x, from the interface at time, t. There are two methods for determining the diffusion coefficient (assuming a one-dimensional flow of atoms, as in a diffusion couple). In the first, the diffusion coefficient is assumed constant, whilst in the second method it varies with solute composition.

Using the first assumption, a solution of Fick's second law was proposed by Grube [101],

$$N_A = N_{A1} + \frac{(N_{A2} - N_{A1})}{2}[1 + erf\ \frac{x}{2\sqrt{\tilde{D}t}}]$$

where, N_A is the composition or atom fraction at a distance x (in cm) from the weld interface, t is the time in seconds, and $\tilde{D}$ is the diffusivity. The symbol $erf\ x/2\sqrt{\tilde{D}t}$ represents the error function, or probability integral, with the argument $y = x/2\sqrt{\tilde{D}t}$, and is defined by the equation

$$erf(y) = \frac{2}{\sqrt{\pi}} \int_0^y e^{-y^2} dy$$

Evaluated tables for this function may be found in standard mathematical tables [102]. Thus the equation may be used to determine the diffusion coefficient of a species in a two-component system (diffusion couple). The $\tilde{D}$ value may then be used to predict the concentration profile for a diffusion couple at time, t.

The second method for describing diffusion in a couple was proposed by Matano, and is again based upon a solution of Fick's Second Law. This method is more complicated than the Grube method, relying on measurement of the concentration profile through a couple from which the diffusion coefficient is calculated. The reader is referred to Reed-Hill [101] for further concise explanation, and to Crank [103] for a more rigorous approach.

Both the Grube and Matano methods have been used with some degree of success to model simple experiments on diffusion couples. It must be pointed out, however, that the diffusion couple has to be of high purity and the two metals must be mutually soluble (such as copper-nickel). For systems such as the aluminium-copper couple the maximum solubility of copper in aluminium is only ~5 wt% (at 548°C) and it is likely that intermetallic phases will be formed once the solubility limit is exceeded [104]. This would create another diffusion couple requiring separate mathematical treatment.

Diffusion occurs not only through bulk metal but also at defect areas where the concentration of vacancies is high, including grain boundaries, dislocations and free surfaces. The radius of curvature of the surface is inversely proportion to the driving force for diffusion and is therefore an important factor in solid-state

bonding since the mating surfaces are microscopically rough. According to Partridge and Ward-Close [93] the solid-state bonding process may be divided into two parts. Stage 1, which involves the plastic deformation and creep deformation of the surface asperities on loading and, Stage 2, where diffusion, recrystallisation and grain boundary migration takes place in the bond region. The latter stage is important if a high strength joint is to be formed, as this removes the planar bond interface. After Stage 1 the joint interface consists of bonded regions of intimate metal-to-metal contact separated by areas of small voids, shown schematically in Fig. 1.10. Voids less than ~20 μm may not be eliminated by the pressure applied during bonding but only by diffusional mechanisms. Hill and Wallach [105] devised a model to predict the rate of void shrinkage during the diffusion bonding of two surfaces of known 'roughness', from which the percentage area of metal-to-metal contact at the bond interface was estimated. The results from this model were subsequently shown to correlate with diffusion bonding experiments on copper [106] and a low-alloy steel [107], where the area of bond was estimated using fractographic analysis in the SEM. Other models, using a similar approach, have also been successful in predicting the bonded area for diffusion-bonded joints in a range of metals [108-111].

These models do not, however, accurately predict the bonding behaviour of aluminium since no allowance is made for the inhibiting effect on diffusion caused by the surface oxide film [93,99].

Modelling liquid-phase diffusion bonding

As mentioned earlier, diffusion in liquid metals is not well understood and it would be even more difficult to model the liquid-phase diffusion bonding process, since variables such as pressure and composition are involved. Although no mathematical description of the bonding process is available, a qualitative description has been proposed [93]. This 'idealised' bonding mechanism, which is divided into two parts, is illustrated in Fig. 1.11. Stage 1 involves the reaction of the interlayer with the base alloy to produce a liquid phase, a process which is believed to occur within a few seconds. In Stage 2, the interlayer element diffuses into the base alloy, via the solid-state, thereby depleting the liquid to result in isothermal solidification of the joint. This is followed by homogenisation of the bond region as the interlayer element diffuses further into the base alloy. As with the solid-state bonding model, no account is taken of any surface oxide or contaminate film which may inhibit bonding.

1.6.2. Diffusion bonding aluminium alloys

Solid-state diffusion bonding

Much of the reported work on the diffusion bonding of aluminium alloys has been carried out in the solid-state. The low pressure bonding methods adopted for other metals do not work because of the surface oxide film which forms a barrier to diffusion [99]. Bonding therefore involves the application of large deformations such that the oxide layer is fragmented and allows metal diffusion [100]. The technique works well for unreinforced aluminium but is not suitable for MMCs since the reinforcement may be damaged. An alternative bonding method uses interlayers, although these may cause intermetallics to form leading to low strength joints [112]. Another technique involves the modification of the aluminium alloy such that the surface oxide film is disrupted by a volume change as a result of a chemical reaction [99]. These alloying additions have a lower free energy of formation with oxygen than aluminium, and include magnesium or lithium. Fortunately, these elements are present in sufficient amounts in several commercially available aluminium alloys (2xxx and 8xxx series).

This bonding method has been used by Maddrell, Ricks and Wallach [113] for Al-Mg and Al-Li alloys who reported that the magnesium-containing alloy formed higher strength joints, due presumably to the greater disruption of the

Al-Li (8090) by Gilmore, Partridge and Dunford [114], shear strengths approaching that of the base alloy (~200 MPa) were achieved. There are no published data, however, on the bonding of 2xxx series aluminium alloy.

Liquid-phase diffusion bonding

Liquid-phase bonding allows the use of shorter process times and lower applied pressures than solid-state methods since it is easier to gain intimate surface contact. Two different bonding methods for aluminium utilising a liquid phase have been reported. These are (a) bonding at a temperature between the solidus and liquidus, without an interlayer and, (b) the use of an interlayer below the solidus temperature of the aluminium such that a liquid eutectic phase is formed.

Enjo and Ikeuchi [115] adopted method (a) for joining an Al-Cu-Mg (2017) alloy, reporting bond strengths close to the base metal. However, the deformation of the workpiece was high (~50%) giving little control over the dimensions of the specimen. This technique would be unsuitable for joining MMCs, particularly with continuous reinforcement, since the large deformations involved would cause extensive damage to the fibres. The only advantage of using technique (a) is that an interlayer material is not required.

Method (b) has been used in a number of studies on bonding aluminium alloys [116-118], the majority of interlayers were based upon copper and silver whose eutectic temperatures with aluminium are low (548°C and 566°C, respectively). Strengths approaching the alloy substrate have been reported, although the main advantage is that the specimen deformation is low (<5%). This technique is therefore a candidate for joining MMCs.

1.6.3. Diffusion bonding metal matrix composites

There is little published work on the joining of MMCs, particularly methods utilising diffusion bonding techniques. This is not through lack of interest, but by the numerous problems associated with primary fabrication methods. Only when reproducible, high quality MMC is produced will secondary fabrication methods, such as diffusion bonding gain significant attention. Nevertheless, if MMCs are to be used commercially, as is often mentioned, these difficulties will have to be overcome.

It has been stated that titanium alloys may be readily diffusion bonded. However, the bonding of titanium-based composites is not so easy, the main difficulty being the inability to join together reinforcements exposed at the

bonding surfaces. Thus the effective area of bond occurs only at regions of metal-to-metal contact. Bonding studies on particulate-reinforced titanium [119], using both solid-state and liquid-phase techniques, showed that the composite joint strength is far less than the bonded unreinforced alloy. The problem is worsened when the reinforcement is in the form of continuous SiC filaments, particularly in a butt-joint, as the filaments could not be bonded [120]. The use of an unreinforced titanium alloy interlayer did, however, produce a higher strength joint by increasing the metal-to-metal contact.

Aluminium-based composites are even more difficult to bond since the surface oxide restricts the degree of metal-to-metal contact as well as the ceramic reinforcement. Even adopting an Al-Li alloy, which is relatively easy to bond, the presence of 17 vol% SiC particulate has been shown [121] to halve the shear strength of the joint (to ~100 MPa). As with the long fibre titanium composite, some strength was regained (~150 MPa) by using an 8090 alloy interlayer which increased the metal-to-metal contact. The highest strength (~170 MPa) was attained, however, when using a liquid-phase bonding method utilising a copper interlayer, since the 'weak' planar interface, normally associated with the solid-state method, was eliminated.

Enjo, Ikeuchi, Murakami and Suzuki [122] bonded aluminium alloy (6061) reinforced with short alumina fibres using a liquid-phase technique using a variety of interlayers, including copper and silver. The tensile strengths of the joints were close to that of the composite material, and this was attributed to the mechanical keying of fibres at the surface with the solidified eutectic phase.

For long fibre reinforcements it is recommended that butt-joints, with fibres end-to-end, be avoided since it is not possible to bond them together [122-125]. Most studies have adopted the liquid-phase bonding route utilising an interlayer (usually copper) with a lap-joint arrangement where the fibres are parallel to the bond interface. However, problems are also encountered using this method, including the inhibition of the diffusion of copper into the aluminium matrix by the presence of the fibres [123], as well as the need for very large overlap areas [124] due to the poor shear strength of the joint. Indeed, in some cases failure occurred not at the joint interface but in the adjacent composite [125], although this is not totally unexpected as the transverse strengths of most unidirectional MMCs are very low.

1.7. Scope of the investigation

From a study of the literature it would appear that only limited studies have been carried out on the diffusion bonding of MMCs. Furthermore, there has been little or no explanation of the mechanisms of the process or how the reinforcement might affect bonding. The present work will focus attention on understanding the mechanisms for diffusion bonding of unreinforced aluminium alloys and then will study the effect on the process caused by the presence of ceramic reinforcements (fibre or particulate).

The composite materials to be investigated are commercial-purity aluminium reinforced with Nicalon fibre and an Al-Cu-Mg alloy (2124) reinforced with particulate silicon carbide.

Bonding studies of composites and unreinforced alloys will be carried out in air using a range of temperatures and applied pressures. In most cases a metal or alloy foil interlayer will be used whose composition is such that a low melting point liquid phase is formed by reaction with the aluminium. This selection is based upon assessment of the relevant phase diagrams and will include the elements magnesium, copper, zinc, nickel and silver.

In order to assess the mechanical strength of bonded joints a jig has been designed which which largely

overcomes the problems of peel normally associated with the more conventional lap-shear test. A method is given for determining the area of a bonded joint which is based on fractographic analysis by means of light and scanning electron microscopy. A detailed and systematic study of the related microstructures will then be carried out using electron-probe microanalysis and transmission electron microscopy.

Based on data from microstructural observations mechanisms for the formation of diffusion bonds will be formulated for both unreinforced alloy and composites. The rôle of the composite reinforcement will be assessed by comparing area of bond and shear strength developed with those for unreinforced alloy.

2. EXPERIMENTAL PROCEDURE

2.1. Materials used in the investigation

2.1.1. Unreinforced aluminium alloys

The alloys used in this work comprised commercial-purity aluminium (IADS No. 1100) supplied as rolled sheet, 6 mm thick, and an aluminium-copper-magnesium alloy (IADS No. 2124) supplied in the T851 condition (solution treated, cold worked and artificially aged, [2]). The nominal compositions of these alloys are given in Table 2.1a.

2.1.2. Commercial-purity aluminium reinforced with Nicalon fibre (Al/Nic)

For the composite material a casting type aluminium alloy (Aluminium Association No. 150.0) of similar composition to the 1100 alloy, Table 2.1a, was used for the matrix, and Nicalon fibre (grade NL 227) for the reinforcement. The composite was manufactured by Cray Advanced Materials by liquid metal infiltration of a fibre preform using an applied pressure of >7 MPa and a melt temperature of ~750°C. It was supplied as 3 mm thick sheet with equal numbers of fibres aligned in the 0° and 90° directions to give a nominal fibre volume fraction of ~0.4.

2.1.3. Aluminium alloy (2124) reinforced with SiC particulate (2124/P)

The composite material was manufactured by British Petroleum and supplied as 25 mm diameter bar. This was produced using the powder metallurgy/extrusion route (described in section 1.3.5.) although the exact details of the process were not disclosed. The SiC reinforcement had a nominal particle size of 3 μm and was present in the composite in volume fractions of 0.25, 0.30, 0.35, and 0.40.

2.1.4. Interlayers for bonding

In this study both solid-state and liquid-phase bonding processes were investigated. In most cases bonding was promoted by the use of an interlayer, the compositions of which are given in Table 2.1b.

Solid-state bonding was carried out using aluminium-copper-magnesium (2124) alloy interlayers, ~200 μm thick, produced from the as-received 2124 alloy billet by successive rolling and annealing.

For liquid-phase bonding a material was chosen which formed a low melting point phase with aluminium and which

was available as a foil. Data obtained from the relevant phase diagrams showing the eutectic temperatures and compositions of selected aluminium alloys are given in Table 2.2. The interlayers used were zinc, copper, nickel-coated copper, copper-silver alloy and a copper-zinc alloy. These were supplied as foils direct from the manufacturer Goodfellow, except for the nickel-coated copper which was prepared using the Buehler Edgemet electroless plating technique.

2.2. Diffusion bonding experiments

2.2.1. Bonding apparatus

At the start of the research programme a high temperature facility, suitable for diffusion bonding, was constructed. This was based on a screw-driven Instron testing machine of 10 tonnes capacity equipped with a tube furnace and stainless steel platens, Figs. 2.1a and 2.1b. Loads applied to the specimen via the platens during bonding were measured by a load cell connected to the bottom platen through a water-cooled coupling. Temperature was monitored using thermocouples placed in the heated region of the furnace and located below the surfaces of the platens. The temperature of the sample was obtained indirectly using results from a calibration experiment; an

aluminium block, in which a thermocouple had been mounted, was slowly heated to 600°C and the platen and furnace temperatures recorded. The sample temperature was found to be ~10°C higher than the platen temperatures, which were within 5°C of each other.

2.2.2. Prior preparation of joint surfaces

The size of the bonding specimens was limited by the 75 mm furnace bore and also by the dimensions of the supplied materials. For unreinforced alloy specimens measuring 25 mm x 60 mm x 6 mm and 45 mm x 45 mm x 6 mm were cut from sheet or ingot using a coarse SiC wheel. For composite material a resin bonded diamond wheel was used to cut samples in a range of sizes, from 30 mm x 30 mm x 3 mm to 45 mm x 45 mm x 3 mm for the fibre composite and 25 mm dia x 6 mm for the particulate composite.

In all cases the surfaces to be bonded were ground, using progressively finer silicon carbide paper, down to 1200 grit followed by ultrasonic cleaning and rinsing in acetone. The copper foil was cleaned in 10% vol H_2SO_4 followed by degreasing in acetone, whilst the other foils were simply degreased. The interlayers were then placed

between the prepared alloy (or composite) plates ready for bonding.

2.2.3. Bonding procedure

With regard to the bonding operation, once the required temperature had been reached the furnace was raised and the sample positioned on the bottom platen. Prior to bonding the thickness of the sample was recorded and this was compared with values obtained after bonding so that the permanent deformation induced during the operation could be determined. To prevent adhesion to the platen surface the sample was sandwiched between steel shims, Fig. 2.2. The furnace was lowered until the platens were in contact with the sample. Load was then applied at a rate of 0.5 mm/min to the required sample pressure. However, a constant pressure could not be maintained during the bonding process because of the absence of automatic load compensation for deformation of the specimen. Also, insertion of the sample resulted in heat loss from the furnace to give a temperature lower than required. In most cases, however, it recovered over a five minute period and was found, in fact, to be a benefit in understanding the formation of liquid-phase joints.

The bonding temperatures studied were between 400°C and 550°C depending on the substrate and interlayer materials. Bonding time was between 4 minutes and 100 minutes, with initial applied pressures ranging from 3 MPa to 10 MPa for unreinforced alloy and 10 MPa to 34 MPa for composite material.

2.3. Mechanical evaluation of as-received and diffusion-bonded materials

2.3.1. Hardness testing of unreinforced alloy and metal matrices

Microhardness measurements were performed on bonded joints for both the unreinforced alloy and the composite matrices. A polished, mounted section of the joint was positioned in an x-y micrometer adjustable stage of the hardness tester. This, coupled with an eyepiece attachment, allowed accurate positioning of the diamond indenter above the sample surface. Microhardness profiles of the joints were carried out using an indent spacing of between 20 μm and 40 μm, depending on the hardness of the material. Comparative isolated measurements were also performed in the alloy away from the bonded interface.

A Leco M-400 microhardness tester was used in this work with an indenter load of 10 g and dwell time of 20 seconds.

2.3.2. Fibre/matrix interfacial friction stress in composite materials

A fibre indentation method [130] was used to estimate the fibre/matrix interfacial friction stress for the Al/Nic composite. Measurements of fibres in the bonded region were compared with values obtained from fibres well away from the joint.

In this technique a Vickers pyramidal indenter is used to depress a fibre into the matrix such that the fibre/matrix bond is broken and the fibre is compressed into the matrix, Fig. 2.3. The slipped length, u, may be calculated from the indent diagonals $2a$ and $2b$, and half-angle ψ, using the geometrical relationship

$$u = (b-a)\ \cot\psi\ .$$

The interfacial friction stress, τ, is given by

$$\tau = F^2/4\pi^2 u R^3 E_f\ ,$$

where E_f is the fibre modulus (~200 GPa) and R is the fibre radius; F, the maximum indentation force, is given by $2a^2H$, where H is the fibre hardness.

A Leco M-400 tester was used for all measurements with indenter loads of 100 g or 200 g and dwell time of 20 seconds.

2.3.3. Bond strength determination

(a) Lap-shear test method

Lap-shear samples were cut from bonded aluminium and tested using a 100 kN 1195 Instron machine at a cross-head speed of 2 mm/min, as illustrated in Fig. 2.4. The shear strength was calculated from measurement of the failure load and the overlap area of each tested coupon. The bonded area of the total joint was established from a study of the fractured surfaces, bonded areas being identified by the presence of ductile dimples and/or metal cleavage facets and non-bonded areas by a planar surface. A value for the specific shear for each tested coupon was calculated using the relevant failure load and bonded area. Results from test coupons were averaged to give the specific shear strength of the whole joint.

(b) A modified shear test method

The shear strength of a bond was determined by carrying out shear tests on a series of coupons cut from half of the original joint, Fig. 2.5, and then averaging the individual data; the remainder of the joint was set aside for microstructural analysis. The choice of test coupon dimensions was based upon results obtained on shear testing pressure-welded aluminium [131] which showed a reduced experimental scatter with increase in overlap-to-thickness ratio (w/t) and an almost constant value when $w/t>0.9$. In the present work the test coupons were ~10 mm long (w) and of a thickness (t) to give w/t values of ~0.9 for unreinforced alloy and particulate composite joints and ~1.7 for fibre composite joints. Tests were carried out using a 100 kN Instron machine fitted with the jig shown in Figs. 2.6a and 2.6b, at a cross-head speed of 2 mm/min. For bonded Al/Nic composite, steel shims were used to fill spaces between the sample and the jig. The shear strength was calculated from measurement of the failure load and the overlap area of each tested coupon.

As with the lap-shear test, the bonded area of the whole joint was established from a study of the fractured surfaces using light and scanning electron microscopy. A value for the specific shear strength for each tested coupon was calculated using the relevant failure load and bonded area. These were then averaged to give the

specific shear strength of the bonded specimen. As-received and heat-treated materials were also tested for purposes of comparison.

2.4. Microstructural analysis

2.4.1. Light microscopy

(a) Principle of the technique

In this technique light reflected by, or transmitted through, a specimen is collected via an objective lens and focused using an eyepiece. The resolution of the microscope is given by the following equation [132]

$$r = 0.61\lambda / \mu \sin\alpha ,$$

r = resolution, λ = wavelength of light,

μ = refractive index, α = semi-angle of the aperture.

To obtain optimum resolution λ has to be as large as possible with μ and α as small as possible. Green light (λ = 400 nm) used along with an oil-immersion objective lens gives a resolution of ~150 nm and a numerical aperture of ~1.7. For high power objectives, such as x100, oil immersion is essential as the aperture semi-angle is large.

Another limiting factor is the depth of field, which is given by the relationship [132]

$$h = 0.61\lambda / \mu \sin\alpha \tan\alpha,$$

h = depth of field, λ = wavelength of light,

μ = refractive index, α = semi-angle of the aperture.

From this equation it is apparent that the depth of field may be increased by decreasing the aperture semi-angle, α, or by increasing the wavelength, λ. Unfortunately, any improvement in the depth of field will simultaneously worsen the resolution. This therefore limits the use of light microscopy for surface observation of very flat specimens.

The depth of focus is approximately the square of the magnification larger than the depth of field and is therefore not so important.

In this work, light microscopy was performed using a Zeiss ICM 405 microscope fitted with a x10 stereo eyepiece. Objective lenses of magnification x4, x8, x16, x40 and x100 were used, the latter with a green filter and oil immersion. Polished sections of the joints were viewed using reflected light with areas of interest being recorded on 35 mm film using a camera attachment. Samples were also viewed using Nomarski Differential Interference Contrast (DIC) in which the path difference of light

reflected from the sample surface is used to enhance the contrast of the image.

(b) Preparation of specimens

Specimens for microscopic examination were cut from the joints, Fig. 2.7, using a resin bonded SiC wheel (diamond wheel for composite materials) and mounted in resin using a hot-pressing technique. A resin was chosen which had a similar wear rate to the specimen material; for unreinforced alloy phenolic resin was used, whereas for composite samples a harder carbon-filled phenolic resin was employed.

The surfaces of these mounted samples were prepared using a Buehler Motopol 12 grinding machine utilising a series of interchangeable grinding surfaces with a variety of abrasive compounds [133]. For each material a preparation routine was attained using an iterative process in which variables such as cutting speed and abrasive size were altered until an acceptable surface finish was obtained. The routines involved coarse grinding on SiC papers to flatten the surfaces and to remove cutting damage. This was followed by grinding on polymer-based wheels using progressively finer diamond abrasive down to 1 μm. The finishing stages usually consisted of grinding using a colloidal suspension of silica. The unreinforced alloys

were relatively easy to prepare often taking only ~20 minutes. However, surface preparation of composite materials was difficult, due mainly to the differences in hardness of the matrix and ceramic reinforcement; specimens were commonly re-ground up to four or five times in order to achieve satisfactory finishes.

2.4.2. Scanning electron microscopy

(a) Principle of the technique

The effect of bombarding a material with an electron beam is shown schematically in Fig. 2.8. These effects can be used to yield detailed information about the physical and chemical properties of the target material.

Electron microscopes utilise electromagnetic lenses for which the refractive index, μ, may be taken as unity reducing the resolution equation to,

$$r = 0.61\lambda / \alpha,$$

values of λ = 0.0037 nm and α = 0.1 rads giving r = 0.02 nm.

This theoretical resolution is not realised because of the presence of spherical lens aberrations. These may be minimised by decreasing the aperture size, although this worsens the resolution. However, there is an optimum size

of aperture for which the net resolution is smallest [132]. The actual resolution of the scanning electron microscope (SEM), ~5 nm, is much better than the light microscope, the main benefit being the improved depth of field due to the short wavelength of electrons used. In the SEM, shown schematically in Fig. 2.9, electrons emitted by a tungsten filament are accelerated by a potential, usually 5 to 40 kV, and then focused (with a converging helical path) by a series of electromagnetic lenses to a spot on the specimen surface, ~5 nm in diameter. A set of x-y coils then direct this beam to produce a raster-type scan. As shown in Fig. 2.8, both backscattered and secondary electrons may be emitted from the specimen surface. The former have sufficient energy (tens of kV) to emerge from deep within the sample, Fig. 2.10, and are relatively unaffected by surface topography. Secondary electrons have much lower energies (<50 eV) and can only escape from within ~20 nm of the specimen surface. These are therefore influenced by the shape of the surface. Electrons are collected in a scintillator light-pipe photomultiplier combination, the output of which is amplified and subsequently displayed on a cathode-ray tube (CRT). This scans synchronously with the electron beam x-y coils to produce an 'electron intensity' mapping image of the specimen. Depending on the type of detector employed, a primary, secondary or mixed electron image may be formed.

In this work a JEOL JSM 35C microscope was used to obtain backscattered and secondary electron images.

(b) Preparation of specimens

Sections of the joint were prepared in a similar manner to those for light microscopy, using the conductive carbon-filled resin. Composite materials were sputtered coated with a thin layer of gold to avoid charge build up on the non-conducting ceramic reinforcement surfaces.

2.4.3. Electron-probe microanalysis

(a) Principle of the technique

As shown in Fig. 2.8, x-rays may be produced when a specimen is bombarded by an electron beam. Two types may be generated as a result of incident electrons interacting with core electrons of atoms within the specimen. Firstly, continuous background or Bremsstrahlung radiation is produced as a result of the slowing down or 'braking' of the incident electron beam. Secondly, specific high intensity peaks, produced by the degeneration of electrons filling vacancies created by the ejection of core electrons, Fig. 2.11, are found 'superimposed' onto this

background radiation, Fig. 2.12. The peaks are unique for a particular target atom, thus offering a method of identification. It is the analysis of these characteristic peaks that forms the basis of electron-probe microanalysis (EPMA).

Measurement of the energy or wavelength of the x-rays provides a means of identifying the element, whilst recording their intensity gives an indirect measure of the element concentration. The two different methods of analysis available are known as energy-dispersive spectrometry (EDS) and wavelength-dispersive spectrometry (WDS).

An energy-dispersive spectrometer uses a lithium-doped silicon semiconductor detector to measure the x-ray energy. Radiation emitted from the sample passes into the detector via a thin beryllium or plastic window (although this can be removed for light-element analysis) which is kept under high vacuum at liquid nitrogen temperature. Electron-hole pairs are created in the silicon, the number of which are proportional to the energy of the incident x-ray photon. This charge is then amplified and fed into a multi-channel analyser which separates the pulses according to amplitude, and stores them in memory channels corresponding to these amplitudes. Computer software enables the resultant spectrum to be displayed on either a CRT, stored on magnetic disc, or printed in hard copy. In

this work a JEOL JSM 35C SEM, equipped with a LINK ANS 10000 EDS, was used for qualitative analysis of microstructural features in the diffusion bonded samples.

The wavelength-dispersive spectrometer uses a crystal of known interplanar spacing, d, to diffract the x-rays. Measurement of the diffraction angle, θ, gives the x-ray wavelength, λ, according to Bragg's law

$$n\lambda = 2d \sin\theta .$$

The intensity of this diffracted beam of x-rays is measured by a gas proportional counter, amplified, and given as x-ray counts per second. This gives an indirect measure of the element concentration. X-ray data from the sample material and from standards of known composition, combined with atomic number, absorption and fluorescence (*ZAF*) correction factors [134] may be used to calculate the weight concentration of constituent elements. In this work a JEOL JXA 8600 SEM fitted with four spectrometers, each containing two crystals, was used for quantitative elemental analysis, *ZAF* corrections were performed using the associated computer software.

Both types of spectrometers have their advantages and disadvantages. The EDS is capable of measuring a wide range of energies simultaneously and is therefore a rapid method but it is less sensitive to light elements ($Z<8$). WDS has a higher spectral resolution which makes it ideal for quantitative analysis since it has a higher detection

sensitivity overall, although the number of elements that may be measured at any one time is limited by the number of detectors.

Samples were first analysed using EDS to establish the composition of microstructural features followed by WDS if quantitative analysis was required.

(b) Measurement of oxide film thickness

A method proposed for measuring the thickness and composition of surface layers, including oxide films, involves electron-probe microanalysis coupled with the application of a simplified correction procedure [135] to convert the x-ray intensity measurements into film thickness data.

We may write the total intensity of x-rays generated in a target as,

$$\int_0^\infty \phi(\rho z)\, d\rho z \ ,$$

and the emitted x-ray intensity as

$$I = \int_0^\infty \phi(\rho z) \exp(-\chi \rho z)\, d\rho z \ ,$$

where $\phi(\rho z)$ represents the variation of x-ray intensity with mass depth (ρz) in the target, Fig. 2.13, and χ takes account of x-ray absorption and is given by $\mu/\rho \operatorname{cosec}\psi$,

where μ/ρ is the mass absorption coefficient and ψ is the x-ray take-off angle.

To represent the $\phi(\rho z)$ distribution a rectangular profile is adopted with a maximum and constant $\phi(\rho z)$ value of $\phi(0)$, Fig. 2.14. This gives the following expression for the emitted x-ray intensity

$$I = \int_0^{2\overline{\rho z}} \phi(0) \exp(-\chi \rho z) d\rho z \qquad (1)$$

The integration limit is now changed to $2\overline{\rho z}$, where $\overline{\rho z}$ represents the mean depth of x-ray production and may be expressed in terms of probe conditions and target composition as [136]

$$\overline{\rho z} = \rho s_m / [2.4+0.07Z+(1.04+0.48\eta)/\ln U_o],$$

where Z is mean atomic number

η is backscatter coefficient

U_o is overvoltage ratio and equals E_o/E_c, the ratio of the incident electron beam energy (E_o) and the critical excitation potential of the target atom (E_c)

ρs_m, the electron range, is given by

$$\rho s_m = (7.87\text{x}10^{-6}\ J^{0.5}\ E_o^{1.5}+7.35\text{x}10^{-7}\ E_o^2)\ \Sigma c_i Z_i/A_i,$$

where A is atomic weight

J is the mean ionisation potential

c_i is the weight fraction of element i.

Integrating equation (1) gives

$$I = [-\phi(0)/\chi\ \exp(-\chi.\overline{\rho z})] = -\phi(0)/\chi[1-\exp(-2\chi.\overline{\rho z})].$$

For an oxide film of mass thickness ρt on an aluminium specimen and using an aluminium oxide standard, the x-ray intensity ratio may be written,

$$\frac{I_{spc}}{I_{std}} = \frac{\phi(0) / \chi\left[1 - \exp(-\chi\rho t)\right]}{\phi(0) / \chi\left[1 - \exp(-2\chi\overline{\rho z})\right]} = \frac{1 - \exp(-\chi\rho t)}{1 - \exp(-2\chi\overline{\rho z})}$$

Hence ρt may be determined from the ratio I_{spc}/I_{std}.

In this work the intensity ratio of oxygen Kα x-rays from both alumina and aluminium specimens was determined using a JXA 8600 electron-probe microanalyser fitted with WDS. Accelerating voltage and beam current were 10 kV and 3×10^{-8} A, respectively, with a multilayer device being used for x-ray diffraction. From calculations of the mean depth of x-ray generation, $\overline{\rho z}$, the above equations were used to determine the oxide thickness on as-received and heat-treated polished aluminium specimens.

2.4.4. Transmission electron microscopy

(a) Principle of the technique

The effect of bombarding a specimen with a beam of electrons is shown in Fig. 2.8. If the beam has sufficient energy (hundreds of kV) electrons may penetrate

a sample a few hundred nm thick, a process which forms the basis for transmission electron microscopy (TEM).

A TEM works on a similar principle to a light microscope except that electrons rather than light are used as the illumination source and the lenses are electromagnetic coils rather than glass, Fig. 2.15. An electron beam produced by a tungsten filament is accelerated using several hundred kV and focused onto the sample using electromagnetic condenser lenses to a spot <0.1 nm in diameter. The beam may pass through the thin specimen unaffected, but some degree of interaction is more likely. Transmitted electrons can be defocused using objective lenses to form an image on a fluorescent screen or be recorded on photographic film. Image contrast is produced by differences in specimen thickness, orientation and elemental composition. Additional contrast may be obtained by inserting an aperture between the sample and screen that allows only the passage of unscattered electrons. This may highlight the presence of features such as dislocations and grain boundaries.

Other phenomena may also be used for analysis, for example, electrons diffracted by atom planes may be focused to produce a spot pattern from which detailed information of the crystal orientation, atom stacking and lattice parameters may be obtained. If the incident electron beam (wavelength, λ) is diffracted by a crystal

of interplanar spacing, d, through an angle, θ, then, according to Bragg's law,

$$n\lambda = 2d\sin\theta .$$

However, as θ is small this reduces to,

$$n\lambda \sim 2d\theta .$$

The diffracted electrons from each set of planes produce a series of spots symmetric about a central axis. The distance between the centre spot and an outer spot, r, is related to the distance from the specimen to the pattern, l, and diffraction angle, θ, by

$$\theta \sim r/l ,$$

combining with Bragg's law gives,

$$d = n\lambda l/r .$$

The 'd' spacings calculated from several diffraction spots may then be compared with ASTM charts to reveal the identity of the diffracting crystal. The unit cell parameter, a, may also be calculated using a geometric relationship, which, for a cubic crystal is

$$d_{hkl} = a/\sqrt{(h^2+k^2+l^2)}$$

where h, k and l are the Miller indices of the diffracting plane. The beam direction is given by the vector product of two diffracting planes $(h_1k_1l_1)$ and $(h_2k_2l_2)$,

$$[uvw] = (h_1k_1l_1) \wedge (h_2k_2l_2)$$

The diffraction technique may be combined with an EDS attachment to provide compositional analysis of microstructural features.

In this work a JEOL 2000FX TEM, with a spatial resolution of 0.2 Å, was used to obtain transmission electron micrographs and diffraction patterns of microstructural features, such as second phases, in the bonded joints. A high take-off angle windowless LINK EDS AN10000 detector was used for compositional analysis.

(b) Preparation of specimens

For TEM the very thin areas required (~200 nm) make specimen preparation difficult, particularly for MMCs as the hardness of the matrix and fibres is markedly different. The procedure adopted in this work is outlined below.

(a) from the bulk sample, a slice of ~0.5 mm is cut,
(b) a disc of 3 mm diameter, containing the bond line, is punched or drilled from this slice.
(c) the disc is then ground and ion-milled.

The first stage of preparation (a) was carried out using a resin bonded silicon carbide cutting wheel for the unreinforced alloys and a diamond wheel for the composite material. All machining was carried out using a Struers Accutom with automatic feed to ensure an even cutting pressure. The 3 mm discs (b) were obtained from the trepanned material using a hand operated punch for the unreinforced alloy and a hollow diamond tipped drill for

the composite material. This stage proved to be the most critical as the bond line had to be located at the centre of the disc and the application of excessive force often fractured the joint.

The discs were then ground (c) on 400 grit SiC paper, on both faces, to a thickness of ~200 μm. The thinned discs were then mounted in wax and dimpled using a VCR group Dimpler, Fig. 2.16. From the diameter of the dimple the depth was calculated using a geometric relationship. Each face was evenly dimpled until the thickness at the centre was ~40 μm. The samples were then ready for thinning in an ion mill.

Ion beam milling uses a high energy stream of argon ions to bombard the specimen and 'knock out' atoms. Depending on the applied potential and incident beam angle, different thinning rates can be achieved. The sample is rotated and thinned from both sides by two ion guns. A Gatan Duomill was used in this work and samples were milled at an angle of 15°, decreasing to 8° once perforated. At this low angle a large thinned area was obtained. Further thinning was performed, if required, after inspection in the TEM.

2.5. Differential scanning calorimetry

Differential scanning calorimetry (DSC) is a technique for measuring the temperature and energy of phase transformations. In this technique two small aluminium pans, one containing the sample material, are heated at a constant rate to a pre-set temperature, Fig. 2.17. This is achieved via thermocouples connected to a comparative amplifier circuit that controls the sample heating element. The difference in heat flow of the pan containing the sample and the reference pan is plotted as a function of temperature and if the system is correctly calibrated a transformation energy may also be obtained. A schematic diagram of the DSC is illustrated in Fig. 2.18.

In this work a computer interfaced DuPont 9900 DSC was used to obtain the melting temperatures of expelled weld beads produced during liquid-phase bonding. Samples were sealed in aluminium pans and heated at 5°C/min. The temperature calibration was carried out using the melting points of indium and water standards.

3. RESULTS

3.1. Comparison of the methods of shear testing

In order to assess the two types of shear test comparative measurements were performed on bonded joints. Commercial-purity aluminium was bonded with a copper foil interlayer at 550°C using an initial pressure of 3 MPa and a total time of 20 minutes. Coupons cut from the bonded specimens were tested using the lap-shear technique as well as the improved shear method utilising a special jig, as described in section 2.3.3. Test data is reported as $x \pm y$, where x is the mean value and y is the standard deviation with Bessel correction [137].

Averaged test data gave a shear strength of 23 ± 2 MPa, a bonded area of 57 ± 12 % and specific strength of 42 ± 7 MPa for the lap-shear test, whilst for the method utilising the shear jig values of 26 ± 19 MPa, 42 ± 33 % and 64 ± 5 MPa were obtained. Examination of the fractured lap-shear specimens revealed that extensive out-of-plane bending occurred during the tests, Fig. 3.1, whereas for samples tested in the shear jig bending was much reduced, Fig. 3.2. These results indicated that the shear-jig method was the preferable testing technique since it reduced peel stresses and this gave a higher and more realistic measure of shear strength. Subsequent testing of bonded joints therefore adopted this method,

shown in the sequence of photographs, Figs. 3.3a to 3.3d, taken during the shear testing of an aluminium alloy. It should also be mentioned that there was an added advantage to the technique in that test coupons were smaller than those employed in the lap-shear test, thereby conserving material.

3.2. Commercial-purity aluminium

3.2.1. As-received material

Examination of a polished section of as-received metal in the light microscope revealed elongated particles several μm in length typical of a rolled structure, Fig. 3.4. The particles were too small for quantitative EPMA but they were found by EDS to contain iron, aluminium and silicon - most probably $FeAl_3$ and $Al_{12}Fe_3Si$ phases [138].

Measurements of the thickness of the oxide on the polished aluminium using EPMA, Table 3.1, gave a value of 2.2 ± 0.4 nm. After heating at 500°C for 5 minutes, approximating to the conditions at the metal surface prior to bonding, the oxide film had increased in thickness to 3.7 ± 0.7 nm. The thickness versus time curve, illustrated in Fig. 3.5, shows that the rate of growth does not follow a parabolic law.

The measured shear strengths for two different batches of as-received aluminium were 97 ± 4 MPa and 112 ± 11 MPa. Heat-treatment at 500°C for 5 minutes reduced these values to 77 ± 3 MPa and 85 ± 4 MPa, respectively. Both as-received and heat-treated samples yielded considerably as evidenced by the stress-displacement curve, Fig. 3.6, and by the deformation of the tested specimens, Fig. 3.7. These results are summarised in Table 3.2.

3.2.2. Bonding without an interlayer

Bonding was carried out at a temperature of ~500°C without an interlayer. Two experiments were performed, the first using an initial pressure of 3 MPa and a time of 60 minutes, to give a permanent specimen through-thickness deformation of ~2%; the second using a pressure 10 MPa for 240 minutes, to give a sample deformation of ~10%. Both experiments, however, failed to produce any sort of joint.

Examination visually of the mating surfaces revealed only a slight discolouration of the outer regions, most likely due to thickening of the oxide film; the central areas of the surfaces were similar in appearance to those prior to bonding.

3.2.3. Bonding with a zinc interlayer

The pressure versus time curve for the bonding experiment carried out with a zinc foil interlayer (12 μm thick) using an initial applied pressure of 3 MPa at 500°C is shown in Fig. 3.8. The pressure was found to decrease gradually (ABC) as the specimen deformed, to reach a constant value of ~2 MPa. Bonding for 30 minutes gave a sample deformation of ~2% and resulted in the expulsion of a small amount of liquid (~0.1 g), which EPMA showed was composed solely of zinc. During subsequent cooling, however, the aluminium plates separated and examination of the mating surfaces showed that, apart from melting of the zinc, little reaction with the aluminium had occurred.

Similar results were obtained for the experiment carried out using an initial applied pressure of 10 MPa and a bonding time of 240 minutes.

3.2.4. Bonding with a copper interlayer

A typical pressure versus time curve produced during a bonding experiment is shown in Fig. 3.9. (A temperature drop to ~530°C was noted at the start of the experiment due to heat loss during specimen insertion but the temperature returned to 550°C within a five minute

period). The curve shows a number of salient features and these were investigated in separate experiments. It may be seen that as plastic flow of the aluminium took place there was a progressive decrease in the initial applied pressure of 3 MPa over the first 10 minutes (ABC) to ~2 MPa, followed by a marked decrease to a steady value of ~1 MPa (DEFG). All samples bonded using the 3 MPa initial pressure showed ~2% permanent deformation.

A section of a sample removed after bonding for 4 minutes, using an initial pressure of 3 MPa, Fig. 3.10, shows a layer of phases at the bond interface (~5 μm thick) surrounded by a two-phase structure. The layered phases (labelled A, B, C, D) are believed to have formed via the solid-state and were shown using EPMA, Table 3.3, to be consistent with copper, Cu_9Al_4 (γ), CuAl (η) and $CuAl_2$ (θ), respectively (see Appendix for aluminium-copper phase diagram). The phase with highest copper content was nearest the centre of the joint. The adjacent two-phase region was composed of $CuAl_2$ and aluminium with a solid-solution of copper, consistent with a typical aluminium-copper eutectic structure [139].

Analysis of a sample bonded for 5 minutes (the condition relating to B) contained a ~60 μm wide reaction zone, Fig. 3.11, consisting of a eutectic-type structure of phases D and E, interspersed with particles of F, Table 3.3. These are believed to be $CuAl_2$ (θ), aluminium and Al_7Cu_2Fe (ω)

phases, respectively (see Appendix for aluminium-copper-iron phase diagram). The remnant aluminium/copper interfaces were still visible and separated by ~40 μm, four times the thickness of the copper foil. Using EPMA copper was detected up to a distance of ~10 μm in the aluminium adjacent to the joint. Within this region thin foil TEM studies revealed particles aligned in the aluminium lattice, Fig. 3.12a, which EDS showed contained copper, 3.12b. The orientation of these precipitates was determined using diffraction data which showed that they lay on the {100} planes of the aluminium lattice, consistent with the θ' phase typically found in age-hardenable aluminium-copper alloys [140,141]. TEM studies also located oxygen-rich particles at the residual aluminium/copper interfaces, Fig. 3.13a, as evidenced by the EDS spectrum of this area, Fig. 3.13b. Two other phases were also identified in the joint region, labelled 'c' and 'd' in Fig. 3.13a, the EDS spectra, electron diffraction patterns and indexed spot patterns for which are shown in Figs. 3.13c and 3.13d, respectively. Comparison of these diffraction data with the standard ASTM charts identified 'c' as the tetragonal $CuAl_2$ phase and 'd' as the cubic Cu_9Al_4 phase.

From the testing of individual coupons cut from the joint the average shear strength of the bond was determined as 20 ± 14 MPa, failure occurring through the intermetallic region. The bonded area was 25 ± 14 % to give a specific

bond strength of 76 ± 11 MPa, Table 3.4. Non-bonded regions present at the interface of coupons extracted from the periphery of the joint were characterised by a blackened appearance which EPMA showed was associated with a film of copper oxide.

After bonding for 10 minutes (point C on the curve, Fig. 3.9, where the pressure suddenly decreased) a liquid bead of mass 0.11 g was expelled from the joint. The bead contained aluminium, $CuAl_2$ and Al_7Cu_2Fe phases, Fig. 3.14a, differential scanning calorimetry (DSC) revealing endothermic reactions at ~545°C and ~548°C, Fig. 3.14b. The reaction zone, Fig. 3.15a, was ~30 μm wide with a much finer microstructure than that of the previous bonding experiment and the residual aluminium/copper interfaces (arrowed) were now only ~10 μm apart; needle-like particles present at the interfaces were identified as Al_7Cu_2Fe. The shear strength was 54 ± 38 MPa; the bonded area was 48 ± 33 %, to give a specific strength of 112 ± 3 MPa. Failure occurred through both the aluminium and intermetallic phases, Fig. 3.15b.

Bonding for 20 minutes (D) again resulted in the expulsion of a bead, with liquefied metal collecting at the periphery of the joint, as evidenced by the solidified microstructure, Fig. 3.16a. In central regions of the joint Al_7Cu_2Fe phases up to 10 μm in size were found, Fig. 3.16b, with copper having diffused up to 50 μm into the

aluminium, Fig. 3.17a. Shear testing gave a shear strength of 26 ± 19 MPa and failure took place at the bond interface. The bonded area was 42 ± 33 % to give a specific strength of 64 ± 5 MPa.

In the samples bonded for 30, 60 and 100 minutes (E, F and G, respectively) the particles of Al_7Cu_2Fe present at the bond line, Fig. 3.18a, were appreciably smaller (~1 μm) than those in sample D, and copper had diffused up to a distance of ~150 μm from the bond line, Fig. 3.17b and 3.17c. At the periphery of the joint the amount of liquefied metal was also reduced, Fig. 3.18b, as evidenced by the increased mass of expelled liquid, Table 3.4. The shear strength reached a maximum value of ~50 MPa after 60 minutes with a progressive increase in the bonded area to 57 % after 100 minutes. Specific strengths lay within the range 90 MPa to 100 MPa for all specimens.

The effect of bonding time on the shear strength, bonded area and specific shear strength is shown graphically in Figs. 3.19a, 3.19b and 3.19c.

The pressure versus time characteristics of aluminium bonded using a higher initial pressure of 10 MPa were generally similar to Fig. 3.9, apart from more significant pressure drops at A and C due to the greater deformation of aluminium and to the increased amount of liquid phase expelled (~0.31 g). Bonding for 30 minutes resulted in a

sample deformation of ~13%. The joint was similar in appearance to sample F, with a shear strength of 96 ± 4 MPa and a bonded area ~100%. Failure occurred away from the joint, through the aluminium.

Using a 4 μm copper foil interlayer and an initial pressure of 3 MPa, bonding for 30 minutes produced a joint with a shear strength of 69 ± 14 MPa; the bonded area was 80 ± 10 % to give a specific strength of 86 ± 10 MPa.

3.2.5. Bonding with a nickel-coated copper interlayer

The pressure versus time curve for the bonding experiment with a nickel-coated copper foil interlayer (~15 μm thick) using an initial pressure of 3 MPa at 550°C was similar to that illustrated in Fig. 3.8. The sample pressure was found to decrease progressively to ~2 MPa over a 30 minute period, with no drop in pressure characteristically associated with the expulsion of liquid. Bonding for 60 minutes gave a specimen deformation of ~2% and resulted in the development of a joint which failed at the bond interface during subsequent machining of shear test coupons. Inspection visually of the mating surfaces revealed that some reaction had taken place as evidenced by discolouration and roughening of the aluminium surfaces.

Bonding at 550°C for 60 minutes, using an initial pressure of 10 MPa, gave a sample deformation of ~9%. A polished section of the central region of the bond region is shown in Fig. 3.20a. The joint was composed of a ~30 μm thick layer of intermetallic phases, labelled G1 and G2, whose composition, Table 3.3, lay within the Al_7Cu_4Ni (δ) and Al_6Cu_3Ni (τ) phase fields on the aluminium-copper-nickel phase diagram (see Appendix). In some places the nickel coating was seen to be perforated, Fig. 3.20b, and here a two-phase structure was present, identified as aluminium with a solid-solution of copper and $CuAl_2$ (H in Table 3.3). In these regions adjacent to the joint copper was located up to a distances of ~40 μm into the aluminium. The shear strength of the joint was 65 ± 18 MPa, with failure occurring mainly through the nickel-containing intermetallic phases. The bonded area was 74 ± 24 % to give a specific strength of 89 ± 8 MPa. Unbonded regions present at the periphery of the joint were associated with unreacted foil. It was noted that little oxidation of the copper interlayer had occurred due to the protective nature of the nickel coating.

3.2.6. Bonding with a copper-silver alloy interlayer

The pressure versus time curve for aluminium bonded with a copper-silver alloy foil (50 μm thick), using an initial

pressure of 3 MPa at 510°C, was similar in appearance to Fig. 3.9, except that was that a greater decrease in pressure, to a value of ~1.5 MPa, was observed at point C. A drop in temperature, to ~490°C, was noted at the start of the experiment due to heat loss during specimen insertion, but the temperature returned to 510°C within a five minute period. Bonding for 30 minutes produced a sample deformation of ~2%, and resulted in the expulsion of a liquid bead from the joint, of mass 0.72 g. A backscattered electron image of the bead taken using the SEM, Fig. 3.21a, shows a three-phase structure. Compositions deduced using EPMA are shown in Table 3.3; the grey phase (I) is aluminium with a solid solution of copper and silver; the dark phase (J) is $CuAl_2$ with some dissolved silver, and the light phase (K) is the Ag_2Al phase with some dissolved copper. Analysis of the bead in the DSC indicated that on heating an endothermic reaction took place at ~505°C, Fig. 3.21b. These results are consistent with the ternary reaction illustrated in the aluminium-copper-silver phase diagram (see Appendix). A section through the joint, Fig. 3.21c, shows a planar reaction zone ~20 μm wide which was found to contain similar phases to the bead, with little remaining evidence of the original aluminium/foil interfaces. Copper and silver were found to have diffused up to a distance of ~100 μm into the aluminium, Figs. 3.22a and 3.22b, and microhardness tests indicated substantial hardening of the aluminium in this region, Fig. 3.22c. TEM studies of the

area of the aluminium adjacent to the bond interface (~40 μm) showed that two types of precipitate had formed, Fig. 3.23a. The first was a coarse, oriented particle of length in excess of 1 μm and apparent width of less than 100 nm. Between these particles are much finer precipitates similarly oriented with respect to the aluminium lattice, generally less than 100 nm in size. Fig. 3.23b is taken at a higher magnification from a different region of the foil, and Fig. 3.23c is the corresponding diffraction pattern. The indexed spot pattern, Fig. 3.23d, indicates that the surface of the foil is approximately parallel to the (001) plane of the aluminium lattice, the <100> directions in the foil are shown in Fig. 3.23b. Further analysis indicates that the precipitates lie on {111} planes of the aluminium lattice and this orientation relationship is identical to that reported for the hexagonal γ' phase found in heat-treated aluminium-silver alloys [127].

It was difficult to obtain a diffraction pattern from the coarse precipitate and therefore it is not possible to say whether it is γ'. More likely the phase is γ which is also hexagonal with similar lattice parameters to γ', a = 0.288 nm and c = 0.462 nm. With regard to composition both γ and γ' phase contain silver and aluminium in the atom proportions Ag_2Al. However, our EDS data obtained from an area of the fine precipitates, Fig. 3.23e, show high levels of aluminium and silver as well as a

relatively high concentration of copper. In fact this was in excess of the solid-solubility level, which may indicate that a considerable amount of copper is contained in the precipitate. Indeed, it was observed that the copper/silver ratio was much higher when the probe was positioned on a coarse particle, Fig. 3.23f.

One possibility is that the coarse copper-containing precipitates form first as the high level of copper is rejected from solid-solution (consistent with the misfit of atoms which is greater for copper than for silver, Al_r = 0.130 nm, Cu_r = 0.117 nm and Ag_r = 0.134 nm, [142]) and that the fine precipitates form between these particles at a later stage.

This could explain why immediately surrounding the coarse particles fine precipitates form; in accord with published work on aluminium-silver alloys, where denuded zones were found [127]. This would suggest that these coarse precipitates are not simply γ-Ag_2Al phase but some other intermetallic. However, it is unlikely to be a simple binary phase of the θ-$CuAl_2$ type since this would be expected to form on {100} planes of the aluminium lattice. Based on the morphology of the coarse precipitate we may refer to it as $(Ag,Cu)_2$ Al, similar to the γ phase. This would be consistent with the EDS trace, Fig. 3.23f, which shows approximately equal concentrations of copper and silver, the higher level of aluminium being the result of

some excitation of the surrounding matrix by the electron-probe. TEM also revealed, within the reaction zone, isolated regions of a phase which EDS showed contained aluminium and oxygen.

The shear strength of the joint was 24 ± 9 MPa with failure occurring through the intermetallic phases. The bonded area was 65 ± 20 % to give a specific strength of 36 ± 6 MPa. Unbonded areas found in peripheral regions were identified by a 'blackened' appearance which EPMA showed was associated with oxidised copper.

The pressure versus time curve for a sample bonded using an initial pressure of 10 MPa exhibited a more pronounced decrease than 3 MPa experiment to give a greater permanent through-thickness deformation (~6 %) and mass of expelled liquid (1.15 g). Analysis of the joint, Fig. 3.24, revealed a more refined, solidified aluminium-$CuAl_2$-Ag_2Al eutectic structure, ~20 μm thick, with diffusion of liquid up grain boundaries which resulted in a non-planar bond interface. Copper and silver had diffused up to 100 μm into the aluminium adjacent to the joint to produce precipitates, similar to the 3 MPa experiment, with hardness tests indicating hardening of this region. The shear strength was 65 ± 20 MPa with failure occurring mainly through the aluminium. The bonded area was 85 ± 21 % to give a specific strength of 76 ± 8 MPa.

3.2.7. Bonding with an aluminium alloy (2124) interlayer

The pressure versus time characteristics for aluminium bonded with a 2124 interlayer using an initial pressure of 10 MPa at 500°C was similar to Fig. 3.8, showing a decrease at A to C from 10 MPa to ~7 MPa. Bonding for 30 minutes gave a specimen deformation of ~3%. A section of a sample, Fig. 3.25a, shows that the foil was reduced in thickness (~170 μm compared with the original value of 200 μm). A microhardness profile of the joint, Fig. 3.26d, revealed a slight softening of the 2124 foil near the bond interfaces and hardening of the aluminium up to ~50 μm away from the joint. EPMA showed that magnesium and copper had diffused into the aluminium up to a distance of ~100 μm Figs. 3.26a and 3.26b, with oxygen concentrated at the foil surfaces, Fig. 3.26c. The variation in the concentration of copper across the 2124 foil was illustrated by the difference in contrast of an etched specimen, shown in Fig. 3.25b; the higher concentrations of copper at the centre of the foil had a darker appearance. Thin foil TEM studies carried out on the bonded specimen revealed within the 2124 alloy interlayer aligned precipitates which contained aluminium, magnesium and copper, Fig. 3.26e. Their morphology and composition is consistent with the S' (Al_2CuMg) phase which forms on {210} planes of the aluminium lattice [140]. Within the aluminium copper-containing precipitates were found, believed to be θ' phase; a small

amount of magnesium was also detected in solid solution. TEM also located particles at the 2124/aluminium interface, Fig. 3.27a, which EDS showed contained aluminium, magnesium and oxygen, Fig. 3.27b; away from the bond interface only aluminium was detected, Fig. 3.27c. The shear strength of the joint was 61 ± 7 MPa, failure taking place mainly in the aluminium well away from the joint. The bonded area was 91 ± 7 % to give a specific strength of 67 ± 4 MPa.

A bonding experiment carried out at 550°C produced a pressure versus time curve with a greater drop, 10 MPa to ~6 MPa, compared with the 500°C experiment. After bonding for 30 minutes the 2124 foil was reduced in thickness from an original value of 200 μm to ~125 μm, Fig. 3.28, (less than the 500°C experiment, 170 μm). The total sample deformation was ~8%. Microhardness tests revealed hardening of the aluminium up to ~70 μm from the bond interfaces, Fig. 3.29d, and copper and magnesium were found up to a distance of ~130 μm, Figs. 3.29a and 3.29b. EPMA also revealed an oxygen-rich layer at the 2124 alloy foil/aluminium interfaces, Fig. 3.29c. The shear strength of the joint was 73 ± 6 MPa, Table 3.4, failure occurring through the aluminium with a bonded area of ~100%.

3.2.8. Bonding with a copper-zinc alloy interlayer

The pressure versus time characteristics for the bonding experiment with a copper-zinc alloy interlayer (12.5 μm thick) at ~500°C, using an initial pressure of 10 MPa, was similar in appearance to Fig. 3.8. A sample pressed for 30 minutes resulted in a deformation of ~7%; examination visually of the mating surfaces revealed that the brass foil had not reacted with the aluminium. The only notable observation was the discolouration of both the foil and aluminium at the periphery of the sample.

3.3. Commercial-purity aluminium reinforced with Nicalon fibre (Al/Nic)

3.3.1. As-received material

The as-received composite appeared to be satisfactory with good infiltration of fibres by the metal to give a fibre volume fraction of ~0.4, Fig. 3.30a. The intermetallic phases present in the aluminium matrix were larger (up to 10 μm) than in the unreinforced aluminium which enabled quantitative EPMA to be carried out. Several phases, labelled L1, L2, L3, L4 and L5 in Table 3.3, were located with compositions corresponding to $Al_{21}Fe_3Si$, Al_9Fe_2Si, Fe_2Al_{13}, Fe_5Al_{22} and $FeAl_5$, respectively. Figs. 3.30b and

3.30c show the structure of the L1 and L2 phases. TEM studies of the fibre/matrix interface revealed the presence of needle-like crystals, Fig. 3.31a, which EDS showed contained aluminium and carbon, Fig. 3.31b. These crystals, probably Al_4C_3, are believed to have formed during composite manufacture by reaction of the liquid aluminium with the free carbon originating from the Nicalon fibre, as reported in a microstructural study of a similar composite material [143]. With regard to the shear strength of the composite no tests were performed as the as-received plate was too thin (3 mm) for use in the shear-jig.

3.3.2. Bonding with a copper interlayer

A pressure versus time curve for a sample bonded at 550°C using a 10 μm copper foil interlayer and an initial pressure of 10 MPa is illustrated in Fig. 3.32. After the maximum was reached (A) a small decrease occurred (AB), probably due to plastic deformation of the copper foil, to be followed by a larger decrease (C) as liquid was expelled from the joint. The expelled bead, Fig. 3.33a, consisted of aluminium, silicon, $CuAl_2$, Al_7Cu_2Fe, and a second iron-containing phase (probably α-$Al_{12}Fe_3Si$) at grain boundaries; DSC indicated endothermic reactions at ~520°C and ~540°C, Fig. 3.33b.

After bonding for 30 minutes (D) the specimen deformation was ~2%. Microstructural studies showed that the $CuAl_2$ phase had formed some tens of μm into the bonded composite, Fig. 3.33c; θ' precipitates were also located within the aluminium adjacent to the joint interface (~100 μm). Where few fibres were present at the bonded surfaces the joint was well developed, Fig. 3.33d. Needle-like particles were found at the fibre/matrix interface which EDS showed contained aluminium and carbon. However, these aluminium carbide crystals were present also in the as-received composite and there was little evidence of any increase in amount during the bonding operation. Micro-indentation tests of fibres, examples of which are shown in Figs. 3.34a and 3.34b, revealed a fibre/matrix interfacial friction stress of 184 ± 74 MPa within the bonded region and 73 ± 19 MPa well away from the joint, Table 3.5a. There was also a corresponding increase in hardness of the aluminium matrix in the joint region from ~35 HV to 75 HV. The shear strength of the bonded composite was 34 ± 12 MPa; 66 ± 16 % of the central area was bonded indicating a specific strength of 51 MPa, Table 3.6. Examination of the fracture surfaces showed fibre/matrix separation, fibre splitting and ductile fracture of the aluminium matrix, Fig. 3.35a. As with unreinforced aluminium, unbonded areas in peripheral regions of the joint had a blackened appearance due to a film of copper oxide, Figs. 3.35b and 3.35c. The

surfaces were strongly bonded and failure took place mostly well away from the original interface.

The pressure versus time characteristics for composites bonded at higher initial pressures, 20 MPa and 30 MPa, were similar to those illustrated in Fig. 3.32. Bonding for 30 minutes produced permanent sample deformations of 2% and 3%, respectively. The shear strength, bonded area and specific strength were all found to increase with increase in pressure, shown graphically in Figs. 3.36a, 3.36b and 3.36c.

3.3.3. Bonding with a nickel-coated copper interlayer

The pressure versus time curve for composite bonded with a nickel-coated copper foil using an initial pressure of 20 MPa at 550°C is shown in Fig. 3.37. In the first 10 minutes the pressure decreased gradually to a steady value of ~19 MPa. Bonding for 60 minutes gave a sample deformation of ~2%. A polished section of the joint, Fig. 3.38a, shows that where aluminium was in contact with the foil a layered structure had formed. As well as identifying copper and nickel EPMA identified two other phases, labelled N and O in Table 3.3, whose compositions lay within the $Al_9Cu_{13}Ni$ (γ) and Al_7Cu_4Ni (δ) phase fields (see Appendix for aluminium-copper-nickel phase diagram).

In regions at the bonded interfaces where fibres were present in the surface interdiffusion of the aluminium and interlayer was inhibited and no intermetallic phases were formed, Fig. 3.38b. The shear strength of the joint was 12 ± 6 MPa, the large unbonded regions associated with unreacted foil.

A sample bonded for 240 minutes was similar in appearance to Fig. 3.38a. The shear strength was ~7 MPa, with a low bonded area due to the limited reaction of the foil with the composite. The copper foil appeared to be well protected by the nickel coating as little oxidation was found to have taken place.

3.3.4. Bonding with a copper-silver alloy interlayer

The pressure versus time curve for Al/Nic composite bonded with a copper-silver alloy interlayer using an initial pressure of 20 MPa at 510°C, Fig. 3.39, showed a more marked decrease at BC than the copper bonded sample (Fig. 3.32). Bonding for 30 minutes gave a sample deformation of ~3% and resulted in the expulsion of a liquid bead of mass 0.31 g, the solidified microstructure of which is shown in Fig. 3.40a. DSC analysis, on heating, indicated endothermic reactions at ~495°C and ~505°C, Fig. 3.40b. A micrograph of the joint, Fig. 3.40c, shows a reaction zone

which extended up to ~100 μm into the composite. The phases present in both the bead and joint were identified using EPMA as aluminium, $CuAl_2$, Ag_2Al along with an intermetallic containing iron and silicon. Within the reaction zone extensive fibre breakage was observed, with solidified eutectic phases present between fibre ends, Fig. 3.40d. This indicated that fibre fracture was not produced as a result of prior surface preparation but had occurred as a consequence of the bonding operation. The aluminium matrix adjacent to the reaction zone contained copper and silver, TEM studies revealing the presence of oriented particles similar to those found in bonded commercial-purity aluminium. Indent tests gave fibre/matrix interfacial strengths of 262 ± 63 MPa within the reaction zone of the bond and 68 ± 25 MPa for those well away from the joint, Table 3.5b. The shear strength of the joint was 54 ± 16 MPa, failure occurring mainly through the composite well away from the bonded interface. The bonded area was 90 ± 22 % to give a specific strength of 61 ± 10 MPa. Unbonded regions at the periphery of the joint were associated with oxidised copper.

3.3.5. Bonding with an aluminium alloy (2124) interlayer

The pressure versus time curve for Al/Nic composite bonded with a 2124 alloy foil using an initial pressure of 20 MPa

at 500°C was similar to Fig. 3.37. Bonding for 240 minutes resulted in a specimen deformation of ~2%. An etched, polished section of a sample, Fig. 3.41, shows surface features produced by EPMA and hardness profiles. Copper and magnesium were found to have diffused up to a distance of 150 μm into the composite, the concentration curves, Figs. 3.42a and Fig. 3.42b, showing similar trends to the microhardness profile, Fig. 3.42d. EPMA also showed a high oxygen content at the 2124 alloy/composite bonded interfaces, Fig. 3.42c. Thin foil TEM studies revealed copper-containing precipitates aligned within the 2124 alloy foil, believed to be S' phase, and particles of θ' in the aluminium matrix adjacent to the joint. TEM/EDS also located oxygen-rich particles at the bonded foil/composite interfaces, similar in appearance and composition to those shown in Figs. 3.27a, 3.27b and 3.27c. The shear strength of the joint was 59 ± 21 MPa with failure taking place mainly through the composite well away from the joint. A bonded area of 74 ± 27 % gave a specific strength of 81 ± 6 MPa.

Bonding the composite for 60 minutes using an initial pressure of 34 MPa resulted in a specimen deformation of ~3%. Analysis of a polished section of the joint, using EPMA, revealed diffusion of copper and magnesium from the 2124 alloy interlayer into the aluminium matrix of the composite. The copper-rich precipitates formed in these areas resulted in localised hardening as evidenced by

microhardness tests. The interfacial friction stress of fibres near to the joint was 104 ± 28 MPa, compared with a value of 37 ± 19 MPa for fibres well away from the bonded interface, Table 3.5c. The shear strength was 54 ± 9 MPa, Table 3.6, failure occurring well away from the joint through the composite, Fig. 3.43a, with a bonded area of ~100%. Closer inspection of the fractured sample using light microscopy, Fig. 3.43b, showed that failure took place where the fibres were packed closely together and through regions where infiltration of fibres by the aluminium was poor, *ie*, fibre tows.

3.4. Aluminium alloy (2124)

3.4.1. As-received material

Microstructural analysis of the as-received alloy revealed the presence of particles several μm in diameter, for which EPMA gave the composition (phase P shown in Table 3.3) as $Al_{40}Cu_9Fe_4Mn$. TEM/EDS studies located particles in the alloy which contained aluminium, copper and magnesium, believed to be of S' and S (Al_2CuMg) phases, Fig. 3.44a, as well as dispersoids containing aluminium, copper and manganese, probably the $Al_{20}Cu_2Mn_3$ phase [141,142]. An etched sample, Fig. 3.44b, shows that the structure of the as-received material consists of elongated grains ~100 μm

in length. The measured shear strength of as-received alloy was 255 MPa, Table 3.2, with some yielding of specimens prior to failure as evidenced by the shear test stress-displacement curve, Fig. 3.44c, and the fractured specimen, Fig. 3.44d. Similar values were obtained for alloy heat-treated in air at 500°C for 240 minutes.

3.4.2. Bonding without an interlayer

The pressure versus time curves for 2124 alloy bonded at temperatures of 400°C, 460°C and 500°C were all generally similar to Fig. 3.8, with the exception of the initial drop in applied pressure (A to C). This was found to decrease with a decrease in bonding temperature (by ~20% of the initial applied pressure at 500°C to ~10 % at 400°C).

Bonding at 500°C

Bonding for 60 minutes using an initial applied pressure of 10 MPa gave a permanent sample deformation of ~2 %. A polished section, Figs. 3.45a and 3.45b, shows grains ~200 μm in length. The large phases (~10 μm) present in the alloy were shown, using EPMA, to have similar composition to the $Al_{40}Cu_9Fe_4Mn$ phase identified in the as-received alloy. Smaller precipitates may also be seen in

the alloy, although these were not analysed as they were beyond the resolution of the EPMA technique (~few μm^3). The bond interface is recognisable by the thin, almost continuous layer of intermetallic phase which spans the centre of the micrograph. Microstructural analysis at higher resolution was carried out using TEM of a thin foil sample. The layer present at the interface was found to contain aluminium, copper and magnesium, believed to be the S phase, along with magnesium- and oxygen-containing particles, similar to those shown in Fig. 3.27a. Two types of fine precipitate were also located in the alloy. The first was the characteristic S' phase (similar to Fig. 3.44a) which forms on {210} planes of the aluminium lattice with composition Al_2CuMg [141]. The second precipitate, Fig. 3.46a, ~200 nm in size, contained aluminium, copper and magnesium, and was also oriented in the aluminium lattice as evidenced by the diffraction pattern, Fig. 3.46b. Analysis of the diffraction pattern indicates that the beam direction in the foil was $[11\bar{2}]$, the indexed spot pattern is given in Fig. 3.46c. The system of weaker spots originates from the precipitate structure. Measurement of the spot marked 'a' gives a corresponding 'd' spacing of 0.44 nm (for 0002 planes), a value half that of the 'c' axis parameter of the precipitate. Measurement of spot 'b' gives a 'd' spacing of 0.45 nm, associated with $(20\bar{2}0)$ planes. Based upon further measurement of the spots in Fig. 3.46b, it is proposed that the structure of the precipitate is

hexagonal with lattice parameter a = 0.521 nm, to give a 'c' to 'a' ratio of 1.69. Furthermore, we may conclude that the precipitates, which lie on {111} planes of the aluminium, have a crystallographic relationship consistent with the close packed planes of the precipitate lying parallel to the close packed planes of the matrix. Thus we may write

$$(0001)_{ppt}//\{111\}_{Al} \; ; \; [100]_{ppt}//[11\bar{2}]_{Al} \; ,$$

similar to the Ω-type precipitate reported for Al-Cu-Mg alloys heat-treated at 370°C for 5 minutes [144-146]. Part of the bonded sample was solutionised at ~530°C and quenched into a water bath. However, this was found to result in deformation of the joint, with some areas becoming unbonded. In light of this no further heat-treatments were carried out.

The samples bonded using an initial pressure of 10 MPa for 240 minutes and 1200 minutes showed deformations of 3% and 5%, respectively, and were similar in appearance to Fig. 3.45. The shear strengths, summarised in Table 3.7, were 133 ± 47 MPa, 138 ± 38 MPa and 149 ± 42 MPa, respectively; the bonded areas were 73 ± 25 %, 75 ± 20 % and 82 ± 22 % to give specific strengths of 182 ± 4 MPa, 185 ± 10 MPa and 182 ± 8 MPa. Alloy bonded using an initial pressure of 20 MPa for 30 minutes showed a permanent deformation of ~8%. The shear strength was 170 ± 41 MPa and the bonded

area was 88 ± 20 % to give a specific strength of 193 ± 5 MPa. In all cases failure occurred at the bond interface.

Bonding at 460°C

The bond formed between 2124 alloy couple using an initial pressure of 10 MPa for 240 minutes had a deformation of ~2%, and was similar in appearance to Fig. 3.45. The bond strength was 104 ± 37 MPa with failure taking place at the interface, whilst the bonded area was 68 ± 24 % to give a specific strength of 153 ± 9 MPa.

Bonding at 400°C

The pressure versus time curve showed only a limited decrease, from an initial value of 10 MPa, to give a sample deformation of ~1%. The shear strength was 59 ± 12 MPa with failure occurring at the joint interface; a bonded area of 48 ± 19 % gave a specific strength of 136 ± 39 MPa.

Alloy bonded using a higher initial pressure of 30 MPa for 30 minutes gave a specimen deformation of ~2% and was similar in appearance to Fig. 3.45. The shear strength was 52 ± 10 MPa with failure occurring at the interface. However, the bonded area was difficult to determine as the fracture surface was relatively smooth.

The effect of bonding temperature on the shear strength, bonded area and specific shear strength are shown in Figs. 3.47a, 3.47b and 3.47c. Bonding conditions and shear data are collated in Table 3.7.

3.4.3. Bonding with a zinc interlayer

The pressure versus time curve for 2124 alloy bonded with a zinc foil using an initial pressure of 10 MPa at 500°C was similar to Fig. 3.8; the pressure decreased during the first 20 minutes of bonding to reach a steady value of ~8 MPa. Pressing for 240 minutes did produce a bond with a sample deformation of ~2%. Unfortunately, it could not be shear tested as the alloy plates separated during cooling of the sample. Examination of the mating surfaces in the SEM revealed that the zinc interlayer had melted, to result in some surface reaction with the alloy, as evidenced by regions of pitting.

3.4.4. Bonding with a copper-silver alloy interlayer

The pressure versus time curve for 2124 alloy bonded with a copper-silver interlayer using an initial applied pressure of 10 MPa at 510°C, Fig. 3.48, shows the

characteristic decrease in pressure at C associated with the ejection of a liquid phase from the joint. Inspection of a sample bonded for 30 minutes (deformed by ~3%) showed that the liquid was not expelled totally from the interface, most had collected beneath the surface of the edges of the aluminium as evidenced by barrelling of the sample. A polished section of a central region of the joint, Fig. 3.49a, shows a reaction zone ~20 μm wide which EPMA showed consisted of aluminium, $CuAl_2$ and Ag_2Al phases. In places the liquid had diffused up to a distance of ~750 μm into the 2124 alloy at grain boundaries, as evidenced from the solidified microstructure shown in Fig. 3.49b. Substantial amounts had also collected in peripheral regions of the joint, Fig. 3.49c. The diffusion profiles for copper, silver and magnesium across the joint, Figs. 3.50a, 3.50b and 3.50c, show increased levels of magnesium within the alloy adjacent to the bond interface as well as the presence of copper and silver. To examine this region more closely samples suitable for analysis in the TEM were to be produced. Unfortunately, fracture occurred at the bond interface during preparation of the specimens, therefore TEM was not performed. We would expect, however, copper-containing precipitates to be present in the alloy and these are most likely be the γ' (Ag_2Al), S' (Al_2CuMg) and Ω (Al-Cu-Mg) phases described in previous sections. There is also the possibility that another Ω-type phase may form which contains silver, as reported by Scott, Kerry and Trumper [24] for Al-Cu-Mg-Ag

alloys. The shear strength was 108 ± 11 MPa, failure taking place through the intermetallic phases present at the joint interface, Fig. 3.49d. The bonded area was 90 ± 6 % to give a specific strength of 120 ± 9 MPa.

3.5. Aluminium alloy (2124) reinforced with SiC particulate (2124/P)

3.5.1. As-received material

Examination of the as-received composite revealed silicon carbide particulate in a range of sizes from 5 μm to less than 1 μm, Fig. 3.51a, which were fairly evenly distributed, although due to the nature of the manufacturing route some matrix-rich regions were present, Fig. 3.51b. Thin foil TEM studies showed that the silicon carbide had not reacted with the aluminium as evidenced by the 'clean' particle/matrix interfaces, Fig. 3.52. TEM also revealed the presence of θ, S and Al-Cu-Mn-Fe phases in the alloy as well as aligned precipitates of θ' and S' although they were not evenly distributed throughout the matrix.

Results from shear tests on specimens cut from as-received composite gave strengths of 260 ± 4 MPa, 278 ± 4 MPa, 288 ± 6 MPa and 289 ± 33 MPa for SiC volume fractions of

25%, 30%, 35% and 40%, respectively, Table 3.2. A typical stress-displacement curve for a tested specimen, Fig. 3.53a, shows that failure was non-catastrophic and this was associated with extensive cracking of the composite, Fig. 3.53b.

3.5.2. Bonding without an interlayer

All specimens were bonded at a temperature of 500°C for 240 minutes using an initial applied pressure of ~10 MPa, to give a specimen deformation of ~2% (unless otherwise stated). The pressure versus time curve for 2124/25P bonded composite, Fig. 3.54, shows a rapid decrease to reach a steady value of ~2 MPa within 100 minutes. A section of a sample bonded for 240 minutes is shown in Fig. 3.55a. Where there was metal-to-metal contact across the interface the bond appeared to be well established, whilst poor bonding was observed between contacting silicon carbide particles, as evidenced by the presence of cracks. The shear strength of the joint was 58 ± 9 MPa with failure occurring at the bonded interface, the fracture surface, Fig. 3.55b, showing both ductile and brittle failure. Closer inspection revealed that the ductile failure occurred at alloy-rich regions, such as grain boundaries, whereas brittle fracture took place

through the areas of the composite containing SiC particulate, Fig. 3.55c.

Bonding experiments carried out using composites with volume fractions of 30%, 35% and 40% SiC gave pressure versus time curves similar in appearance to Fig. 3.54. Analyses of light micrographs obtained from polished sections showed that the amount of metal-to-metal contact across the joint decreased with increase in volume fraction of silicon carbide. The shear strengths of the joints were 43 ± 14 MPa, 22 ± 10 MPa and 36 ± 14 MPa, respectively, with failure occurring at the bond interface for all specimens. The fracture surface of the 40% sample, Fig. 3.56, was relatively smooth compared with the 25% bonded sample due to the higher content of SiC particulate which reduced the regions of unreinforced metal. The effect of volume fraction of the SiC_p on the shear strength of the bonded composite is shown graphically in Fig. 3.57. As a comparison, the shear strength of a bonded joint of unreinforced 2124 alloy (138 ± 38 MPa) is included on the graph.

The effect of specimen deformation on joint microstructure and shear strength was also studied for the 2124/25P composite. Samples were bonded using deformations of 8%, 13% and 19%, and in each case the maximum applied pressure was found to be ~10 MPa, which is approximately the flow stress of the composite. It was noted that the increase

in deformation resulted in a greater barrelling of the bonded specimens, to increase the area of the mating surfaces. A micrograph of the specimen bonded using 19% deformation, Fig. 3.58, shows a slightly more uneven bond line than the 2% experiment, Fig. 3.55, due to the increased amount of movement of aluminium and SiC particulate at the interface. For all samples shear testing resulted in failure at the bond line with strengths 49 ± 9 MPa, 46 ± 22 MPa and 119 ± 4 MPa, for deformations of 8%, 13% and 19%, respectively, Table 3.8. The effect of sample deformation on shear strength is illustrated in Fig. 3.59, which shows clearly the presence of a 'threshold' value at ~20%.

3.5.2. Bonding with a copper-silver alloy interlayer

The pressure versus time curve for 2124/35P composite bonded with a copper-silver alloy foil using an initial pressure of 4 MPa at 510°C was similar to Fig. 3.54; there was no characteristic drop in pressure associated with the expulsion of liquid. After bonding for 30 minutes the permanent deformation was ~3%. A polished section, Fig. 3.60a, shows a reaction zone at the joint interface ~2 μm thick, a value considerably less than the original copper-silver interlayer thickness of ~50 μm. The phases present at the bond interface were too small for quantitative EPMA

analysis, although EDS did show that they contained copper, aluminium and silver. These phases were probably $CuAl_2$ and Ag_2Al, similar to those formed in bonding experiments on unreinforced 2124 alloy using a copper-silver interlayer. Within the intermetallic zone particles of SiC were found; this movement of the reinforcement indicated that a liquid phase was present at the interface. However, no liquid was expelled from the joint during the bonding experiment; it is believed to have been 'absorbed' by the composite, as evidenced by results from EPMA which found significant amounts of copper and silver up to a distance of ~150 μm away from the bond interface. TEM analysis of this region was to be used to establish the nature of the precipitates. Unfortunately, this was not possible as fracture of the joint occurred during the preparation of specimens. However, in the copper-silver diffusion zone particles aligned in the aluminium lattice, other than the θ' and S' already present in the 2124 alloy, would be expected. Results from previous sections indicate that the γ' and Ω precipitates may be formed. The shear strength was 99 ± 32 MPa with failure occurring in the joint region; the bonded area was difficult to establish due to the flat, featureless nature of the fracture surfaces.

After bonding using an initial pressure of 8 MPa a greater deformation of the composite, compared with the 4 MPa experiment, was noted (from 3% to 6%). The pressure

versus time curve was similar to Fig. 3.54. No liquid was expelled from the joint, although the presence of SiC particles in the joint area, Fig. 3.60b, and the remnant solidified copper- and silver-rich phases at the bond line indicated that a liquid had formed. The shear strength of the joint was 193 ± 91 MPa with failure taking place mainly at the bonded interface, although the roughened appearance of the fracture surfaces indicated that some failure occurred through the composite.

3.5.4. Bonding with an aluminium alloy (2124) interlayer

The pressure versus time curve for 2124/30P composite bonded with a 2124 interlayer using an initial pressure of 10 MPa at 500°C was similar to Fig. 3.54. Bonding for 240 minutes produced a specimen deformation of ~2%. In a section of the joint, Fig. 3.61, the interlayer may be clearly seen. EPMA showed little difference in the concentration of copper and magnesium between the foil and composite matrix and this was reflected in the microhardness profile which indicated a uniform hardness across the interlayer. Examination of the bond in the TEM was not performed due to the difficulty of preparing samples. However, a reaction of the magnesium, present in both the interlayer and composite matrix, with the surface aluminium oxide layer would have been expected. The shear

strength was 111 ± 46 MPa with failure occurring at one of the interlayer/composite interfaces.

3.6. The bonding of dissimilar materials

The following bonding experiments were carried out without an interlayer using an initial pressure of 10 MPa at 500°C for 240 minutes. The pressure versus time curve for bonding unreinforced alloy was similar to Fig. 3.8; for particulate composites the pressure versus time curves were similar to Fig. 3.54. All samples were deformed permanently by ~2% except for the aluminium/2124P bond which was close to 3%. Results from shear tests are collated in Table 3.9.

3.6.1. Aluminium bonded to 2124 alloy

A commercial-purity aluminium to 2124 alloy joint, Fig. 3.62, appears to be fully bonded across the whole section, with little sign of any porosity at the interface. EPMA showed that copper and magnesium had diffused from the 2124 alloy into the aluminium up to a distance of ~100 μm, Figs. 3.63a and 3.63b. TEM studies of the joint region revealed particles of S' in the 2124 alloy θ' in the

commercial-purity aluminium as well as magnesium- and oxygen-containing particles at the bond interface, Fig. 3.63c. An etched sample, Fig. 3.64, highlights the grain structure of the 2124 alloy, and the commercial-purity aluminium where copper was present. The hardness profile, Fig. 3.63d, indicates local hardening of the aluminium and softening of the 2124 alloy in regions adjacent to the bond interface. The shear strength of the joint was 67 ± 9 MPa, the bonded area of 92 ± 11 % gave a specific strength of 73 ± 2 MPa. Failure took place mainly in the aluminium with the unbonded regions occurring at the periphery of the joint.

3.6.2. Aluminium bonded to 2124/P composite

Commercial-purity aluminium bonded to 2124/25P is shown in Fig. 3.65. Copper and magnesium were found, using EPMA, to have diffused from the composite 2124 matrix into the aluminium up to a distance of ~100 μm, Figs. 3.66a and 3.66b. Within this region particles of S' and θ' were located, which were found to locally harden the aluminium, Fig. 3.66d. EPMA also showed that the concentration of oxygen in the composite was higher than for unreinforced 2124 alloy, Fig. 3.66c. This is a characteristic feature of the powder metallurgy manufacturing route, as the total surface area of the alloy is high. The shear strength was

55 ± 7 MPa, failure taking place mainly through the aluminium. The bonded area was 94 ± 12 % to give a specific strength of 59 ± 2 MPa.

3.6.3. Alloy (2124) bonded to Al/Nic composite

For 2124 alloy bonded to Al/Nic composite, Fig. 3.67a, copper and magnesium were detected up to a distance of ~150 μm into the aluminium matrix of the composite with the formation of S' and θ' precipitates. In some regions of the joint only the aluminium matrix was in contact with the 2124 alloy, Fig. 3.67b. The shear strength of the joint was 76 ± 11 MPa with failure occurring well away from the interface through the composite, Fig. 3.67c. Results from fibre indent tests indicated a shear strength of ~70 MPa for fibres in the composite, Table 3.5d. In the joint region although only several fibres were tested values were ~200 MPa. The bonded area was 94 ± 11 % to give a specific strength of 81 ± 6 MPa; unbonded regions were present at the periphery of the joint.

3.6.4. Alloy (2124) bonded to 2124/P composite

A 2124 alloy - 2124/40P bond was similar in appearance to Fig. 3.65. EPMA found little difference in the concentrations of copper and magnesium across the joint, although TEM studies did locate particles at the interface rich in magnesium and oxygen. The shear strength was 132 ± 3 MPa, failure occurring at the joint interface.

3.6.5. Al/Nic bonded to 2124/P composite

The Al/Nic - 2124/35P bonded couple is shown in Fig. 3.68a. In regions where there was metal-to-metal contact at the interface, Fig. 3.68b, copper and magnesium had diffused from the 2124 alloy into the aluminium matrix of the Al/Nic composite up to a distance of ~100 μm. Microhardness tests of the matrix revealed a hardness of 65 HV near the joint and 34 HV away from the joint. Tests on the fibre/matrix interfacial strength revealed values of 72 ± 11 MPa for fibres in the composite away from the bond and ~180 MPa for fibres in the joint region, Table 3.5e. The shear strength was measured as 75 ± 10 MPa with failure taking place through the fibre composite in a catastrophic manner, as indicated by the stress-displacement curve, Fig. 3.68c. The bonded area was ~100%.

4. DISCUSSION

This chapter commences with a discussion of the shear testing of bonded joints, in particular the modified shear test used in the present study, and relates results from fibre/matrix indentation tests with the shear strength of the corresponding joint.

The solid-state bonding of aluminium alloys, with and without reinforcement, is then discussed. This is followed by a section on liquid-phase bonding of these materials. The major part of the discussion is concerned with the use of metal interlayers as they affect the efficacy of joining using the two methods.

4.1. Assessment of the modified shear test method

There is no standard technique for the testing of diffusion-bonded joints, most studies adopting the lap-shear method developed originally for adhesively-bonded joints [147,148]. It should, however, be mentioned that the high strength of diffusion-bonded joints often causes bending of the metal substrate, a feature that does not occur for the weaker adhesive bonds. Indeed, in the case of aluminium, the degree of substrate bending may be sufficient to induce failure of the bond by 'peel' rather than 'true shear' [114,149], as

discovered in preliminary tests carried out on diffusion-bonded aluminium. In order, then, to minimise bending and subsequent 'peeling' of samples, the lap-shear technique may have to be modified, either by using thicker metal substrates or by restraining samples during testing. Since the former technique was impractical for the present study due to the large amount of composite material required the latter approach had to be adopted. It should be pointed out that the method has been used with some success by Partridge and Dunford who, in studies on diffusion-bonded aluminium alloy (8090), reported an increase in measured strength for restrained lap-shear samples compared with the conventional testing method [150-152].

A clamping arrangement to reduce bending was considered too awkward to use during testing, and, a jig was therefore designed and constructed, Fig. 2.6, such that during testing coupons were restrained laterally and compressive forces applied in order to induce failure by shear. Results showed that the design was successful, with the exception of commercial-purity aluminium where high ductility led to off-axis stresses and bending, see Fig. 3.7.

Comparison of the measured shear strength values for aluminium with published data for a similar alloy gives a measure of the accuracy of the test. Thus the close agreement between the values of ~100 MPa for as-received metal and ~80 MPa for heat-treated specimens with the values

of 80 MPa to 90 MPa given by Tabata *et al* [131] for annealed aluminium (IADS 1050) tested using a similar shear jig is considered to be validation of the modified test method.

The precision of the shear test may be determined by assessing the methods used for obtaining shear strength and specific strength. The former is calculated on the basis of the maximum load experienced by a test coupon and its original overlap area, whilst the latter is obtained from the maximum load and bonded area. The measurements of bonded area are believed most subject to error for two reasons. Firstly, the bonded area is difficult to measure from fracture surfaces due to their flat and often featureless nature (particularly noticeable for bonded 2124/P composite). Secondly, since shear test coupons were usually cut from only one-half of the bonded joint, the averaged test data will be representative of the whole specimen only if the bonded area is symmetrical. Then, of course, the averaged bonded area of test coupons may be used to determine the shear strength of the original joint (assuming that the sum of the failure loads of individual coupons is equal to the failure load of the whole joint). A further point relating to the scatter in the averaged data concerns the nature of the bonded area in the joint, a large scatter being characteristic of a large bonded region, as found for the liquid-phase copper bond in which the joint was developed only in central regions, Fig. 4.1a, and a small scatter implying that the bonded area was patchy, Fig. 4.1b.

4.2. Fibre/matrix indentation test data as related to the shear test values

The indentation technique was developed by Marshall [130] for measuring the interfacial friction stress of fibres in ceramic matrix composites, conditions which are fundamentally different from MMCs in that the matrices are often harder than the fibre reinforcement and the fibre/matrix bond strength is low (typically several MPa). Thus a fibre displaced readily by the indenter causes little deformation of the surrounding matrix except for the impressions left by the diamond.

For MMCs, particularly aluminium-based, the matrix is softer than the fibre reinforcement and the fibre/matrix bond strength is high (>30 MPa). Consequently, when a fibre is displaced by the diamond indenter, substantial plastic deformation of the matrix will occur along its length and the measured values of interfacial friction stress will be closer to the bond strength between fibre and matrix and/or the shear strength of the matrix.

Results from both fibre/matrix interfacial stress measurements and shear tests support this proposition. For Al/Nic composite the fibre/matrix strength was within the range 35 MPa to 75 MPa. These values compared favourably with the specific shear strengths for the bonded composite (~55 MPa to 80 MPa), where failure took place away from the

joint mainly at fibre/matrix interfaces. It is interesting to note that these results are in accord with previously published values for a similar composite material [143].

Another technique which was considered for measuring the friction strength between fibre and matrix involved a push-out test in which fibres in a thin section of composite are 'pushed out' from the matrix using a micro-indenter; their displacement is measured using scanning electron microscopy and the friction stress is given by the force per sliding area. Watson and Clyne [153] have used this technique for a SiC monofilament/titanium composite, but the method was not used in the present work due to the difficulty of preparing the sections of Al/Nic composite and the need to use a small indenter (<10 μm diameter) for Nicalon fibres.

4.3. Solid-state bonding of aluminium and aluminium-based composites with and without alloy (2124) interlayers

4.3.1. Bonding unreinforced aluminium

Commercial-purity aluminium

Bonding studies on commercial-purity aluminium at 500°C using an initial pressure of 3 MPa for 30 minutes failed to produce a joint. Even when the pressure was increased to 10 MPa and the time to 240 minutes (producing a deformation of ~10%) it was unsuccessful. The inability to form a bond, even with appreciable plastic deformation, is indicative of a surface condition which prohibits interdiffusion of the aluminium. This, EPMA has shown, is associated with a continuous layer of aluminium oxide. The oxide is present as a ~2 nm thick film on freshly prepared aluminium and was shown to thicken to ~40 nm when heated in air at 500°C for 240 minutes. Presumably, during the bonding experiment the thickness of the alumina film lies between these two values. Published work [99] has shown that the oxide, which consists of 'amorphous' Al_2O_3 at ambient temperatures and forms a duplex layer with crystalline γ-Al_2O_3 above 475°C, is stable up to temperatures approaching the melting point of the aluminium (~660°C).

It is our contention, therefore, that the difficulty of bonding samples of aluminium may be attributed mainly to the presence of the oxide, as proposed in the following

mechanism, illustrated schematically in Figs. 4.2a to 4.2d. In the initial stage of bonding, pressure is applied to the aluminium couple, Fig. 4.2a, and surface asperities deform plastically to cause fracture of the overlying oxide film. This is brought about by shearing stresses induced as a result of asperity contact, Fig. 4.2b. For a bond to become established the oxide layer on both of the aluminium surfaces must fracture at similar locations to obtain metal-to-metal contact and allow metal diffusion, Fig. 4.2c, (as described by Mohamed and Washburn in studies on pressure welding aluminium, [154]). The total area of the metal-to-metal bond is, however, likely to be limited due to the immediate reformation of oxide at fracture sites before the joint can be established, Fig. 4.2d.

Satisfactory joints with unalloyed aluminium have, however, been obtained only by using large strain rates and deformations since good metal-to-metal bonds can be established at freshly created surfaces at the joint interface before the oxide reforms. This is the basis of friction welding [131,154,155] where the deformation often exceeds 30%, although for MMCs such large deformations should be avoided since the reinforcement may be damaged and the mechanical performance of the composite degraded.

Bonding aluminium alloy (2124)

In marked contrast to the poor diffusion bonding behaviour of aluminium, 2124 alloy readily formed a joint. Examination of the joint bonded at 500°C for 240 minutes using an initial pressure of 10 MPa showed that a planar interface was present, indicative of a solid-state bond, and that interdiffusion of copper and magnesium from the alloy, had occurred, as evidenced by the presence of S phase (Al_2CuMg).

The development of a good joint with this alloy is attributed to the lower stability of the surface oxide on the alloy compared with unalloyed aluminium. This view is supported by studies on the surface oxidation of aluminium-magnesium alloys in air [99,156-159], which showed that although the alumina layer present on a freshly exposed surface is similar to unalloyed aluminium, the crystalline form of oxide is produced at a lower temperature (350°C compared with 475°C). These oxides, which form as particles and thereby disrupt the alumina film, are produced via one of the following reactions [160],

$$Al_2O_3 + 3Mg \rightarrow 3MgO + 2Al \qquad (1)$$

$\Delta G^\circ = -140\ kJmol^{-1}$ at 500°C

$$4Al_2O_3 + 3Mg \rightarrow 3MgAl_2O_4 + 2Al \qquad (2)$$

$\Delta G^\circ = -280\ kJmol^{-1}$ at 500°C

The more negative free energy of reaction (2) would favour the formation of the spinel oxide ($MgAl_2O_4$) but, in reality

the oxidation of aluminium-magnesium alloys is more complex and depends on factors such as alloy composition. The amount of magnesium ions absorbed by the alumina layer controls the rate of oxidation and determines the type of oxidation product formed. Although it is not established which oxide causes maximum disruption to the alumina film, based on volume difference the MgO would appear more favourable for bonding. Thus the stability of the oxidation products is an important factor, and data [99] for high temperatures (>375°C) indicate that the oxide MgO is stable if the magnesium content is >1 at%, the spinel oxide $MgAl_2O_4$ is stable for 10^{-4} to 1 at% magnesium, and 'amorphous' oxide Al_2O_3 is stable below 10^{-6} at% magnesium. To a lesser degree, the availability of oxygen affects the reaction, with the spinel oxide, $MgAl_2O_4$, forming in preference to the MgO at very low pressures.

Field, Scamans and Butler [159] have proposed a four-stage model for the oxidation of Al-4.2 wt% Mg alloy in air at 500°C, as illustrated in Figs. 4.3a to 4.3d. Initially, magnesium enters the amorphous Al_2O_3 surface film, thereby increasing the number of anion vacancies to result in more rapid transport of oxygen to the oxide/metal surface, Fig. 4.3a. This allows the nucleation and subsequent growth of primary MgO which leads to the fracture of the oxide film, due to a difference in volume. At the same time, secondary oxides form via reduction of the Al_2O_3 film by magnesium, Fig. 4.3b. Any freshly exposed metal rapidly develops an

oxide layer of Al_2O_3 beneath which further primary nucleation takes place. This process of MgO formation continues and results in localised depletion of magnesium within the alloy, Fig. 4.3c, a process by which the aluminium surface becomes corrugated and fully covered by MgO crystals, Fig. 4.3d.

Work by Ritchie, Sanders and Weickhardt [160] identified the nature of the oxide at the surface of an aluminium alloy with a lower magnesium content of 1.2 wt%. On exposure to air at 500°C for a time, t, the following oxides were observed at the surface

Al_2O_3	$t < 5$ mins,
MgO and Al_2O_3	5 mins $< t <$ 30 mins,
MgO and $MgAl_2O_4$	30 mins $< t <$ 60 mins,
$MgAl_2O_4$	$t >$ 60 mins.

In the present bonding studies, thin foil TEM revealed particles at the joint interface which were associated with aluminium, magnesium and oxygen. However, the limited resolution of the electron-probe used in the EDS mode probably resulted in excitation of the adjacent aluminium and it is, therefore, difficult to distinguish between MgO or $MgAl_2O_4$ particles. The presence of oxide particles at the joint interface is consistent with observations by Maddrell *et al* [113] in work on vacuum diffusion-bonded Al-5 wt% Mg alloy.

It has been reported [99,159] that, as with magnesium, copper and silver ions may be absorbed by the surface alumina film to affect subsequent high temperature oxidation. Since, however, the 2124 aluminium alloy contains iron as well as copper and magnesium, Table 2.1, the high temperature oxidation reactions will be more complicated than for the aluminium-magnesium binary system. It would be interesting to carry out bonding experiments on Al-Mg and Al-Cu alloys to assess the individual contribution of magnesium and copper to the formation of the joint. In the present study, however, for the purposes of devising a mechanism for the bonding of 2124 alloy, the presence of elements other than magnesium will be ignored.

For bonding 2124 alloy, the model proposed for unalloyed aluminium (Figs. 4.2a to 4.2d) may be modified to take into account the results from microstructural observation and published work [154-159]. The mechanism is shown schematically in Figs. 4.4a to 4.4f. At the start of bonding, Fig. 4.4a, load is applied to the diffusion couple and, as with unalloyed aluminium, the surface asperities deform plastically to fracture the surface oxide films, Fig. 4.4b. If metal-to-metal contact occurs as a result of the oxide fracturing at adjacent sites a joint may be established, Fig. 4.4c. It is more likely, however, that the alumina film reforms since there is insufficient magnesium present at the interface to form MgO or $MgAl_2O_4$. Simple calculation indicates that there is enough magnesium present

within a 0.5 μm thick layer of a Al-1 wt% Mg alloy to reduce an alumina film, 4 nm thick. As a consequence magnesium diffuses within minutes to the joint interface where reduction of the alumina film commences, Fig. 4.4d. The reduced oxide is believed to consist initially of a mixture of MgO, $MgAl_2O_4$ and Al_2O_3, the discontinuous nature of the spinel and magnesia allowing interdiffusion of the alloy constituents and the establishment of a joint, Fig. 4.4e. After ~30 minutes the alumina layer has been completely disrupted, diffusion at the bond interface being driven mainly by the energy differences associated with the topography of the bonding surfaces (*ie*, interfacial voids, [106,107]. With longer bonding times these irregularities are eliminated by the redistribution of aluminium via solid-state mass-transfer mechanisms, Fig. 4.4f, the process being analogous to sintering [161].

Bonding was found to take place only within the central region of the joint (~75%), the lack of bonding in the peripheral regions being attributed to a lower pressure (Fig. 4.5a) caused by friction at the platen/sample interface [162]. Thus the greater flow of aluminium at the centre of the mating surfaces gives the overall specimen deformation illustrated in Fig. 4.5b. However, as the sample deformation is only ~2% this effect will be small, although, it would be more marked for specimens which experience larger deformations during bonding [163].

With regard to the mechanical properties of the joint, shear strength, bonded area and specific shear strength all decreased with decrease in bonding temperature, Figs. 3.47a, 3.47b and 3.47c. This trend may be attributed to the fact that at lower temperature (a) the magnesium reduction reaction is less effective, (b) the 2124 alloy is more resistant to deformation, thus reducing the degree of surface flattening and (c) the lower rate of diffusion of aluminium reduces the degree of joint consolidation, *ie*, void elimination.

Results showed also a slight increase in the shear strength and bonded area of the joint with bonding time due to increased surface flattening associated with time-dependent mass transfer processes such as creep and diffusion [106,107]. The specific strength was constant ~185 MPa for each bond condition indicating that the joint developed within 60 minutes. However, the base metal strength (~250 MPa) was not attained, even after bonding for 1200 minutes because the planar bond interface offered an easy fracture path, particularly where grain growth across the joint interface was inhibited by the presence of second phases such as Al_2CuMg, dispersoids of $Al_{20}Cu_2Mn_3$ and oxide particles of MgO and $MgAl_2O_4$.

The pressure applied during bonding affected the shear strength and bonded area of the joint, and a sample bonded using an initial pressure of 20 MPa had a greater strength

and bonded area than the 10 MPa sample. Again, this may be attributed to an increase in the degree of surface flattening with increase in pressure. Furthermore, it may be presumed that the threshold of deformation, below which a bond is not established, is likely to be lower for 2124 alloy than for commercial-purity aluminium due to the difference in the stability of the respective surface oxide films.

Thus it may be concluded that to form a strong joint with large bonded area, a high pressure (>20 MPa) applied for a short period of time (<60 minutes) would be more beneficial than a low pressure for longer bonding times (say 10 MPa for 240 minutes). This is an important factor to be considered when joining MMCs as exposure to diffusion bonding temperatures for prolonged periods of time would encourage fibre/matrix interfacial reactions to the detriment of the strength of the composite. On the other hand, pressure should not be so high as to cause excessive deformation of the matrix and gross fibre breakage.

Post heat-treatment of a joint caused debonding during quenching of samples, probably due to the presence of residual stresses which were not relieved fully during the solutionising stage. It would be interesting, however, to investigate further the ageing characteristics of bonded joints since TEM studies indicated the presence of Ω-type (Al-Cu-Mg) precipitates within the air-cooled bonded specimens. If these have a similarly stable character as the

Ω precipitates found in Al-Cu-Mg-Ag alloys [24,164] then appropriate heat-treatment may improve the high temperature properties of the alloy.

A review of the literature revealed very few studies of the solid-state bonding of aluminium alloys. Enjo and Ikeuchi [115] bonded Al-Cu-Mg alloy (2017) at 500°C and reported strengths of ~20 MPa. The low value is probably due to insufficient breakdown of the alumina film due to the low magnesium content (0.3 wt%) coupled with the application of too low a pressure (~4 MPa). No grain growth across the interface was observed, and as a result of quenching from a solutionising temperature (500°C), the joints fractured. Joints approaching the tensile strength of the alloy (400 MPa) were obtained only for alloy bonded above the solidus temperature (580°C) where the presence of liquid stimulated grain growth across the interface. Partridge and Dunford [151,152,114] have bonded 8090 aluminium alloy in the solid-state (~560°C) and reported shear strengths of ~190 MPa for samples after subsequent heat-treated. The formation of the joint was attributed to the breakdown of the surface alumina film by lithium and magnesium. As both the above studies were carried out in vacuum (10^{-2} Pa) and no mention was given of the area of bond it is difficult to compare results with the present work.

Bonding commercial-purity aluminium to aluminium alloy (2124)

The bonding experiment using a commercial-purity aluminium/2124 alloy couple gave a satisfactory joint with a shear strength of ~70 MPa, a bonded area of ~90%, and a specific strength of ~75 MPa (a value similar to that for heat-treated aluminium). Failure in the commercial-purity aluminium away from the joint is attributed to localised strengthening of the metal caused by precipitation of θ' phase, the copper having diffused in from the 2124 alloy. As evidenced by microhardness measurements, Fig. 3.63d, the shear failure occurs in the softer region of metal immediately adjacent to this precipitation hardened structure.

With regard to the development of the joint, a mechanism based on the previous two bonding models is proposed. Initially, the surfaces of the 2124 alloy and aluminium are in contact and the asperities deform plastically under the applied pressure. Magnesium present in the 2124 alloy then diffuses to the joint interface to reduce the alumina film, firstly, on the 2124 alloy and then on the unalloyed aluminium. This is followed by diffusion of aluminium, and other alloy constituents, at the interface to consolidate the joint by eliminating interfacial porosity.

Bonding commercial-purity aluminium with an aluminium alloy (2124) interlayer

Results from the previous section prompted a study into the viability of bonding commercial-purity aluminium using a 2124 alloy interlayer. This involved an initial pressure of 10 MPa at 500°C and, as in the experiment on the 2124 alloy/aluminium couple, the joint was established within 240 minutes. The shear strength of the joint was ~60 MPa, a value similar to heat-treated aluminium. Failure took place well away from the joint, again due to strengthening of the aluminium adjacent to the joint by precipitation hardening (θ' phase) as a consequence of the diffusion of copper from the 2124 alloy interlayer.

Summary of bonding unreinforced alloy in the solid-state

Bonding experiments have shown that commercial-purity aluminium does not form a joint even when using deformations up to ~10%. The presence of magnesium, as in the 2124 alloy, is a crucial factor in forming a satisfactory solid-state joint and need be present only on one side of the diffusion couple to promote bonding. Thus 2124 alloy may be used as an interlayer.

4.3.2. Bonding composite materials

Bonding Al/Nic composite

It has been demonstrated that unreinforced aluminium cannot be bonded without an interlayer using low deformations (<10%), as the surface alumina films form a barrier to diffusion. A similar result was expected for Al/Nic composite therefore bonding experiments were not performed.

Bonding aluminium alloy (2124) to Al/Nic composite

Since aluminium readily formed a bond with the aluminium alloy (2124) a similar technique was employed for the Al/Nic composite. Examination of a joint revealed that the dominant bonding mechanism was reduction of the alumina films by the magnesium present in 2124 alloy, although this reaction was inhibited where fibres were present in the composite surface. In spite of this, however, results from shear tests were very encouraging, with a shear strength of ~75 MPa and a bonded area of ~95% to give a specific strength of ~80 MPa, a value comparable with shear strength data reported elsewhere [19] for this composite material. Failure took place well away from the joint and this is attributed to local matrix hardening of the composite by θ' precipitates; the copper had diffused into the aluminium from the 2124 alloy. The matrix hardening effect was reflected in a higher interfacial friction stress within the joint region (~200 MPa) compared with the rest of the composite (~70 MPa).

Bonding Al/Nic composites with an aluminium alloy (2124) interlayer

To take advantage of the high strength joint formed between Al/Nic composite and 2124 alloy, bonding experiments were carried out on the composite using a 2124 alloy interlayer. The shear strength of the joint using an initial pressure of 20 MPa was ~60 MPa, a value comparable with the strength of the Al/Nic - 2124 alloy couple. The bonded area of ~75%, lower than for the unreinforced aluminium joined with a 2124 alloy interlayer (~90%), is attributed to (a) the high stiffness of the composite causing a reduction in the degree of surface flattening, and (b) the presence of fibres in the mating surfaces which inhibit bonding. Failure away from the bond interface through the composite was due to the local precipitation hardening of the aluminium matrix, as evidenced by thin foil TEM studies. It was also noted that the fracture path occurred mainly through fibre tows and this is accredited to the presence of voids between closely packed fibres, a feature due to poor infiltration of the metal during manufacture. Similar observations, of failure through fibre tows during mechanical testing, have been reported by Yang and Scott [83] for a carbon fibre/aluminium alloy composite.

The use of a higher bonding pressure (34 MPa) produced a joint with similar shear strength of ~55 MPa to the 20 MPa experiment although now the bonded area was ~100%, due to (a) increased flattening of the composite at the higher pressure

to give a more intimate contact of the mating surfaces and, (b) increased break-up of the surface alumina film.

Aluminium alloy (2124) reinforced with silicon carbide particulate

Since it has been demonstrated that 2124 alloy may be readily bonded by virtue of the magnesium reduction reaction of the surface alumina films at the joint interface, it should be possible to join 2124/P composite. It is likely, however, that the shear strength of the joint will be less than bonded unreinforced alloy since bonds will be established only at areas where there is metal-to-metal contact.

The more rapid decrease in the pressure versus time curve at the start of the experiment compared with the unreinforced alloy may be attributed to the differences in microstructure caused by the presence of the SiC reinforcement. For example, the thermal expansion mismatch between matrix and reinforcement means that composites have a higher dislocation density than unreinforced alloy, and this would lead to more rapid recovery during subsequent high temperature processing [13].

It was established that the shear strength of bonded joints was inversely proportional to the volume fraction of SiC, Fig. 3.57, decreasing from ~60 MPa for 25% SiC to ~35 MPa for 40% SiC. This is attributed to the inhibition of bonding at

regions of SiC-to-SiC or SiC-to-metal contact. The bonded area, as given by the total metal-to-metal contact will vary with the degree of overlap of the SiC particles. An upper-bound value of bonded area is obtained where complete SiC-to-SiC contact occurs, Fig. 4.6a, and a lower-bound value where there is no overlap of SiC, Fig. 4.6b. Assuming that the area fraction of particles at the surface of a section cut through the composite is equal to the volume fraction of SiC, these metal-to-metal limiting values, A_m, may be defined numerically as $(1-V_f)$ and $(1-2V_f)$, respectively, where V_f is the volume fraction of the SiC. If the strength for 100% bonded area is taken as the specific strength for bonded unreinforced alloy, σ_a (~180 MPa), then the joint strength is given by $\sigma_a \times A_m$. For a 25 vol% SiC composite the predicted upper-bound strength is ~135 MPa and the lower-bound strength ~90 MPa, assuming that bonding is fully established at all regions of metal-to-metal contact.

From micrographs of polished sections of bonded composites it is possible to estimate the area fraction of metal-to-metal contact at the joint interface, illustrated in Fig. 4.7. This value, which would lie between the lower- and upper-bound limits, may be used to predict the shear strength of the joint. Inspection of a section of the bonded 25 vol% sample, Fig. 3.55a, revealed ~40% metal-to-metal contact across the joint interface, to give an estimated shear strength of ~70 MPa. (This assumes that 100% contact area gives a specific strength of 2124 alloy when bonded under

similar conditions, ~180 MPa). The predicted value of strength is, however, less than the lower-bound value of ~90 MPa and this may be due to (a) errors introduced during the measurement of the metal-to metal contact or (b) incomplete joint formation at regions of metal-to-metal contact as a result of incomplete breakdown of the oxide film. The strength does, however, compare favourably with the measured value of ~60 MPa.

A similar approach may be used for higher volume fraction composites. The upper- and lower-bound shear strength values for the composites with SiC volume fractions of 30%, 35% and 40% are illustrated graphically in Fig. 4.8, along with the strengths estimated from micrographs and the measured data. The measured shear strengths are generally less than the lower-bound values, which indicates that a bond is not established at every site where there is metal-to-metal contact. This is attributed to the incomplete breakdown of the oxide film in these areas, Fig. 4.9a, which may, in turn, be due to a shortage of magnesium within the composite matrix and/or lack of sufficient metal-to-metal contact at the joint interface.

Studies of the effect of specimen deformation on the bond strength showed that the shear strength of the joints was approximately constant at ~50 MPa for deformations of 2% and 8%, but increased to ~120 MPa for the sample deformed by 19%, Fig. 3.59. The increase is attributed to (a) greater

flattening of the composite surfaces to give more intimate contact, and (b) an increase in the overlap area of the joint, as evidenced by barrelling of the sample, to result in greater fragmentation of the alumina film, Fig. 4.9b. The fact that the measured shear strength for the sample deformed by 19% lies between the upper- and lower-bound values (135 MPa and 90 MPa, respectively) indicates that the bond is fully established at regions of metal-to-metal contact. This deformation threshold is slightly lower than the 20% to 30% reported for pressure-welded and roll-bonded commercial-purity aluminium [154,155] because the very short periods of time (several seconds) involved with these processes relied more on instantaneous friction welding than interdiffusion of aluminium.

As mentioned earlier, large deformations are to be avoided when processing MMCs as unwanted reinforcement damage may occur, although particulate-reinforced composites, which already contain short reinforcement, would be an ideal candidate for a secondary fabrication process that combines diffusion bonding with some sort of metal forming.

Partridge, Shepard and Dunford [165] carried out a complex statistical analysis of bonded 8090/17% SiC_p composite in which the total area of metal-to-metal bonds was used to predict the shear strength of the joint, although without much success. The discrepancy may be due to the fact that the specimen deformation was too low; our results indicate

that prediction of the bond strength is accurate only for specimens deformed by ~20%, where the bond is established at every region of metal-to-metal contact due to breakdown of oxide at the interface.

Bonding aluminium alloy (2124) to 2124/P composite

The average strength for 2124 alloy bonded to a 2124/40P composite was ~130 MPa, greater than that for bonded 2124/40P composite (~35 MPa) due to the increased metal-to-metal contact across the joint. The bond strength may be estimated by taking the area of metal-to-metal contact at the interface as $(1-V_f) \times \sigma_a$, where V_f is volume fraction of SiC and σ_a is the specific strength for 2124 alloy bonded under identical conditions (~180 MPa). This gives a value of ~110 MPa, less than the measured shear strength of the joint, but greater than the 2124/40P joint (~35 MPa). There are no upper- and lower-bound values as SiC is present only in one half of the joint.

Bonding 2124/P composites with an aluminium alloy (2124) interlayer

The higher strength obtained by bonding 2124/P composite to unreinforced aluminium alloy (2124) suggested an advantage was to be gained by bonding together 2124/30P composites using an aluminium alloy (2124) interlayer. Indeed, the resultant joint had a shear strength of ~110 MPa, higher than

for composite of similar volume fraction bonded without an interlayer (~45 MPa). This improvement may be explained by considering the effective bonded area of the joint. Without an interlayer, the composite interface contains regions of SiC-to-SiC contact, SiC-to-metal contact and metal-to-metal contact, Fig. 4.10a. Only the latter regions may form a bond, and as shown previously, lower- and upper-bound values of bond strength may be calculated, as given by the relationships $(1-2V_f) \times \sigma_a$ and $(1-V_f) \times \sigma_a$, respectively, where V_f is the volume fraction of the reinforcement and σ_a is the specific shear strength of a 2124 alloy joint bonded under identical conditions (~180 MPa). For $V_f = 0.3$ (30% SiC) these limiting values are ~70 MPa and ~125 MPa, respectively. The introduction of an unreinforced alloy interlayer increases the proportion of the metal-to-metal contact, Fig. 4.10b, and the predicted strength is given by the upper-bound value of ~125 MPa, close to the measured shear strength (110 MPa).

Partridge and Dunford [121] reported a similar effect when diffusion bonding 8090/17% SiC_p composite without and with an 8090 interlayer, an increase in strength from ~100 MPa to ~150 MPa being quoted.

Bonding commercial-purity aluminium to 2124/P composite

Shear testing of 2124/25P composite bonded to commercial-purity aluminium resulted in failure mainly through the

aluminium adjacent to the joint with a strength of ~55 MPa, a value similar to the strength of the 2124 alloy - commercial-purity aluminium couple (~65 MPa). The strength of the bond was not fully realised, the adjacent aluminium being stronger than the rest of the sample due to precipitation hardening. An estimate for the bond strength of regions of metal-to-metal may be obtained using the expression $\sigma_a /(1-V_f)$, where V_f is the volume fraction of silicon carbide within the composite (0.25), and σ_a is the failure strength obtained from the shear test (~55 MPa). This gives a bond strength of ~75 MPa.

Bonding Al/Nic to 2124/P composite

The shear strength of a joint of Al/Nic bonded to 2124/35P composite was ~75 MPa with failure occurring through the Al/Nic composite well away from the joint. Again, this was due to local hardening of the aluminium by copper-rich precipitates as evidenced by microhardness values of 65 HV adjacent to the joint compared with 34 HV well away from the interface. There was also a corresponding increase in the fibre/matrix interfacial friction stress, from ~70 MPa in the composite to ~180 MPa in the bond region. It is suprising that failure took place away from the joint as the metal-to-metal contact at the interface was low (estimated to be ~50%) due to reinforcements exposed at the mating surfaces. There is therefore little benefit in bonding these composites together using a 2124 alloy interlayer.

Summary of solid-state bonding of unreinforced alloys and composites

The presence of magnesium was found to be crucial a factor in forming a solid-state bond since, by disrupting the surface alumina film, it enabled diffusion to take place across the interface.

With composite materials the use of an interlayer improved the bond strength by increasing the metal-to-metal contact across the joint, although the values were less than unreinforced alloy. In most cases fracture during shear testing took place at the bond interface; however, for the Al/Nic composite failure occurred away from the joint with a strength less than the unreinforced aluminium. Where precipitation hardening of the matrix occurred adjacent to the bond interface, the composite strength was enhanced as evidenced by microhardness tests and interfacial friction stress measurements. It would therefore be interesting to substitute the aluminium matrix with an age-hardenable aluminium alloy so that the full strength of the joint could be realised.

4.4. Liquid-phase bonding of aluminium and aluminium-based composites using metal and alloy interlayers

4.4.1. Use of a zinc interlayer

Commercial-purity aluminium

In terms of forming a liquid phase with aluminium the zinc interlayer appeared very attractive because of the low eutectic temperature of ~380°C, Table 2.2. Bonding experiments at 500°C showed, however, that although the zinc foil had melted, as evidenced by the expulsion of a liquid bead, a bond was not established. The failure is attributed to (a) the inhibiting effect of the aluminium surface oxide films on metal diffusion and (b) the lack of oxide break-up by contacting asperities as the molten zinc distributes the stresses over the whole mating surface. Point (a) is supported by that fact that the presence of zinc promotes the surface formation of alumina at these temperatures [166].

Similar problems have been encountered in studies involving the use of zinc interlayers for the diffusion bonding of unreinforced aluminium alloys, and alternative methods have been investigated. Ricks, Ball, Stoklossa, Winkler and Grimes [167] reported lap-shear strengths of up to 150 MPa for liquid-phase bonded zinc-clad 8090 aluminium alloy; the thickness of the zinc used was found to be a crucial factor in developing a good bond. Another successful technique involves plasma spraying the aluminium, prior to bonding,

with a mixture of zinc and aluminium powders [168]. When bonding particulate-reinforced aluminium, Mahoney [125] used an aluminium-zinc alloy interlayer and reported that although zinc diffused readily into the composite matrix a satisfactory joint was not always produced. Samples often fractured during unloading from the bonding rig due to the release of stored elastic strain energy. Thicker interlayers were able to tolerate this more readily and remained intact. One of the few studies carried out on the diffusion bonding of long fibre reinforced aluminium [123] reported that the zinc interlayer employed inhibited bonding as a result of oxidation.

Aluminium alloy (2124)

A joint was initially established when bonding 2124 alloy with a zinc interlayer, although the substrates separated on cooling due to the release of stored elastic strain energy and to the complex stress state within the sample caused by friction at the platen/sample interface [162]. Some reaction between the zinc and alloy had taken place, as evidenced by the roughened bonded surfaces, although no liquid was expelled from the joint. Reaction at the interface is attributed to the magnesium reduction of the alumina film on the alloy, followed by diffusion of zinc into the adjacent aluminium.

Composite materials

As the use of a zinc interlayer was unsuccessful for the unreinforced alloys, its application to bonding composite materials was not pursued.

4.4.2. Use of an aluminium alloy (2124) interlayer

Commercial-purity aluminium

The shear strength of aluminium bonded using a 2124 alloy interlayer at 550°C was ~75 MPa, failure occurring away from the interface due to strengthening of the adjacent aluminium by precipitation hardening. The bonded area is 100%, a value greater than the 500°C experiment of ~90%. This is attributed to (a) the increased rate of diffusion of magnesium to the bonded interfaces to reduce the alumina film more rapidly and (b) the softening of the 2124 interlayer to give a greater flattening and surface contact at the interface. In addition, it is likely that a low melting point phase has exuded onto the surfaces of the 2124 alloy interlayer to aid the disruption of the oxide layers. Melting probably involved eutectics in the Al-Cu-Mg (507°C) and Al-Cu (548°C) systems, but the amount was limited due to the low copper and magnesium content of the alloy. The disruption of the surface oxide film on Al-Si-Mg alloys, caused by low melting eutectics, has been reported by McGurran and Nicholas [169].

Enjo *et al* [115], in bonding experiments on Al-Cu-Mg alloy (2017) at temperatures above the solidus of the alloy (580°C), considered that a liquid phase had formed which stimulated grain growth across the interface to give a strong joint with a tensile strength of ~400 MPa after ageing. In the present work there appeared to be little advantage in operating at higher bonding temperatures when using a 2124 alloy interlayer as the area of the joint is essentially complete, ~100%, at 550°C.

Composite materials

The Al/Nic composite bonded at ~500°C had a joint area of ~100%, shear testing showing failure away from the interface. Thus it would seem that there is little advantage in bonding at higher temperatures to reduce the process time, since this would encourage fibre/matrix reactions. Bonding studies under vacuum (10^{-2} Pa) of MMC using an aluminium alloy (A2017) interlayer have been carried out by Enjo, Ikeuchi, Murakami and Suzuki [122]. Al-Mg-Si alloy (A6063) reinforced with short alumina fibres was bonded at a temperature of 600°C, and a pressure of 2 MPa applied for 30 minutes. The tensile strength of the joint was ~180 MPa, but the lack of information concerning the area of bond makes it difficult to assess the benefit of the low pressure atmosphere.

4.4.3. Use of a copper interlayer

Bonding commercial-purity aluminium

The shear strength of the joint bonded for 5 minutes at 550°C using an initial pressure of 3 MPa was ~20 MPa. The increased strength (~55 MPa) after 10 minutes bonding time was associated with the greater coverage of the interface by liquid metal, as evidenced by the expulsion of a liquid bead. The increase in specific strength during this period, from ~75 MPa to ~110 MPa, may be attributed to (a) the thinner reaction zone offering easier load transfer between the bonded aluminium plates and, (b) the greater crack resistance of the refined $CuAl_2$-Al eutectic stucture (see Fig. 3.15a). Longer bonding times produced a relatively small increase in bonded area, from ~48% to ~50% and with a corresponding increase in bond strengths, giving specific strengths lying in the range ~90 MPa to ~100 MPa. The one exception was the joint developed after 20 minutes (~65 MPa) which we associate with the large particles of Al_7Cu_2Fe at the bond line, see Fig. 3.16b. The restoration of strength when longer bonding times were used (from 30 minutes to 100 minutes) is attributed to a reduction in size of the particles as copper diffused away from them into the aluminium.

Microstructural analysis revealed that a bond was established in the central region of the joint within 4 minutes and that the phases Cu_9Al_4, CuAl and $CuAl_2$ were present at the bond interface, in agreement with published work on Al-Cu

diffusion couples [170,171]. However, according to the Al-Cu binary phase diagram (see Appendix) six intermetallic phases might be expected, which would indicate that either the layers of the other three phases were too thin to be resolved by the EPMA technique, or their formation was not so favoured energetically. With regard to the formation of the joint, the surface oxide films on both aluminium substrate and the copper interlayer are ruptured during the deformation of asperities, Fig. 4.11. Since the copper oxide is softer and less stable than the alumina [154] intimate metal-to-metal contact is more likely to be established when copper is present than for the bonding together of aluminium. Also, the diffusion of copper ions into the alumina layer may affect its high temperature stability [99]. Thus it may be concluded that the oxides were readily disrupted in the central region to allow diffusion across the interface. Heavy oxidation of the copper foil at the periphery of the joint during the bonding operation was responsible for restricting the extent of the bonded area.

The use of a thinner (4 μm) copper interlayer resulted in ~80% coverage of the joint. This was attributed to the fact that the thinner foil was consumed more rapidly in the eutectic reaction, bringing the edges of the joint in to contact more quickly and minimising the extent of oxidation of the remaining copper.

Bonding using an initial pressure of 10 MPa for 30 minutes increased the degree of deformation of the copper and the aluminium to result in a bonded area close to 100%, with a corresponding increase in the mass of liquid metal expelled from the joint, 0.31 g compared with 0.15 g in the 3 MPa experiment (see Table 3.4).

There are only limited published studies on the mechanisms of liquid phase bonding. Tuak-Poku, Dollar and Massalski [172] investigated the bonding of silver using a copper interlayer at 820°C, some 40°C above the copper-silver eutectic temperature. Bonded specimens comprised a copper interlayer sandwiched between small silver discs (~10 mm in diameter) with a tantalum washer to contain the liquid phase. Based on their observations a four-stage model was proposed which involved (a) dissolution of the interlayer, a process which occurred within several seconds, (b) homogenisation of the eutectic liquid over the next few minutes, (c) isothermal solidification and, (d) homogenisation, the latter processes both relying on solid-state diffusion of copper through the silver and taking several hours.

Dunford and Partridge, in reporting their observations for the liquid phase bonding of an aluminium alloy (8090) with a copper interlayer [116], describe a process similar to that above. However, their study uses a lead bath for the fast heating of specimens and the results may not be representative of a larger-scale bonding operation where the

heating rates will be much lower. Also, quantitative analysis of the resultant microstructure was not carried out which makes it difficult to establish how the joint formed.

Our microstructural observations showed that at the start of bonding solid-state phases are formed prior to joint liquefaction. Thus, a more comprehensive bonding mechanism may be constructed, the sequence for which is shown schematically in Figs. 4.12a to 4.12h. At the start of bonding, Fig. 4.12a, the sample is at a temperature of ~530°C and disruption of the alumina film allows solid state diffusion to produce a layered structure of aluminium-copper phases, Fig. 4.12b. The intermetallics Cu_9Al_4, CuAl and $CuAl_2$ are indicated on the diagram, with the phase of highest copper content adjacent to the remaining copper; iron impurities in the aluminium are shown as particles of $FeAl_x$. This layered structure was deduced using results from the sample bonded for 4 minutes, Fig. 3.10. Very quickly the iron impurities react with aluminium and copper to form regions of ternary liquid of eutectic composition, Fig. 4.12c. This occurs at ~545°C, consistent with DSC observations on the bead expelled from the joint which showed a reaction at this temperature, Fig. 3.14b. Melting of the joint is, however, incomplete and the bond can still support load with no liquid being expelled from the interface. A binary reaction between aluminium and copper then occurs at 548°C to form another, but more extensive liquid of eutectic composition, Fig. 4.12d. The liquid spreads across the

interfaces, Fig. 4.12e, increasing the bonded area and wetting the surface of the aluminium. It is proposed that the aluminium oxide film becomes detached at this stage of the process, and that the detachment is aided by the volume increase which accompanies the melting process [173], causing the oxide to be swept to outer edges of the joint. At the same time, liquid is expelled by the action of the applied pressure, Fig. 4.12f, any liquid remaining in the joint subsequently solidifying isothermally as copper is diluted by diffusion into the aluminium, Figs. 4.12g and 4.12h. Clearly, in peripheral regions where oxidised copper is present such reaction between the aluminium and copper is inhibited.

Bonding Al/Nic composite

Although the shear strength of bonded joints increased with increase in applied pressure (Fig. 3.36a) and areas of ~80% coverage of the interface were achieved at a bonding pressure of no more than 20 MPa (Table 3.6), full development of the joint was never achieved because of the copper foil oxidation problem. However, regions where the bond was established survived the shear test and it was the rest of the composite which had failed, the measured shear strength of the joint of ~50 MPa being comparable with shear strength of the composite [19]. It is our contention that composite failure took place away from the joint because matrix strengthening occurred close to the interface as a result of precipitation hardening

(θ' phase) and the development of a greater fibre/matrix interfacial friction stress (~185 MPa compared with ~70 MPa away from the joint). Similar observations, where fracture occurred away from the joint, have been reported for 6061 aluminium/carbon fibre composites bonded using an aluminium-zinc interlayer [125].

Although the fibre reinforcement is chemically inert at this bonding temperature, it will have a physical effect on the formation of the joint. As mentioned earlier, the major difficulty is the bonding of fibres exposed during prior surface preparation, either to metal or to other fibres, during the joining operation. Thus the presence of a copper interlayer is crucial as it provides an increase in the effective area of metal-to-metal contact. Whilst, however, fibres at the surface are difficult to bond, they may contribute to break-up of the alumina film and encourage diffusion. Also, the surfaces of fibres may offer easy diffusion paths, particularly for eutectic liquid, as proposed by Moshier, Ahearn and Cooke in their work on the wetting of MMCs by liquid eutectic alloys [174].

Bonding at 550°C was always accompanied by the formation of a low melting point eutectic phase, as evidenced by the ejection from the joint of a liquid bead. The bead consisted of aluminium, silicon, $CuAl_2$, Al_7Cu_2Fe and $Al_{12}Fe_3Si$ phases and similar phases were found in the joint. The silicon is considered to have originated from impurities in the

aluminium; there was no evidence to indicate that it was introduced from a fibre reaction. DSC analysis of the bead indicated melting at ~520°C and ~540°C, Fig. 3.33b. The reaction at ~540°C is associated with the Al-Cu-Fe eutectic liquid, as identified in studies on bonding unreinforced aluminium. However, owing to the much higher level of iron impurity in the composite material this ternary reaction was much more extensive and was the major cause of joint liquefaction and bead expulsion. The reaction at ~520°C is attributed to the melting of Al-Cu-Si eutectic phase which was less pronounced than that at 540°C due to the lower silicon impurity level compared with iron [175]. This low melting point reaction could be used to advantage in future studies by substituting the aluminium matrix with an Al-Si alloy, so as to allow complete liquefaction, as reported by Niemann and Wille [176] for the bonding of A356.0 (Al-Si-Mg) alloy using a copper interlayer. Apart from the effect of the fibre reinforcement, the bonding mechanism and the associated diffusion reactions in the composite are essentially controlled by liquid-state processes similar to those identified for unreinforced aluminium.

Bonding aluminium alloy (2124) and 2124/P composite

Attempts were not made to bond these materials at 550°C since analysis of the relevant phase diagram indicated that melting would occur to soften the alloy and result in excessive deformation during the bonding operation. At these

temperatures the alloy is better used as an interlayer, as demonstrated in the bonding experiment on commercial-purity aluminium.

4.4.4. Use of a nickel-coated copper interlayer

Bonding commercial-purity aluminium

A nickel-coated interlayer was used in an attempt to increase the bonded area of joints by reducing oxidation of the copper. Unfortunately, the nickel was protective to such a degree that the use of an initial pressure of 3 MPa was not sufficient to form a joint, therefore a higher pressure of 10 MPa was employed.

The shear strength of the joint was ~65 MPa and the bonded area ~75%, values lower than for aluminium bonding with a copper interlayer using a similar pressure (~95 MPa, ~100%). Considering that the majority of the joint had formed via the solid-state, as evidenced by the microstructure, Fig. 3.20b, which showed the presence of Al_7Cu_4Ni and Al_6Cu_3Ni phases as well as regions of solidified $CuAl_2$-Al eutectic, these values were satisfactory.

With regard to the formation of the joint, the mechanism described in Figs. 4.12a to 4.12h, is modified to take into account our microstructural observations. The bonding

sequence is illustrated in Figs. 4.13a to 4.13d. Initially the specimen is at a temperature of ~530°C, Fig. 4.13a. After pressure is applied, the surface alumina films are disrupted by mechanical interference of asperities, thereby allowing interdiffusion of aluminium and nickel, Fig. 4.13b. The copper-nickel interlayer is then consumed via a solid-state reaction to give the intermetallic phases Al_7Cu_4Ni and Al_6Cu_3Ni, labelled in Fig. 4.13c. Within 5 minutes the temperature reaches 550°C and in places where residual copper is present an Al-Cu eutectic liquid forms, Fig. 4.13d. Melting in isolated regions is attributed to the nickel coating being generally too thick to allow reaction between the copper and aluminium. Thus it may be concluded that the use of thinner nickel coating would allow the Al-Cu eutectic reaction to occur more readily, whilst still offering resistance to oxidation. The coating thickness is therefore a crucial part of the bonding operation and needs to be optimised in future investigations.

Bonding Al/Nic composite

The low strength of the joint for Al/Nic composite bonded with a nickel-coated copper interlayer (~10 MPa) is attributed to (a) the fibres present at the bonding surfaces restricting the development of the joint and, (b) the nickel coating preventing the formation of the liquid phase shown to penetrate the composite and enhance 'keying'. These arguments were supported by microstructural observations

which showed that the intermetallic phases $Al_9Cu_{13}Ni$ and Al_7Cu_4Ni had formed only at areas of metal-to-metal contact. Indeed, in some places, fibres at the surface completely prevented reaction between aluminium and nickel, Fig. 3.38b. Thus apart from the inhibiting effect of the fibres, the bonding mechanism is believed to be similar to that for unreinforced aluminium.

As with the unreinforced aluminium, it is concluded that a thinner coating of nickel would allow the aluminium-copper eutectic reaction to take place more readily and reducing oxidation to give a joint with a larger bonded area than the equivalent bonding experiment using a copper interlayer.

4.4.5. Use of a copper-silver alloy interlayer

Bonding commercial-purity aluminium

It was encouraging to observe that a liquid phase was produced within 5 minutes at 510°C, when using a copper-silver alloy interlayer, as evidenced by the characteristic decrease in the pressure versus time curve. In fact, after bonding for 30 minutes, using 3 MPa pressure, more liquid was expelled from the joint than for the experiment using a copper interlayer at 550°C (0.71 g compared with 0.15 g), the formation of more liquid being a consequence of using a thicker foil (50 μm compared with 10 μm). An increase in the

bonded area was also observed (~65% compared with ~50%), although the shear strength (~25 MPa) was not commensurate with the improved coverage, failure taking place at the interface through the coarse eutectic structure, Fig. 3.21c.

The use of a higher applied pressure of 10 MPa increased the amount of expelled liquid (0.71 g to 1.15 g), a feature accredited to the greater flattening at the joint interface promoting liquefaction over a larger area (~85%). This, in turn, resulted in an increase in shear strength, from ~25 MPa to ~65 MPa, with failure occurring through the aluminium due to a more refined 'crack resistant' eutectic structure and a more extensive region of precipitation-hardened aluminium adjacent to the joint (γ' phase).

Examination of the joint revealed that melting took place by means of the eutectic reaction involving aluminium, copper and silver, a process more complex than for aluminium bonded with a copper interlayer. The associated bonding mechanism is therefore modified accordingly, as shown in Figs. 4.14a to 4.14f. At the start of bonding, Fig. 4.14a, the specimen is at a temperature of ~490°C and after the application of pressure, asperities deform and fracture the surface alumina films. This physical effect may be aided by the destabilisation of the oxide layer by copper and silver ions [99,159]. At areas of intimate aluminium/interlayer contact $CuAl_2$ and Ag_2Al phases form via solid-state diffusion, Fig. 4.14b. Within several minutes the temperature reaches 505°C

and Al-Cu-Ag eutectic liquid forms, Fig. 4.14c, as evidenced by DSC observations of the expelled bead which indicated a reaction at this temperature. During this process the oxide becomes detached and is swept to the outer edges of the joint by the eutectic liquid, some of which is subsequently expelled from the joint, Fig. 4.14d. This process of melting and expulsion continues, bringing the mating surfaces into more intimate contact, Fig. 4.14e. Complete liquefaction of the joint does not take place, however, due to the difference in composition between the interlayer and the ternary eutectic (71.5 wt% Ag compared with 32 wt% Ag, 20 wt% Cu). Thus, when eutectic melting occurs at the joint the copper within the interlayer is consumed to leave silver at the bond line which forms as particles of Ag_2Al, via the solid-state, Fig. 4.14f. These residual Ag_2Al particles may be removed slowly by further heat-treatment at this temperature, or more rapidly by heating the joint, under pressure, to ~566°C whereupon the Ag-Al eutectic liquid will form and be expelled from the joint.

A review of the literature revealed only one study of aluminium bonded with a copper-silver interlayer. Hauser, Kamner and Dedrick [112] investigated a wide range of interlayer materials including a copper-silver alloy foil (128 μm thick) of eutectic composition. After bonding for 4 hours at 480°C, 16 MPa they found interdiffusion of the silver, copper and aluminium and the development of a three-

phase structure at the joint, probably aluminium, $CuAl_2$ and Ag_2Al.

With regard to reducing the bonding temperature further, it would be interesting to employ the low melting point Cu-Ag-Zn-Cd solder, as used by Elahi and Fenn [177] in their studies on joining titanium alloys.

Bonding Al/Nic composite

The effect of a copper-silver alloy interlayer on the shear strength of Al/Nic composite was similar to that of a copper interlayer (~50 MPa), although the bonded area was greater (~90% compared with 80%). This is due to (a) the increased amount of liquid formed at the joint to give greater coverage and, (b) the reduced oxidation of the copper in peripheral regions, as a result of bonding at the lower temperature (510°C). It was encouraging to observe that in bonded areas failure occurred away from the joint interface, the enhanced strength of the matrix in the joint region being due to (a) the 'crack-resistant' nature of the solidified eutectic and, (b) precipitation hardening of the adjacent aluminium by γ' phase. This is supported by the higher values of the interfacial friction stress in the joint region, ~260 MPa compared with ~70 MPa well away from the joint.

It has already been mentioned that fibres exposed at the surface are difficult to bond, therefore, the presence of an

interlayer is crucial as it increases the areas of metal-to-metal contact. Although fibres restrict the initial stages of bonding, they do offer easy diffusion paths, as evidenced by the depth of penetration of eutectic liquid, Fig. 3.40c. The numerous fibre fractures found within this liquefied region were formed as a result of the pressure applied during bonding causing breakage at points of fibre-fibre contact, a mechanism proposed by Durrant and Scott [178] in their work on forging of Saffil fibre/Al-Si alloy composites above the eutectic temperature.

The characteristic decrease in pressure during the initial stages of bonding was due to the expulsion of liquid from the joint, analysis of the solidified structure revealing aluminium, $CuAl_2$, Ag_2Al phases as well as the iron-containing intermetallic $Al_{12}Fe_3Si$. As for Al/Nic composite bonded with a copper interlayer, the silicon is considered to have originated from impurities in the aluminium; there was no evidence to indicate that it was introduced as a result of a fibre reaction. DSC analysis of the bead indicated melting at ~495°C and ~505°C. The reaction at 505°C is associated with the formation of Al-Cu-Ag eutectic liquid as established in bonding studies on unreinforced aluminium. Melting at the lower temperature is attributed to the modification of this reaction by silicon, although the reaction is limited due to the low level of silicon impurity in the composite matrix. It would be interesting to substitute the composite matrix

with an Al-Si alloy so that full melting could be achieved when bonding at the lower temperature.

Apart from the effect of the fibre reinforcement on restricting the metal-to-metal contact at the joint, the bonding mechanism and associated diffusion reactions in the composite are essentially similar to those proposed for unreinforced aluminium.

Bonding aluminium alloy (2124)

The shear strength of 2124 alloy bonded with a copper-silver interlayer at 510°C (~110 MPa) was considerably less than solid-state bonding experiments on 2124 alloy carried out at 500°C. This is due to the easy fracture path offered by residual intermetallics (mainly Ag_2Al) at the joint interface, formed as a result of incomplete melting due to a deficiency of copper in the interlayer. The fact that EPMA indicated increased levels of copper, silver and magnesium adjacent to the joint, Fig. 3.50, suggests that precipitation of the more stable Ω phase may have been stimulated during cooling [24,164], although this was not established experimentally due to the difficulty of preparing thin foils suitable for TEM. However, any local improvement in matrix strength would not have been realised as failure took place prematurely at the joint interface.

The bonded area of ~90% was greater than both 2124 alloy bonded at 500°C (~75%) and the aluminium bonded with a copper-silver interlayer (~85%). In the first case this is due to the liquid phase giving a better coverage at the joint interface. The second is attributed to the presence of silver which is known to speed the reduction reaction of alumina when combined with aluminium and magnesium [99].

With regard to the bonding mechanism, a combination of magnesium reduction of the surface alumina film and the formation of a ternary liquid phase is proposed, both of which have been discussed individually in previous sections.

Bonding 2124/P composite

The shear strength of the joint produced using a copper-silver alloy interlayer at 510°C was ~100 MPa, even though the composite (2124/35P) was bonded for only 30 minutes using 4 MPa applied pressure. The strength is comparable with a similar composite bonded using a 2124 alloy interlayer (~110 MPa) at 500°C for 240 minutes, 10 MPa applied pressure. The production of a strong bond indicated that a liquid phase had formed, although this was not commensurate with the pressure versus time curve which did not exhibit the characteristic drop in pressure. However, microstructural analysis of the joint revealed that a liquid had formed and, contrary to the unreinforced 2124 alloy, was absorbed readily by the composite with diffusion occurring via SiC/matrix

interfaces. As a consequence, the SiC particulate within the joint region was able to move within the liquid under the applied pressure and eliminate the crack-sensitive planar interface normally found in these bonded composites.

The shear strength of the joint was increased to ~200 MPa when using a higher bonding pressure of 8 MPa, and this is attributed to the increased flattening of the mating surfaces as a consequence of using a higher specimen deformation (~6%). The strength is higher than for unreinforced 2124 alloy bonded using a copper-silver interlayer, in complete contrast to solid-state bonding experiments where the inclusion of SiC reinforcement was found to reduce the bond strength. As for the solid-state experiments, it would be interesting to investigate the effect of volume fraction on the joint strength of the liquid-phase bonded particulate composites.

The strength of ~190 MPa is comparable with values obtained (~170 MPa) by Partridge and Dunford [121] for liquid-phase diffusion bonded 8090/17% SiC_p composite, which is encouraging as this composite has half the volume fraction of SiC particulate. Although the exact bonding conditions are not reported, it is known that these experiments were carried out in a low pressure atmosphere, as apposed to our experiments which were performed in air.

4.4.6. Use of a copper-zinc alloy interlayer

Commercial-purity aluminium

Aluminium bonded with a copper-zinc alloy interlayer at 500°C did not produce a joint, examination of the mating surfaces revealing that no interface reaction had occurred. Reference to the aluminium-copper-zinc phase diagram (see Appendix) indicates that a liquid phase should be produced at this temperature with composition ~30 wt% zinc, 25 wt% copper. In future investigations the zinc content of the alloy will be increased (to ~90%) to encourage the formation of ternary liquid (377°C). Zinc interlayers with small additions of copper, either in the form of an alloy or as a surface coating will be used.

Composite materials

For joining composite materials the reinforcement will have a similar effect to those encountered previously, such as restricting the interface reaction during the initial stages of bonding, in the solid state, as well as promoting diffusion of liquid into the composite once the reaction is established.

Summary of liquid-phase bonding of unreinforced alloys and composites

The bonding temperature was lowered, from 550°C to 510°C, by using interlayers of copper-silver alloy rather than copper metal, with no apparent loss in strength or bonded area. For aluminium and Al/Nic composite failure during shear testing occurred mainly away from the bond interface, due to local precipitation hardening, and the full strength of the joint was not realised. When a precipitation-hardenable alloy (2124) was bonded at the lower temperature, however, the joint failed at the interface with a relatively low strength. Higher bond strengths were achieved using the 2124/P composites, as the SiC particulate provided extensive 'keying' with the solidified eutectic phases.

5. CONCLUSIONS

Conclusions to be drawn from the research are summarised in the following sections, including recommendations concerning the most suitable bonding practice for materials used in the study.

5.1. Mechanical test techniques

The modified shear test developed in this work successfully avoided the peel stresses associated with the more conventional lap-shear method. The observed scatter in results was due mainly to the variability of samples cut from the bonded plate, rather than appreciable errors in the shear test method. Once, however, the measured values were normalised with respect to the bonded area of individual samples, variability in the data was reduced.

Values of fibre/matrix interfacial friction stress, recorded for bonded Nicalon fibre reinforced aluminium using the micro-indentation test method, were found to be similar to the strength of the shear tested composite. The reduction in interfacial friction stress with distance from the joint could be correlated with a lower composite strength and a greater tendency for it to provide the easier fracture path.

5.2. Solid-state bonding methods

Commercial-purity aluminium did not form a joint at a bonding temperature of 500°C, even when appreciable deformation was applied (10%). This was attributed to the tenacious surface layer of oxide, some tens of nm thick, which inhibited metal diffusion between the mating surfaces. A joint was established when an aluminium alloy (2124) interlayer was used, the magnesium present in the alloy diffusing to the bond interface and disrupting the alumina films by a chemical reduction process. Shear tests showed that a bond area of ~100% could be achieved using a deformation of as little as 2%. The occurrence of the failure well away from the joint was attributed to local strengthening of the aluminium associated with precipition of θ' phase caused by copper diffusing from the interlayer.

A 2124 alloy interlayer was adopted also for the bonding of Nicalon fibre reinforced aluminium, although a higher applied pressure was required (34 MPa compared with 10 MPa) to bring the surfaces of this stiffer material into intimate contact. Shear testing resulted in failure away from the interface (100% bond area), and this was again due to localised precipitation hardening.

When bonding aluminium alloy (2124) no interlayer was required. A bond was formed at a temperature as low as

400°C, although the area of bond was only ~50%. A bonded area approaching 100% was, however, achieved at a temperature of 500°C, as a result of the alloy deforming more readily to facilitate intimate surface contact.

The presence of SiC particulate in the aluminium alloy (2124) radically affected the bond strength due to the decrease in metal-to-metal contact at the joint interface. Indeed, the bond strength was found to be inversely proportional to the volume fraction of SiC. An increase in the area of metal-to-metal contact was produced by using an aluminium alloy (2124) interlayer, to result in a higher shear strength.

Data on the joining of dissimilar materials were very encouraging. Particulate-reinforced 2124 alloy was successfully bonded to aluminium, with shear testing resulting in failure away from the joint interface through the aluminium. Furthermore, even when the metal-to-metal contact was only ~50%, where Nicalon fibres were present in the aluminium, failure still occurred away from the joint, indicative of it being stronger than the actual composite.

5.3. Liquid-phase bonding methods

Bonding experiments on both commercial-purity aluminium and aluminium alloy (2124) at 500°C using a zinc interlayer did not produce a joint due to the inhibiting effect of the oxide films on aluminium.

Using a copper interlayer and a temperature of 550°C gave more success. A liquid phase was formed within a few minutes, although the area of bond (~25%) was restricted by oxidation of the copper in peripheral regions. The bonded area was, however, increased (to ~100%) by using a higher applied pressure (10 MPa compared with 3 MPa) and increasing the bonding time to 30 minutes.

For aluminium reinforced with Nicalon fibre the maximum area of bond was ~80%, even with an applied pressure as high as 30 MPa, oxidation of copper again being responsible for poor bonding in peripheral regions due to the lack of intimate surface contact. Where the joint was developed it remained intact during shear testing and failure occurred away from the bond interface through the composite. The joint exhibited high strength due to the 'keying' action of solidified eutectic around fibres and some local precipitation hardening of the aluminium. Attempts to reduce the oxidation by using a nickel coating on the copper were successful. A bond was not

established, however, as the nickel coating inhibited the formation of a liquid eutectic phase.

It was found that a copper-silver alloy interlayer enabled the bonding temperature for aluminium to be decreased to 510°C. This was attributed to a ternary liquid phase forming within several minutes, such that after 30 minutes ~90% bond area was achieved. A higher pressure of 20 MPa had to be used for Nicalon fibre reinforced aluminium to give a bond area of ~90%.

The use of a copper-silver alloy interlayer for bonding aluminium alloy (2124) formed a joint whose strength was inferior to the solid-state bonds produced at 500°C; this was due to the presence of large intermetallic phases at the bond interface which offered an easy path of fracture. For the bonding of particulate-reinforced 2124 alloy, however, the copper-silver interlayer produced a joint with a strength approaching 200 MPa. This was attributed to the 'keying' action of the solidified eutectic around the SiC particulate.

5.4. Recommended bonding techniques

The following techniques are recommended for the bonding of materials used in this work.

Commercial-purity aluminium

Use of an aluminium alloy (2124) interlayer which allows magnesium reduction reaction of the surface oxide films.

Conditions: 500°C, 30 mins, 10 MPa.

Commercial-purity aluminium reinforced with Nicalon fibre

Similar to unreinforced aluminium, except that a higher pressure is required to attain sufficient surface contact with the stiff composite.

Conditions: 500°C, 60 mins, 34 MPa.

Aluminium alloy (2124)

Bonding without an interlayer since the magnesium level in the alloy is sufficient to reduce the surface oxide films and form a joint.

Conditions: 500°C, 30 mins, 20 MPa.

Aluminium alloy (2124) reinforced with SiC particulate

A copper-silver alloy interlayer to form a liquid phase and modify the the morphology of the bond interface to give a high strength joint.

Conditions: 510°C, 30 mins, 10 MPa (6% deformation).

6. FUTURE WORK

(i) The aluminium alloy (2124) used in this study contained both magnesium and copper, found to be beneficial in reducing the surface oxide and causing local strengthening of the joint by precipitation hardening when bonded to aluminium. It would therefore be interesting study the diffusion bonding of Al-Cu and Al-Mg alloys so that the individual contributions of magnesium and copper to the bonding process can be assessed.

(ii) The use of a lower bonding temperature (<500°C) would reduce oxidation of the joint and be more economical. Solid-state process are not suitable candidates since the bonding pressure and bonding time have to be increased. Future studies should therefore concentrate on developing alloy interlayers which readily form a low melting point phase when combined with the aluminium (copper-zinc alloy). Our results indicate that melting of the joint is also facilitated by the presence of silicon; it may therefore be appropriate to use Al-Si alloy for the substrates.

(iii) An improvement in the transverse strength of the Nicalon fibre composite would avoid its premature failure during shear testing. Our results indicate that this may be achieved by using a precipitation hardenable alloy, such as Al-Cu-Mg (2124).

(iv) For the aluminium alloy (2124) reinforced with SiC particulate volume fraction of 25%, 30%, 35% and 40% were used. It would, however, be useful to bond lower volume fraction composites to substantiate the proposed joint strength versus volume fraction relationship.

(v) Oxidation of the periphery of the interlayer often restricted the area of bond. It would be useful in future studies to use a protective atmosphere such as argon.

7. REFERENCES

1. Gordon, J.E. 'The new science of strong materials, 2nd ed. (1976) Penguin Books, London, chapter 8.

2. Polmear, I.J. 'Light alloys - Metallurgy of the light metals' 2nd edn. (1989) Edward-Arnold.

3. Peel, C.J., Evans, B. and McDarmaid, D.S. 'Development of aluminium-lithium alloys in the UK' Metals and Materials, *J Inst Met* **3**, 8 (1987) 449-455.

4. Trumper, R.L. 'Metal matrix composites - Applications and prospects' Metals and Materials, *J Inst Met* **3**, 11 (1987) 662-667.

5. Driver, D. 'Near net shape manufacture of aero engine components' Metals and Materials, *J Inst Met* **4**, 8 (1988) 493-497.

6. Crocker, P. 'Structural effects of oxidation of carbon-carbon composites' *PhD Thesis*, University of Bath (1992).

7. Bleay, S.M. 'Microstructure and micromechanics in glass and glass-ceramics reinforced with ceramic fibres' *PhD Thesis*, University of Bath (1991).

8. Le Petitcorps, Y., Della Martina, F. and Quenisset, J.M. 'An overview on intermetallic matrix composites' *Proc 12th Risø Int Symp on Materials Science: Metal Matrix Composites - Processing, Microstructure and Properties*. eds. N. Hansen, D. Juul Jensen, T. Leffers, H. Lilholt, T. Lorentzen, A.S. Pedersen, O.B. Pedersen and B. Ralph. Risø National Laboratory, Roskilde, Denmark (1991) 461-474.

9. Taya, M. and Arsenault, R.J. 'Metal matrix composites - Thermomechanical behaviour' (1989) Pergamon, p6.

10. Bacon, M. 'Metal matrix composites, engineering materials solutions' *Materials Edge* **12** (1989) 33-48.

11. Friend, C.M. 'Toughness in metal matrix composites' *Mater Sci and Tech* **5** (1989) 1-7.

12. Ibrahim, I.A., Mohamed, F.A. and Lavernia, E.J. 'Particulate reinforced metal matrix composites - A review' *J Mater Sci* **26** (1991) 1137-1156.

13. Humphreys, F.J., Basu, A. and Djazeb, M.R. 'The microstructure and strength of particulate metal matrix composites' *Proc 12th Risø Int Symp on Materials Science: Metal Matrix Composites - Processing, Microstructure and Properties*. eds. N. Hansen, D. Juul Jensen, T. Leffers, H. Lilholt, T. Lorentzen, A.S. Pedersen, O.B. Pedersen and B. Ralph. Risø National Laboratory, Roskilde, Denmark (1991) 51-66.

14. Girot, F.A., Quenisset, J.M. and Naslain, R. 'Discontinuously-reinforced aluminium matrix composites' *Comp Sci and Tech* **30** (1987) 155-184.

15. Harris, B. 'Engineering composite materials' (1986) The Institute of Metals, London.

16. Harris, S.J. 'Fiber reinforced aluminum alloys' *Aluminum Alloys - Contemporary Research and Applications*. eds. A.K. Vasudevan and R.D. Doherty, vol 1, Treatise on Materials Science and Technology, Academic Press, London (1989) 255-294.

17. Harris, S.J. 'Cast metal matrix composites' *Mater Sci and Tech* **4** (1988) 231-239.

18. Davies, L.G., Powers, W.M. and Shaver, R.G. 'Low cost metal-matrix composite fabrication' SAMPE QUART **3**, 1 (1971) 32-40.

19. Chapman, A.R. 'Manufacturing method, microstructure and mechanical property relationships for a metal matrix composite' *PhD Thesis*, University of Bath (1991).

20. Chou, S.C., Green, J.L. and Swanson, R.A. 'Mechanical behavior of silicon carbide/2024 aluminum composite' *Testing Technology of Metal Matrix Composites, ASTM STP 964*. eds. P.R. DiGiovanni and N.R. Adsit, ASTM Philadelphia (1988) 305-316.

21. Liaw, P.K., Greggi, J.G. and Logsdon, W.A. 'Microstructural characterisation of a silicon carbide whisker reinforced 2124 aluminium metal matrix composite' *J Mater Sci* **22** (1987) 1613-1617.

22. Arsenault, R.J. and Fisher, R.M. 'Microstructure of fiber and particulate SiC in 6061 Al composites' *Scripta Metall* **17** (1983) 67-71.

23. Scheuller, R.D. and Wawner, F.E. 'An analysis of high-temperature behaviour of AA2124/SiC whisker composites' *Comp Sci and Tech* **40** (1991) 213-223.

24. Scott, V.D., Kerry, S. and Trumper, R.L. 'Nucleation and growth of precipitates in Al-Cu-Mg-Ag alloys' *Mater Sci and Tech* **3** (1987) 827-834.

25. O'Rourke, J. and Scott, V.D. unpublished work (1992).

26. Prangnell, P.B. and Stobbs, W.M. 'The effect of internal stresses on precipitation behaviour in particulate reinforced Al matrix MMCs' *Proc 12th Risø Int Symp on Materials Science: Metal Matrix Composites - Processing, Microstructure and Properties*. eds. N. Hansen, D. Juul Jensen, T. Leffers, H. Lilholt, T. Lorentzen, A.S. Pedersen, O.B. Pedersen and B. Ralph. Risø National Laboratory, Roskilde, Denmark (1991) 603-610.

27. Kingery, W.D., Bowen, H.K. and Uhlmann, D.R. 'Introduction to ceramics', 2nd ed. (1976) Wiley, p8.

28. Yajima, S., Okamura, K., Hayashi, J. and Omuri, M. 'Synthesis of fibers with high tensile strength' *J Amer Ceram Soc* **59**, 7-8 (1976) 324-327.

29. Yajima, S., Hasegawa, Y., Hayashi, M. and Iimura, M. 'Synthesis of continuous silicon carbide fibre with high tensile strength and high Young's modulus, Part 1: Synthesis of polycarbosilane as precursor' *J Mater Sci* **13** (1978) 2569-2576.

30. Hasegawa, Y., Iimura, M. and Yajima, S. 'Synthesis of continuous silicon carbide fibre, Part 2: Conversion of polycarbosilane fibre into silicon carbide fibres' *J Mater Sci* **15** (1980) 720-728.

31. Hasegawa, Y. and Okamura, K. 'Synthesis of continuous silicon carbide fibre, Part 3: Pyrolysis process of polycarbosilane and structure of the products' *J Mater Sci* **18** (1983) 3633-3648.

32. Hasegawa, Y. and Okamura, K. 'Synthesis of continuous silicon carbide fibre, Part 4: The structure of polycarbosilane as the precursor' *J Mater Sci* **21** (1986) 321-328.

33. Ichikawa, H., Machino, F., Mitsuno, S., Ishikawa, T., Okamura, K. and Hasegawa, Y. 'Synthesis of continuous silicon carbide fibre, Part 5: Factors affecting stability of polycarbosilane to oxidation' *J Mater Sci* **21** (1986) 4352-4358.

34. Hasegawa, Y. 'Synthesis of continuous silicon carbide fibre, Part 6: Pyrolysis process of cured polycarbosilane fibre and structure of SiC fibre' *J Mater Sci* **24** (1989) 1177-1190.

35. Bunsell, A.R., Simon, G., Abe, Y. and Akiyama, M. 'Ceramic fibres' in Fibre reinforcements for composite materials, Composite Materials Series. ed A.R. Bunsell, vol 2 (1988) Elsevier, chapter 9.

36. Simon, G. and Bunsell, A.R. 'Mechanical and structural characterisation of the Nicalon silicon carbide fibre' *J Mater Sci* **19** (1984) 3649-3657.

37. Sasaki, Y., Nishina, Y., Sato, M. and Okamura, K. 'Raman study of SiC fibres made from polycarbosilane' *J Mater Sci* **22** (1987) 443-448.

38. Porte, L. and Sartre, A. 'Evidence for a silicon oxycarbide phase in the Nicalon silicon carbide fibre' *J Mater Sci* **24** (1989) 271-275.

39. Laffon, C., Flank, A.M., Lagarde, P., Laridjani, M., Hagege, R., Olry, P., Cotteret, J., Dixmier, J., Miquel, J.L., Hommel, H. and Legrand, A.P. 'Study of Nicalon-based ceramic fibres and powders by EXAFS spectrometry, x-ray diffractometry and some additional methods' *J Mater Sci* **24** (1989) 1503-1512.

40. Bleay, S.M., Chapman, A.R., Love, G. and Scott, V.D. 'Electron-probe microanalysis of Nicalon fibres' *J Mater Sci* **27** (1992) 5389-5396.

41. Nicalon product information, Nippon Carbon Company, Japan.

42. De, A.K. and Phani, K.K. 'Gauge length effect on strength of silicon carbide and sapphire filaments' *J Comp Mater* **24** (1990) 220-231.

43. Andersson, C-H. and Warren, R. 'Silicon carbide fibres and their potential for use in composite materials. Part 1' *Composites* **15**, 1 (1984) 16-24.

44. Warren, R. and Andersson, C-H. 'Silicon carbide fibres and their potential use in composite materials. Part 2' *Composites* **15**, 2 (1984) 101-111.

45. Maniette, Y. and Oberlin, A. 'TEM characterization of some crude or air heat-treated SiC Nicalon fibres' *J Mater Sci* **24** (1989) 3361-3370.

46. Simon, G. and Bunsell, A.R. 'Creep behaviour and structural characterization at high temperatures of Nicalon SiC fibres' *J Mater Sci* **19** (1984) 3658-3670.

47. Mah, T., Hecht, N.L., McCullum, J.R., Hoenigman, J.R., Kim, H.M., Katz, A.P. and Lipsitt, H.A. 'Thermal stability of SiC fibres (Nicalon)' *J Mater Sci* **19** (1984) 1191-1201.

48. Clark, T.J., Prack, E.R., Haider, M.I. and Sawyer, L.C. 'Oxidation of SiC ceramic fiber' *Ceram Eng Sci Proc* **8**, 7-8 (1987) 717-731.

49. Chou, T.W., Kelly, A. and Okura, A. 'Fibre-reinforced metal-matrix composites' *Composites* **16**, 3 (1985) 187-205.

50. Mortensen, A. 'Solidification processing of reinforced metals' *Proc 12th Risø Int Symp on Materials Science: Metal Matrix Composites - Processing, Microstructure and Properties*. eds. N. Hansen, D. Juul Jensen, T. Leffers, H. Lilholt, T. Lorentzen, A.S. Pedersen, O.B. Pedersen and B. Ralph. Risø National Laboratory, Roskilde, Denmark (1991) 101-121.

51. Mykura, N. 'Casting MMCs by liquid pressure forming' Metals and Materials, *J Inst Met* **7**, 1 (1991) 7-11.

52. Booth, S.E., Clifford, A.W. and Parratt, N.J. 'Casting fibre reinforced metals' UK Patent No GB 2, 115, 327 A, September 7 (1983).

53. Feest, E.A. 'Exploitation of the metal matrix composite concept' Metals and Materials, *J Inst Met* **4**, 5 (1988) 273-278.

54. Baker, A.R. and Gazzard, S. 'Developments in materials for pistons' *Materials and Design* **9**, 1 (1988) 28-33.

55. Bader, M.G., Clyne, T.W., Cappleman, G.R. and Hubert, P.A. 'The fabrication and properties of metal-matrix composites based on aluminium alloy infiltrated alumina fibre preforms' *Comp Sci and Tech* **23** (1985) 287-301.

56. Clyne, T.W. and Mason, J.F. 'The squeeze infiltration process for fabrication of metal-matrix composites' *Metall Trans* **18A** (1987) 1519-1530.

57. Henriksen, B.R. 'The microstructure of squeeze-cast SiC_w reinforced Al4Cu base alloy with Mg and Ni additions' *Composites* **21**, 4 (1990) 333-338.

58. Ohuri, K., Watanabe, H. and Takeuchi, Y. 'Silicon carbide whisker reinforced aluminium composites - fabrication and properties' *Mater Sci and Tech* **3** (1987) 57-60.

59. Milliere, C. and Suery, M. 'Fabrication and properties of metal matrix composites based on SiC fibre reinforced aluminium alloys' *Mater Sci and Tech* **4** (1988) 41-51.

60. Fryatt, J. 'Ceramic fibres for metal-ceramic composites' *Industrial Ceramics* **7**, 1 (1987) 44.

61. Coleman, S.L. 'The corrosion of metal matrix composites' *PhD Thesis*, University of Bath (1991).

62. Bhagat, R.B. 'High pressure squeeze casting of stainless steel wire reinforced aluminium matrix composites' *Composites* **19**, 5 (1988) 393-399.

63. Flemings, M.C., Rick, R.G. and Young, K.P. 'Rheocasting' *Mater Sci and Eng* **25** (1976) 103-117.

64. Willis, T.C. 'Spray deposition process for metal matrix composites manufacture' Metals and Materials, *J Inst Mets* **4**, 8 (1988) 485-488.

65. Jensen, P.S. and Kahl, W. 'Particulate reinforced aluminium MMCs produced by spray deposition' *Proc 12th Risø Int Symp on Materials Science: Metal Matrix Composites - Processing, Microstructure and Properties*. eds. N. Hansen, D. Juul Jensen, T. Leffers, H. Lilholt, T. Lorentzen, A.S. Pedersen, O.B. Pedersen and B. Ralph. Risø National Laboratory, Roskilde, Denmark (1991) 405-410.

66. Tanikawa, E., Takeyama, S. and Sakakibara, T. 'Mechanical properties and fabricability of MMC by roll diffusion bonding proces' *Proc 4th Japan-US Conf on Comp Mater*, Washington (1988) 449-457.

67. Mittnick, M.A. and McElmann, J. 'Continuous silicon carbide fiber reinforced metal matrix composites' *Proc Conf Advanced Comp Tech*, Dearborn, Michegan USA, ASM Int Ohio (1988) 447-452.

68. Mittnick, M.A. 'Continuous SiC fibre-reinforced metals' *Adv Mater Tech Int* (1990) 111-114.

69. Dudek, H-J., Leucht, R. and Zeigler, G. 'SiC-reinforced titanium alloys: processing, interfaces and mechanical properties' *ECCM4* eds. J. Fuller, G. Gruninger, K. Schulte, A.R. Bunsell and A. Massiah, Elsevier, Stuttgart (1990) 339-344.

70. Yajima, S., Okamura, K., Tanaka, J. and Hayase, T. 'Synthesis of aluminium composite reinforced with continuous SiC fibre obtained from the precursor fibre of an organosilicon polymer' *J Mater Sci Lett* **15** (1980) 2130-2131.

71. Yajima, S., Okamura, K., Tanaka, J. and Hayase, T. 'High-temperature strengths of aluminium composite reinforced with continuous SiC fibre' *J Mater Sci* **16** (1981) 3033-3038.

72. Arsenault, R.J. and Pande, C.S. 'Interfaces in metal matrix composites' *Scripta Metall* **18** (1984) 1131-1134.

73. Lloyd, D.J., Lagace, H., McLeod, A. and Morris, P.L. 'Microstructural aspects of aluminium-silicon carbide particulate composites produced by a casting method' *Mater Sci and Tech* **A107** (1989) 73-80.

74. Lloyd, D.J. 'The solidification microstructure of particulate reinforced aluminium/SiC composites' *Comp Sci and Tech* **35** (1989) 159-179.

75. Peteves, S.D., Tambuyser, P., Helbach, P., Audier, M., Laurent, V. and Chatain, D. 'Microstructure and morphology of the Al/SiC interface' *J Mater Sci* **25** (1990) 3765-3772.

76. Liu, H., Madaleno, U.,Shinoda, T., Mishima, Y. and Suzuki, T. 'Interfacial reaction and strength of SiC fibres coated with aluminium alloys' *J Mater Sci* **25** (1990) 4247-4254.

77. Hughes, A.E., Hedges, M.M. and Sexton, B.A. 'Reactions at the $Al/SiO_2/SiC$ layered interface' *J Mater Sci* **25** (1990) 4856-4865.

78. Barlow, C.Y. 'Microstructural evolution during straining of discontinuously reinforced metal matrix composites' *Proc 12th Risø Int Symp on Materials Science: Metal Matrix Composites - Processing, Microstructure and Properties*. eds. N. Hansen, D. Juul Jensen, T. Leffers, H. Lilholt, T. Lorentzen, A.S. Pedersen, O.B. Pedersen and B. Ralph. Risø National Laboratory, Roskilde, Denmark (1991) 1-15.

79. Humphreys, F.J., Miller, W.S. and Djazeb, M.R. 'Microstructural development during thermomechanical processing of particulate metal-matrix composites' *Mater Sci and Tech* **6** (1990) 1157-1166.

80. Henriksen, B.R. 'The microstructure of squeeze-cast SiC_w-reinforced Al4Cu base alloy with Mg and Ni additions' *Composites* **21**, 4 (1990) 333-338.

81. Nutt, S.R. and Carpenter, R.W. 'Non-equilibrium phase distribution in an Al-SiC composite' *Mater Sci and Eng* **75** (1985) 169-177.

82. Papazian, J.M. 'Effects of SiC whiskers and particles on precipitation in aluminium matrix composites' *Metall Trans* **19A** (1988) 2949-2953.

83. Yang, M. and Scott, V.D. 'Interface and fracture of carbon fibre reinforced Al-7 wt% Si alloy' *J Mater Sci* **26** (1991) 1609-1617.

84. Weisinger, M.D. 'Metal matrix composite structures tooling and fabrication processes' SAE paper 700732, Oct 5-9 (1970) 1-12.

85. Durrant, G., Scott, V.D., Clift, S.E. and Trumper, R.L. 'Forging of Saffil reinforced aluminium alloy' *Proc 12th Risø Int Symp on Materials Science: Metal Matrix Composites - Processing, Microstructure and Properties*. eds. N. Hansen, D. Juul Jensen, T. Leffers, H. Lilholt, T. Lorentzen, A.S. Pedersen, O.B. Pedersen and B. Ralph. Risø National Laboratory, Roskilde, Denmark (1991) 311-316.

86. Durrant, G., Scott, V.D., Clift, S.E. and Trumper, R.L. 'Forging of short alumina fibre reinforced aluminium alloys' Developments in the Science and Technology of Composite Materials, *Proc 5th Euro Conf on Comp Mater (ECCM5)*, eds A.R Bunsell, J.F. Jamet and A. Massiah, EACM, Bordeaux, France (1992) 639-644.

87. Cronjäger, L. and Biermann, D. 'Turning of metal matrix composites' *Proc 2nd Euro Conf on Advanced Materials and Processes*, Euromat 91, eds. T.W. Clyne and P.J. Withers, Institute of Metals, Cambridge, (1991) vol 1, 73-80.

88. Chadwick, G.A. and Clegg, A.J. 'Machining metal matrix composites' Metals and Materials, *J Inst Met* **6**, 2 (1990) 73-76.

89. Gindy, N.N.Z. and Clegg, A.J. 'Machining of metal matrix composites', The materials revolution through the 90's, *BNF Metal Technology Centre 7th Int Conf*, vol 2, Oxford, UK, (1989) paper 32, 1-16.

90. 'Metals handbook', 9th edn, vol 2, 'Properties and selection: Non-ferrous alloys and pure metals' (1979) ASM, p191.

91. Partridge, P.G., Harvey, J. and Dunford, D.V. 'Diffusion bonding in Al-alloys in the solid-state' *AGARD CP398, Advanced Joining of Aerospace Metallic Materials* (1985) paper 8-1.

92. Calvo, F.A., Gómez de Salazar, J.M., Ureña, A., Canión, J.G. and Perosanz, F. 'Diffusion bonding of Ti-6Al-4V alloy at low temperature: Metallurgical aspects' *J Mater Sci* **27** (1992) 391-398.

93. Partridge, P.G. and Ward-Close, C.M. 'Diffusion bonding of advanced materials' Metals and Materials, *J Inst Met* **5**, 6 (1989) 334-339.

94. Ueki, M., Naka, M. and Okamoto, I. 'Joining and wetting of CaO-stabilised ZrO_2 with Al-Cu alloys' *J Mater Sci* **23** (1988) 2983-2988.

95. Suganuma, K., Okamoto, T., Miyamoto, Y., Shimada, M. and Koizumi, M. 'Joining Si_3N_4 to type 405 steel with soft metal interlayers'
Mater Sci and Tech **2** (1986) 1156-1161.

96. Beraud, C., Courbiere, M., Esnouf, C., Juve, D. and Treheux, D. 'Study of copper-alumina bonding'
J Mater Sci **24** (1989) 4545-4554.

97. Winkler, P.-J. 'Diffusion bonding and superplastic forming, two complementary techniques' *Proc Conf on Superplasticity and Superplastic Forming*, eds. C.H. Hamilton and N.E. Paton, The Minerals, Metals and Materials Society (1988) 491-506.

98. Maehora, Y., Komizo, Y. and Langdon, T.G. 'Principles of superplastic diffusion bonding'
Mater Sci and Tech **4** (1988) 669-674.

99. Field, D.J. 'Oxidation of aluminum and its alloys' *Aluminum Alloys - Contemporary Research and Applications*. eds. A.K. Vasudevan and R.D. Doherty, vol 1, Treatise on Materials Science and Technology, Academic Press, London (1989) 523-537.

100. Wallach, E.R. 'Solid-state joining: Techniques and applications' *Proc Conf Inst Metallurgists*, Coventry, UK, vol 2 (1981), 23-31.

101. Reed-Hill, R.E. and Abbaschian, R. 'Physical metallurgy principles' 3rd edn (1991) PWS-Kent, Boston, USA.

102. CRC 'Standard mathematical tables' 26th edn, ed. W.H. Beyer (1981) CRC Press, p527.

103. Crank, J. 'The mathematics of diffusion' 2nd edn (1975) Oxford University Press.

104. Rhines, F.N. 'Phase diagrams in metallurgy: Their development and application' (1956) McGraw-Hill, London, p108.

105. Hill, A. and Wallach, E.R. 'Modelling solid-state diffusion bonding'
Acta Metall **37**, 9 (1989) 2425-2437.

106. Derby, B. and Wallach, E.R. 'Diffusion bonds in copper' *J Mater Sci* **19** (1984) 3140-3148.

107. Derby, B. and Wallach, E.R. 'Diffusion bonds in iron and a low-alloy steel'
J Mater Sci **19** (1984) 3149-3158.

108. Derby, B. and Wallach, E.R. 'Diffusion bonding - Assessment of a theoretical model' *Proc Conf Inst Metallurgists*, Coventry, UK, vol 2 (1981), 89-95.

109. Eckman, D.C., Rosenblum, B.Z. and Boules, C.Q. 'Diffusion bonding of beryllium-copper alloys' *J Mater Sci* **27** (1992) 49-54.

110. Garmong, G., Paton, N.E. and Argon, A.S. 'Attainment of full interfacial contact during diffusion bonding' *Metall Trans A* **6A** (1975) 1269-1279.

111. Guo, Z.X. and Ridley, N. 'Modelling of diffusion bonding of metals' *Mater Sci and Tech* **3** (1987) 945-953.

112. Hauser, D., Kamner, P.A. and Dedrick, J.H. 'Solid-state welding of aluminium' *Weld J Res Suppl* **46** (1967) 11s-22s.

113. Maddrell, E.R., Ricks, R.A. and Wallach, E.R. 'Diffusion bonding of aluminium alloys containing lithium and magnesium' *Proc 5th Int Conf on Al-Li Alloys*, eds. T. Sanders and E. Stroke, vol 1 (1989) 451-460

114. Gilmore, C.J., Dunford, D.V. and Partridge, P.G. 'Microstructure of diffusion-bonded joints in Al-Li 8090 alloy' *J Mater Sci* **26** (1991) 3119-3124.

115. Enjo, T. and Ikeuchi, K. 'Diffusion welding of Al-Cu-Mg series 2017 alloy' *Trans JWRI* **13**, 2 (1984) 63-68.

116. Dunford, D.V. and Partridge, P.G. 'Diffusion bonding of Al-Li alloys - Overview' *Mater Sci and Tech* **8** (1992) 385-398.

117. Anderson, W.A. 'Metallurgical studies of the vacuum brazing of aluminium' *Weld J Res Suppl* **56** (1977) 314s-318s.

118. Schmatz, D.J. and Winterbottom, W.L. 'A fluxless process for brazing aluminium heat exchangers in inert gas' *Weld J.* **62**, 10 (1983) 31-38.

119. Kuriyama, K. and Wallach, E.R. 'Diffusion bonding SiC-Ti metal-matrix composites' Composites - Design, Manufacture and Application, *Proc 8th Int Conf on Composite Materials (ICCM8)* eds. S.W. Tsai and G.S. Springer, (1991) Honolulu, 9-G, 1-10.

120. Hirose, A., Kotoh, M., Fukumoto, S. and Kobayashi, K.F. 'Diffusion bonding of SiC fibre reinforced Ti-6Al-4V alloy' *Mater Sci and Tech* **8** (1992) 811-815.

121. Partridge, P.G. and Dunford, D.V. 'The role of interlayers in diffusion bonded joints in metal-matrix composites' *J Mater Sci* **26** (1991) 2255-2258.

122. Enjo, T., Ikeuchi, K., Murakami, Y. and Suzuki, N. 'Diffusion bonding of Al-Mg-Si series 6063 alloy reinforced with alumina short fibres' *Trans JWRI* **16**, 2 (1987) 57-64.

123. Hersh, M.S. and Featherby, M. 'Joining of boron/aluminium composites' *Proc 13th Conf 'Structures, structural dynamics and materials'* AIAA/ASME/SAE, vol 2, (1972) San Antonio, paper 72-360.

124. Sakamoto, A. 'Fabrication and joining of fibre-reinforced metals' *J Jap Weld Soc* **56**, 1 (1987) 20-29.

125. Mahoney, M. 'Joining of reinforced aluminium alloys' Composites - Design, Manufacture and Application, *Proc 8th Int Conf on Composite Materials (ICCM8)* eds. S.W. Tsai and G.S. Springer, (1991) Honolulu, 9B, 1-10.

126. 'Smithells metals reference book' 6th edn, ed. E.A. Brandes (1983) Butterworths, London-Boston.

127. Mondolfo, L.F. 'Aluminium alloys: structure and properties' (1976) Butterworths, London-Boston.

128. 'Metals handbook' 9th edn, vol 8, 'Metallography, structures and phase diagrams' (1979) ASM.

129. 'Equilibrium diagrams of aluminium alloy systems' The Aluminium Development Association. Information Bulletin 25 (1961).

130. Marshall, D.B. 'An indentation method for measuring matrix-fiber frictional stresses in ceramic composites' *Comm Amer Ceram Soc* **67** (1984) C259-260.

131. Tabata, T., Masaki, S. and Azekura, K. 'Bond criterion in cold pressure welding of aluminium' *Mater Sci and Tech* **5** (1989) 377-381.

132. Goodhew, P.J. and Humphreys, F.J. 'Electron microscopy and analysis' 2nd edn. (1988) Taylor-Francis.

133. Bousfield, B. 'A systematic approach to sample preparation' Metals and Materials, *J Inst Met* **4**, 12 (1988) 758-761.

134. Scott, V.D. and Love, G. 'Quantitative electron-probe microanalysis' (1983) Ellis-Horwood, London.

135. Love, G. and Scott, V.D. 'Evaluation of a new correction procedure for quantitative electron-probe microanalysis' *J Phys D; Appl Phys*, **11** (1978) 1369.

136. Sewell, D., Love, G. and Scott, V.D. 'Universal correction procedure for electron-probe microanalysis: II The absorption correction' *J Phys D; Appl Phys*, **18** (1985) 1245-1268.

137. Chatfield, C. 'Statistics for technology - A course in applied statistics' 3rd edn (1983) Chapman and Hall, London, p32.

138. Sanders, R.E., Baumann, S.F. and Stumpf, H.C. 'Wrought non-heat treatable aluminum alloys' *Aluminum Alloys - Contemporary Research and Applications.* eds. A.K. Vasudevan and R.D. Doherty, vol 1, Treatise on Materials Science and Technology, Academic Press, London (1989) 65-103.

139. Wilson, P.W., Kattamis, T.L. and Shiohara, Y. 'Coarsening during solidification of aluminium-copper alloys' *J Mater Sci* **23** (1988) 2882-2892.

140. Starke, E.A. 'Heat-treatable aluminum alloys' *Aluminum Alloys - Contemporary Research and Applications.* eds. A.K. Vasudevan and R.D. Doherty, vol 1, Treatise on Materials Science and Technology, Academic Press, London (1989) 35-63.

141. Staley, J.T. 'History of wrought-aluminum-alloy development' *Aluminum Alloys - Contemporary Research and Applications.* eds. A.K. Vasudevan and R.D. Doherty, vol 1, Treatise on Materials Science and Technology, Academic Press, London (1989) 3-31.

142. 'Book of data' Revised Nuffield Advanced Science, (1984) Longman, Harlow, pp12-22.

143. Scott, V.D., Bleay, S.M., Chapman, A.R. and Love, G. 'Interface compatibility in Nicalon-fibre reinforced metal and ceramic composites' *J Microscopy* **169**, 2 (1993), *in press*.

144. Fonda, R.W., Cassada, W.A. and Shiflet, G.J. 'Accommodation of the misfit strain surrounding {111} precipitates (Ω) in Al-Cu-Mg-(Ag)' *Acta Metall Mater* **40**, 10 (1992) 2539-2546.

145. Garg, A. and Howe, J.M. 'Nucleation and growth of Ω phase in an Al-4.0Cu-0.5Mg-0.5Ag alloy - An *in situ* hot-stage TEM study' *Acta Metall Mater* **39**, 8 (1991) 1925-1937.

146. Garg, A. and Howe, J.M. 'Convergent-beam electron diffraction analysis of the Ω phase in an Al-4.0Cu-0.5Mg-0.5Ag alloy'
Acta Metall Mater **39**, 8 (1991) 1939-1946.

147. ASTM D1002-72 'Strength properties of adhesives in shear by tension loading' (1978) American Society for Testing and Materials.

148. BS 5320:Part C5 'Bond strength in longitudinal shear' (1976) British Standards Institution.

149. Harvey, J., Partridge, P.G. and Snooke, C.L. 'Diffusion bonding and testing of Al-alloy lap shear test pieces' *J Mater Sci* **20** (1985) 1009-1014.

150. Partridge, P.G. and Dunford, D.V. 'On the testing of diffusion-bonded overlap joints between clad Al-Zn-Mg alloy (7010) sheet' *J Mater Sci* **22** (1987) 1597-1608.

151. Dunford, D.V. and Partridge, P.G. 'Strength and fracture behaviour of diffusion-bonded joints in Al-Li (8090) alloy. Part I: Shear strength'
J Mater Sci **25** (1990) 4957-4964.

152. Dunford, D.V. and Partridge, P.G. 'Strength and fracture behaviour of diffusion-bonded joints in Al-Li (8090) alloy. Part II: Fracture behaviour'
J Mater Sci **26** (1991) 2625-2629.

153. Watson, M.C. and Clyne, T.W. 'Interfacial bond strength measurements in monofilament-reinforced titanium' *Proc 2nd Euro Conf on Advanced Materials and Processes, Euromat 91*, vol 1, eds. T.W. Clyne and P.J. Withers, Institute of Metals (1991) Cambridge, 235-240.

154. Mohamed, H.A. and Washburn, J. 'Mechanism of solid-state pressure welding'
Weld J Res Suppl **54**, 9 (1975) 302s-310s.

155. Cantelejos, N.A. and Cusminsky, G. 'Morphology of the interface of roll-bonded aluminium'
J Inst Met **100** (1972) 20-23.

156. Hine, R.A. and Guminski, R.D. 'High-temperature oxidation of aluminium-magnesium alloys in various gaseous atmospheres' *J Inst Met* **89** (1960) 417-422.

157. Lea, C. and Molinari, C. 'Magnesium diffusion, surface segregation and oxidation in Al-Mg alloys'
J Mater Sci **19** (1984) 2336-2352.

158. Malis, T. and Chaturved, M.C. 'Grain-boundary segregation in an Al-8 wt% Mg alloy'
J Mater Sci **17** (1982) 1479-1486.

159. Field, D.J., Scamens, G.M. and Butler, E.P. 'The effect of trace alloying additions on the high-temperature oxidation of Al-4.2wt% Mg and Al-3wt% Li alloys' *Proc 2nd Int Conf on Environmental Degradation of Engineering Materials* (1981) Virginia, USA, 393-405.

160. Ritchie, I.M., Sanders, J.V. and Weickhardt, P.L. 'Oxidation of a dilute aluminium magnesium alloy' *Oxid of Met* **3**, 1 (1971) 91-101.

161. Allen, D.J. and White, A.A.L. 'Sintering processes in diffusion bonding' *Proc Conf Inst Metallurgists*, vol 2 (1981) Coventry, UK, 96-106.

162. Dieter, G.E. 'Mechanical metallurgy' (1961) McGraw-Hill, pp479-483.

163. Durrant, G. 'The forging of Saffil fibre reinforced aluminium' *PhD Thesis*, University of Bath (1992).

164. Muddle, B.C. and Polmear, I.J. 'The precipitate Ω phase in Al-Cu-Mg-Ag alloys' *Acta Metall* **37**, 3 (1989) 777-789.

165. Partridge, P.G., Shepard, M. and Dunford, D.V. 'Statistical analysis of particulate interface lengths in diffusion bonded joints in a metal-matrix composite' *J Mater Sci* **26** (1991) 4953-4960.

166. Birks, N. and Meier, G.H. 'Introduction to high temperature oxidation of metals' (1983) Edward-Arnold, p105.

167. Ricks, R.A., Ball, J., Stoklossa, H., Winkler, P.J. and Grimes, R. 'Bonding of aluminium-lithium base alloys using roll clad zinc interlayers' *Proc Int Conf on Superplasticity and Superplastic Forming*, eds. C. Hamilton and N. Paton (1988) Blaine, Washington, USA, 557-561.

168. Barta, I.M. 'Low temperature diffusion bonding of aluminium alloys' *Weld J Res Suppl* **43** (1964) 241s-247s.

169. McGurran, B. and Nicholas, M.G. 'A study of aluminium brazing filler metals using hot stage scanning electron microscopy' *Weld J Res Suppl* **63** (1984) 295s-299s.

170. Calvo, F.A., Ureña, A., Gómez de Salazar, J.M. and Molleda, F. 'Special features of the formation of the diffusion bonded joints between copper and aluminium' *J Mater Sci* **23** (1988) 2273-2280.

171. Tarento, R.J. and Blaise, G. 'Etude par analyse en profondeur de l'interdiffusion en couches minces du couple Al-Cu: Cinctique de croissance des phases entre 200 et 300°C'
Acta Metall **36**, 4 (1988) 1035-1041.

172. Tuak-Poku, I., Dollar, M. and Massalski, T.B. 'A study of the transient liquid phase bonding process applied to an Ag/Cu/Ag sandwich joint'
Metall Trans A, **19A** (1988) 675-684.

173. Kehl, W. and Fischmeister, H.F. 'Liquid phase sintering of Al-Cu compacts'
Powder Metallurgy **3** (1980) 113-119.

174. Moshier, W.C., Ahearn, J.S. and Cooke, D.C. 'Interaction of Al-Si, Al-Ge, and Zn-Al eutectic alloys with SiC/Al discontinuously reinforced metal matrix composites' *J Mater Sci* **22** (1987) 115-122.

175. Gwyer, A.G.C., Phillips, H.W.L. and Mann, L. 'The constitution of the alloys of aluminium with copper, silicon and iron' *J Inst Met* **40** (1928) 297-358.

176. Niemann, J.T. and Wille, G.W. 'Fluxless diffusion brazing of aluminium castings'
Weld J Res Suppl **57**, 10 (1978) 285s-291s.

177. Elahi, M. and Fenn, R. 'The joining of a titanium alloy using a copper/silver intermediate layer' *Proc Conf Inst Metallurgists*, vol 2 (1981) Coventry, UK, 137-144.

178. Durrant, G. and Scott, V.D.'Effect of forging on the properties and microstructure of Saffil fibre reinforced aluminium' *Comp Sci and Tech, in press.*

APPENDIX

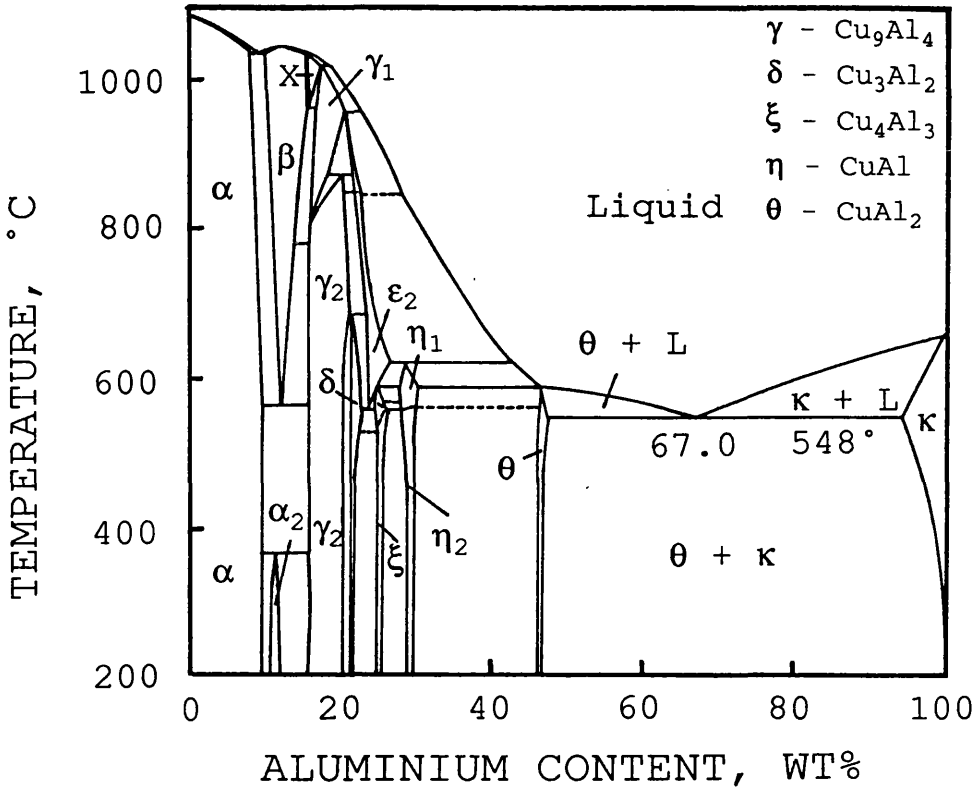

Aluminium-copper phase diagram [126].

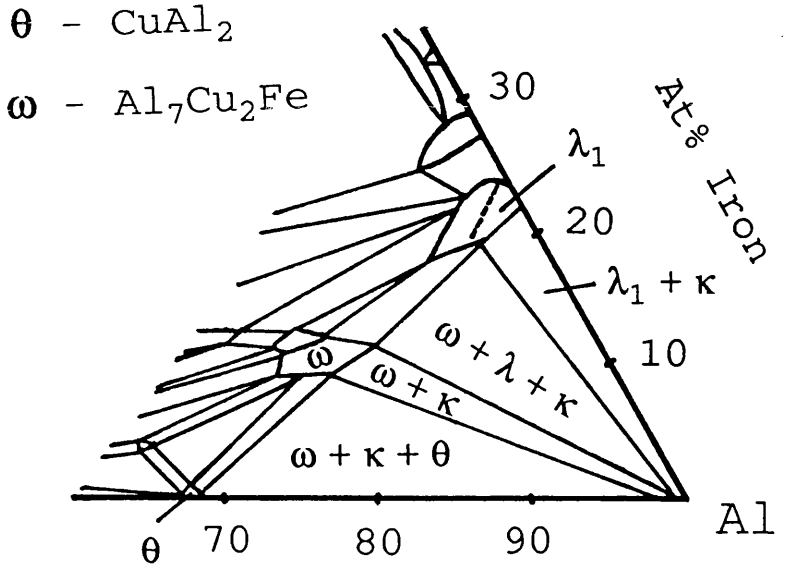

Aluminium corner of the aluminium-copper-iron system. Phases present at room temperature [126].

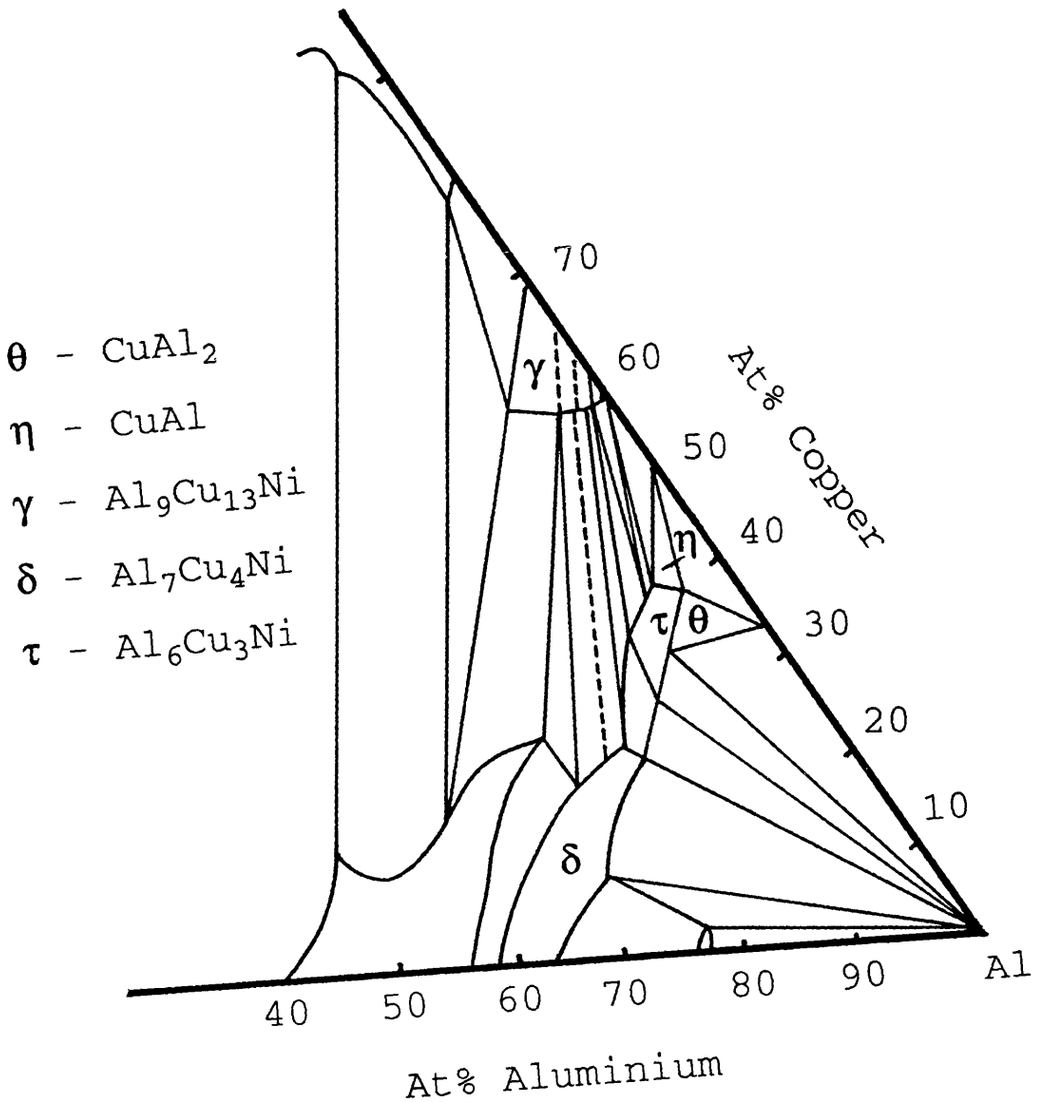

Aluminium corner of the aluminium-copper-nickel system. Phases present at room temperature [126].

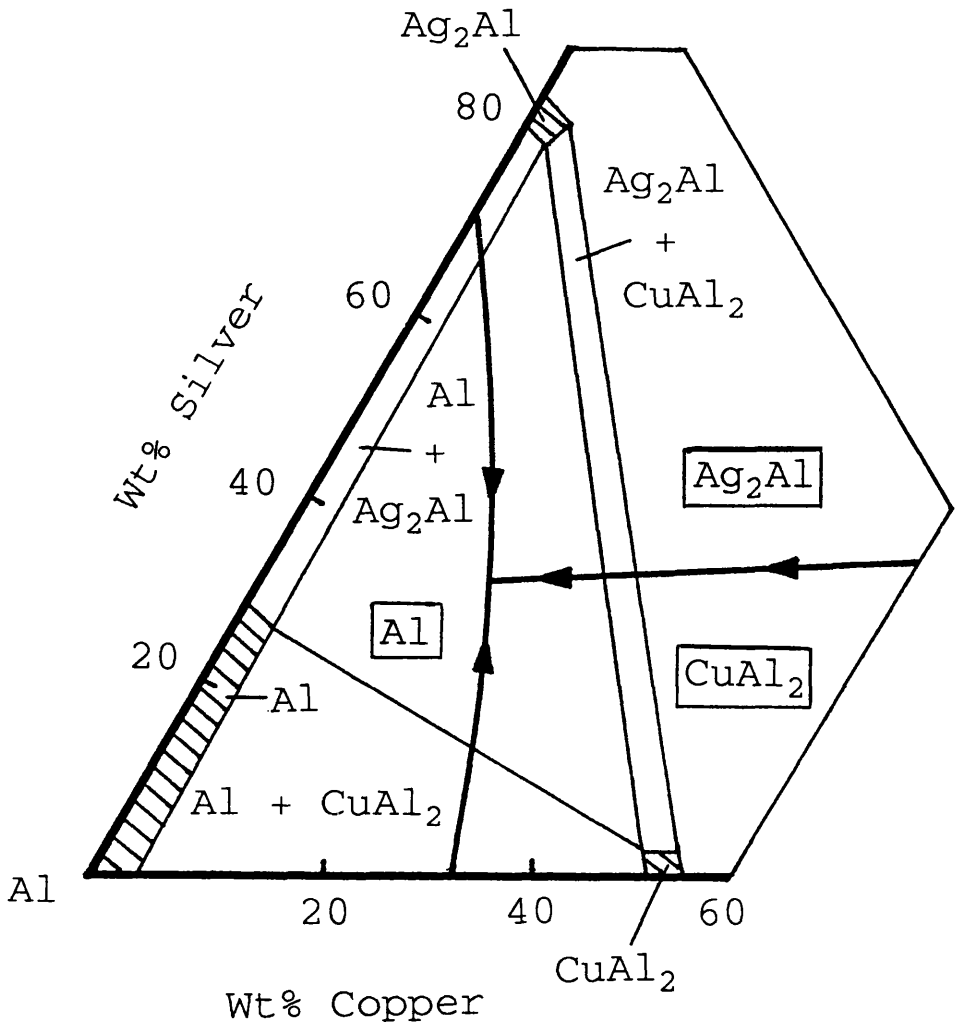

Aluminium corner of the aluminium-copper-silver system. Heavy lines, liquidus; boxed symbols, primary phases; light lines, phase distribution at 477°C [127].

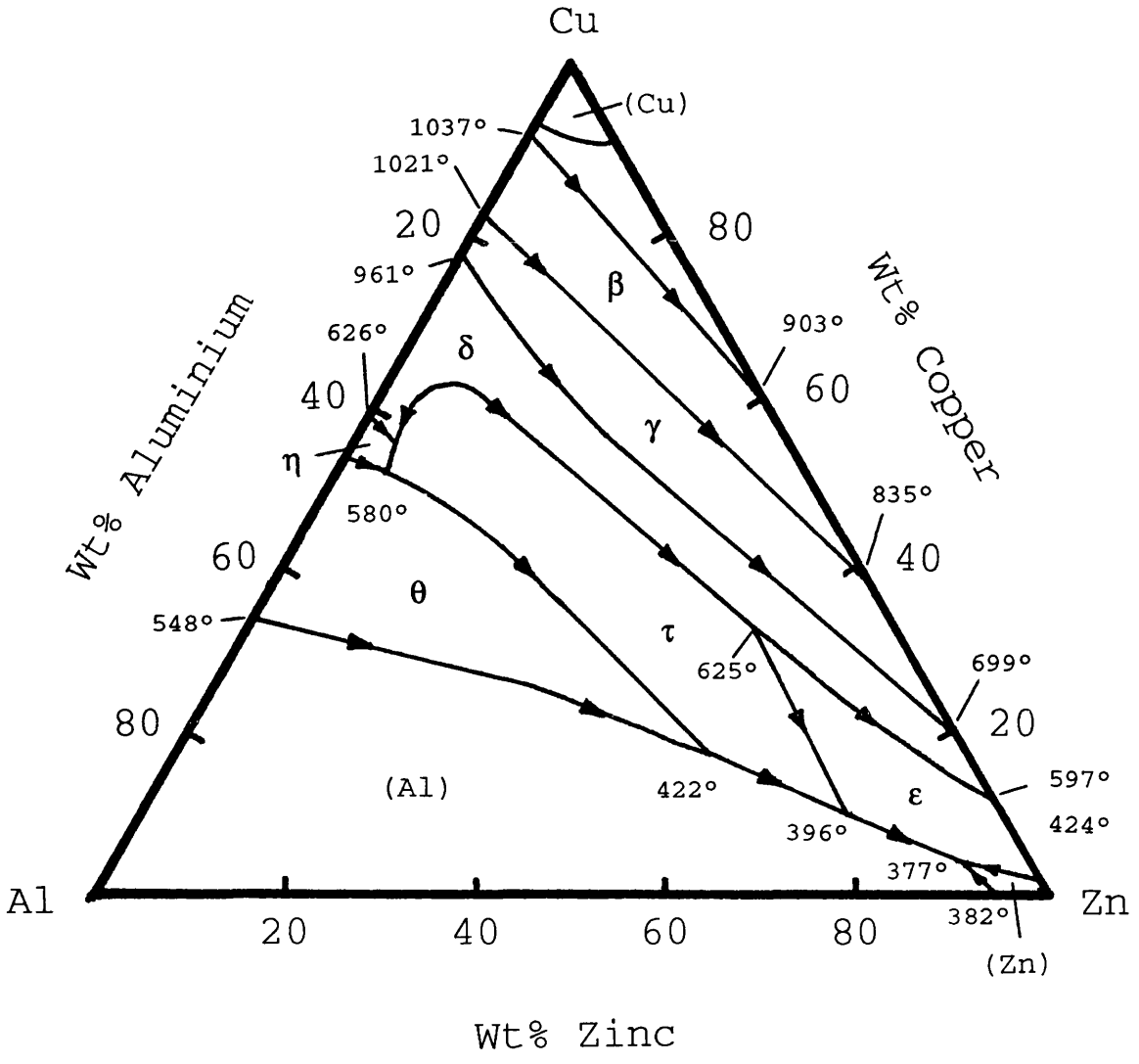

Aluminium-copper-zinc phase diagram; liquidus [136] (temperature in °C).

(a)

IADS No	Si	Fe	Cu	Mn	Mg	Zn	Cr	Ti	Other
1100	1.0 Si +Fe		0.05-0.20	0.05		0.10		0.05	Al min 99.0
2124	0.20	0.30	3.8-4.0	0.30-0.9	1.2-1.8	0.25	0.10	0.15	0.20 Zr + Ti

Compositions are in % maximum by weight unless shown as a range or a minimum.

(b)

Interlayer	Composition wt%	Thick μm	Form of interlayer
Zinc	99.99 Zn	12	Supplied as foil
Copper	99.99 Cu	4 and 10	Supplied as foil
Nickel-copper	99.99 Cu, >99 Ni	~15	Ni-plated copper
Copper-silver	28.5 Cu	50	Supplied as foil
2124 alloy	see Table 2.1a	~200	Rolled from 6 mm sheet
Copper-zinc	63.0 Cu	12	Supplied as foil

Table 2.1. Designation and compositions of alloys and interlayers used in this work.
a. Wrought alloys.
b. Metal and alloy interlayers.

Alloy	Eutectic temperature °C	Composition weight %	Source of reference
Al-Sn	228	99.5 Sn	126
Al-Zn	382	94.9 Zn	126
Al-Ge	424	54 Ge	126
Al-Mg	450	35 Mg	126
Al-Cu	548	33 Cu	126
Al-Ag	566	28 Ag	126
Al-Sn-Zn	197	77 Sn, 21.7 Zn	127
Al-Sn-Cu	228	99 Sn, 0.5 Cu	127
Al-Sn-Pb	273	61.7 Sn, 38.1 Pb	127
Al-Zn-Mg	343	93 Zn, 3 Mg	128
Al-Zn-Cu	377	89.2 Zn, 3.8 Cu	127
Al-Zn-Si	380	95 Zn, 0.05 Si	127
Al-Cu-Cr	437	32 Cu, 1.5 Cr	127
Al-Mg-Ge	442	33 Mg, 0.5 Ge	127
Al-Mg-Ni	449	33 Mg, 0.5-1.7 Ni	127
Al-Mg-Pb	449	34.4 Mg, 1.57 Pb	127
Al-Mg-Si	449		127
Al-Mg-Cu	451	32 Mg, 2.7 Cu	129
Al-Ag-Cu	502	32 Ag, 20 Cu	128
Al-Cu-Mg	507	33 Cu, 6.2 Mg	129
Al-Cu-Si	525	26.7 Cu, 5.25 Si	129
Al-Cu-Fe	545	32.5 Cu, 0.3 Fe	127

Table 2.2. Eutectic temperatures and compositions for binary and ternary aluminium alloys.

Sample	Net intensity CPS	Oxide thickness nm
Alumina	59962 ± 444	
Aluminium	52 ± 9	2.2 ± 0.4
5 minutes*	88 ± 16	3.7 ± 0.7
15 minutes*	102 ± 33	4.2 ± 0.3
45 minutes*	183 ± 33	8.3 ± 1.5
90 minutes*	366 ± 159	16.8 ± 6.5
180 minutes*	576 ± 153	26.4 ± 7.0
240 minutes*	840 ± 130	38.4 ± 6.0

*Heat-treated at 500°C

Table 3.1. EPMA data for oxide thickness measurements on aluminium.

Material	Max load N	Overlap mm^2	Shear strength MPa
Aluminium	4720 ± 432	48 ± 3	97 ± 4
Aluminium	6410 ± 755	57 ± 3	112 ± 11
Aluminium*	3375 ± 150	44 ± 2	77 ± 3
Aluminium*	4230 ± 448	50 ± 3	85 ± 4
2124 alloy	9470 ± 363	37 ± 2	255 ± 5
2124 alloy+	13660 ± 518	54 ± 3	251 ± 8
2124/25% SiC_p	17550 ± 1597	68 ± 7	260 ± 4
2124/30% SiC_p	18500 ± 1134	67 ± 4	278 ± 4
2124/35% SiC_p	13675 ± 2480	48 ± 9	288 ± 6
2124/40% SiC_p	14725 ± 3093	51 ± 8	289 ± 33

*Heat-treated at 500°C for 5 minutes
+Heat-treated at 500°C for 240 minutes

Table 3.2. Shear strengths of as-received and heat-treated aluminium and composite.

Phase	Element	Net intensity CPS Standard	Specimen	Intensity ratio	ZAF corrected weight%	atom%
A	Al	64545	13	0.0002	0.07	0.16
	Cu	13307	13026	0.9789	98.00	98.59
B	Al	65023	4519	0.0695	19.69	37.44
	Cu	13311	10023	0.7530	77.47	62.56
C	Al	65728	7769	0.1182	30.77	51.62
	Cu	13656	8876	0.6500	67.87	48.34
C	Al	65727	7112	0.1082	28.60	50.48
	Cu	13648	9005	0.6598	68.73	49.48
D	Al	65757	13638	0.2074	46.36	68.17
	Cu	13656	6522	0.4776	50.94	31.80
D	Al	65538	13914	0.2123	47.25	68.54
	Cu	13011	6230	0.4788	51.08	31.46
D	Al	65544	13797	0.2105	46.79	68.63
	Cu	13018	6143	0.4719	50.37	31.37
D	Al	65543	13790	0.2104	46.87	68.45
	Cu	13015	6208	0.4770	50.89	31.55
E	Al	65974	56751	0.8602	94.73	98.08
	Cu	13712	524	0.0382	4.31	1.90
F	Al	63802	15504	0.2430	49.91	70.15
	Cu	13332	4274	0.3206	34.91	20.83
	Fe	12372	1659	0.1341	13.17	8.94
F	Al	63810	15525	0.2432	49.83	70.55
	Cu	13335	4241	0.3180	34.62	20.81
	Fe	12371	1584	0.1280	12.56	8.59
G1	Al	62067	11476	0.1849	42.44	63.02
	Cu	13759	4267	0.3101	33.20	20.93
	Ni	13775	3123	0.2267	23.20	15.83
G1	Al	62098	10755	0.1732	40.58	60.85
	Cu	13763	4430	0.3219	34.38	21.89
	Ni	13780	3332	0.2418	24.68	17.00
G1	Al	61713	11257	0.1824	41.96	62.74
	Cu	13685	4248	0.3104	32.22	21.09
	Ni	13705	3106	0.2266	23.18	15.93
G1	Al	62141	10589	0.1704	39.82	60.10
	Cu	13776	3368	0.2445	16.18	16.78
	Ni	13795	4471	0.3241	33.18	23.00
G1	Al	62164	10549	0.1697	39.86	60.51
	Cu	13778	4311	0.3129	33.42	21.54
	Ni	13794	3438	0.2492	25.44	17.75
G1	Al	61472	10752	0.1749	39.78	60.72
	Cu	13630	947	0.0695	7.51	4.87
	Ni	13644	6477	0.4747	48.99	34.37

Table 3.3. EPMA data for analysis of phases (values averaged from two measurements).

Phase	Element	Net intensity CPS Standard	Specimen	Intensity ratio	ZAF corrected weight%	atom%
G1	Al	62039	12060	0.1944	42.89	63.49
	Cu	13757	651	0.0473	5.13	3.22
	Ni	13774	6498	0.4718	48.86	33.24
G1	Al	62156	10449	0.1681	38.82	59.31
	Cu	13779	1239	0.0899	9.69	6.28
	Ni	13800	6556	0.4751	48.94	34.36
G2	Al	62162	10611	0.1707	40.37	61.03
	Cu	13782	5657	0.4105	43.68	28.04
	Ni	13801	2095	0.1518	15.44	10.73
G2	Al	62061	10358	0.1669	39.75	60.45
	Cu	13756	5907	0.4294	45.62	29.45
	Ni	13778	1914	0.1389	14.11	9.86
G2	Al	62010	10281	0.1658	39.39	60.41
	Cu	13749	5513	0.4010	42.65	27.77
	Ni	13768	2233	0.1622	16.49	11.62
G2	Al	61909	10271	0.1659	39.49	60.34
	Cu	13545	5650	0.4171	43.77	28.39
	Ni	13740	2138	0.1556	15.81	11.10
G2	Al	61395	10198	0.1661	39.45	60.54
	Cu	13624	5518	0.4054	43.12	28.09
	Ni	13622	2126	0.1561	15.86	11.19
H	Al	62060	14584	0.2350	50.60	71.02
	Cu	13757	6090	0.4427	47.44	28.27
	Ni	13704	134	0.0098	0.99	0.64
H	Al	61198	13574	0.2218	48.75	69.39
	Cu	13565	6216	0.4582	48.99	29.60
	Ni	13621	197	0.0145	1.49	0.97
I	Al	62471	34453	0.5515	74.11	91.22
	Cu	13101	468	0.0357	3.95	2.07
	Ag	12147	1851	0.1524	19.35	5.96
J	Al	62403	13385	0.2145	47.53	68.47
	Cu	13084	6232	0.4763	50.81	31.08
	Ag	12132	110	0.0091	1.15	0.41
J	Al	62443	13250	0.2122	47.17	68.38
	Cu	13090	6252	0.4776	50.95	31.35
	Ag	12175	69	0.0057	0.72	0.26
K	Al	62399	4767	0.0764	14.27	40.07
	Cu	13080	311	0.0238	2.41	2.87
	Ag	12134	9332	0.7691	81.21	57.00
K	Al	62469	4691	0.0751	14.00	39.12
	Cu	13103	318	0.0243	2.46	2.91
	Ag	12144	9578	0.7887	83.10	57.92

Table 3.3. continued.

Phase	Element	Net intensity CPS Standard	Specimen	Intensity ratio	ZAF corrected weight%	atom%
L1	Al	65170	36485	0.5598	76.13	83.73
	Fe	11832	2500	0.2113	22.94	12.19
	Si	67195	1035	0.0154	3.81	4.02
L2	Al	65176	26220	0.4023	60.27	74.06
	Fe	11833	3257	0.2752	29.67	17.61
	Si	67380	2001	0.0297	6.93	8.18
L3	Al	65183	35681	0.5474	75.67	86.20
	Fe	11838	2604	0.2200	23.83	13.11
	Si	67400	153	0.0023	0.57	0.63
L4	Al	65205	28677	0.4398	66.49	80.89
	Fe	11840	3463	0.2925	31.43	18.47
L5	Al	65195	32623	0.5004	74.14	82.45
	Fe	11838	3508	0.2963	31.89	17.13
M	Al	65650	20	0.0003	0.10	0.24
	Cu	13851	13625	0.9837	98.42	99.10
	Ni	13729	81	0.0059	0.56	0.61
	Fe	12560	7	0.0006	0.04	0.05
N	Al	63199	4683	0.0741	20.82	38.45
	Cu	13842	9785	0.7069	72.97	57.23
	Ni	13822	705	0.0510	5.04	4.28
O	Al	62842	10199	0.1623	38.66	59.40
	Cu	13774	4793	0.3480	37.07	24.18
	Ni	13753	3137	0.2281	23.22	16.39
O	Al	62880	10671	0.1697	39.62	60.35
	Cu	13782	3476	0.2522	27.00	17.46
	Ni	13762	4233	0.3076	31.48	22.04
O	Al	63279	10745	0.1698	39.65	60.23
	Cu	13873	3484	0.2512	26.91	17.35
	Ni	13849	4306	0.3109	31.82	22.21
O	Al	63290	10766	0.1701	39.77	60.27
	Cu	13871	3571	0.2574	27.56	17.73
	Ni	13853	4264	0.3078	31.50	21.93
P	Al	62427	20457	0.3277	62.02	75.21
	Cu	13768	3961	0.2877	31.20	16.06
	Mn	10260	304	0.0296	3.11	1.85
	Fe	11832	1338	0.1131	11.32	6.63
	Mg	48714	34	0.0007	0.18	0.24

Table 3.3. continued.

Inter-layer	Pres MPa	Temp °C	Time mins	Def %	Bead mass g	Max load N	Overlap mm^2	Shear str MPa	Bonded area %	Spec shear str MPa
	3	500	30	2						
	10	500	240	10						
Zn	3	500	30	2						
Zn	10	500	240	8						
Cu	3	550	5	2		2304 ± 1476	117 ± 13	20 ± 14	25 ± 14	76 ± 11
Cu	3	550	10	2	0.11	6130 ± 4264	114 ± 3	54 ± 38	48 ± 33	112 ± 3
Cu	3	550	20	2	0.14	2580 ± 2150	94 ± 8	26 ± 19	42 ± 33	64 ± 5
Cu	3	550	30	2	0.15	3875 ± 1317	94 ± 4	42 ± 16	47 ± 17	88 ± 11
Cu	3	550	60	2	0.14	4708 ± 2615	91 ± 8	53 ± 32	52 ± 29	102 ± 13
Cu	3	550	100	2	0.18	4440 ± 1139	90 ± 4	49 ± 13	57 ± 11	97 ± 29
Cu	10	550	30	13	0.31	7570 ± 694	79 ± 9	96 ± 4	~100	96 ± 4
Cu*	3	550	30	2	0.08	5640 ± 1101	82 ± 3	69 ± 14	80 ± 10	86 ± 10
Ni-Cu	3	550	60	2						
Ni-Cu	10	550	60	9		6340 ± 2180	97 ± 7	65 ± 18	74 ± 24	89 ± 8
Cu-Ag	3	510	30	2		1800 ± 660	77 ± 5	24 ± 9	65 ± 20	36 ± 6
Cu-Ag	10	510	30	6		5220 ± 1536	79 ± 5	65 ± 20	85 ± 21	76 ± 8
2124	10	500	30	3		3270 ± 500	54 ± 4	61 ± 7	91 ± 7	67 ± 4
2124	10	550	30	8		5250 ± 480	72 ± 4	73 ± 6	~100	73 ± 6
Cu-Zn	10	500	30	7						

*4 μm copper foil interlayer

Table 3.4. Shear test data for bonded aluminium.

Bonded sample	Interlayer	IFFS of joint MPa	IFFS of composite MPa
Al/Nic	Cu	184 ± 74	73 ± 19
Al/Nic	Cu-Ag	262 ± 63	68 ± 24
Al/Nic	2124	104 ± 28	37 ± 19
Al/Nic-2124		~200	~70
Al/Nic-2124/35P		~180	72 ± 11

Table 3.5. Summary of interfacial friction stress measurements for bonded Al/Nic composite.

I.

Fibre dia μm	2a μm (i)	2a μm (ii)	2b μm (i)	2b μm (ii)	u μm	τ MPa
15.5	9.0	9.0	24.5	23.0	2.11	68.4
17.0	10.0	11.0	27.0	27.0	2.37	85.8
16.0	9.0	9.0	22.0	21.5	1.83	71.9
15.0	8.5	9.5	27.5	26.5	2.58	61.8
16.0	9.5	9.5	26.5	25.0	2.33	70.1
17.0	9.5	10.0	23.0	23.5	1.94	78.0
14.5	8.5	8.5	24.0	23.5	2.19	64.3
16.75	9.0	9.0	20.0	22.5	1.76	65.2
16.75	9.5	9.5	22.0	20.0	1.65	86.3
16.0	10.0	9.0	25.5	24.5	2.22	73.4

II.

Fibre dia μm	2a μm (i)	2a μm (ii)	2b μm (i)	2b μm (ii)	u μm	τ MPa
16.75	9.0	9.0	21.0	21.0	1.72	66.6
13.75	8.5	8.0	25.5	25.0	2.44	60.0
14.75	10.0	10.5	19.5	20.5	1.40	202.0
12.75	8.5	9.0	16.0	16.5	1.08	215.9
17.5	12.5	13.0	30.0	30.0	2.47	163.6
16.5	12.0	12.5	28.0	29.0	2.33	176.6
17.0	13.0	12.5	29.0	31.0	2.47	178.5
15.5	12.5	12.0	28.5	28.5	2.33	213.0
17.5	14.0	14.5	28.0	30.0	2.11	298.6
25.0	18.5	20.0	40.0	38.0	2.83	254.7

Table 3.5a. Interfacial friction stress data for Al/Nic composite bonded using a copper interlayer, 10 MPa, 30 mins, 550°C.
I. Away from joint.
II. Joint region.

I.

Fibre dia μm	2a μm (i)	(ii)	2b μm (i)	(ii)	u μm	τ MPa
19.5	9.0	9.0	23.0	23.0	2.0	36.2
16.0	10.0	10.0	24.0	24.0	2.0	99.8
18.0	10.0	9.0	25.0	24.0	2.2	53.3
17.0	9.5	10.0	23.5	23.5	2.0	76.6
15.0	9.0	9.0	25.0	23.0	2.2	74.2

II.

Fibre dia μm	2a μm (i)	(ii)	2b μm (i)	(ii)	u μm	τ MPa
17.5	14.0	14.0	26.5	27.5	1.86	315.6
17.5	11.5	12.5	24.0	24.0	1.72	184.6
17.0	13.0	13.0	26.0	28.0	2.01	237.7
17.0	13.0	14.0	25.0	25.0	1.65	336.5
17.5	13.0	13.0	25.5	26.5	1.86	234.7

Table 3.5b. Interfacial friction stress data for Al/Nic composite bonded using a copper-silver alloy interlayer, 20 MPa, 30 mins, 510°C.
I. Away from joint.
II. Joint region.

I.

Fibre dia μm	2a μm (i)	2a μm (ii)	2b μm (i)	2b μm (ii)	u μm	τ MPa
17.5	9.0	9.0	31.0	31.0	3.15	31.9
20.0	9.0	9.0	29.0	29.0	2.87	23.5
18.5	8.5	9.0	32.0	32.5	3.37	22.6
18.0	9.0	9.5	23.0	22.0	1.90	54.2
15.5	9.0	9.5	27.0	29.0	2.69	60.0
18.0	8.5	8.5	31.5	33.0	3.43	21.6
18.0	9.5	9.5	21.0	22.0	1.72	66.6
18.0	9.0	9.0	33.0	34.0	3.51	26.3
20.0	9.5	9.5	23.0	21.0	1.79	46.6
18.0	8.5	8.0	42.0	42.0	4.84	13.5

II.

Fibre dia μm	2a μm (i)	2a μm (ii)	2b μm (i)	2b μm (ii)	u μm	τ MPa
15.0	9.0	9.0	19.5	20.0	1.52	103.5
16.0	10.0	9.0	21.0	21.5	1.65	96.9
17.0	10.0	10.0	20.5	20.0	1.47	113.7
18.0	9.0	9.0	20.0	19.5	1.53	59.9
15.0	9.0	9.0	21.0	21.0	1.72	92.7
19.0	9.0	10.0	18.0	18.0	1.22	80.0
16.0	9.0	10.0	19.0	19.0	1.36	119.8
15.0	9.5	9.5	20.0	19.5	1.46	134.8
14.5	8.5	8.5	20.0	20.5	1.69	83.4
14.0	8.5	9.5	18.0	17.5	1.25	156.4

Table 3.5c. Interfacial friction stress data for Al/Nic composite bonded using an aluminium alloy (2124) interlayer, 20 MPa, 240 mins, 500°C.
I. Away from joint.
II. Joint region.

I.

Fibre dia μm	2a μm (i)	2a μm (ii)	2b μm (i)	2b μm (ii)	u μm	τ MPa
15.5	9.0	9.0	24.5	24.0	2.19	66.1
18.0	10.0	10.0	23.0	23.0	1.86	75.5

II.

Fibre dia μm	2a μm (i)	2a μm (ii)	2b μm (i)	2b μm (ii)	u μm	τ MPa
15.5	12.0	12.5	28.0	28.5	2.29	216.0

Table 3.5d. Interfacial friction stress data for Al/Nic composite bonded to 2124 alloy, 10 MPa, 240 mins, 500°C.
I. Away from joint.
II. Joint region.

I.

Fibre dia μm	2a μm (i)	2a μm (ii)	2b μm (i)	2b μm (ii)	u μm	τ MPa
16.0	9.0	9.0	22.5	23.0	2.01	65.5
16.0	9.0	9.0	22.5	23.0	1.97	66.7
17.0	9.5	9.0	23.0	23.5	2.01	60.9
16.0	9.0	9.5	21.0	22.0	1.76	83.5
16.5	9.0	10.0	22.0	22.0	1.79	83.0

II.

Fibre dia μm	2a μm (i)	2a μm (ii)	2b μm (i)	2b μm (ii)	u μm	τ MPa
18.0	12.0	12.5	25.0	24.0	1.76	180.0

Table 3.5e. Interfacial friction stress data for Al/Nic composite bonded to 2124/35P composite, 10 MPa, 240 mins, 500°C.
I. Away from joint.
II. Joint region.

Inter-layer	Press MPa	Temp °C	Time mins	Def %	Max load N	Overlap mm^2	Shear strength MPa	Bonded area %	Specific shear strength MPa
Cu	10	550	30	2	3838 ± 1380	111 ± 14	34 ± 12	66 ± 16	51 ± 5
Cu	20	550	30	2	4731 ± 2133	111 ± 19	41 ± 13	80 ± 24	52 ± 2
Cu	30	550	30	3	5644 ± 2051	109 ± 11	51 ± 13	77 ± 14	66 ± 10
Ni-Cu	20	550	60	2	1057 ± 573	90 ± 23	12 ± 6		
Ni-Cu	20	550	240	2	500	70	~7		
Cu-Ag	20	510	30	3	4200 ± 1358	77 ± 4	54 ± 16	90 ± 22	61 ± 10
2124	20	500	240	2	2955 ± 1021	50 ± 3	59 ± 21	74 ± 27	81 ± 6
2124	34	500	60	3	4300 ± 394	81 ± 7	54 ± 9	~100	54 ± 9

Table 3.6. Shear test data for bonded Al/Nic composite.

Inter-layer	Press MPa	Temp °C	Time mins	Def %	Max load N	Overlap mm^2	Shear strength MPa	Bonded area %	Specific shear strength MPa
	10	500	60	2	9300 ± 3370	70 ± 1	133 ± 47	73 ± 25	182 ± 4
	10	500	240	3	9940 ± 3430	72 ± 10	138 ± 38	75 ± 20	185 ± 10
	10	500	1200	5	10200 ± 2893	69 ± 4	149 ± 42	82 ± 22	182 ± 8
	20	500	30	8	11450 ± 2775	67 ± 2	170 ± 41	88 ± 20	193 ± 5
	10	460	240	2	5990 ± 2380	57 ± 6	104 ± 37	68 ± 24	153 ± 9
	10	400	240	1	3869 ± 800	65 ± 1	59 ± 12	48 ± 19	136 ± 39
	30	400	60	2	3308 ± 677	64 ± 2	52 ± 10		
Zn	10	500	240						
Cu-Ag	10	510	30	3	6800 ± 752	63 ± 5	108 ± 11	90 ± 6	120 ± 9

Table 3.7. Shear test data for bonded aluminium (2124) alloy.

Interlayer /Sample	Press MPa	Temp °C	Time mins	Def %	Max load N	Overlap mm^2	Shear strength MPa
25 SiC	10	500	240	2	2775 ± 527	49 ± 11	58 ± 9
30 SiC	10	500	240	2	2750 ± 414	69 ± 16	43 ± 14
35 SiC	10	500	240	2	1425 ± 742	63 ± 11	22 ± 10
40 SiC	10	500	240	2	2313 ± 862	65 ± 8	36 ± 14
25 SiC	10	500	240	8	3538 ± 629	72 ± 5	49 ± 9
25 SiC	12	500	240	13	3700 ± 1500	83 ± 20	46 ± 22
25 SiC	12	500	240	19	7767 ± 930	65 ± 7	119 ± 4
Ag-Cu/35 SiC	4	510	30	3	7238 ± 1539	75 ± 9	99 ± 32
Ag-Cu/35 SiC	8	510	30	6	11075 ± 4735	63 ± 17	193 ± 91
2124/30 SiC	10	500	240	2	6525 ± 2668	60 ± 8	111 ± 46

Table 3.8. Shear test data for bonded 2124/P composite.

Interlayer	Press MPa	Temp °C	Time mins	Def %	Max load N	Overlap mm^2	Shear strength MPa	Bonded area %	Specific shear strength MPa
2124-Al	10	500	240	2	3844 ± 417	58 ± 6	67 ± 9	92 ± 11	73 ± 2
Al-2124P*	10	500	240	3	4163 ± 806	75 ± 8	55 ± 7	94 ± 12	59 ± 2
2124-Al/Nic	10	500	240	2	4794 ± 647	63 ± 4	76 ± 11	94 ± 11	81 ± 6
2124-2124P#	10	500	240	2	9175 ± 1156	70 ± 9	132 ± 3		
Al/Nic-2124P+	10	500	240	2	5638 ± 914	75 ± 11	75 ± 10	~100	75 ± 10

*25 vol%
+35 vol%
#40 vol%

Table 3.9. Shear test data for dissimilar materials bonded without an interlayer.

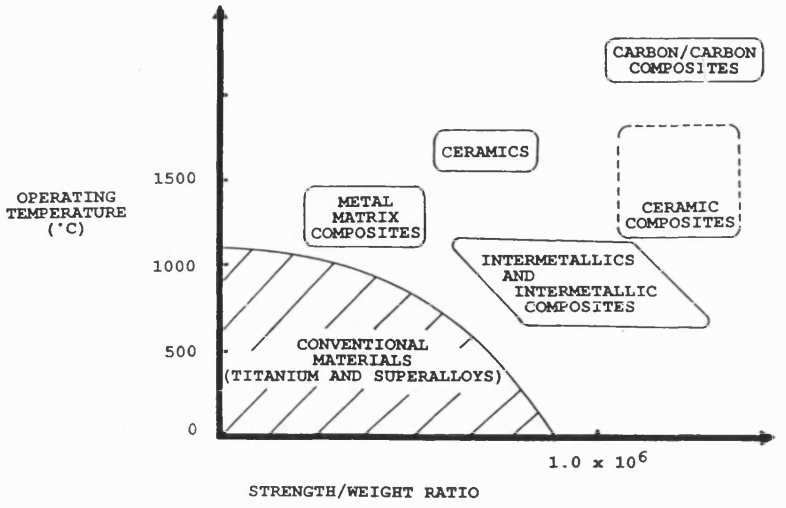

Fig. 1.1. Performance map of various high-temperature engine materials in terms of operating temperature (°C) and strength/weight ratio, [after Taya and Arsenault,9].

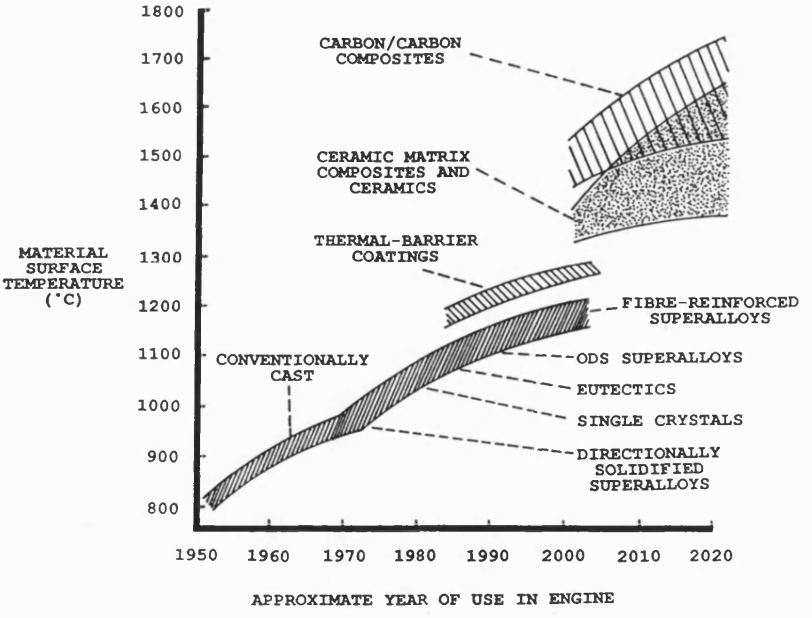

Fig. 1.2. Trends of turbine engine materials [9].

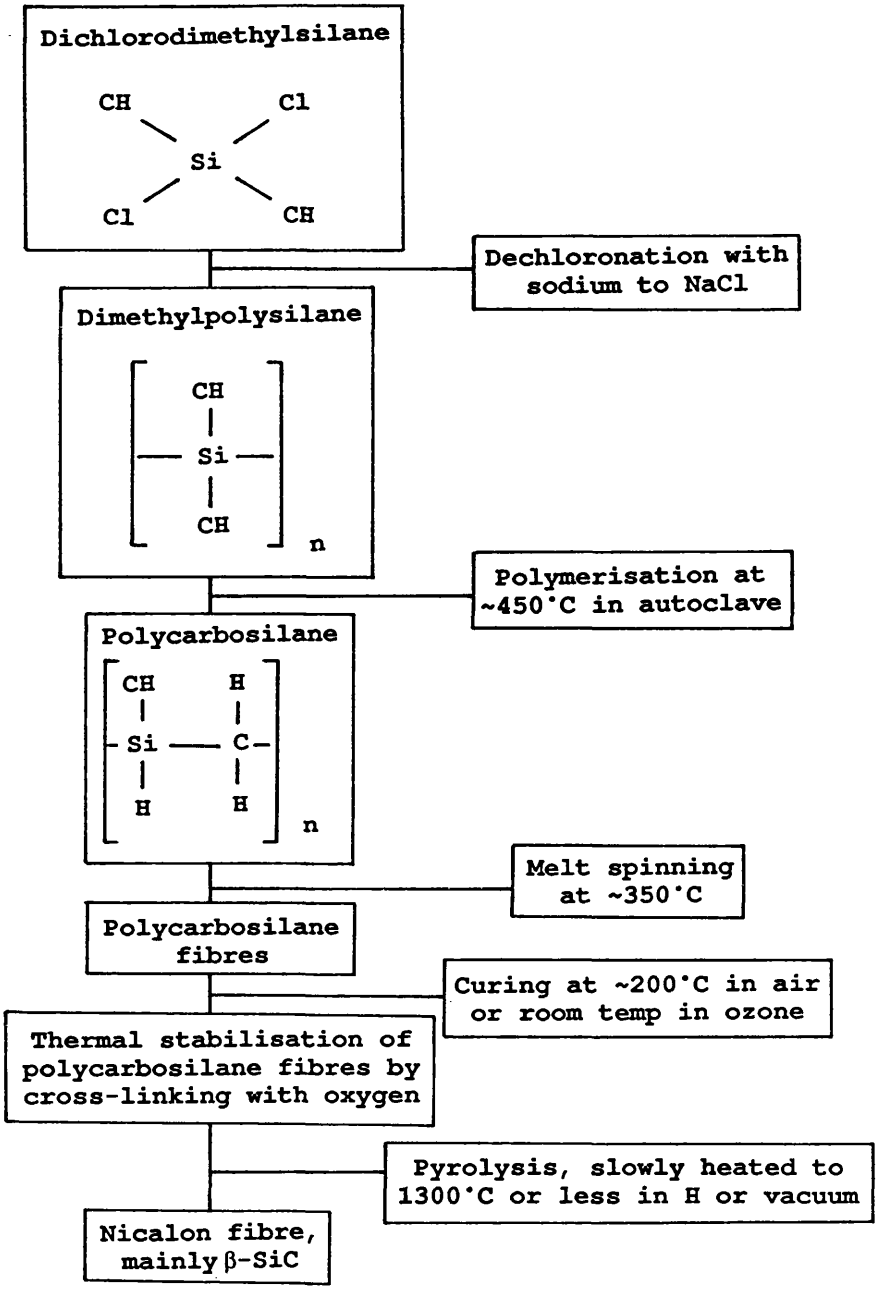

Fig. 1.3. Fabrication route for Nicalon fibres [29].

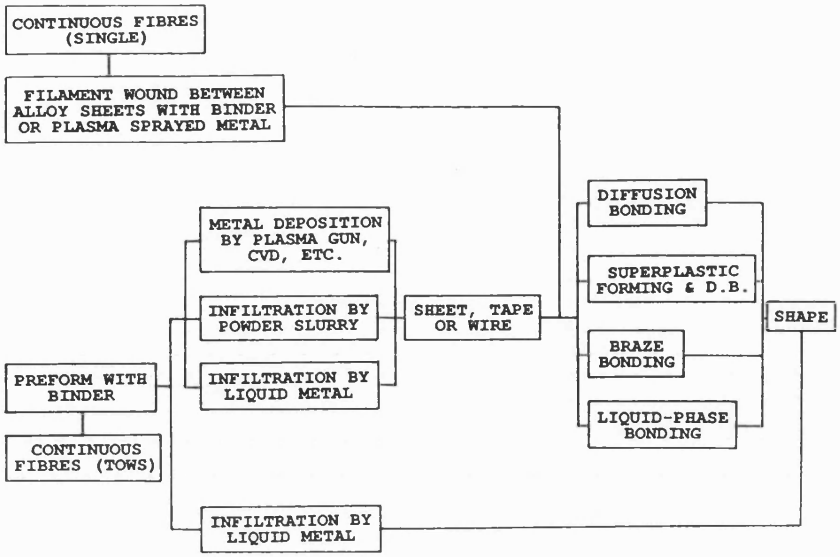

Fig. 1.4a. Process routes for production of continuous fibre reinforced composites [16].

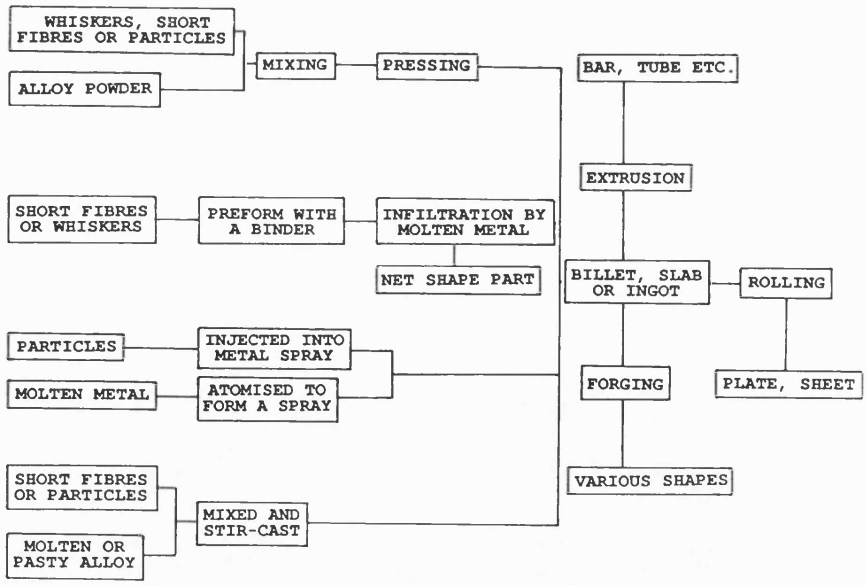

Fig. 1.4b. Process routes for production of discontinuous fibre or particulate composites [16].

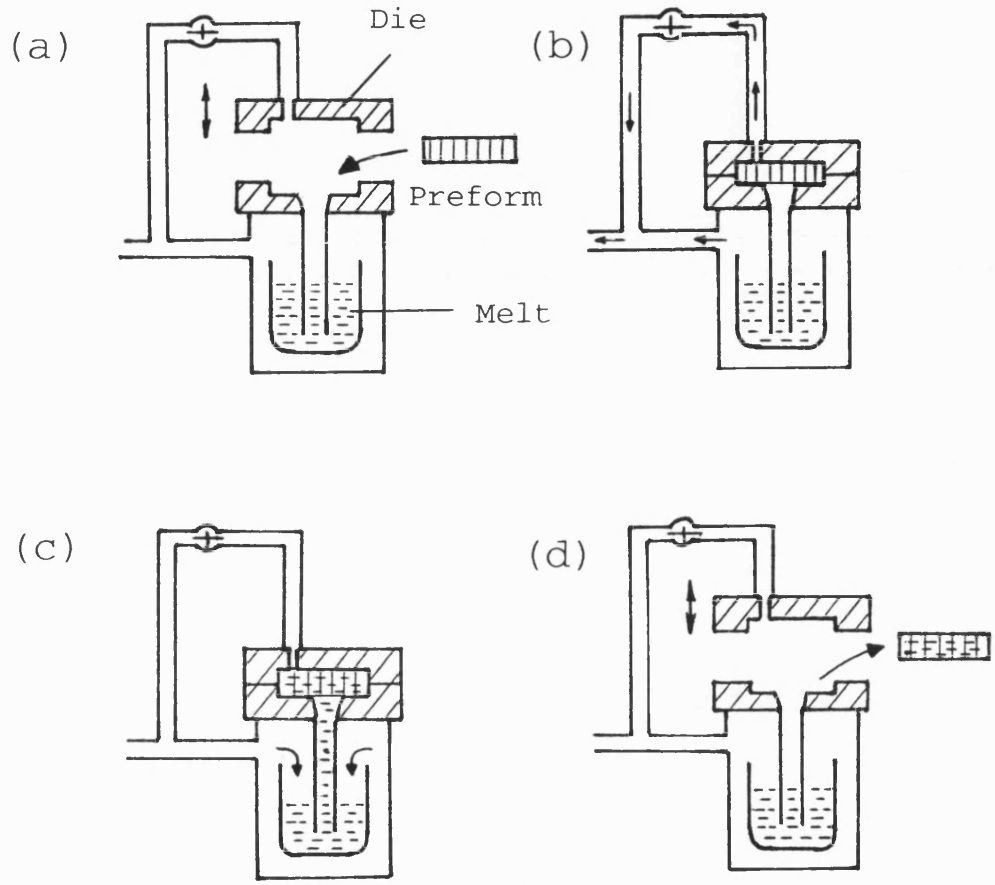

Fig. 1.5. The liquid metal infiltration process [51].
a. Preform placement.
b. Evacuation.
c. Pressurisation and infiltration.
d. Ejection.

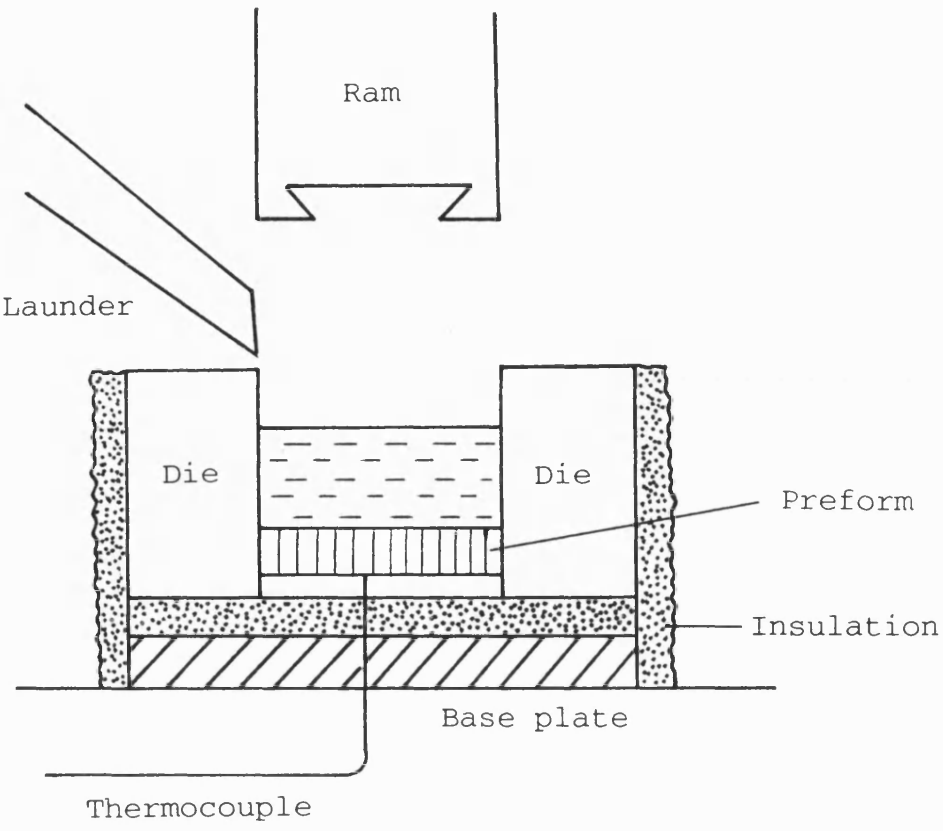

Fig. 1.6. Schematic diagram of squeeze casting apparatus; the die is heated by electric cartridge heaters [55].

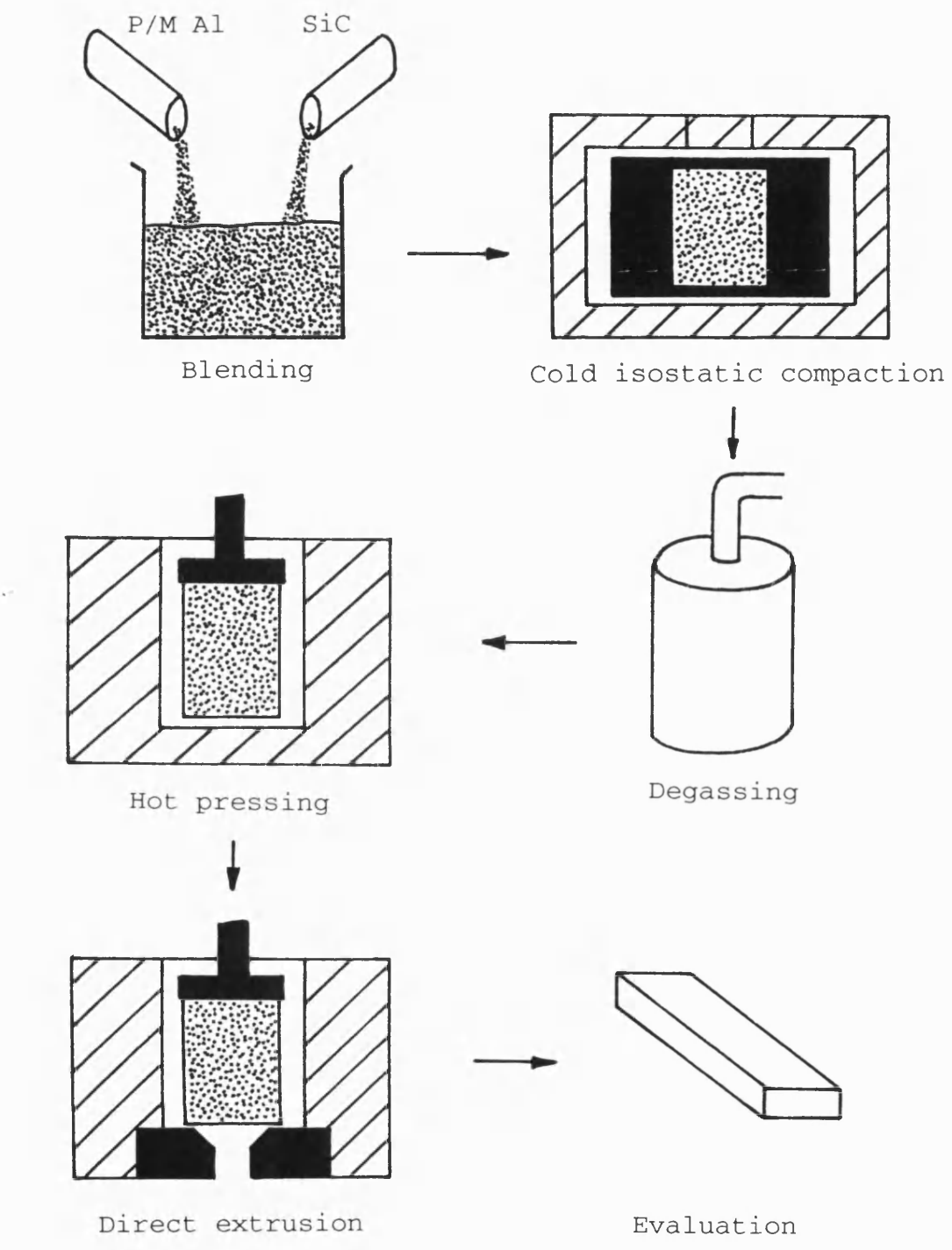

Fig. 1.7. The powder metallurgy/extrusion route for MMC components [12].

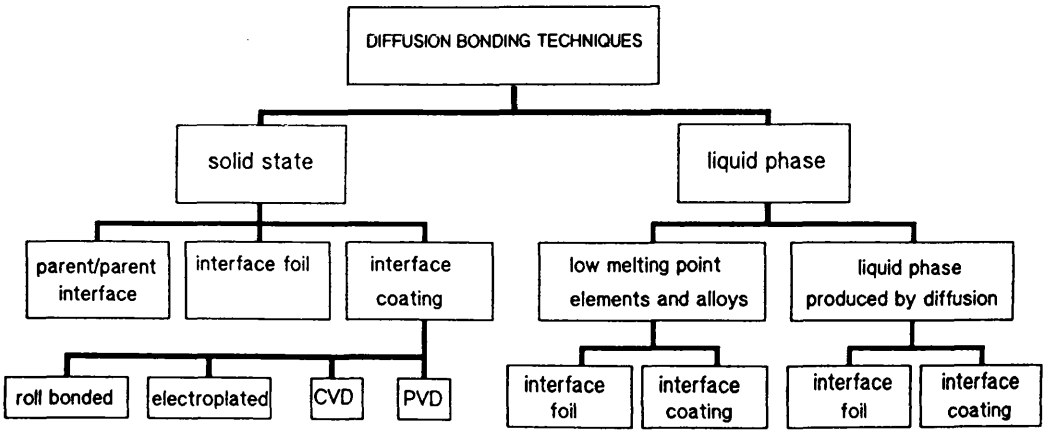

Fig. 1.8. Summary of solid-state and liquid-phase diffusion bonding techniques [115].

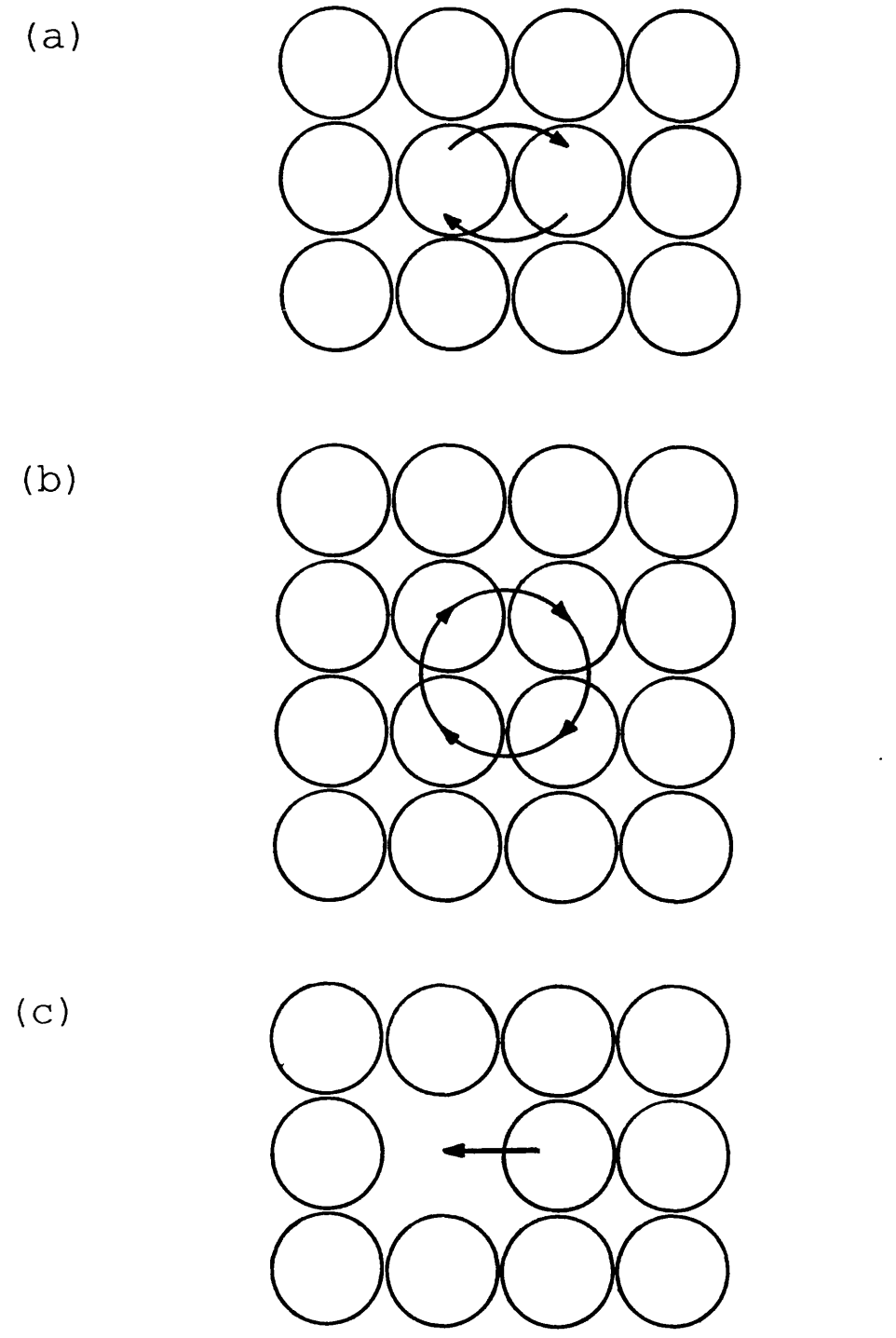

Fig. 1.9. Mechanisms for diffusion in metals [101].
a. Direct interchange of atoms.
b. Zener ring method.
c. Movement of vacancies.

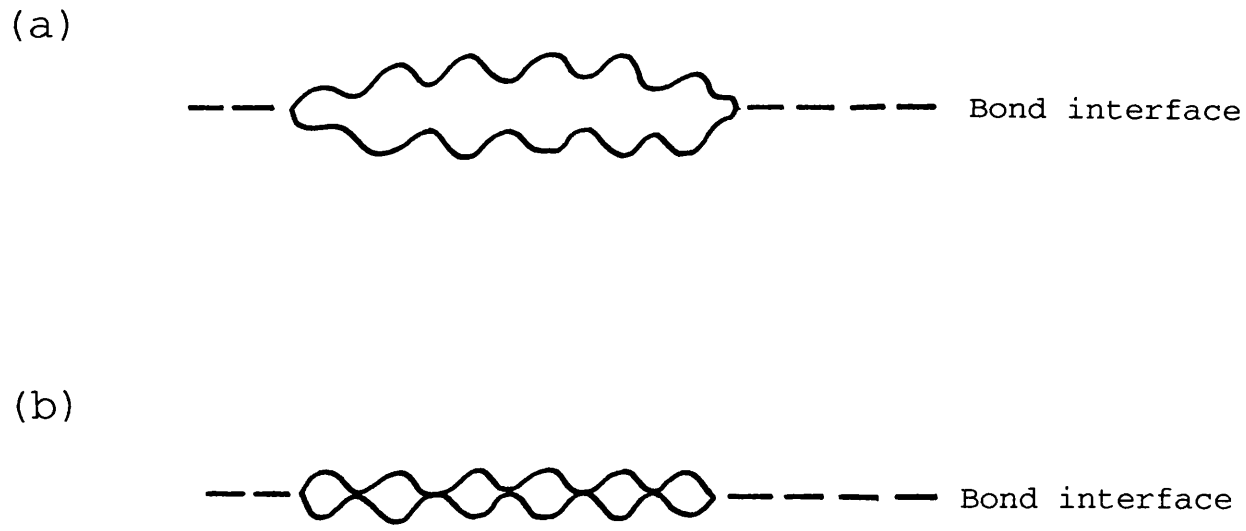

Fig. 1.10. Development of joint interface in solid-state diffusion bonding [93].
a. Stage I, plastic deformation of asperities.
b. Stage II, shrinkage of voids via diffusion.

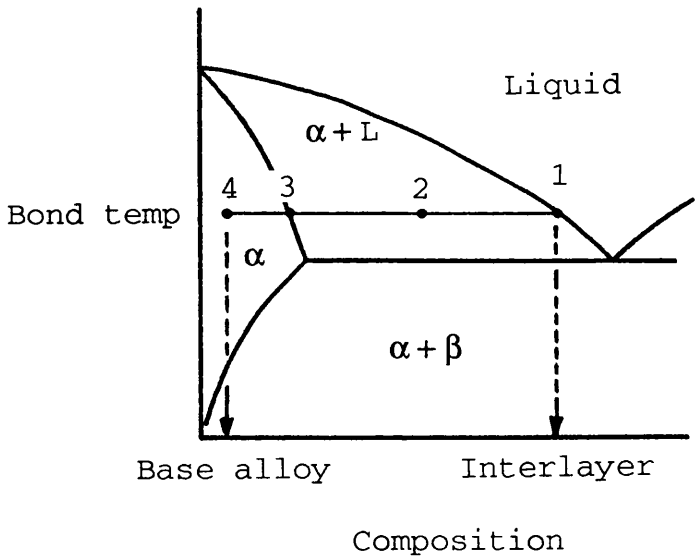

Fig. 1.11. Theoretical model of transient liquid phase bonding using an interlayer; melting of the interlayer with base alloy (1), isothermal solidification (1 to 3), homogenisation of joint region (3 to 4) [93].

(a)

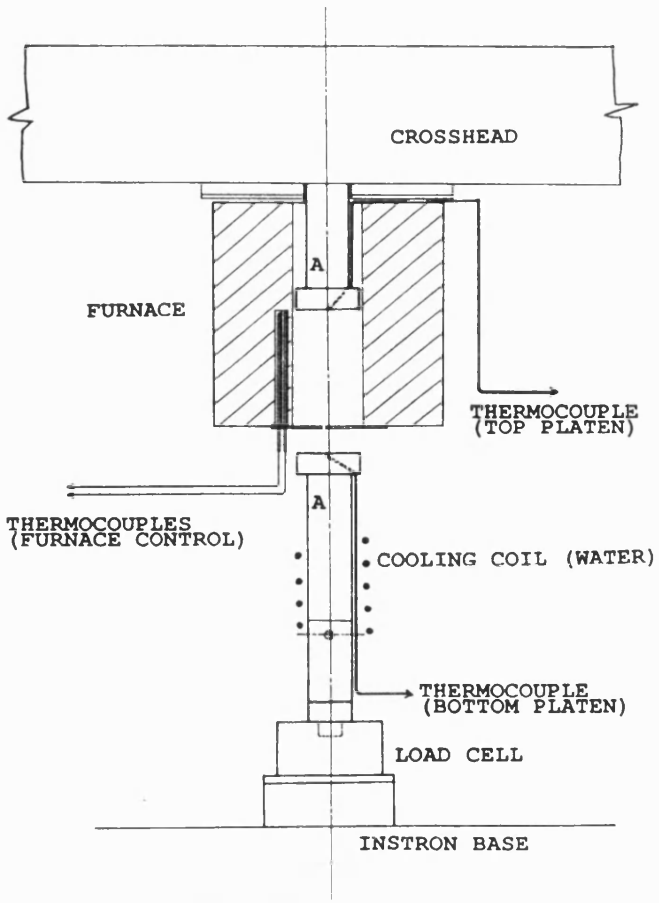

(b)

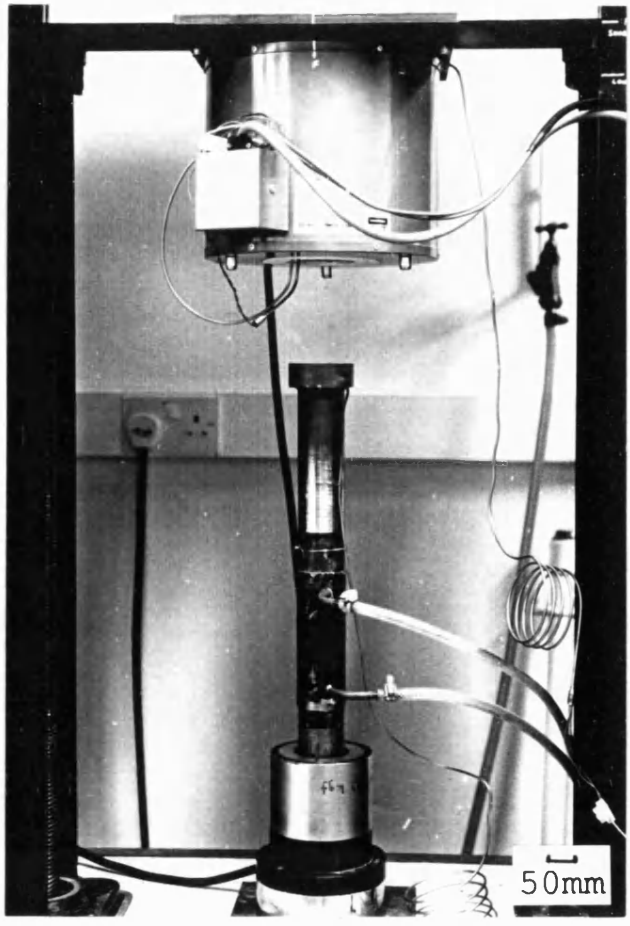

Fig. 2.1. Diffusion bonding rig,
a. Schematic diagram; components labelled A made in stainless steel.
b. Photograph.

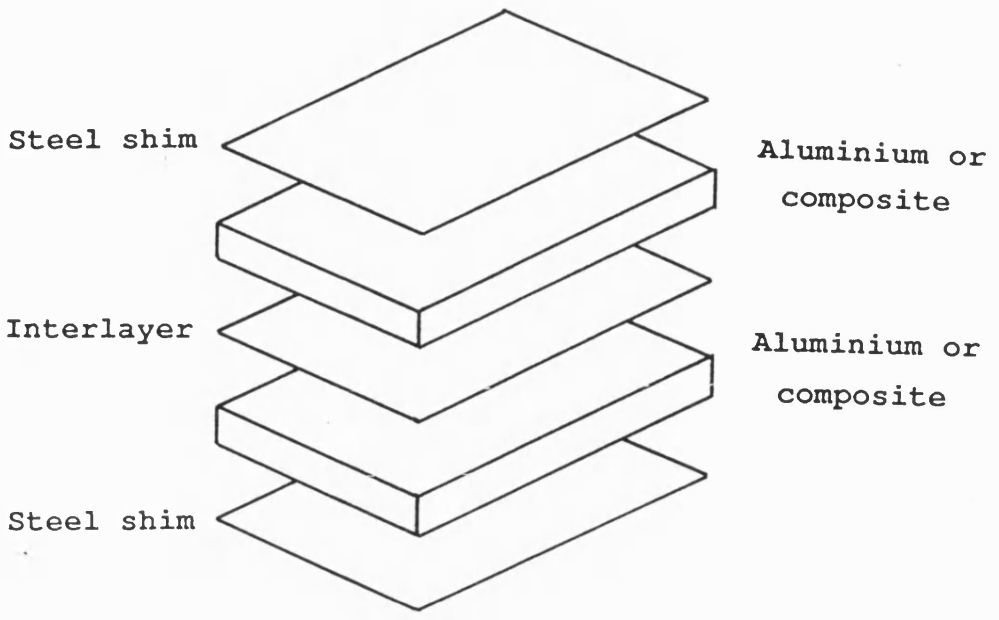

Fig. 2.2. Configuration of specimens for bonding.

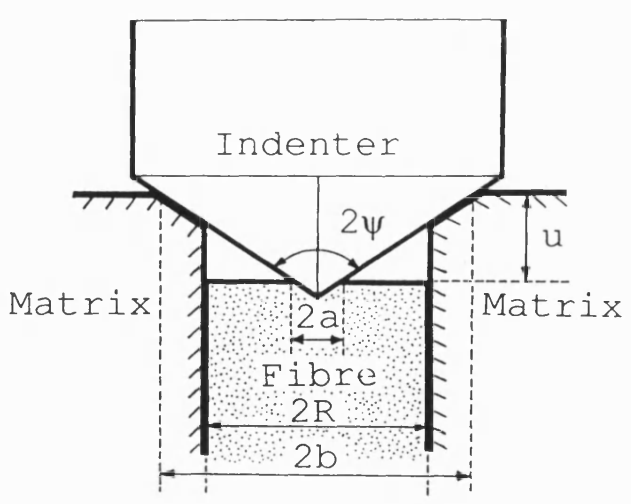

Fig. 2.3. Indent method for determining fibre/matrix interfacial friction strength [130].

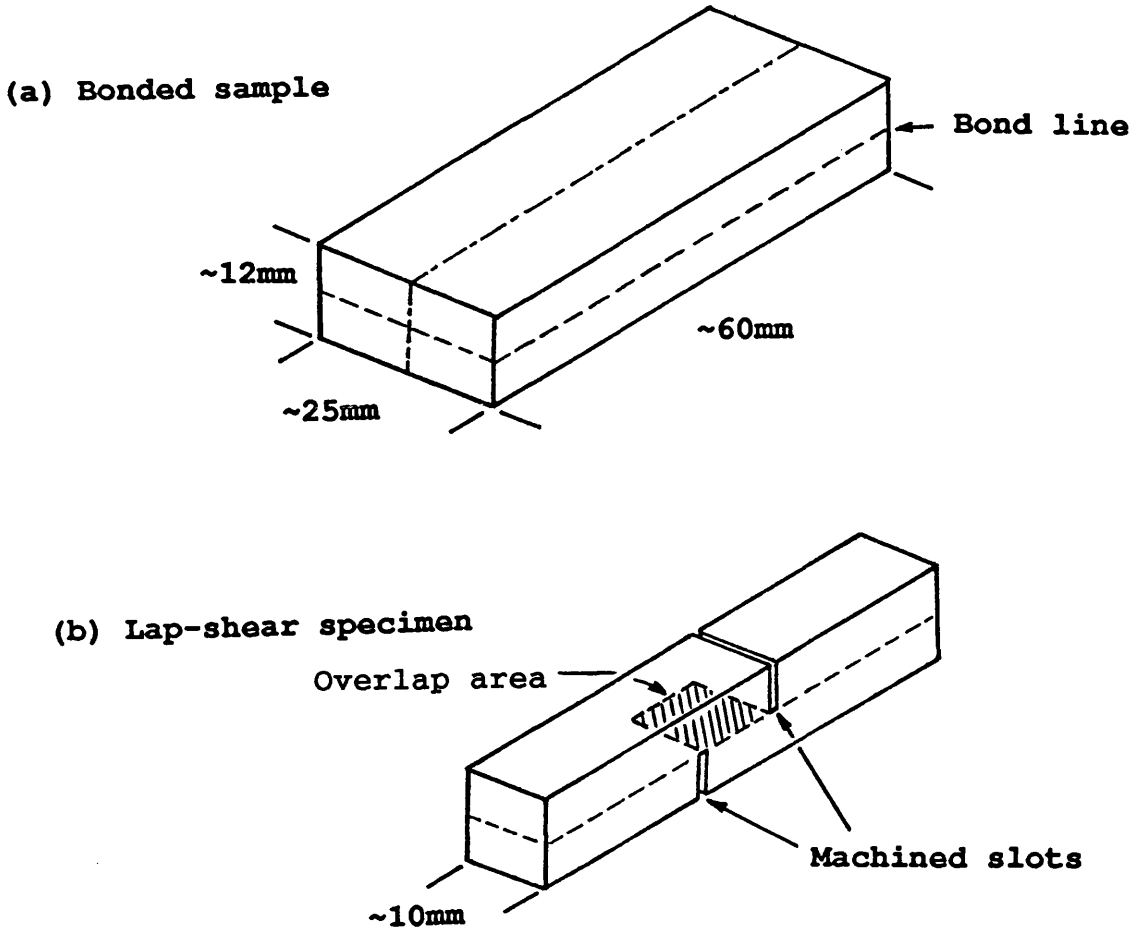

Fig. 2.4. Preparation and testing geometry of lap-shear specimens.

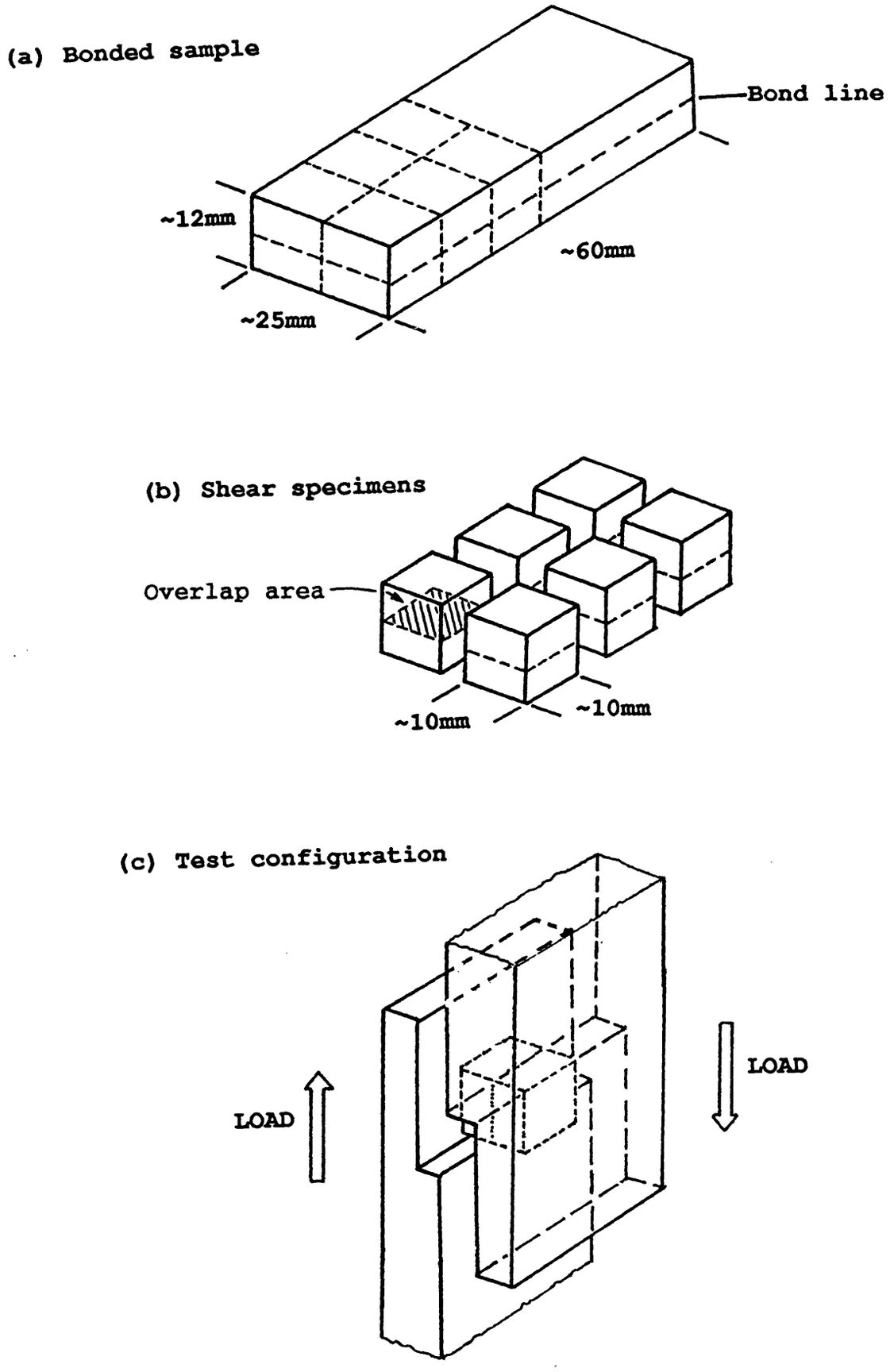

Fig. 2.5. Preparation and testing geometry of specimens for the modified shear jig.

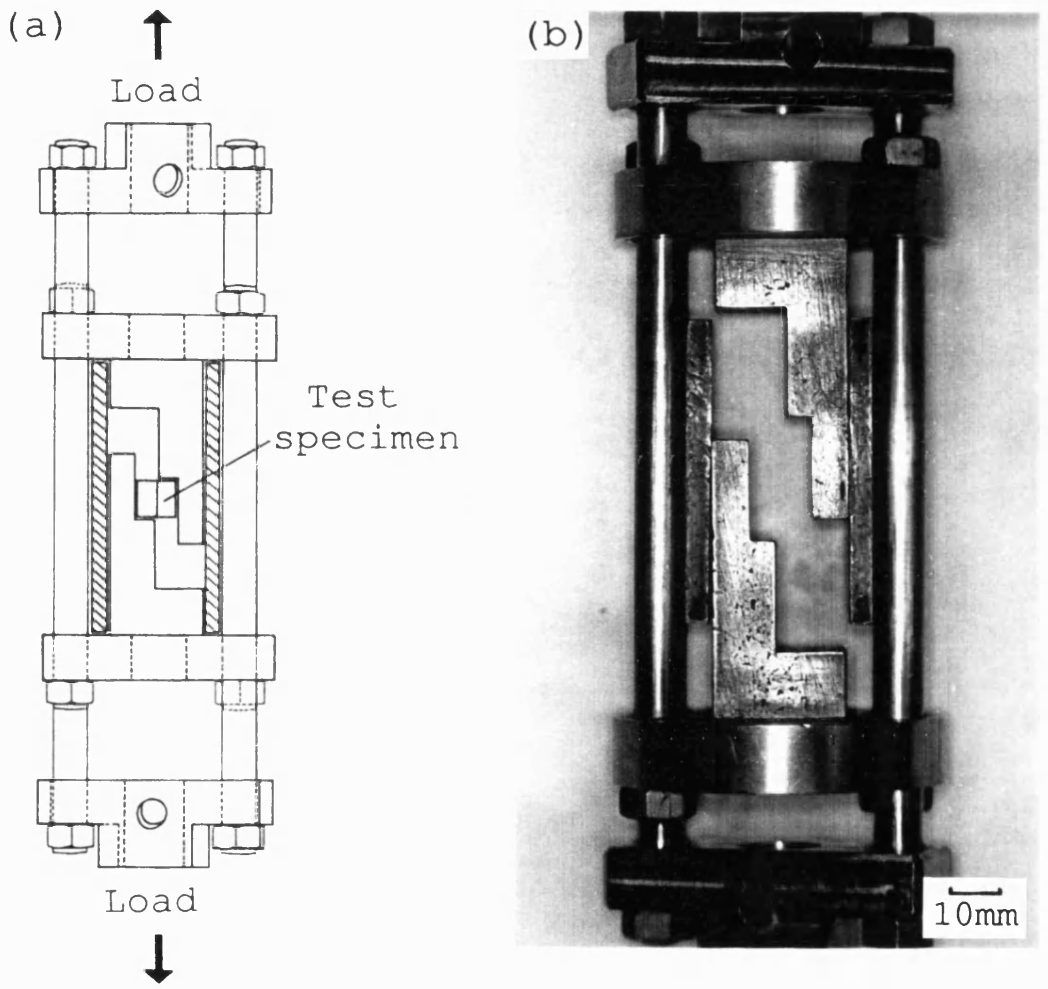

Fig. 2.6. The modified shear jig
a. Scale drawing.
b. Photograph.

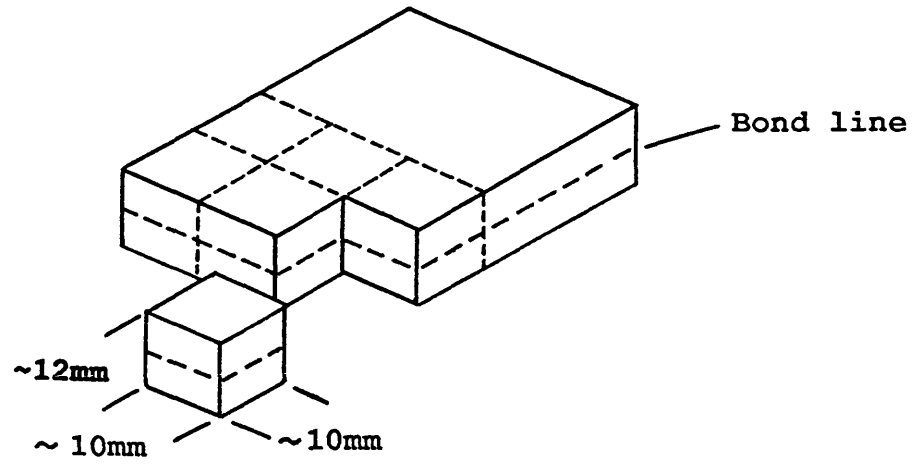

Fig. 2.7. Extraction of specimens from bonded joints for metallographic preparation.

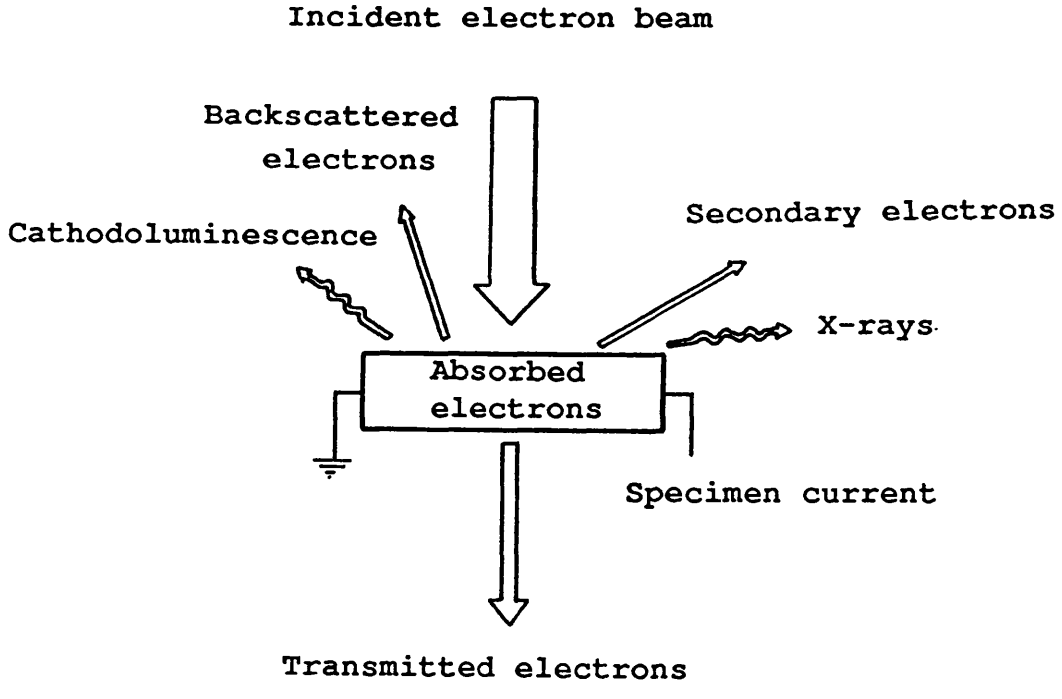

Fig. 2.8. Schematic diagram showing electron/specimen interactions.

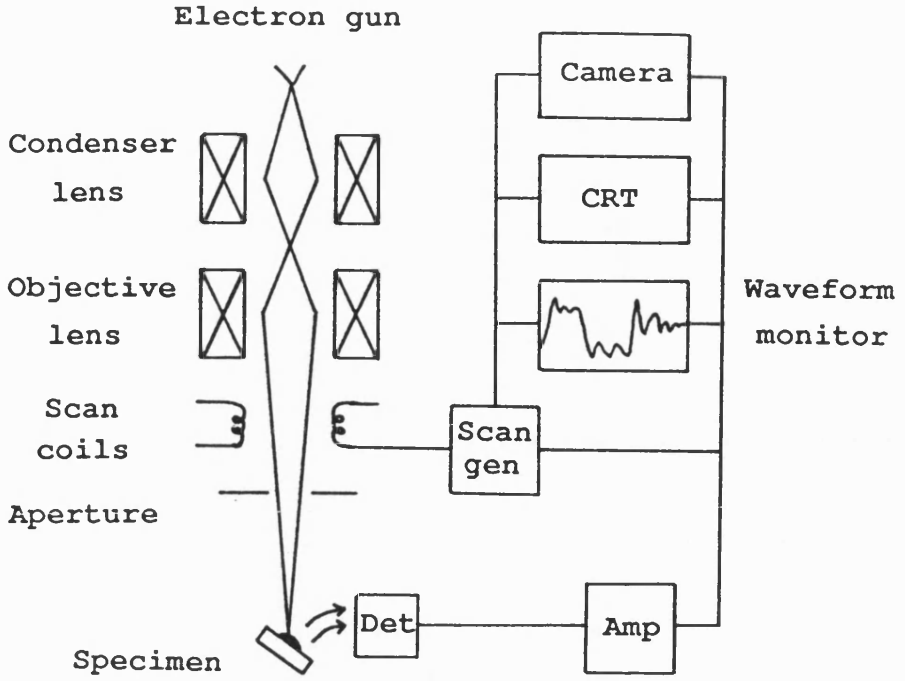

Fig. 2.9. Schematic diagram of the scanning electron microscope (SEM).

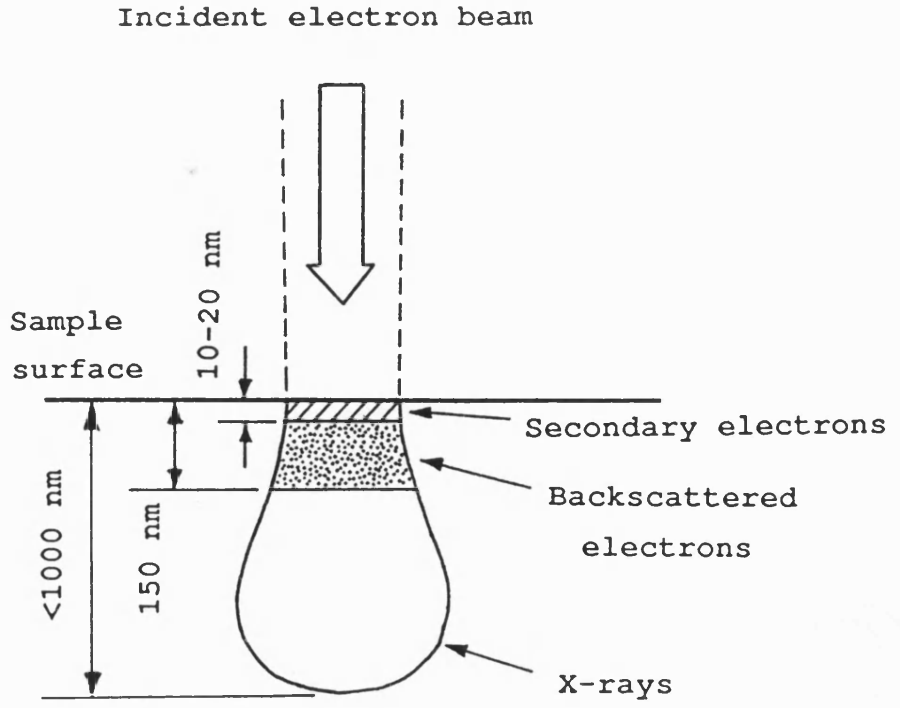

Fig. 2.10. Schematic diagram showing the extent of generation zones for electrons and x-rays.

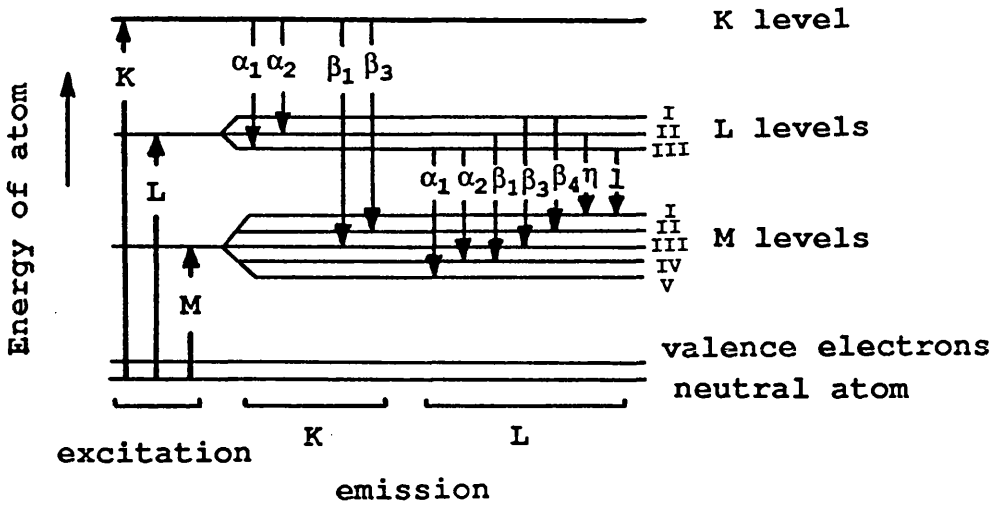

Fig. 2.11. Common x-ray emission lines with their designation for an element with atomic number Z, where $29<Z<37$ [134].

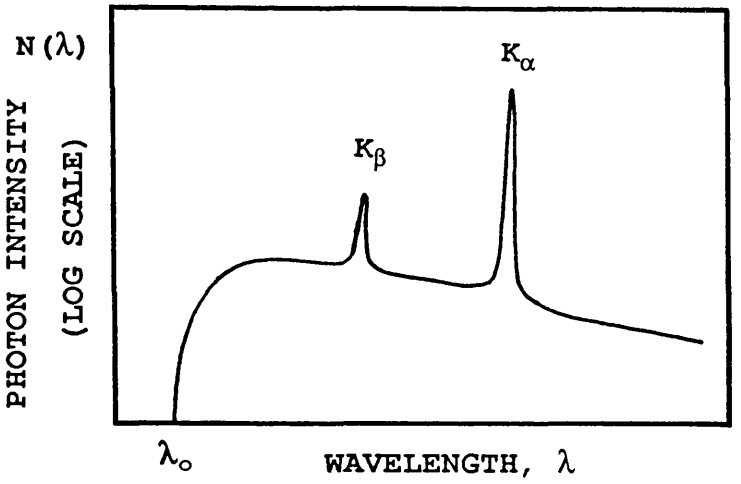

Fig. 2.12. Schematic diagram showing the x-ray emission of a specimen bombarded with an electron beam.

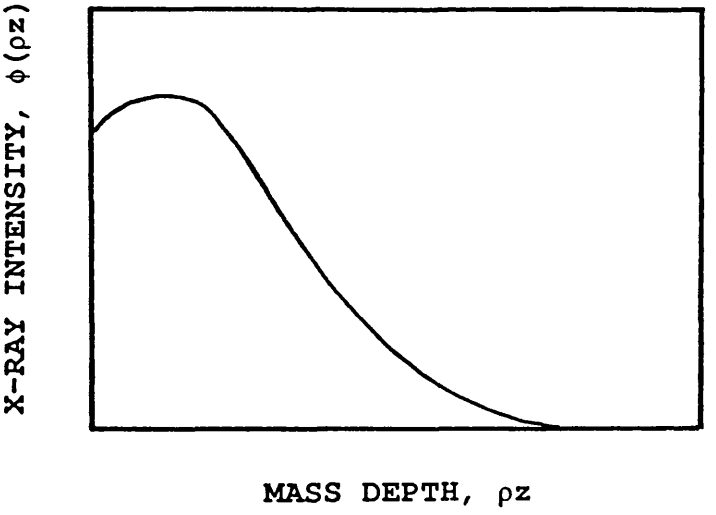

Fig. 2.13. Schematic curve showing the variation of x-ray intensity with mass depth in the target.

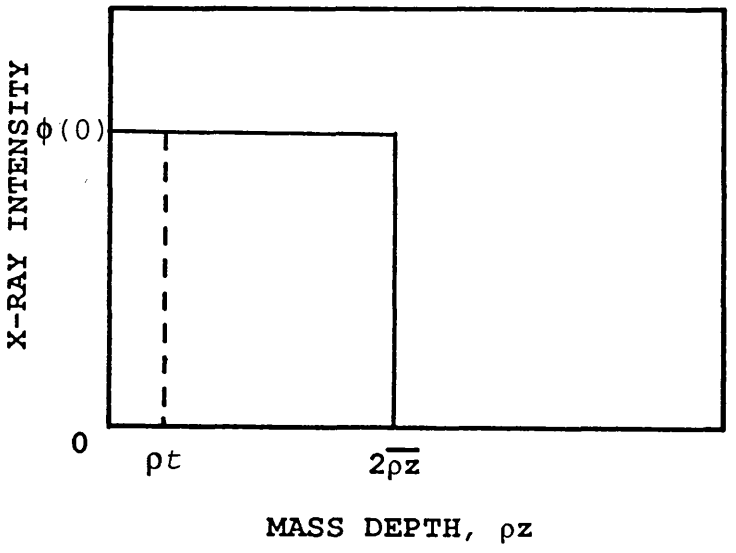

Fig. 2.14. Rectangular $\phi(\rho z)$ approximation for thin film analysis.

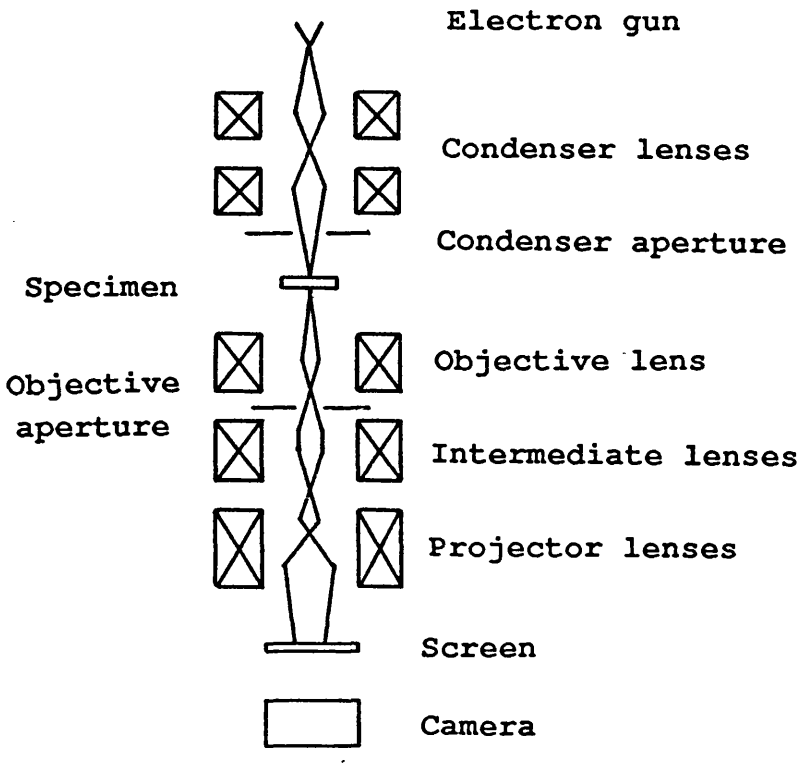

Fig. 2.15. Schematic diagram of the transmission electron microscope (TEM).

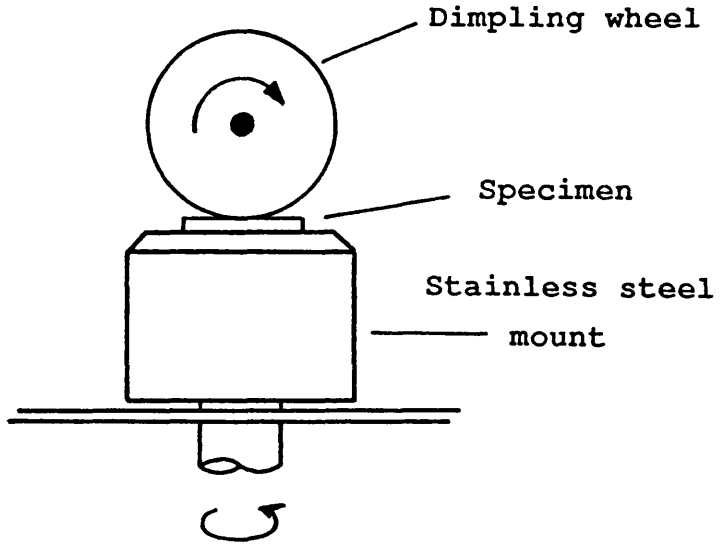

Fig. 2.16. 'Dimpling' stage for TEM sample preparation.

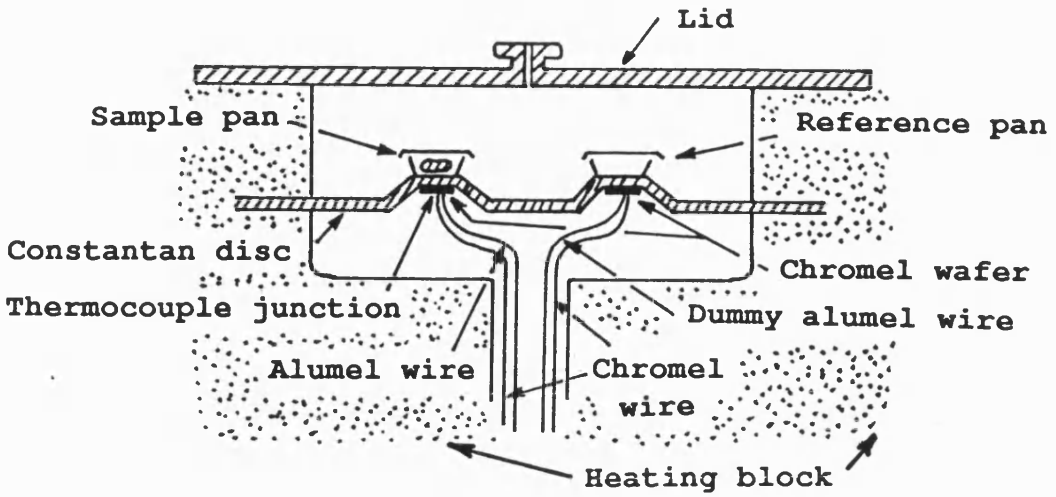

Fig. 2.17. Diagram of the differential scanning calorimeter (DSC) cell.

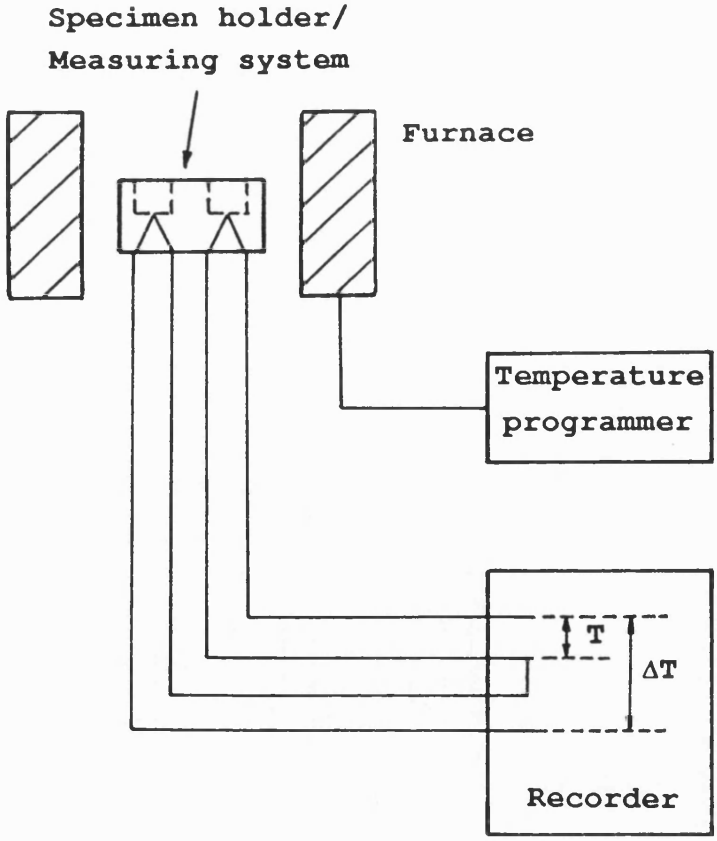

Fig. 2.18. Schematic diagram of the DSC.

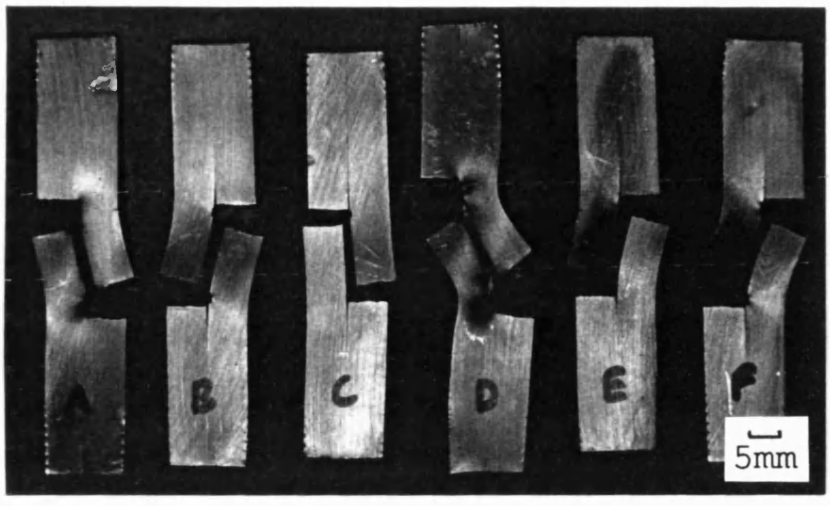

Fig. 3.1. Failed lap-shear test specimens.

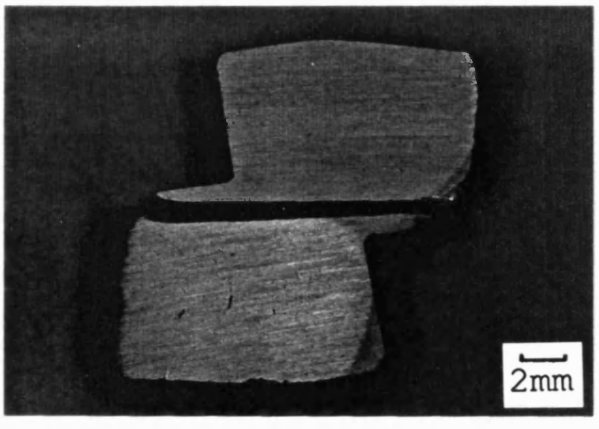

Fig. 3.2. Failed specimen tested using modified shear jig.

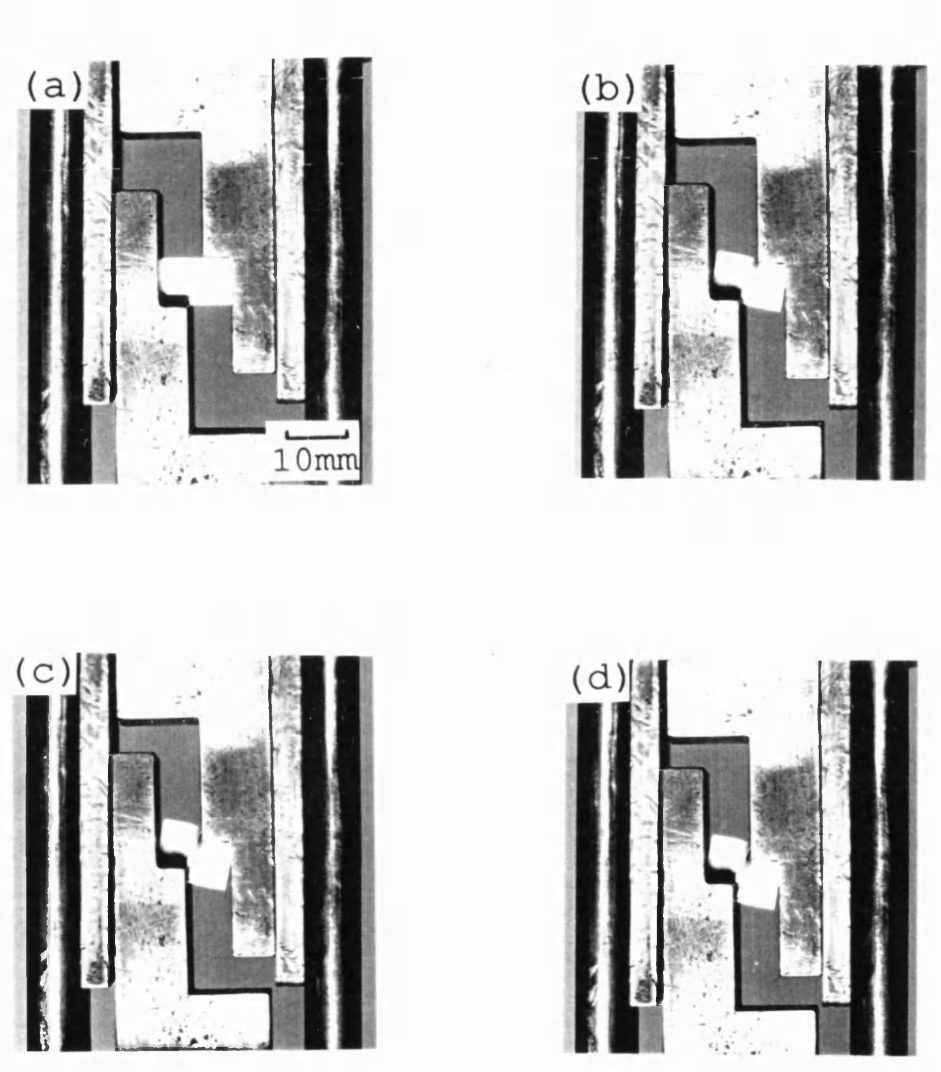

Fig. 3.3 Shear testing of an aluminium alloy using the modified technique.

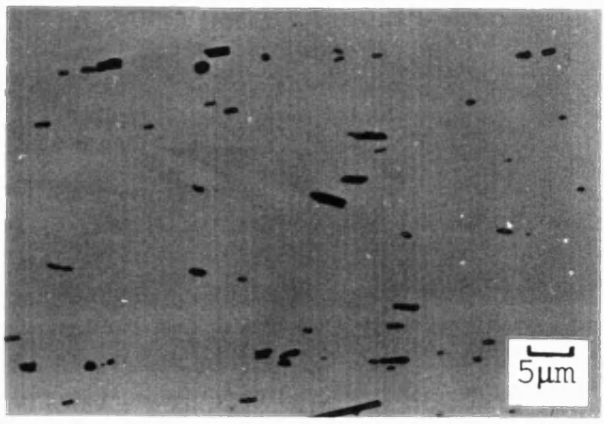

Fig. 3.4. Impurities in commercial-purity aluminium, OM.

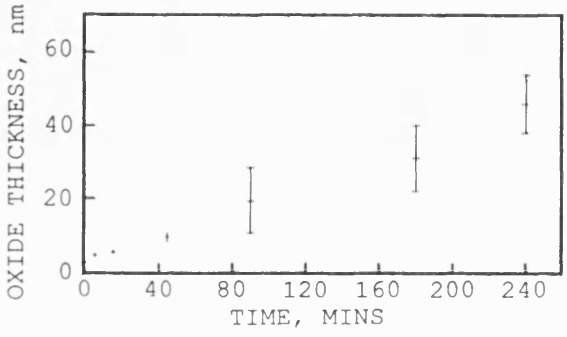

Fig. 3.5. Effect of time on the oxide thickness on aluminium heated in air at 500°C.

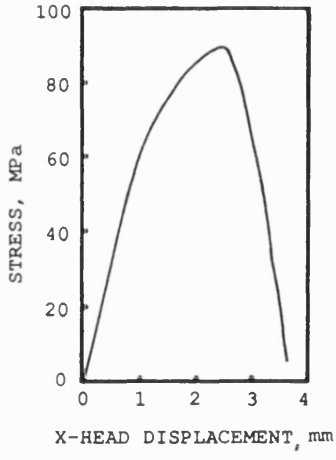

Fig. 3.6. Shear test stress-displacement curve for as-received commercial-purity aluminium.

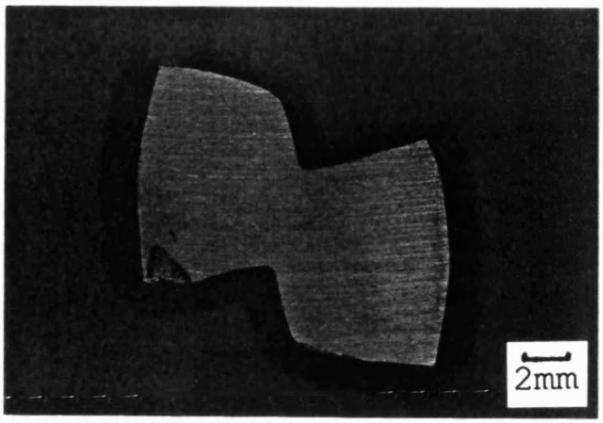

Fig. 3.7. Sheared aluminium test specimen.

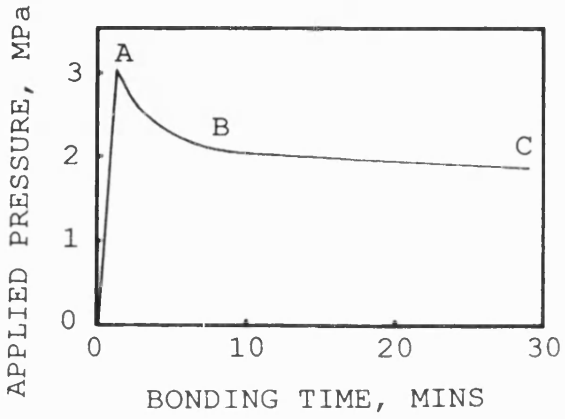

Fig. 3.8. Pressure-versus-time curve for aluminium bonded with a zinc interlayer, 3 MPa, 500°C.

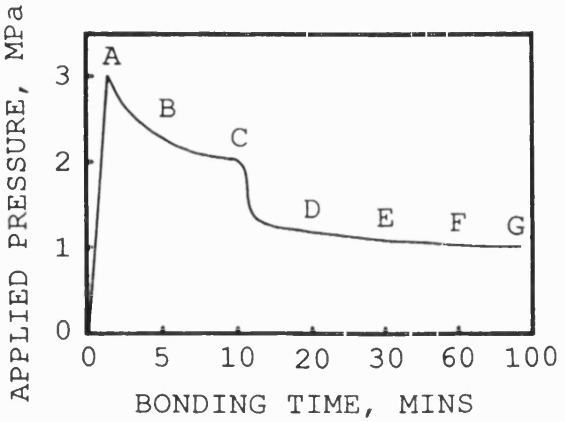

Fig. 3.9. Pressure-versus-time curve for aluminium bonded with a copper interlayer, 3 MPa, 550°C.

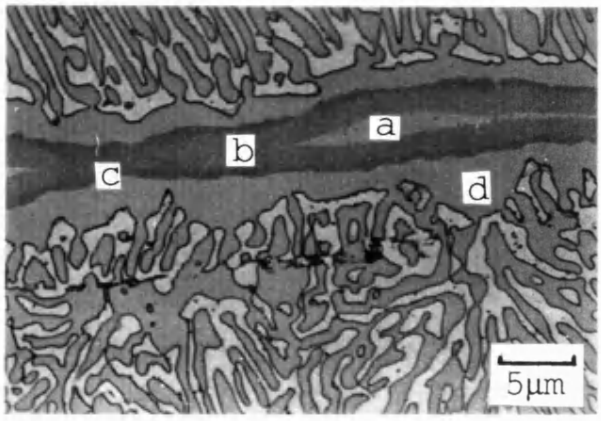

Fig. 3.10. Aluminium bonded with a copper interlayer, 3 MPa, 4 mins, ~550°C, OM, DIC.

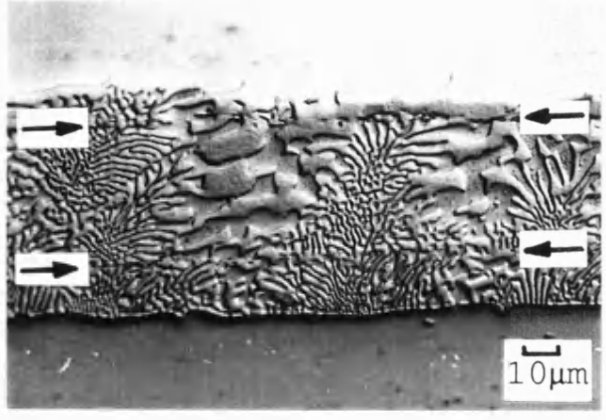

Fig. 3.11. Aluminium bonded with a copper interlayer, 3 MPa, 5 mins, ~550°C (sample B) OM, DIC; arrows mark residual aluminium-copper interfaces

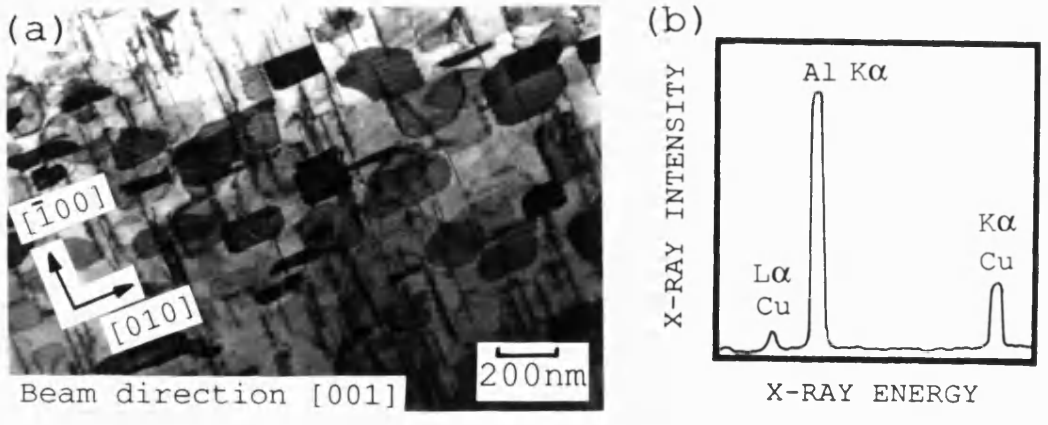

Fig. 3.12. Precipitates in the aluminium adjacent to the joint (sample B).
a. TEM micrograph.
b. EDS.

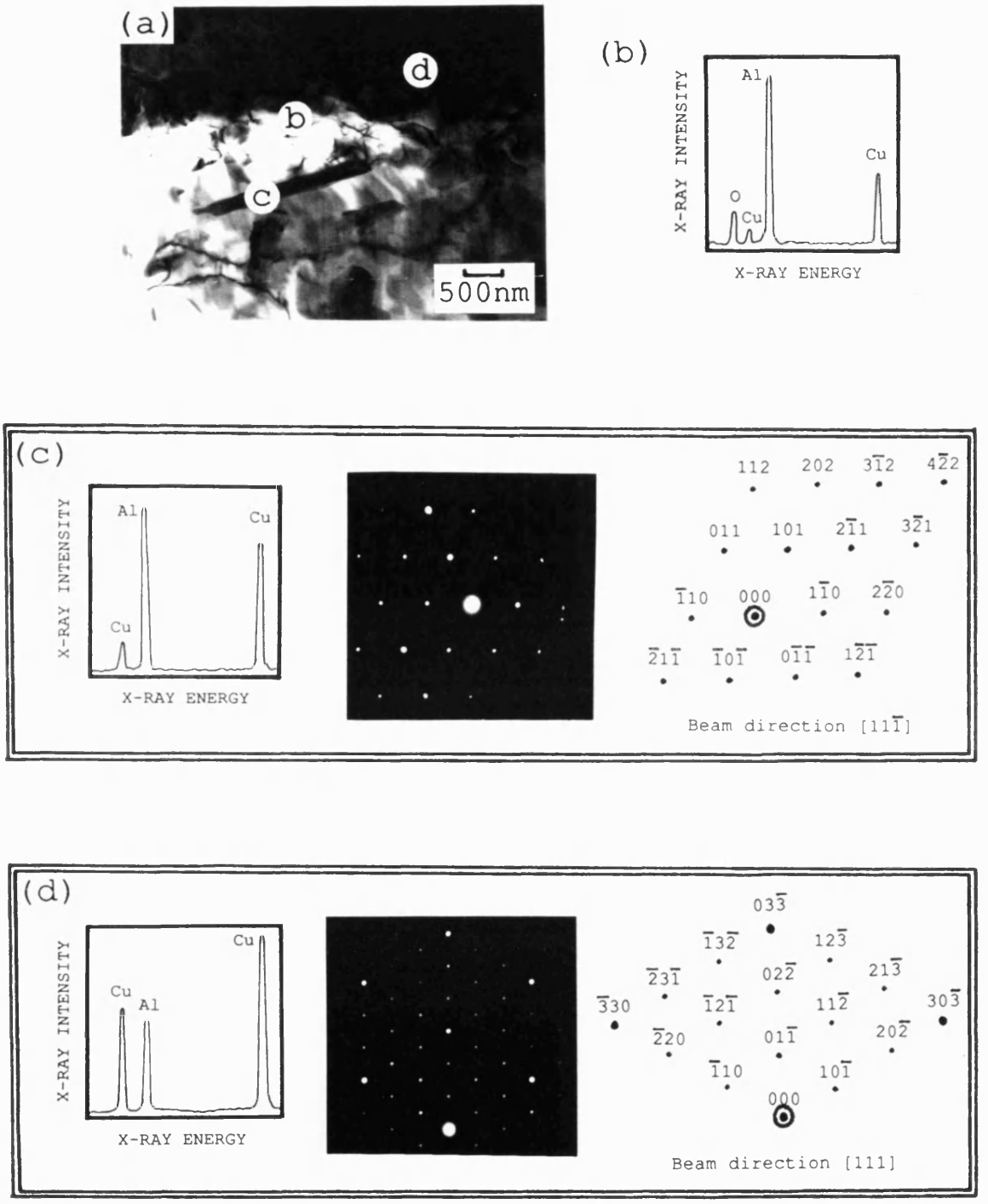

Fig. 3.13. Aluminium bonded with a copper interlayer, 3 MPa, 5 mins, 550°C (sample B).

a. Joint interface, TEM.
b. EDS of interface region.
c. EDS and diffraction data of phase in aluminium.
d. EDS and diffraction data of phase in joint.

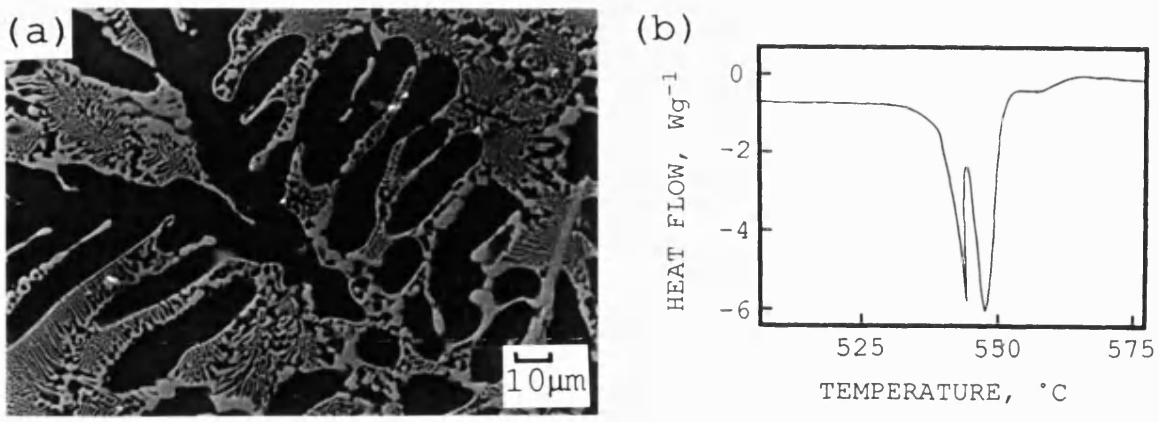

Fig. 3.14. Aluminium bonded with a copper interlayer, 3 MPa, 10 mins, 550°C (sample C) expelled bead.
a. Solidified microstructure, BEI.
b. DSC curve.

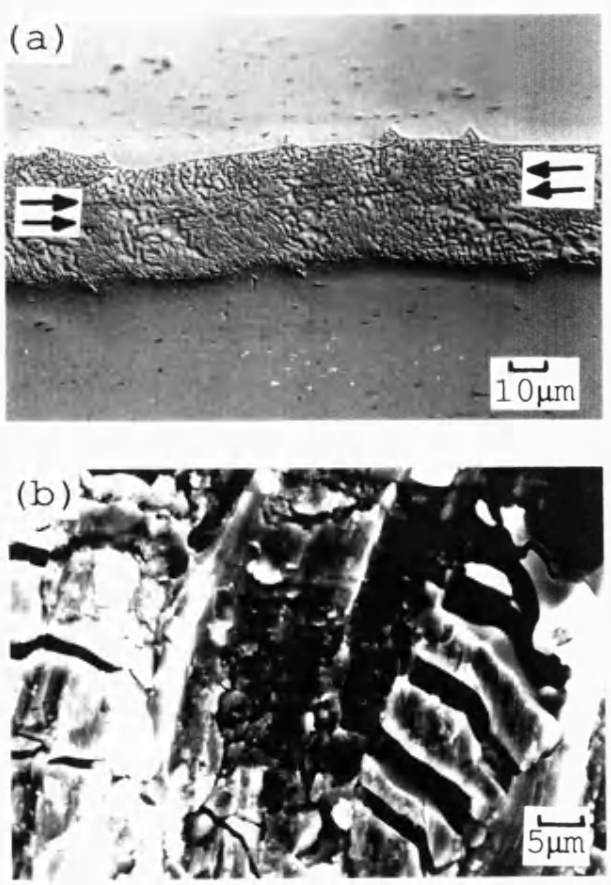

Fig. 3.15. Aluminium bonded with a copper interlayer, 3 MPa, 10 mins, 550°C (sample C).
a. Section of joint, OM, DIC; arrows mark residual aluminium-copper interfaces.
b. Fracture surface, SEI.

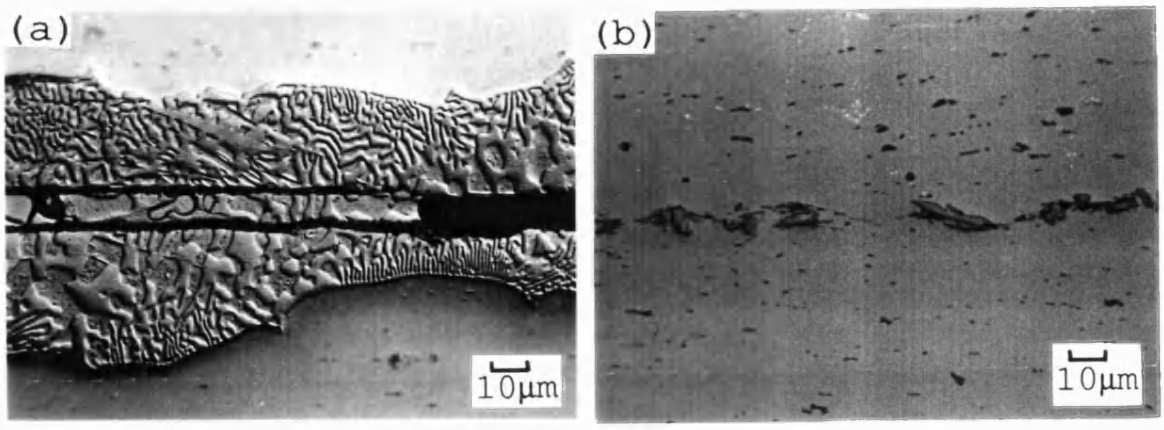

Fig. 3.16. Aluminium bonded with a copper interlayer, 3 MPa, 20 mins, 550°C (sample D).
a. Periphery of joint, OM, DIC.
b. Centre of joint, OM, DIC.

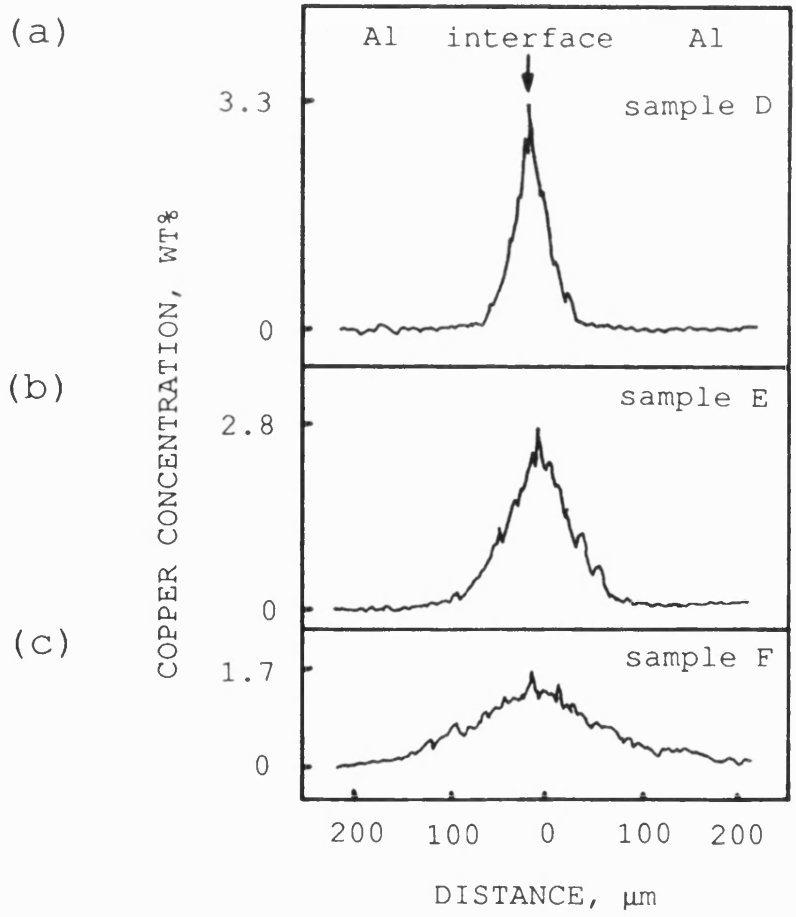

Fig. 3.17. Aluminium bonded with a copper interlayer, 3 MPa, 550°C, copper concentration profiles.
a. 20 mins (sample D).
b. 30 mins (sample E).
c. 60 mins (sample F).

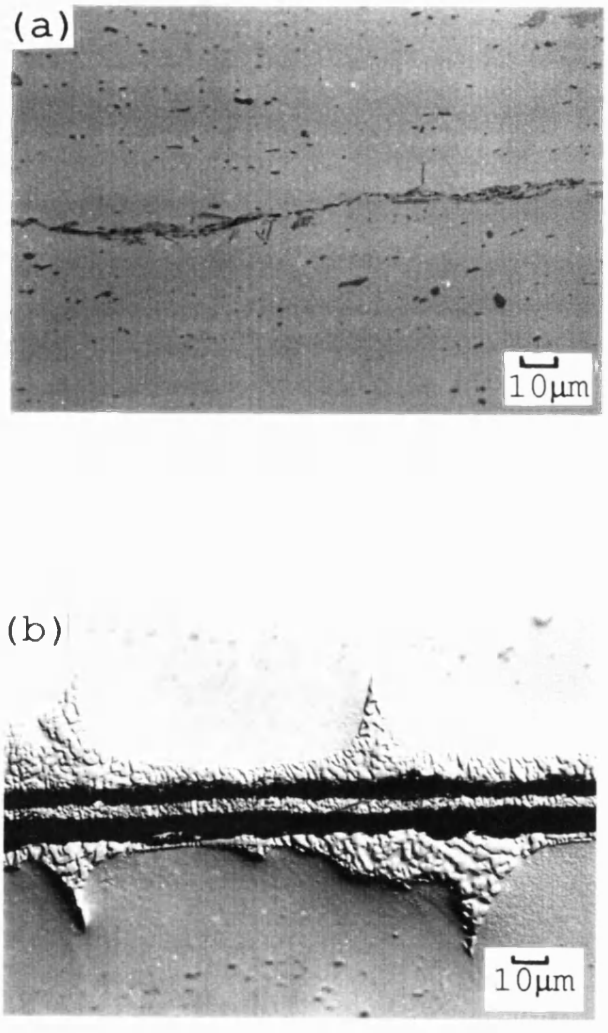

Fig. 3.18. Aluminium bonded with a copper interlayer, 3 MPa, 60 mins, 550°C (sample F).
a. Centre of joint, OM, DIC.
b. Periphery of joint, OM, DIC.

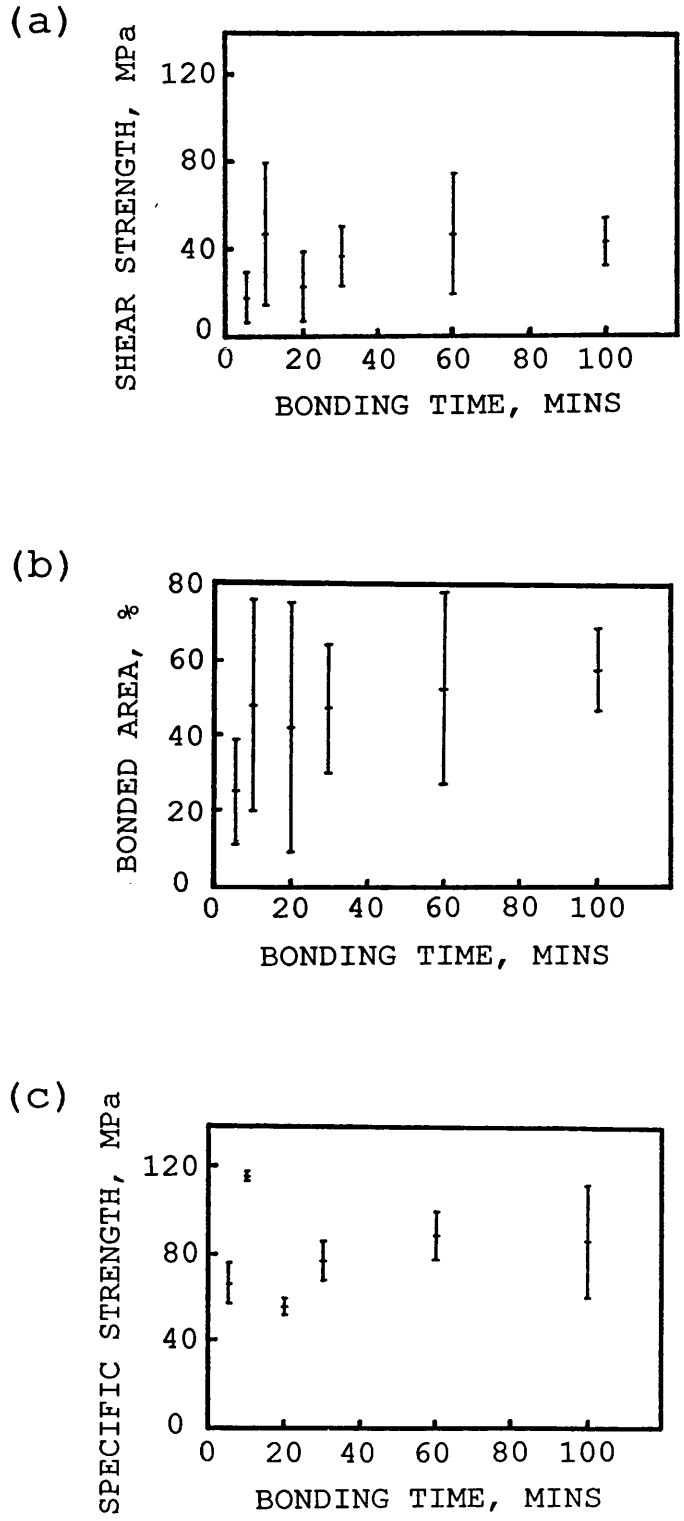

Fig. 3.19. Effect of bonding time on mechanical properties for aluminium-copper joints, 3 MPa, 550°C.
a. Shear strength.
b. Bonded area.
c. Specific strength.

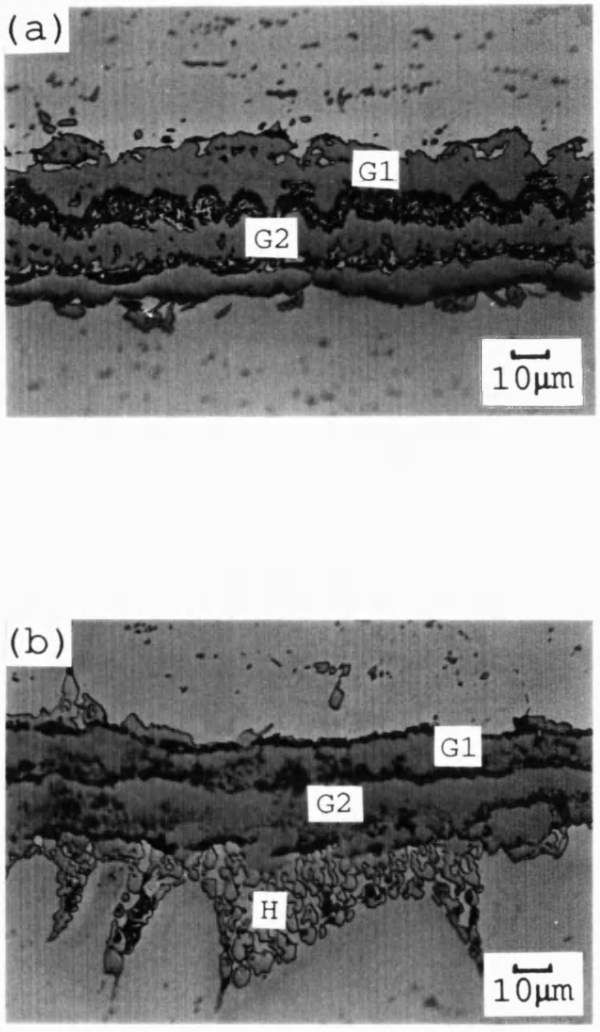

Fig. 3.20. Aluminium bonded with a nickel-coated copper interlayer, 10 MPa, 60 mins, 550°C.
a. Section of joint, OM, DIC.
b. Formation of liquid (labelled H) OM, DIC.

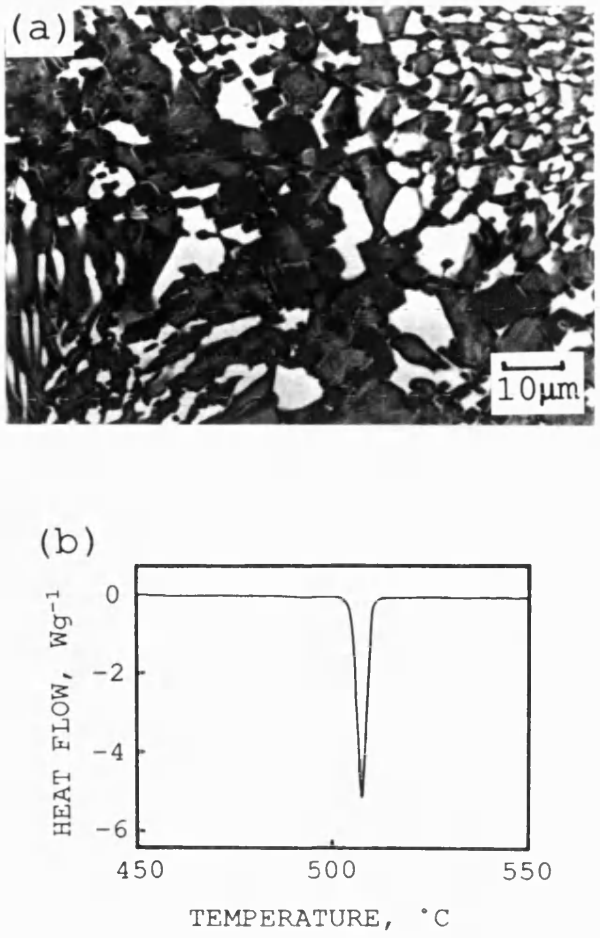

Fig. 3.21. Aluminium bonded with a copper-silver alloy interlayer, 3 MPa, 30 mins, 510°C.
a. Expelled bead, BEI.
b. DSC curve of bead.
c. Section of joint, OM, DIC.

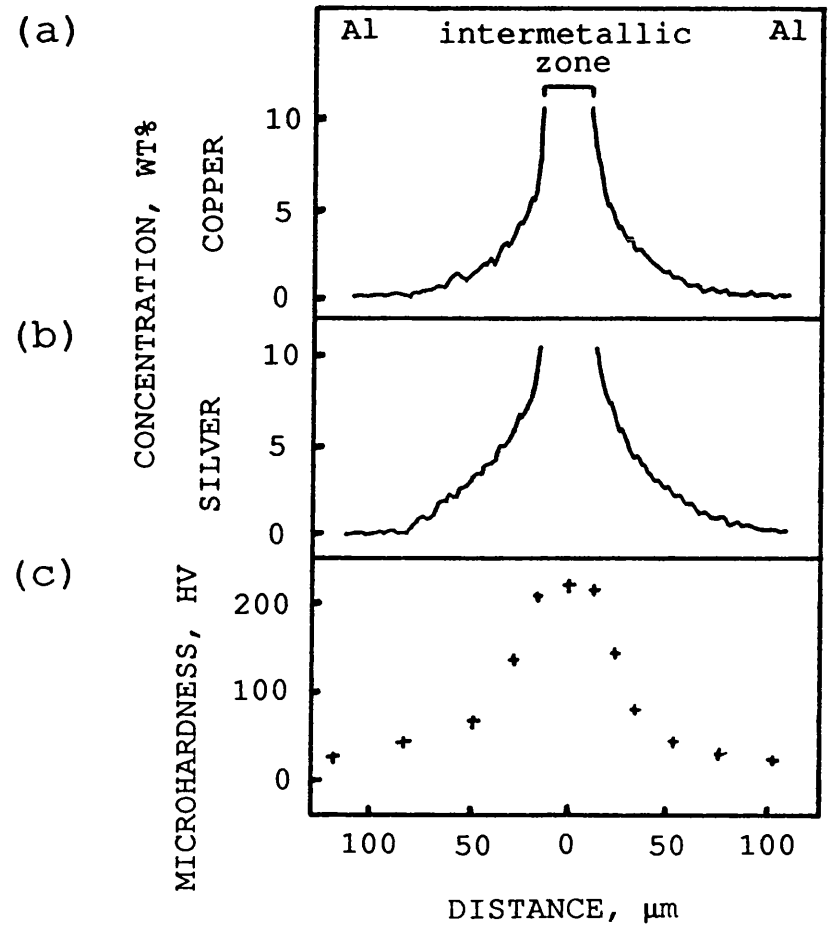

Fig. 3.22. Aluminium bonded with a copper-silver alloy interlayer, 3 MPa, 30 mins, 510°C, concentration and hardness profiles.
a. Copper.
b. Silver.
c. Microhardness.

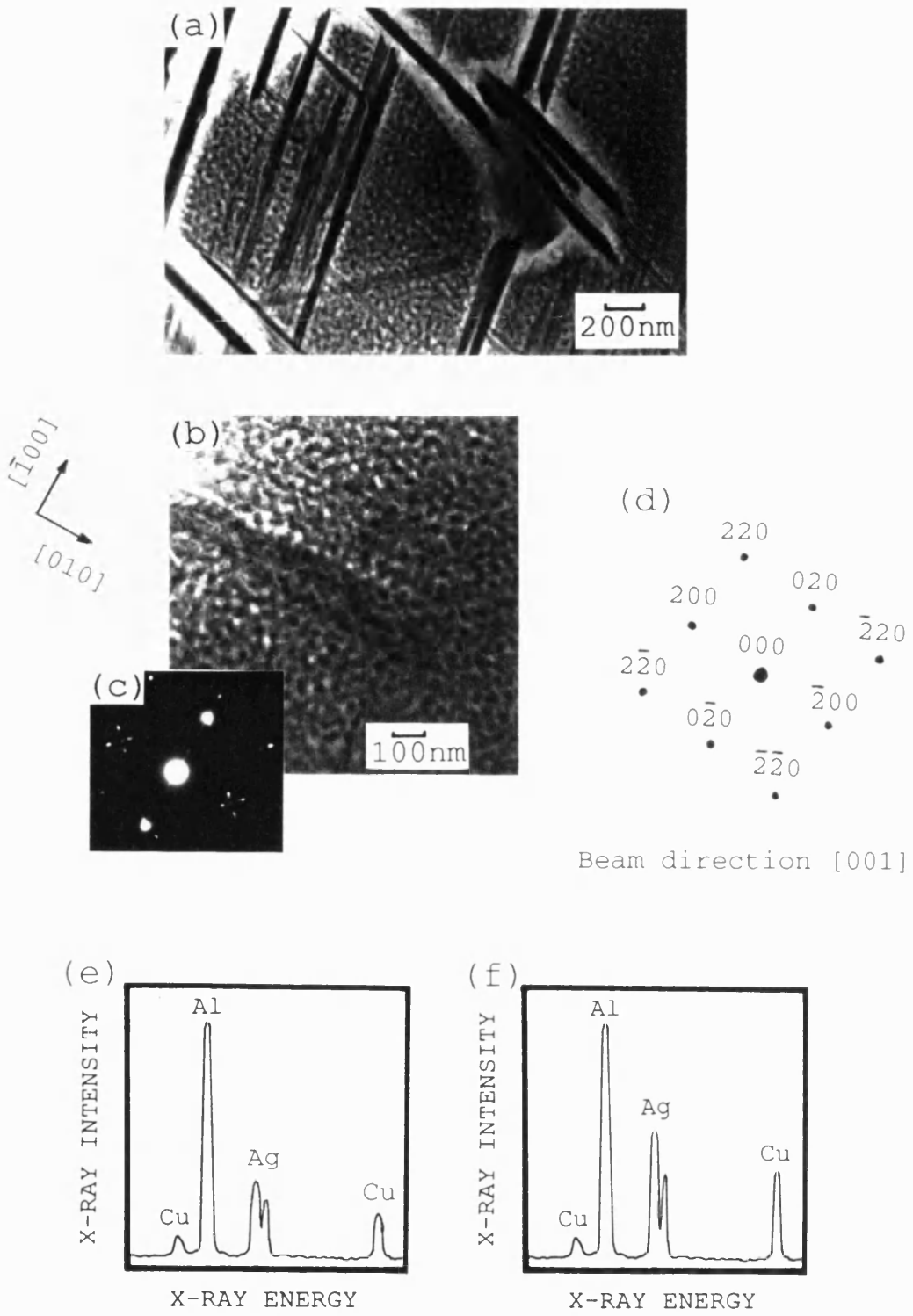

Fig. 3.23. Aluminium bonded with a copper-silver alloy interlayer, 3 MPa, 30 mins, 510°C; region adjacent to joint.

a. Needle-like particles, TEM.
b. Fine precipitates, TEM.
c. Diffraction pattern
d. Indexed diffraction pattern.
e. EDS of small precipitates.
f. EDS of large particles.

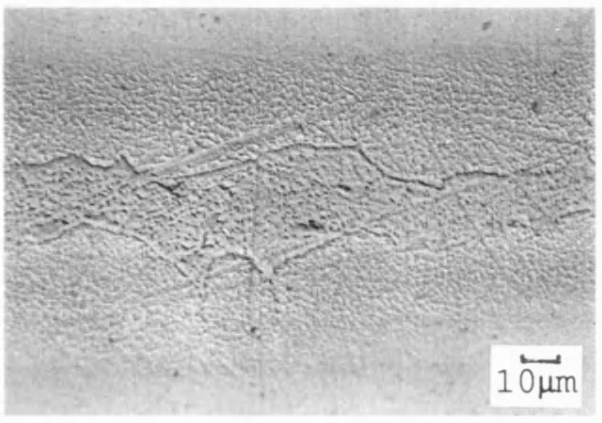

Fig. 3.24. Aluminium bonded with a copper-silver alloy interlayer, 10 MPa, 30 mins, 510°C, OM, DIC.

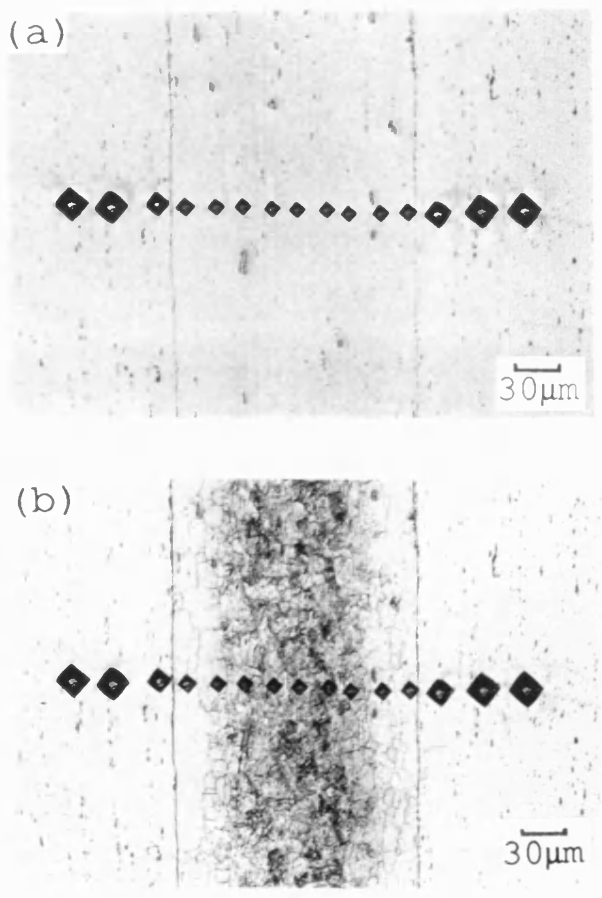

Fig. 3.25. Aluminium bonded with an aluminium alloy (2124) interlayer, 10 MPa, 30 mins, 500°C.
a. Microhardness profile of polished section.
b. Etched section of joint.

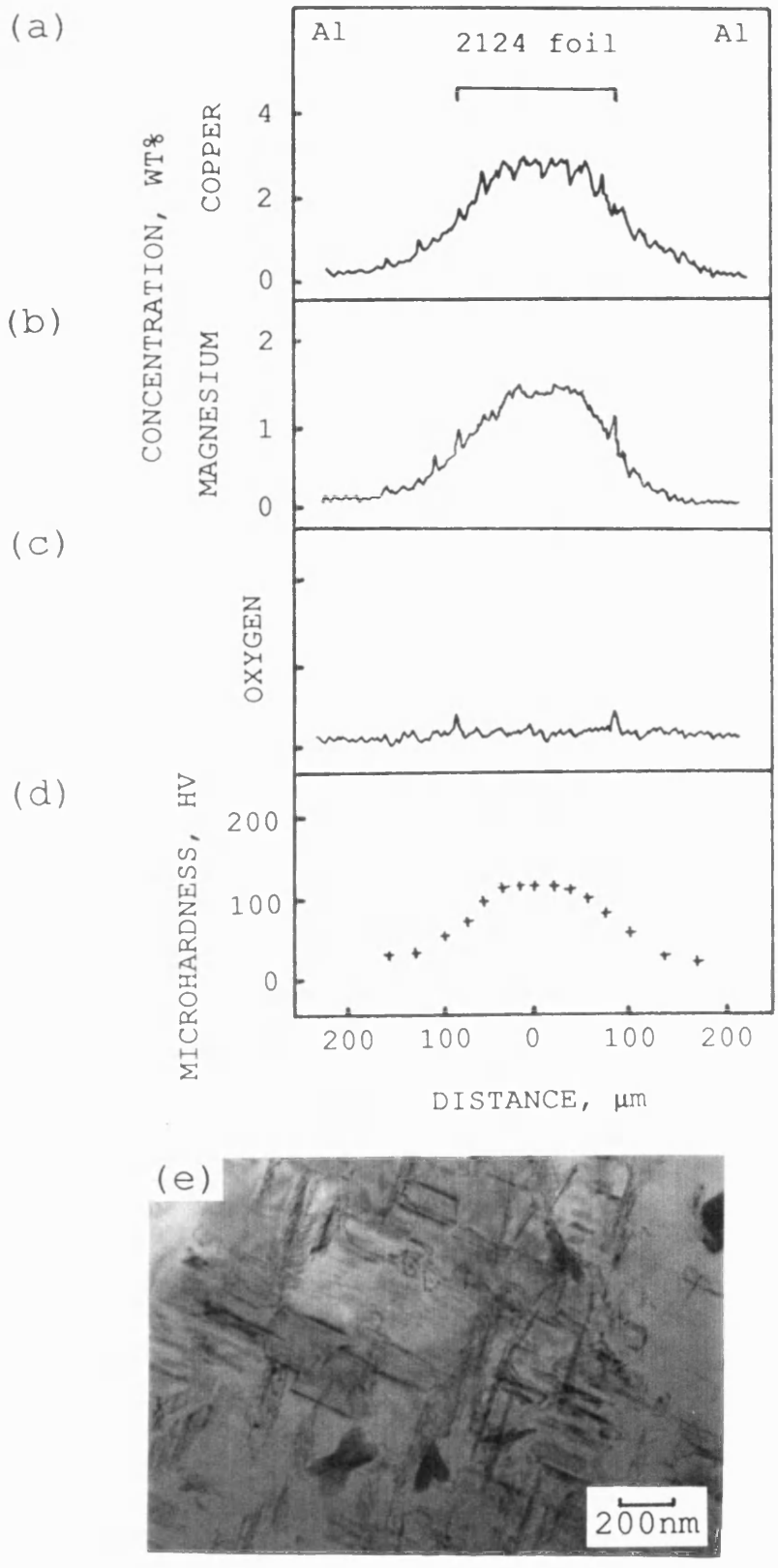

Fig. 3.26. Aluminium bonded with an aluminium alloy (2124) interlayer, 10 MPa, 30 mins, 500°C, concentration and hardness profiles.

a. Copper.
b. Magnesium.
c. Oxygen.
d. Microhardness.
e. Precipitates in the 2124 alloy, TEM.

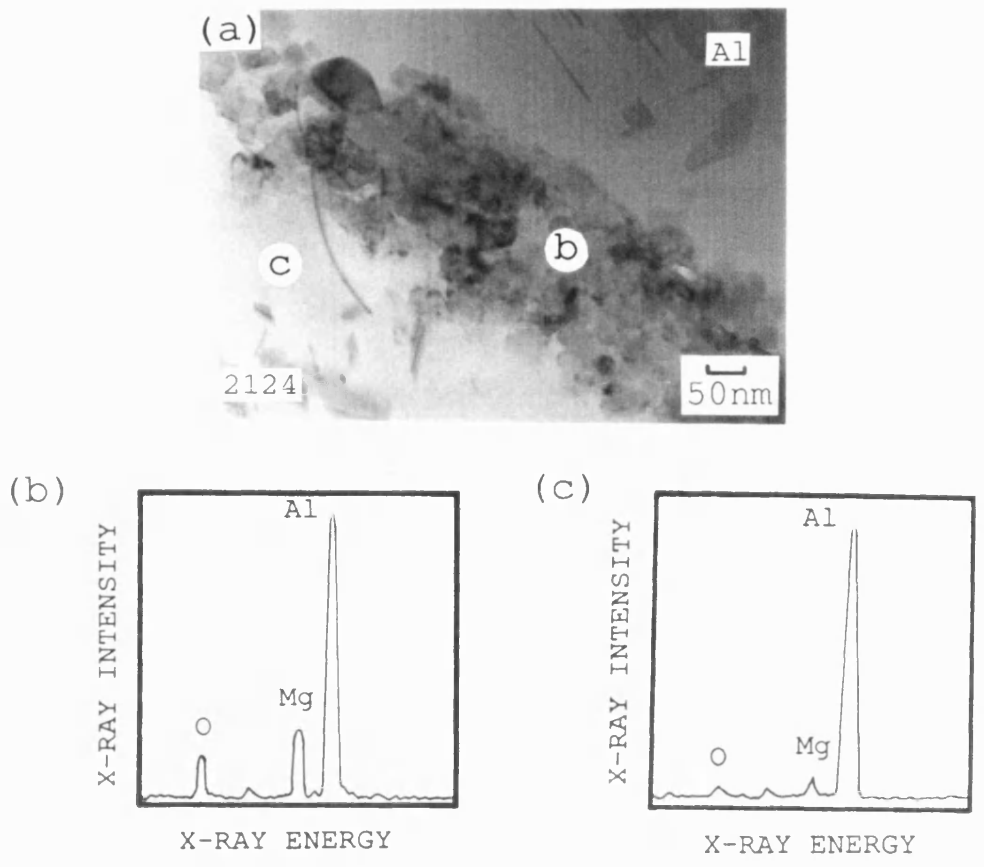

Fig. 3.27. Aluminium bonded with an aluminium alloy (2124) interlayer, 10 MPa, 30 mins, 500°C.
a. Aluminium/2124 interface, TEM.
b. EDS of interface.
c. EDS away from joint.

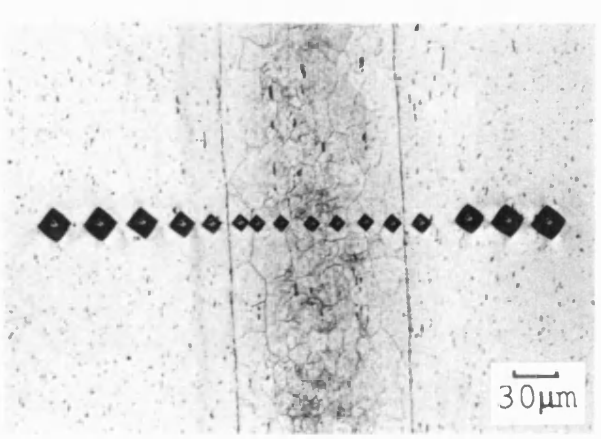

Fig. 3.28. Aluminium bonded with an aluminium alloy (2124) interlayer, 10 MPa, 30 mins, 550°C, OM.

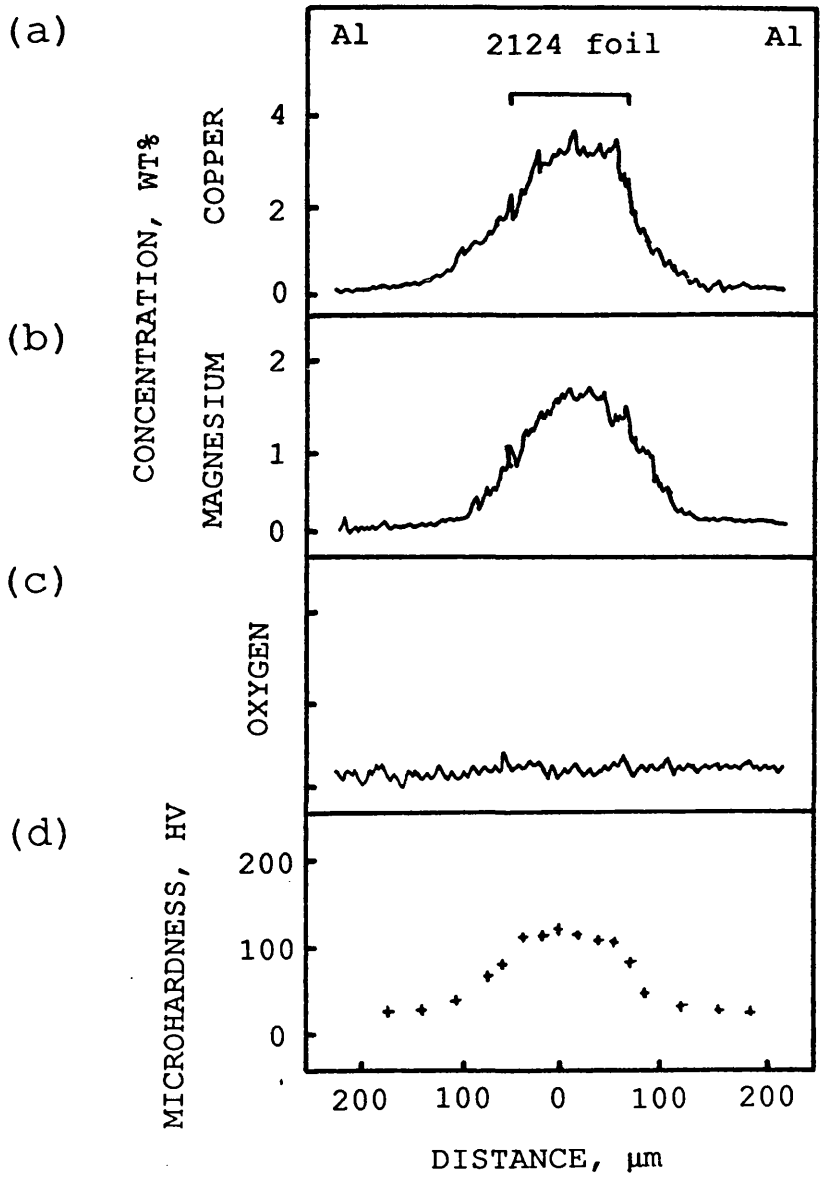

Fig. 3.29. Aluminium bonded with an aluminium alloy (2124) interlayer, 10 MPa, 30 mins, 550°C, concentration and hardness profiles.
a. Copper.
b. Magnesium.
c. Oxygen.
d. Microhardness.

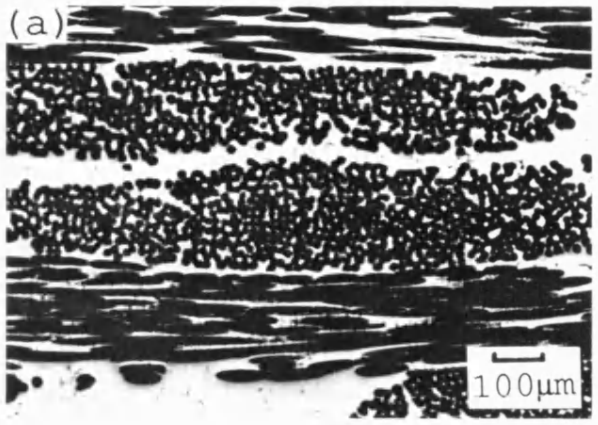

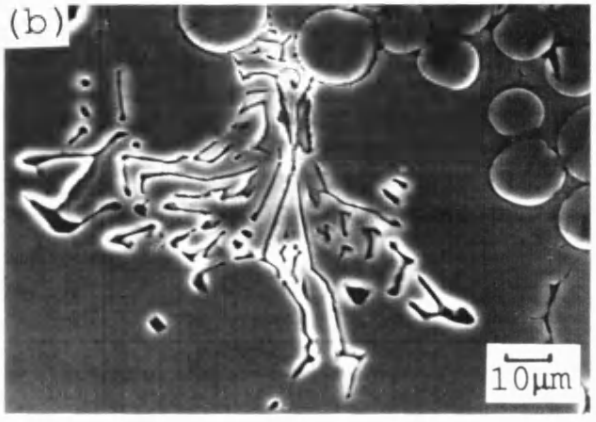

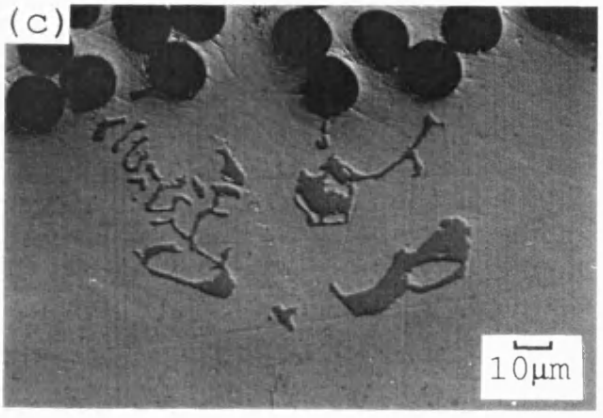

Fig. 3.30. As-received Al/Nic composite.
a. Distribution of fibres, OM.
b. Phase L1 in aluminium matrix, SEI.
c. Phase L2 in aluminium matrix, OM.

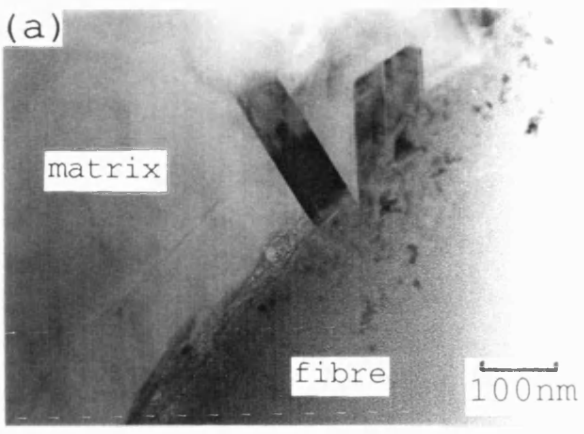

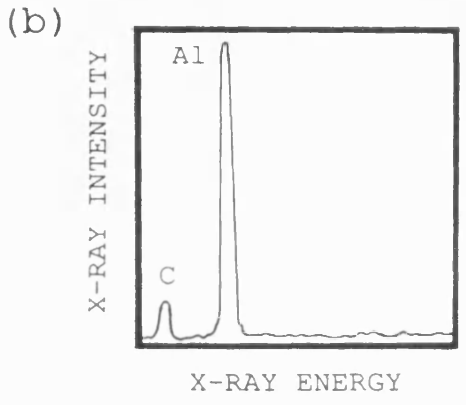

Fig. 3.31. Crystals at fibre/matrix interface.
a. TEM.
b. EDS.

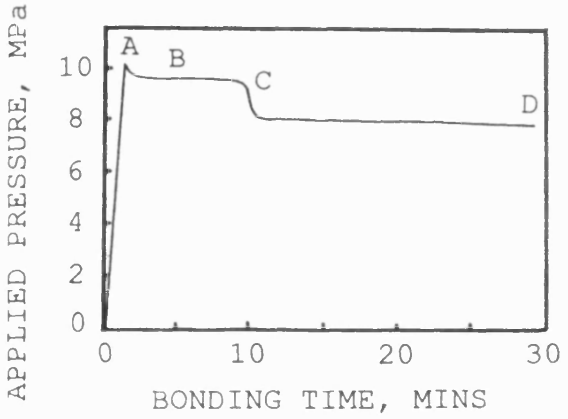

Fig. 3.32. Pressure-versus-time curve for Al/Nic composite bonded with a copper interlayer, 10 MPa, 550°C.

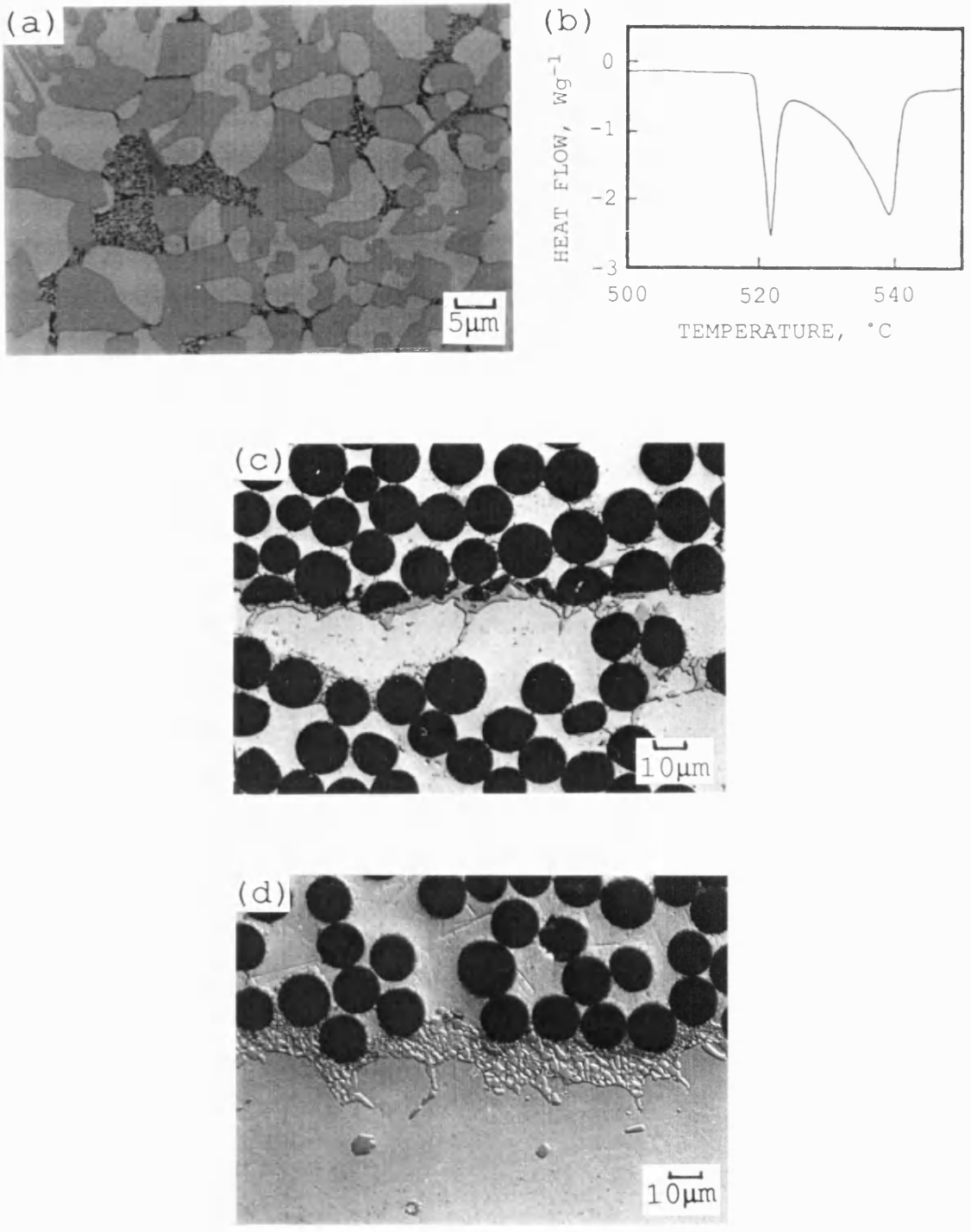

Fig. 3.33. Al/Nic composite bonded with a copper interlayer, 10 MPa, 30 mins, 550°C.
a. Microstructure of expelled bead, OM.
b. DSC curve of expelled bead.
c. Section of the bond, OM.
d. Aluminium-rich region at joint, OM.

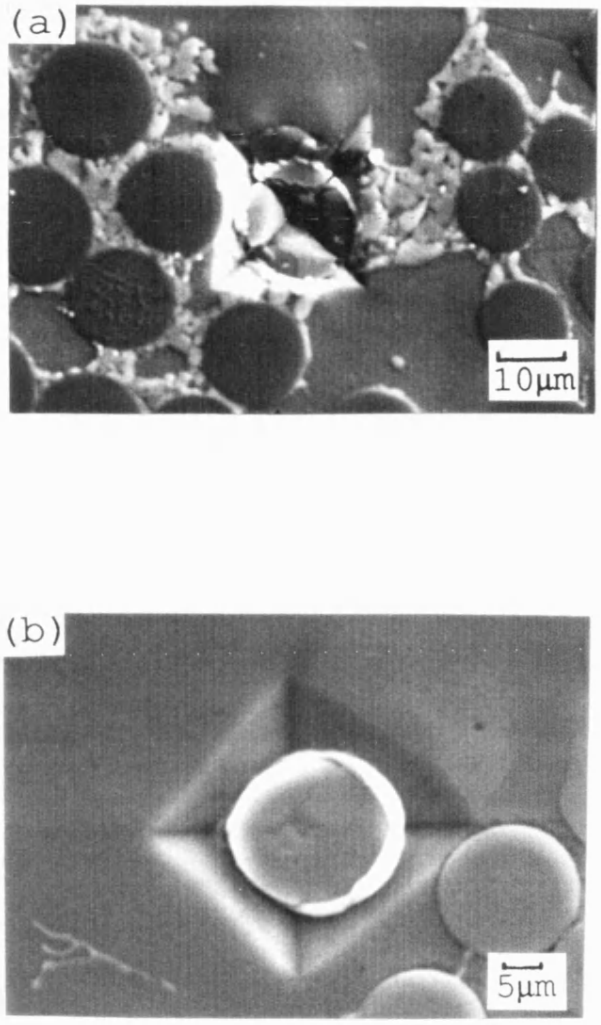

Fig. 3.34. Al/Nic composite bonded with a copper interlayer, 20 MPa, 30 mins, 550°C.
a. Indented fibre in the bond region, 200 gf, SEI.
b. Indented fibre in the composite, 100 gf, SEI.

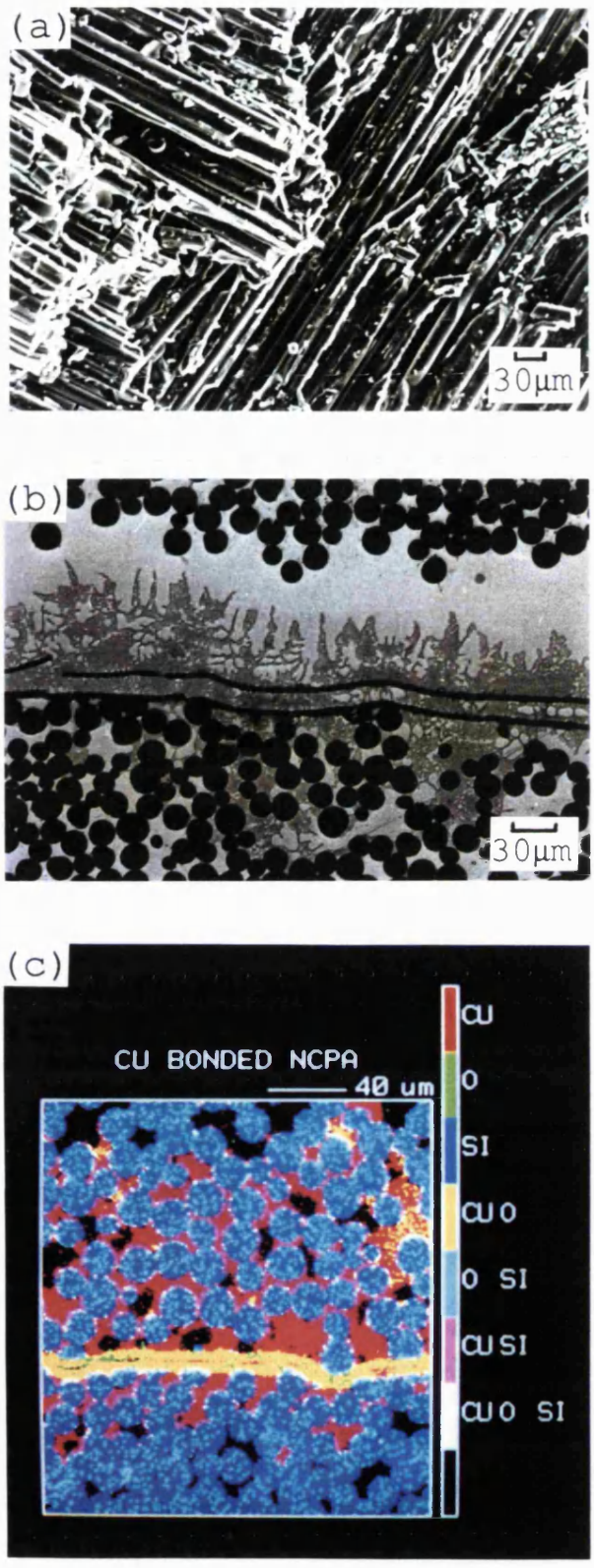

Fig. 3.35. Al/Nic composite bonded with a copper interlayer, 10 MPa, 30 mins, 550°C.
a. Fracture surface of sheared specimen, SEI.
b. Oxidation at periphery of joint composite, OM.
c. X-ray map of oxidised region.

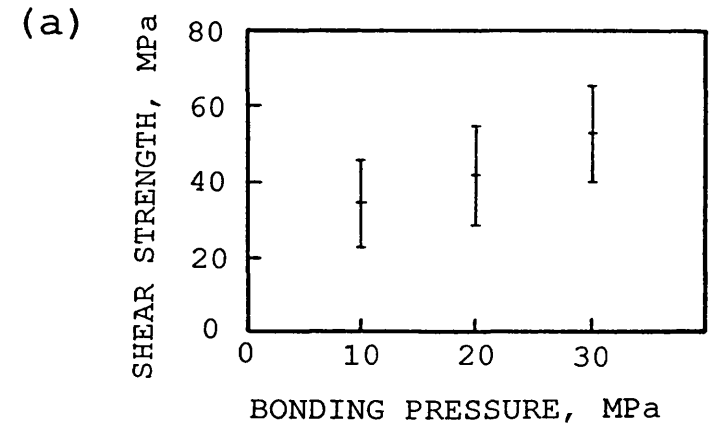

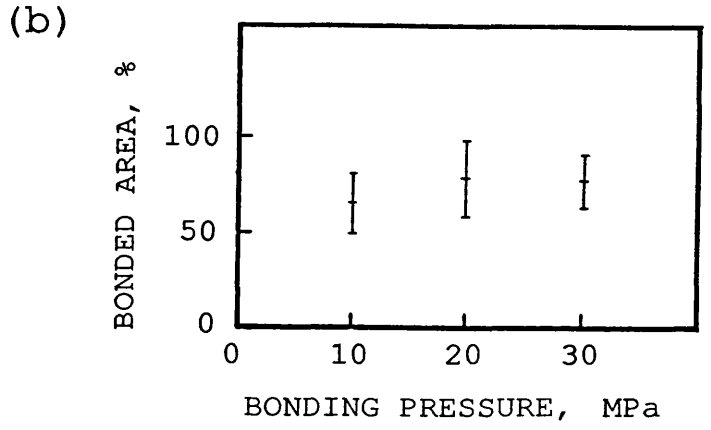

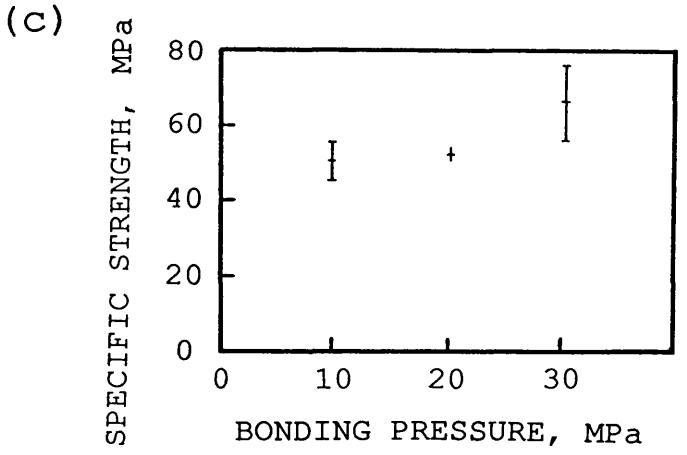

Fig. 3.36. Effect of bonding pressure on mechanical properties for Al/Nic composite bonded with a copper interlayer, 30 mins, 550°C.
a. Shear strength.
b. Bonded area.
c. Specific strength.

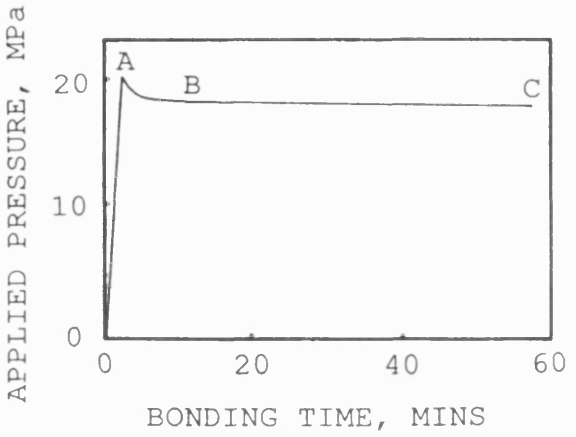

Fig. 3.37. Pressure-versus-time curve for Al/Nic composite bonded with a nickel-coated copper interlayer, 20 MPa, 550°C.

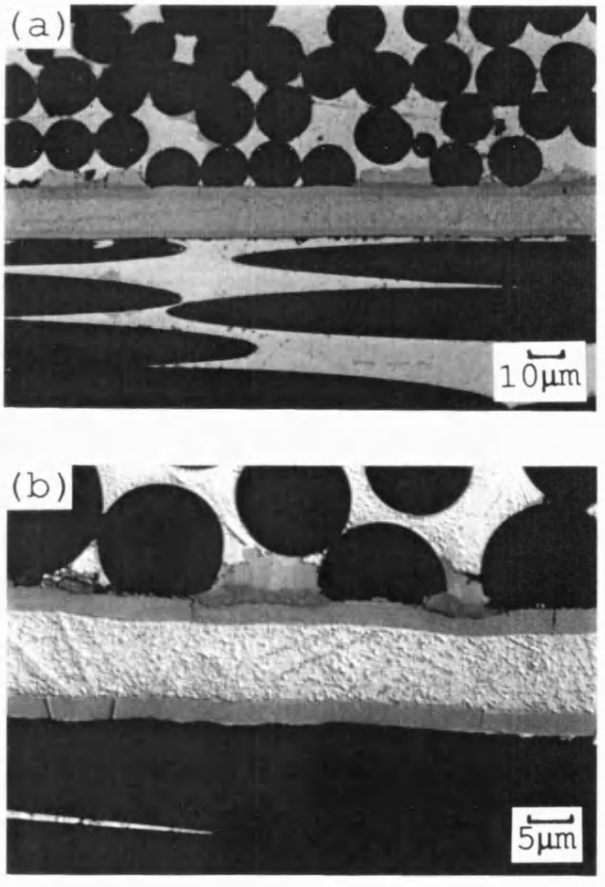

Fig. 3.38. Al/Nic composite bonded with a nickel-coated copper interlayer, 20 MPa, 60 mins, 550°C.
a. Section of joint, OM, DIC.
b. Fibres inhibiting diffusion, OM, DIC.

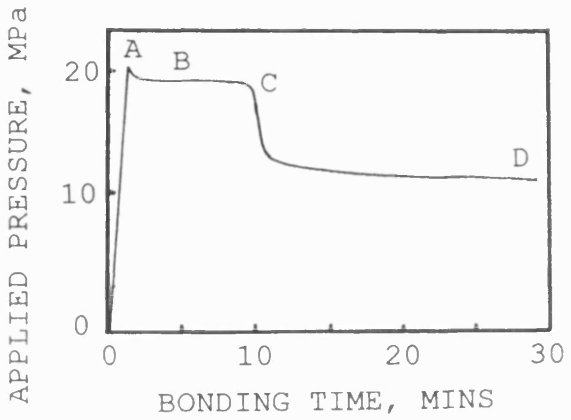

Fig. 3.39. Pressure-versus-time curve for Al/Nic composite bonded with a copper-silver alloy interlayer, 20 MPa, 510°C.

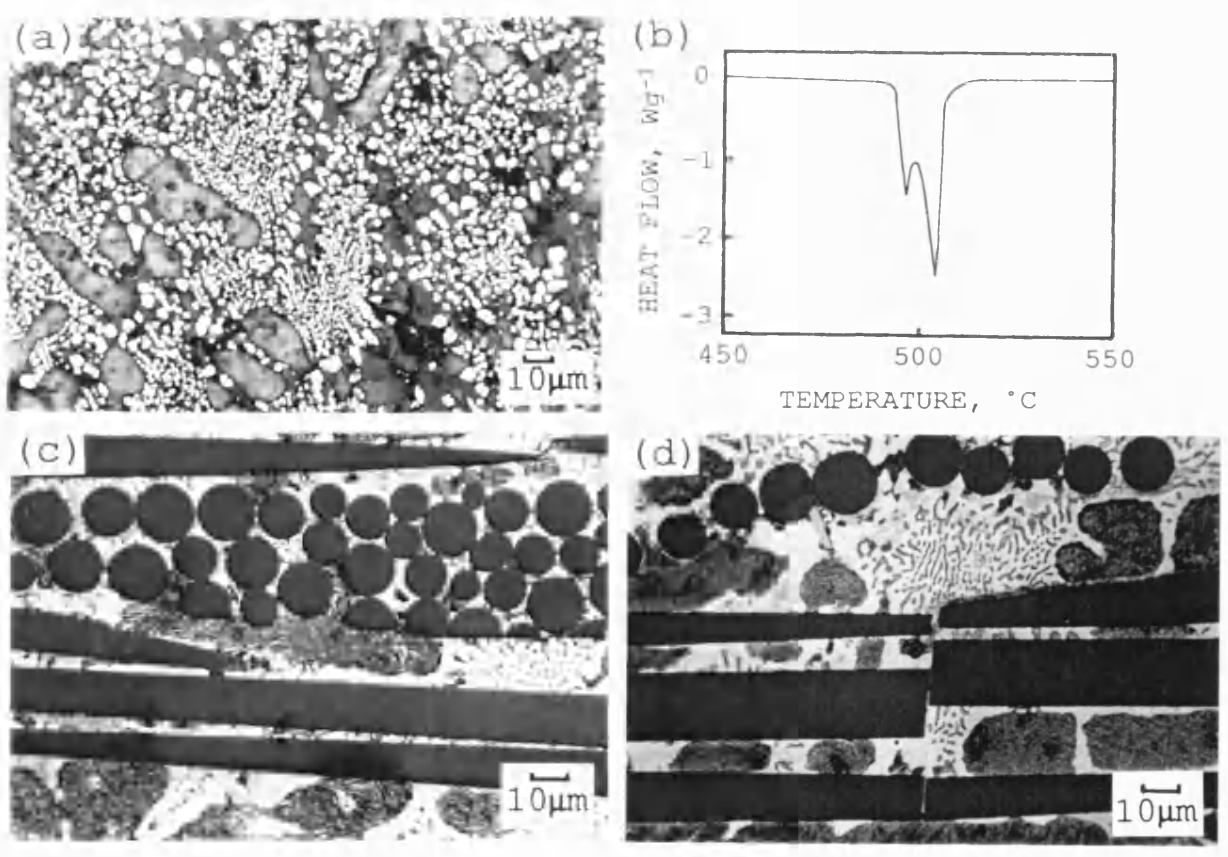

Fig. 3.40. Al/Nic composite bonded with a copper-silver alloy interlayer, 20 MPa, 30 mins, 510°C.
a. Microstructure of expelled bead, BEI.
b. DSC curve of expelled bead.
c. Section of joint, OM.
d. Broken fibres in bond region, OM.

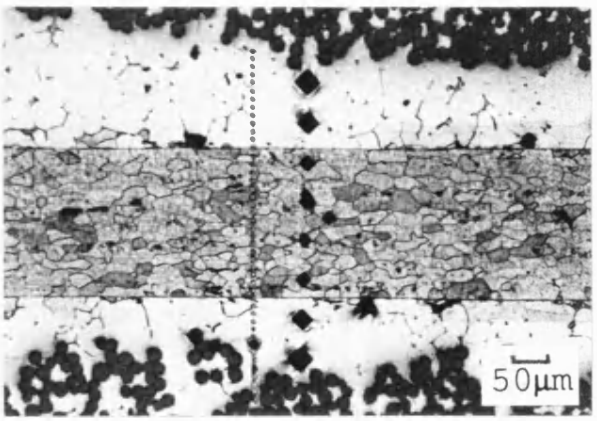

Fig. 3.41. Al/Nic composite bonded with an aluminium (2124) alloy interlayer, 20 MPa, 240 mins, 500°C, etched section showing EPMA and microhardness profiles, OM.

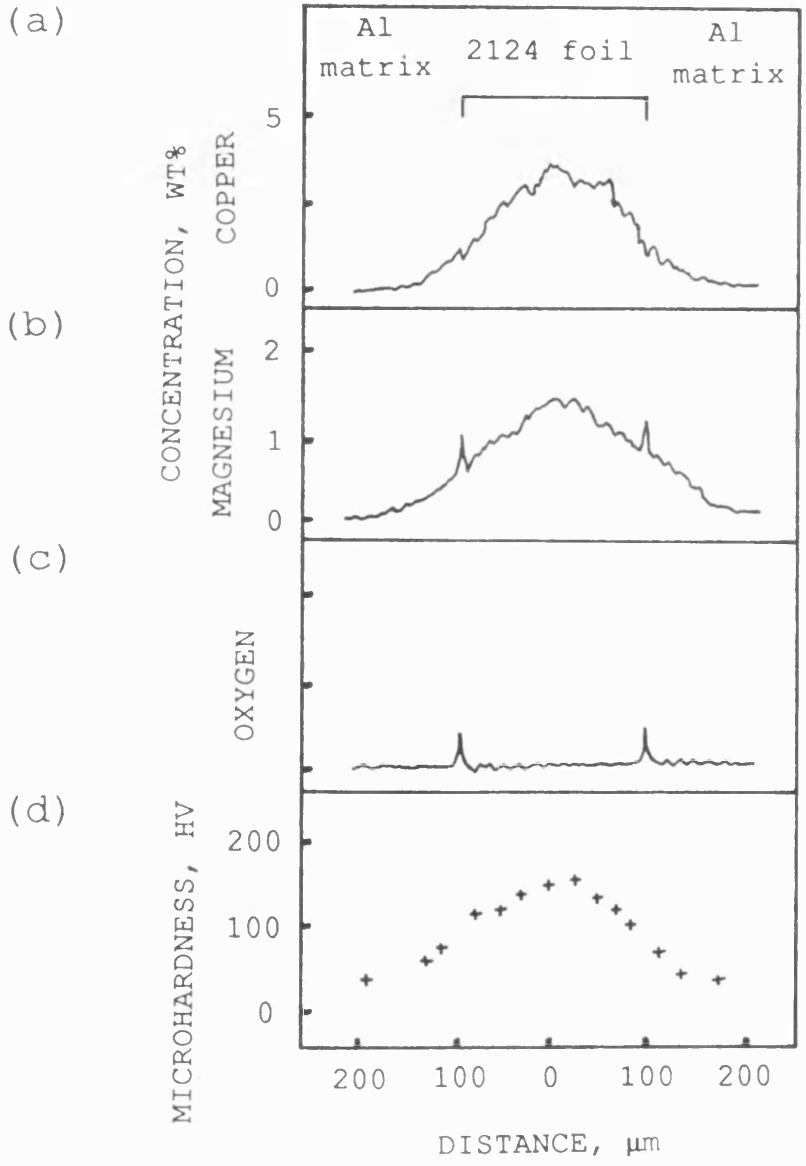

Fig. 3.42. Al/Nic composite bonded with an aluminium (2124) alloy interlayer, 20 MPa, 240 mins, 500°C, concentration and hardness profiles.
a. Copper
b. Magnesium
c. Oxygen
d. Microhardness

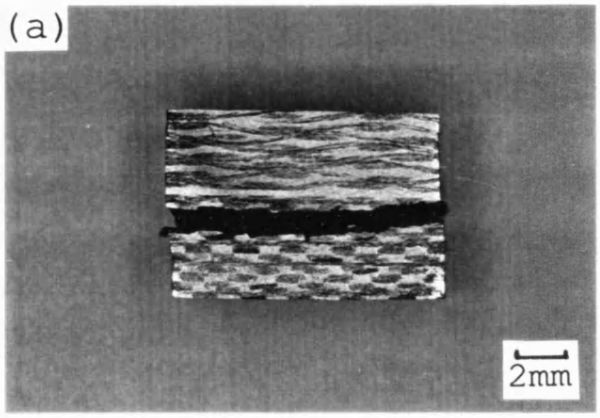

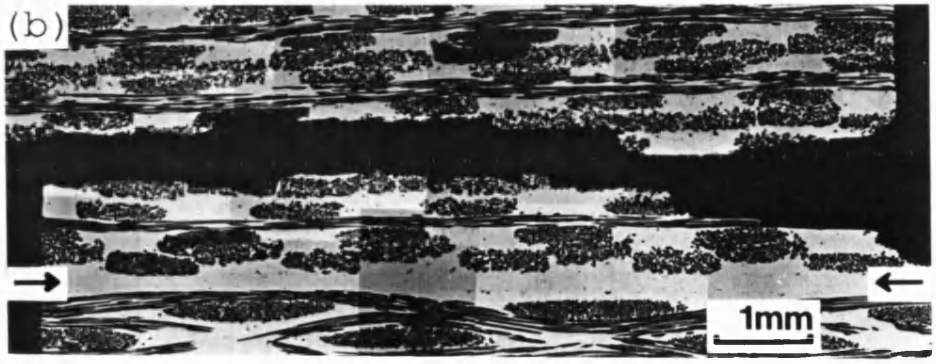

Fig. 3.43. Al/Nic composite bonded with an aluminium alloy (2124) interlayer, 34 MPa, 60 mins, 500°C.
a. Fractured shear specimen.
b. Fracture through fibre tows, OM.

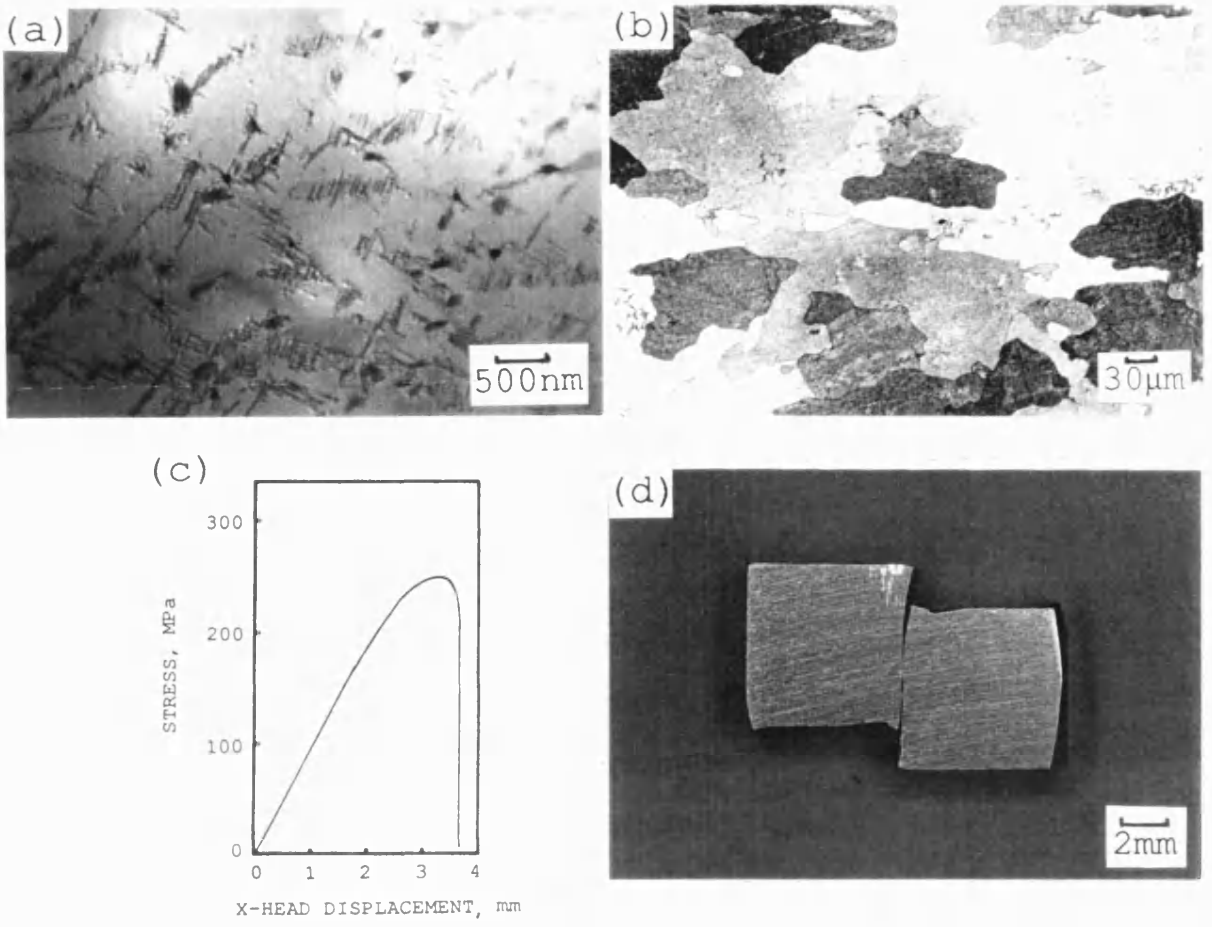

Fig. 3.44. As-received 2124 aluminium alloy.
a. S' precipitates and Al-Cu-Mn-Fe particles, TEM.
b. Etched section showing grain size, OM.
c. Shear test stress-displacement curve.
d. Fractured shear test specimen.

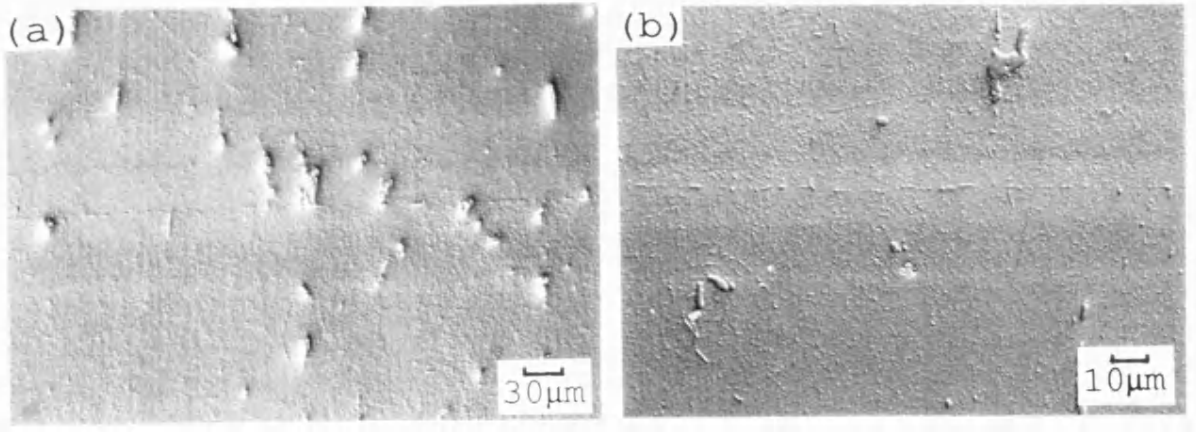

Fig. 3.45. 2124 alloy bonded without an interlayer, 10 MPa, 240 mins, 500°C.
a. Section of joint, OM, DIC.
b. Section of joint, OM, DIC.

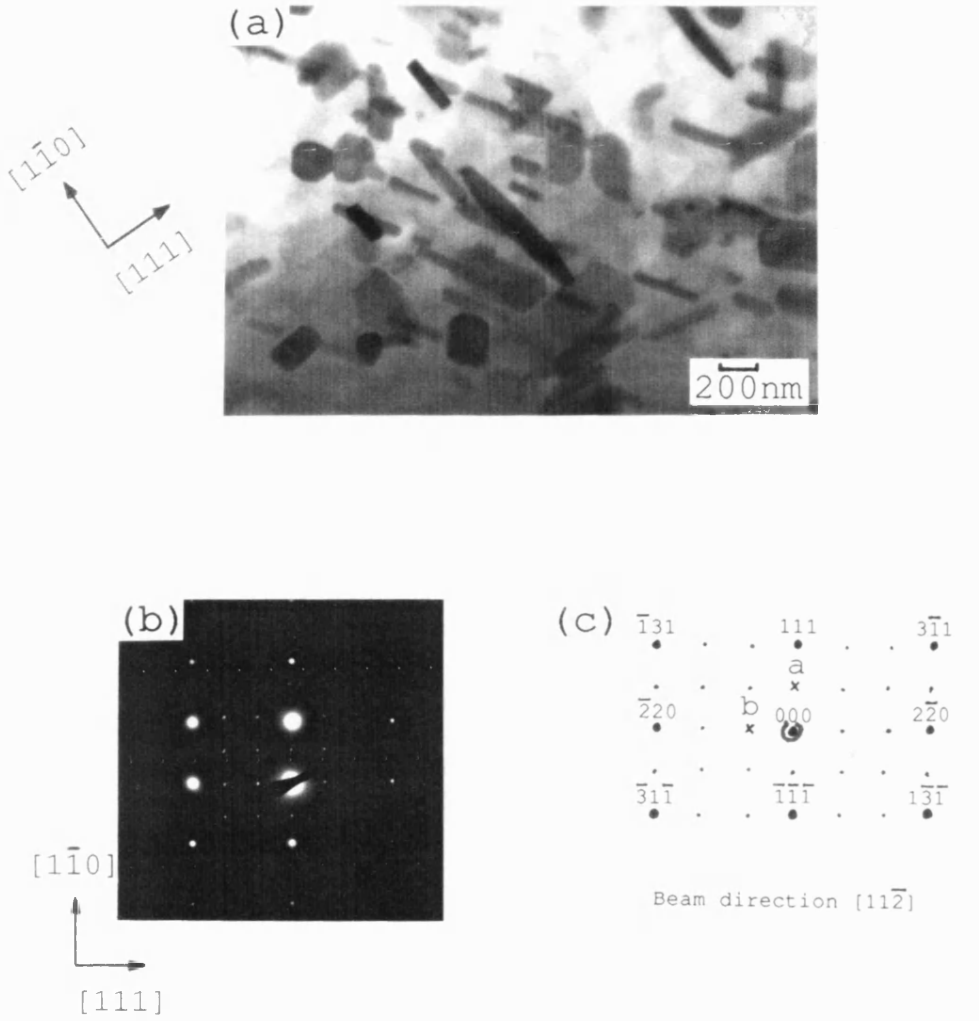

Fig. 3.46. 2124 alloy bonded without an interlayer, 10 MPa, 240 mins, 500°C.
a. Oriented precipitates, TEM.
b. Diffraction pattern.
c. Indexed diffraction pattern.

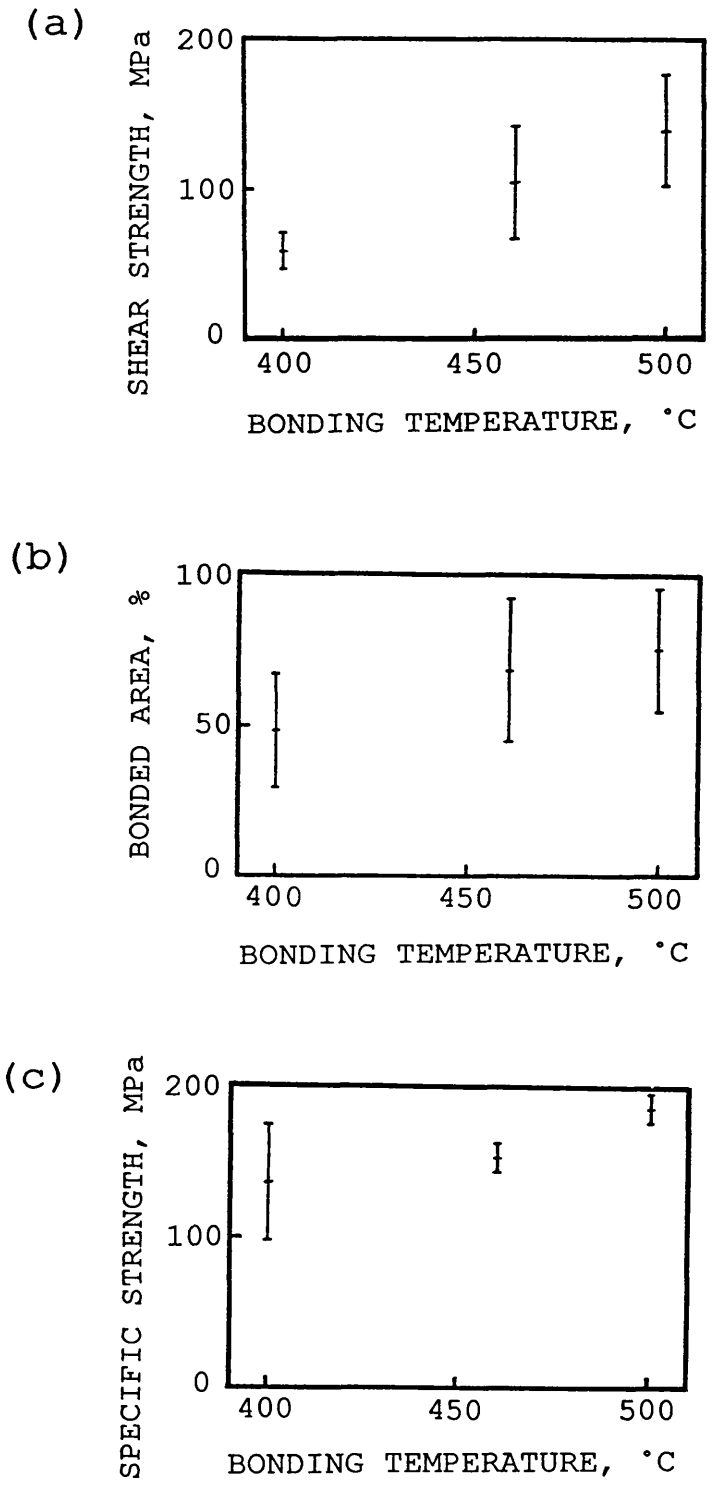

Fig. 3.47. Effect of bonding temperature on mechanical properties of 2124 alloy bonded without an interlayer, 10 MPa, 240 mins.
a. Shear strength.
b. Bonded area.
c. Specific strength.

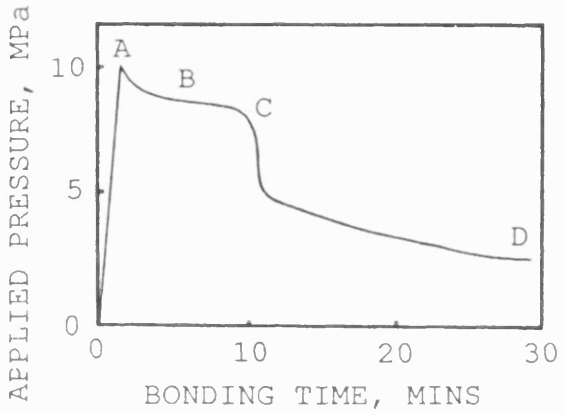

Fig. 3.48. Pressure-versus-time curve for 2124 alloy bonded with a copper-silver alloy interlayer, 10 MPa, 510°C.

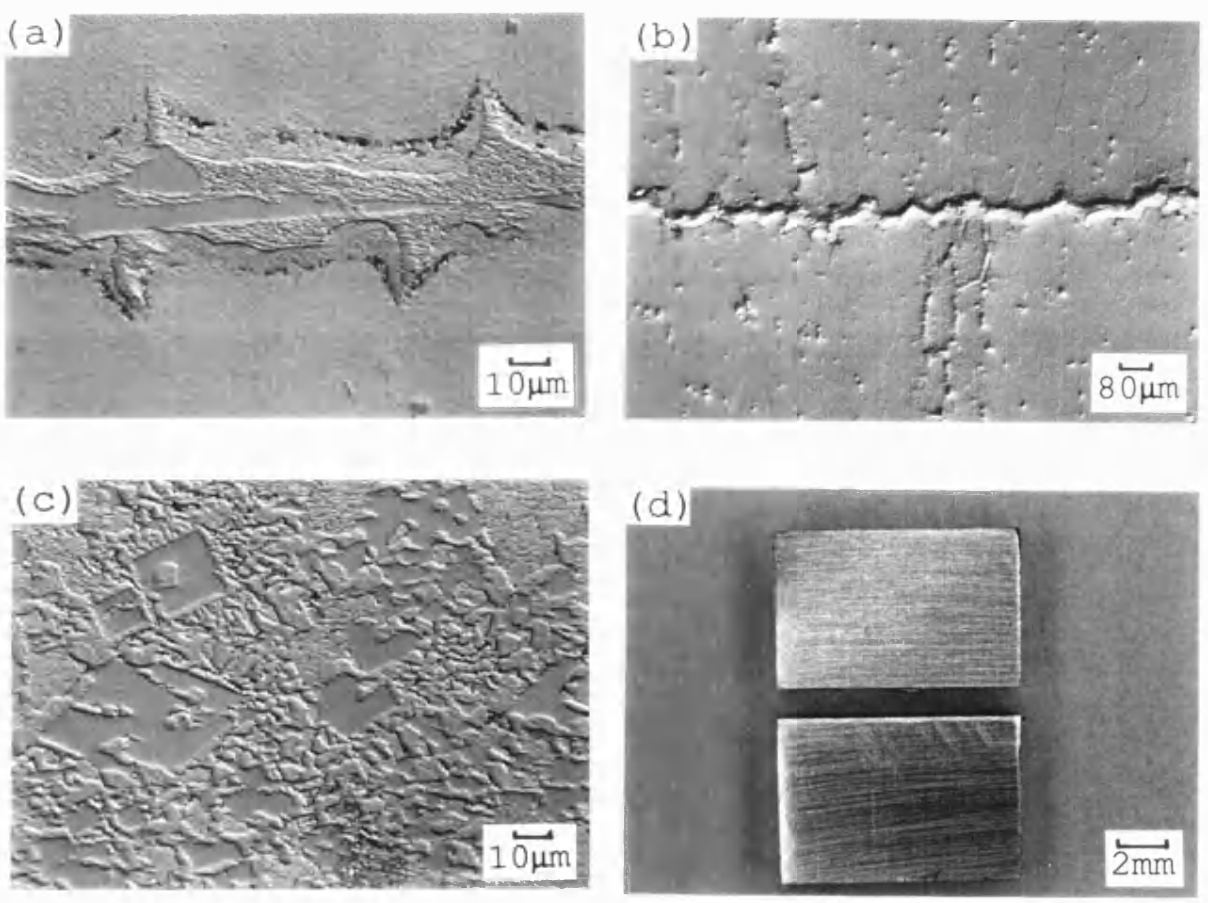

Fig. 3.49. 2124 alloy bonded with a copper-silver alloy interlayer, 10 MPa, 30 mins, 510°C.
a. Section of joint, OM, DIC.
b. Phases at grain boundaries, OM, DIC.
c. Periphery of joint, OM, DIC.
d. Failed shear-test specimen.

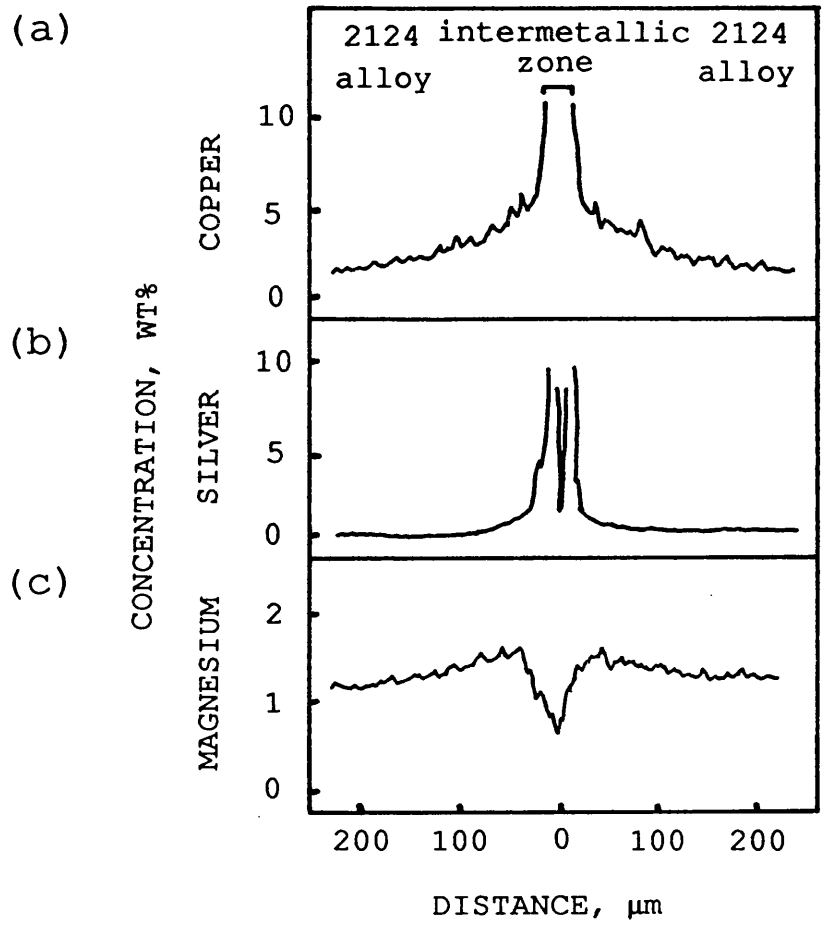

Fig. 3.50. 2124 alloy bonded with a copper-silver alloy interlayer, 10 MPa, 30 mins, 510°C, concentration profiles.
a. Copper
b. Silver
c. Magnesium

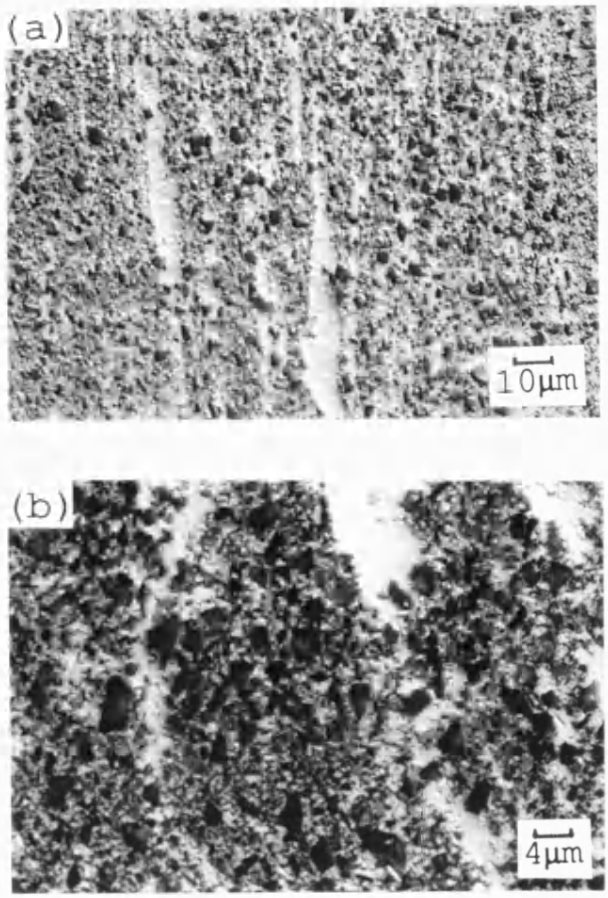

Fig. 3.51. As received 2124/P composite.
a. Polished section, OM, DIC.
b. Uneven particle distribution, OM.

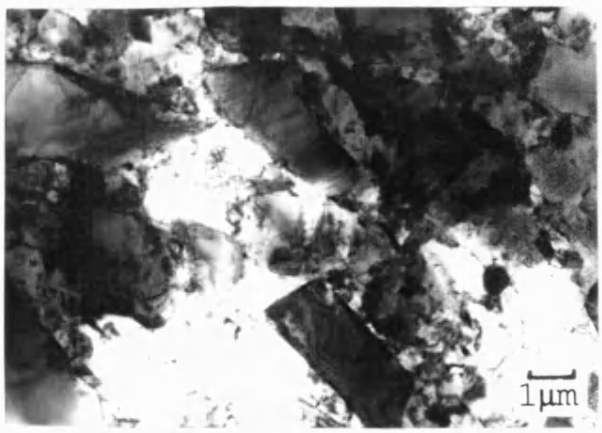

Fig. 3.52. 2124/25P composite, TEM.

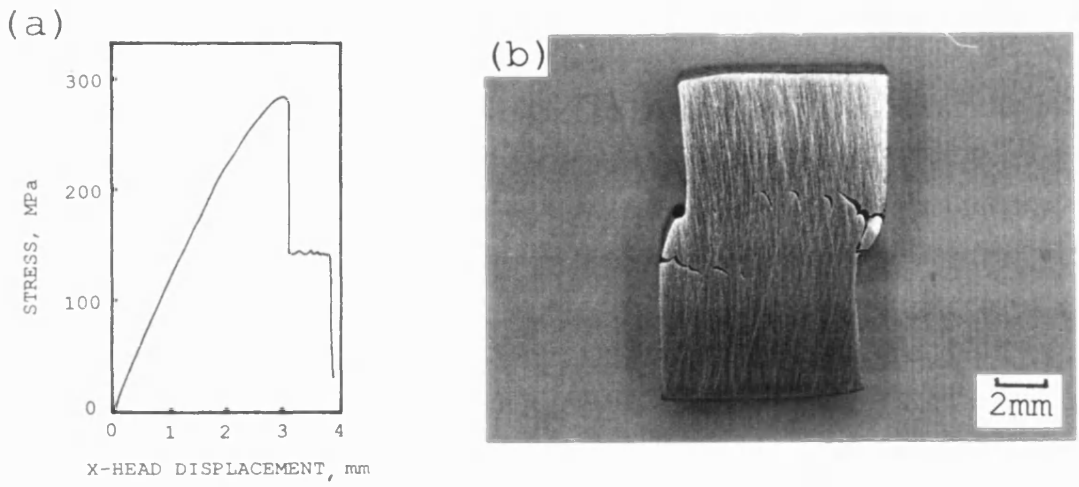

Fig. 3.53. As-received 2124/35P composite.
a. Shear test stress-displacement curve.
b. Failed shear test specimen.

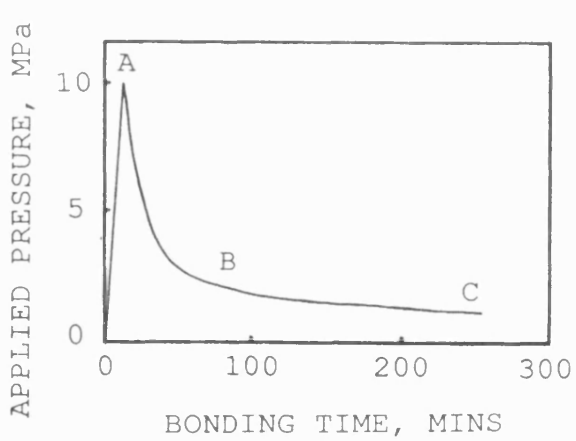

Fig. 3.54. Pressure-versus-time curve for 2124/35P bonded composite 10 MPa, 240 mins, 500°C.

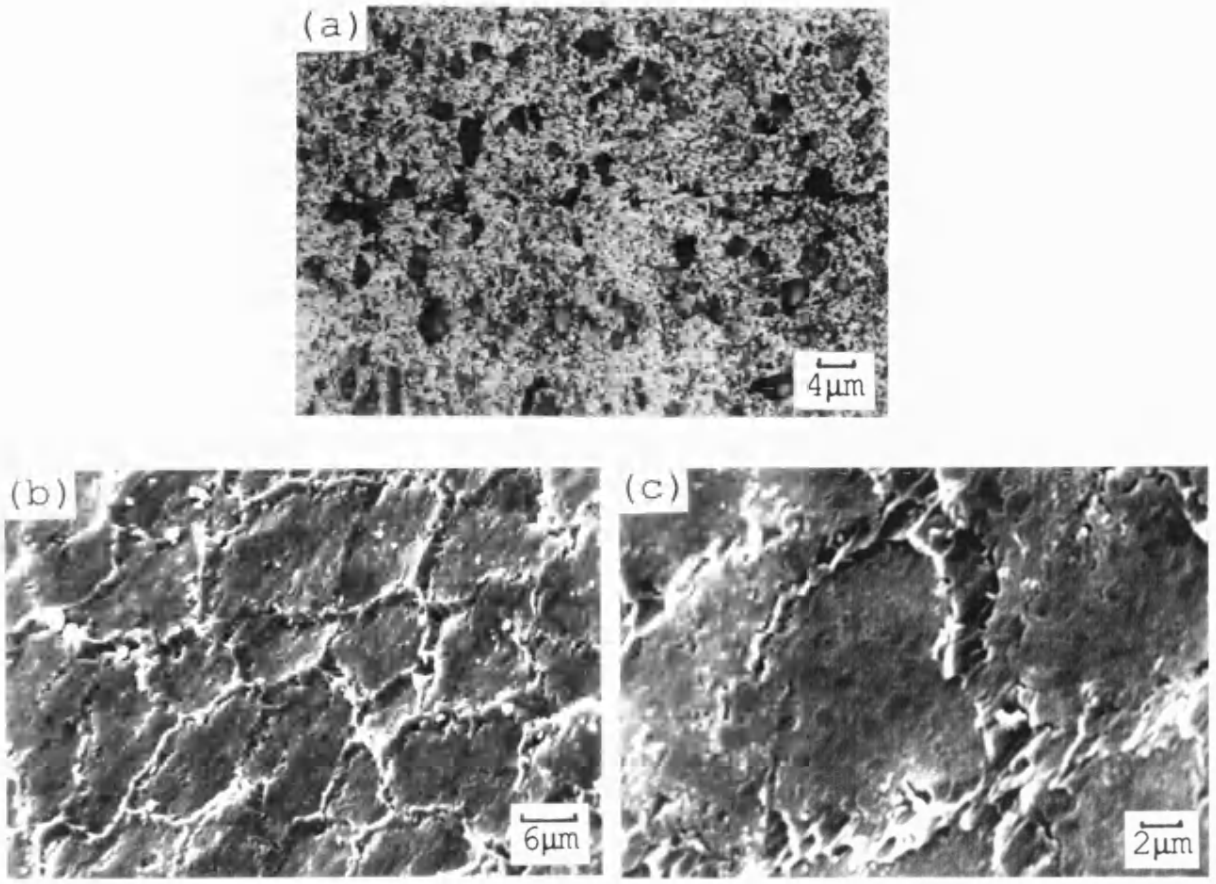

Fig. 3.55. 2124/25P composite bonded without an interlayer, 10 MPa, 240 mins, 500°C, 2% deformation.
a. Section of joint, OM.
b. Fracture surface, SEI.
c. Fracture surface, SEI.

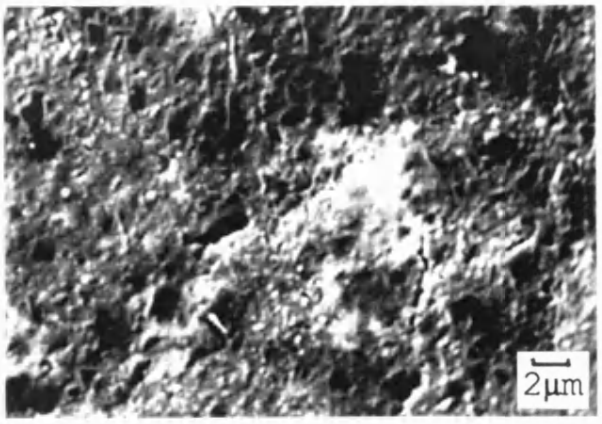

Fig. 3.56. 2124/40P composite bonded without an interlayer, 10 MPa, 240 mins, 500°C, 2% deformation, fracture surface, SEI.

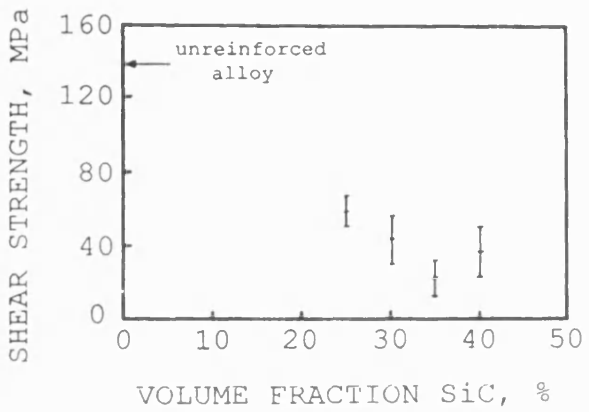

Fig. 3.57. Effect of volume fraction on the shear strength for bonded 2124/P composite.

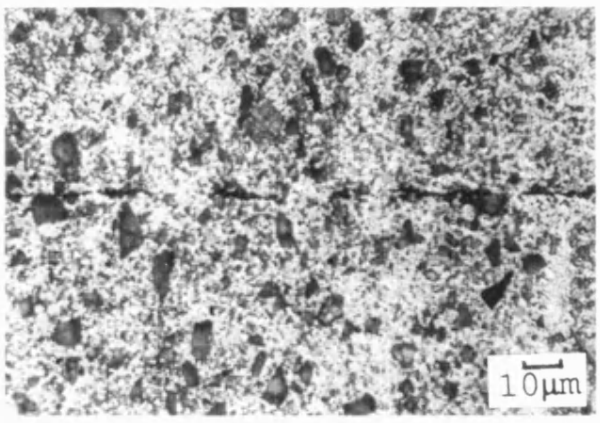

Fig. 3.58. 2124/25P composite bonded without an interlayer, 10 MPa, 240 mins, 500°C, 19% deformation, OM.

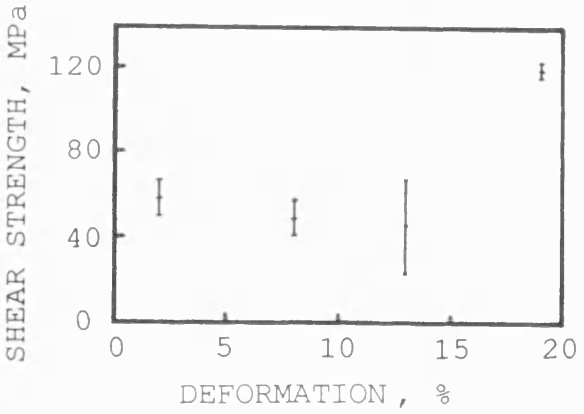

Fig. 3.59. Effect of deformation on the shear strength for bonded 2124/25P composite.

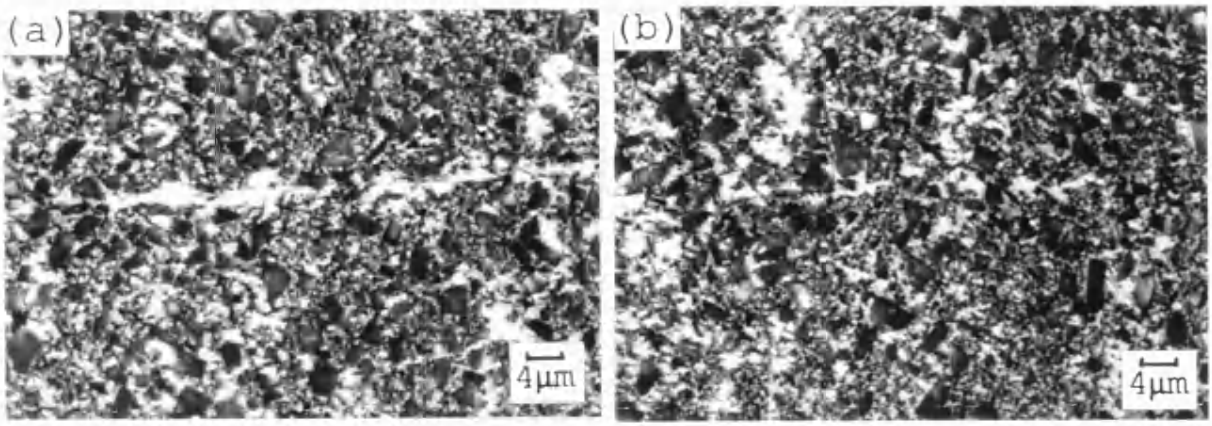

Fig. 3.60. 2124/35P composite bonded with a copper-silver alloy interlayer.
a. 4 MPa, 30 mins, 510°C, OM.
b. 8 MPa, 30 mins, 510°C, OM.

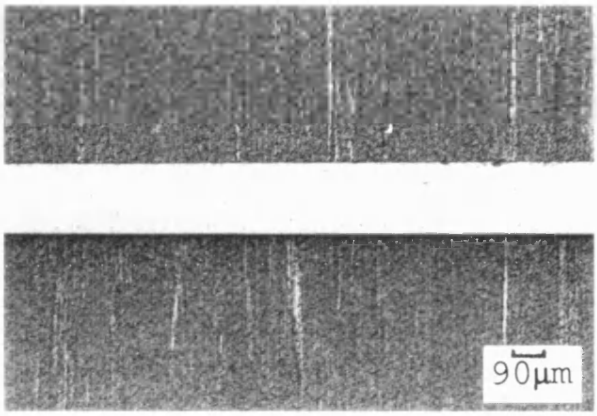

Fig. 3.61. 2124/30P composite bonded with an aluminium alloy (2124) interlayer, 10 MPa, 240 mins, 500°C, section of joint, OM.

Fig. 3.62. Aluminium bonded to 2124 alloy without an interlayer, 10 MPa, 240 mins, 500°C, section of joint, OM.

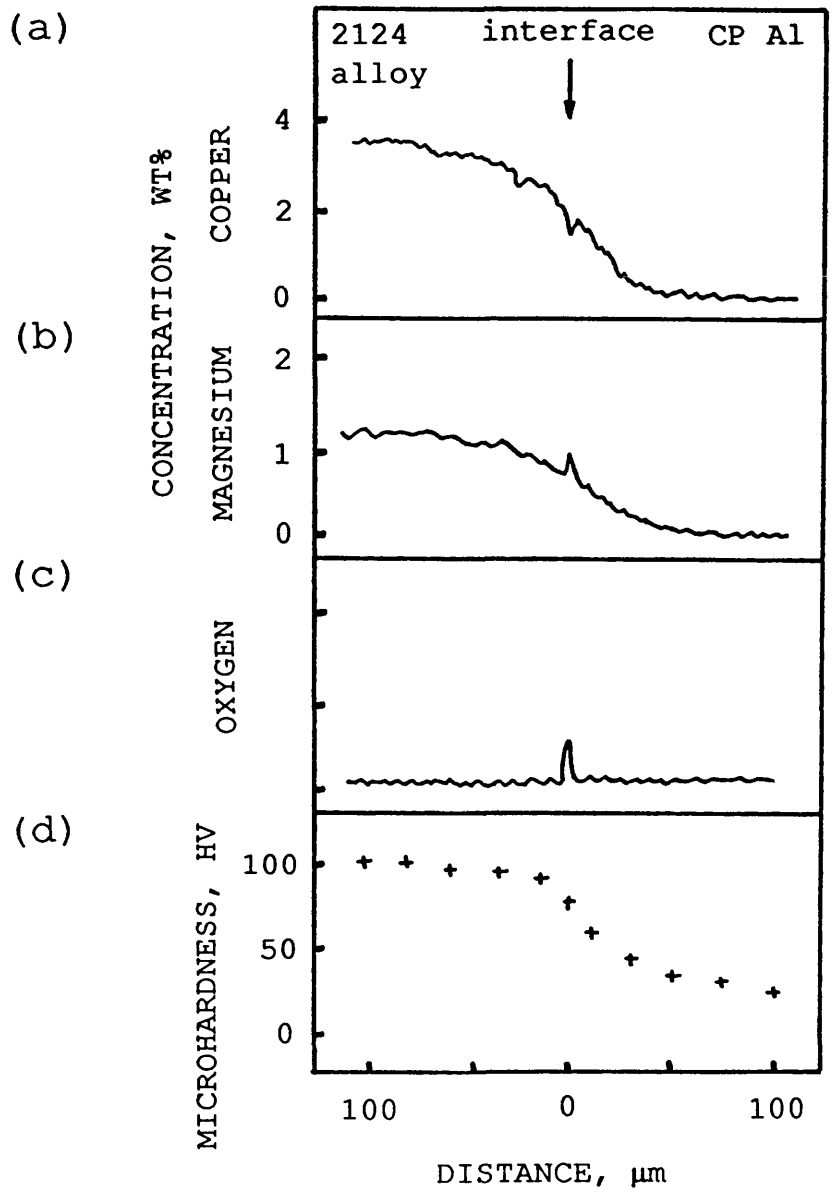

Fig. 3.63. Aluminium bonded to 2124 alloy without an interlayer, 10 MPa, 240 mins 500°C, concentration and hardness profiles.

a. Copper.
b. Magnesium.
c. Oxygen.
d. Microhardness.

Fig. 3.64. As Fig. 3.62, etched section of joint, OM.

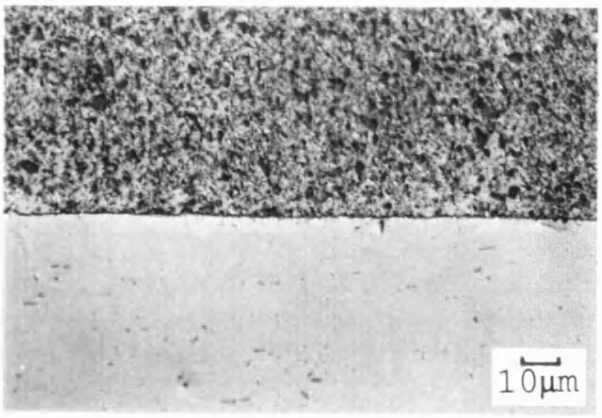

Fig. 3.65. Aluminium bonded to 2124/25P composite without an interlayer, 10 MPa, 240 mins, 500°C, section of joint, OM.

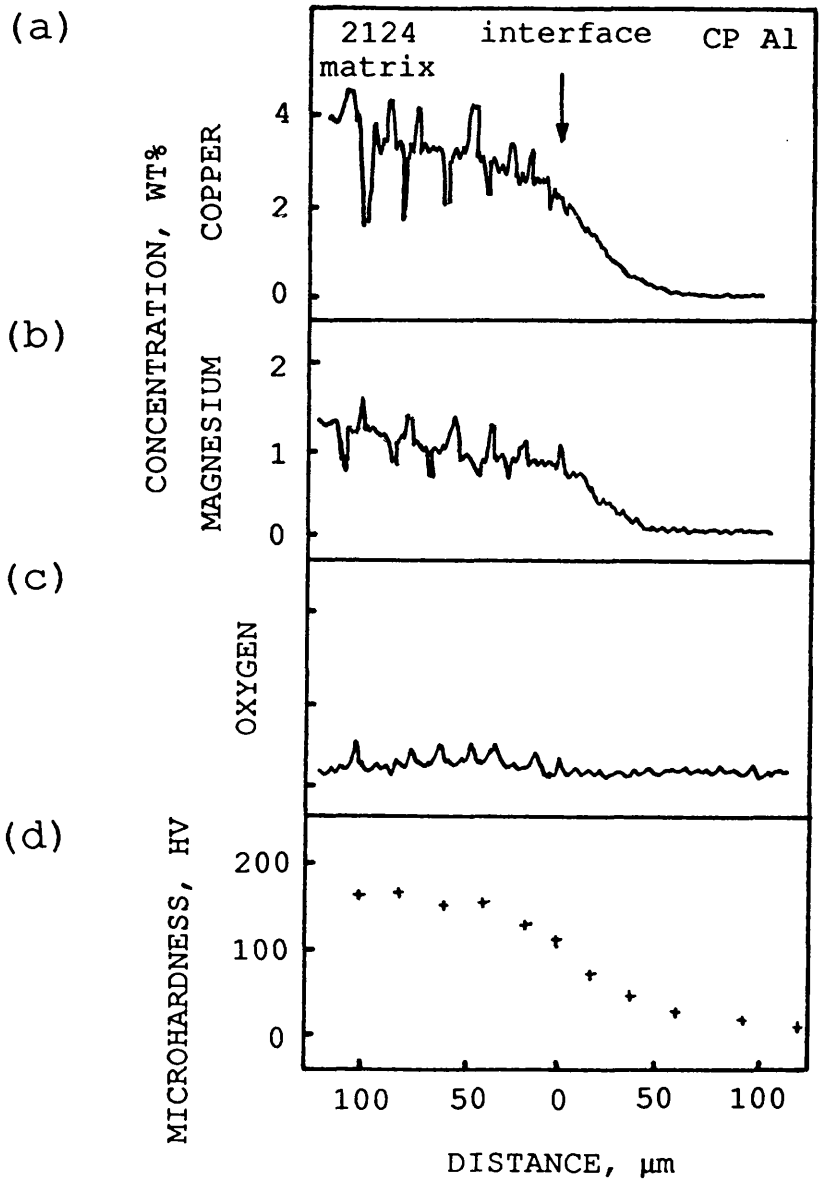

Fig. 3.66. Aluminium bonded to 2124/25P composite without an interlayer, 10 MPa, 240 mins, 500°C, concentration and hardness profiles.
a. Copper.
b. Magnesium.
c. Oxygen.
d. Microhardness.

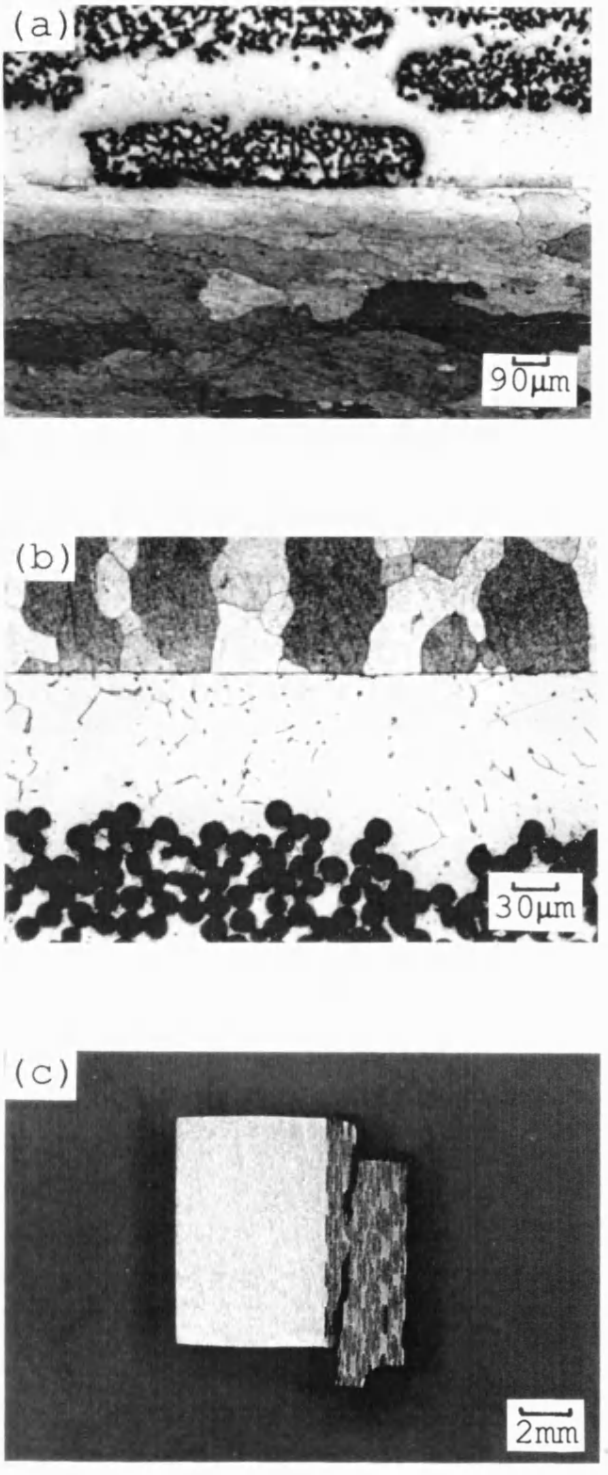

Fig. 3.67. 2124 alloy bonded to Al/Nic composite without an interlayer, 10 MPa, 240 mins, 500°C.
a. Section of joint, OM.
b. Metal-to-metal contact at joint, OM.
c. Fractured shear test specimen.

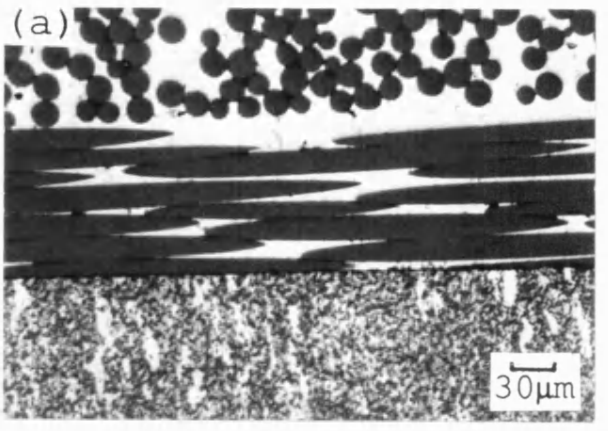

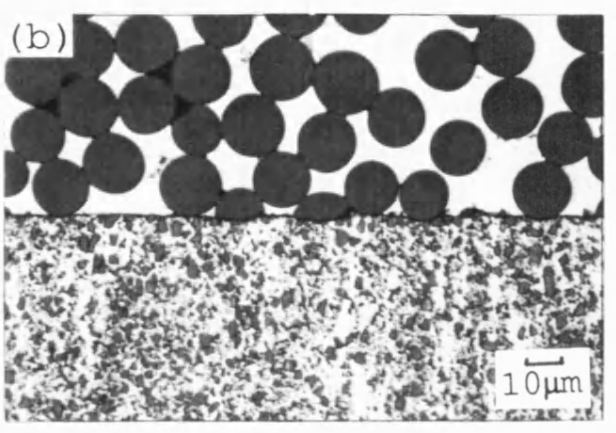

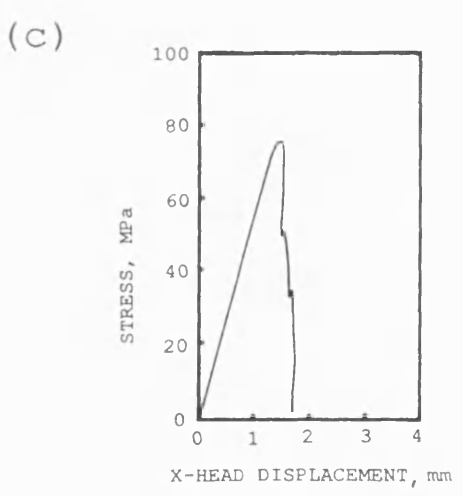

Fig. 3.68. Al/Nic bonded to 2124/35P composite without an interlayer, 10 MPa, 240 mins, 500°C.
a. Section of joint, OM.
b. Metal-to-metal contact at the joint, OM.
c. Shear test stress-displacement curve.

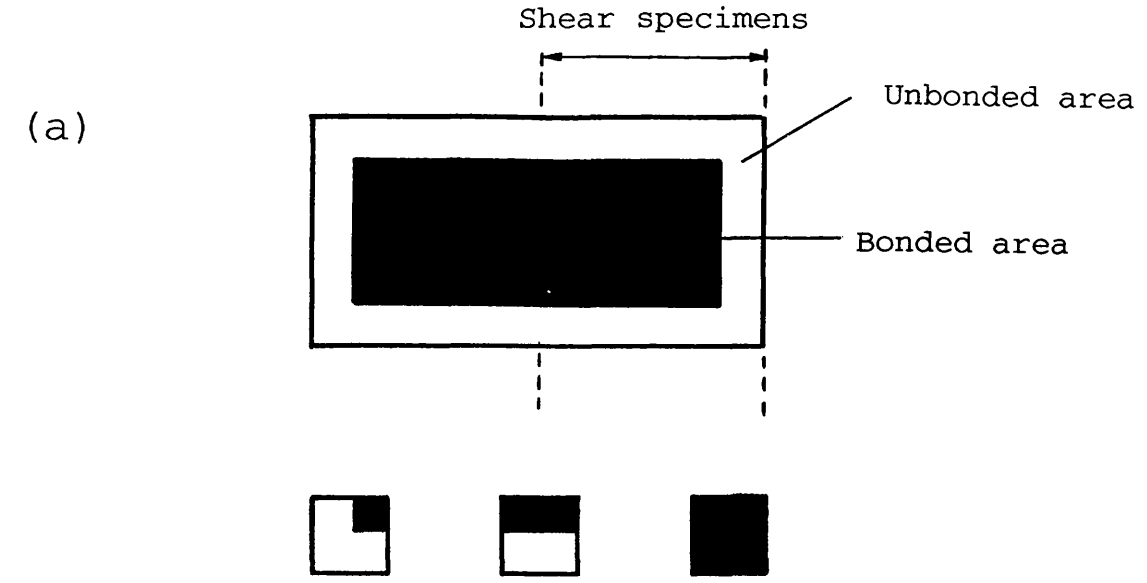

2 samples 10.1% 5 samples 43% 2 samples 100%

Average: 50 ± 30 %

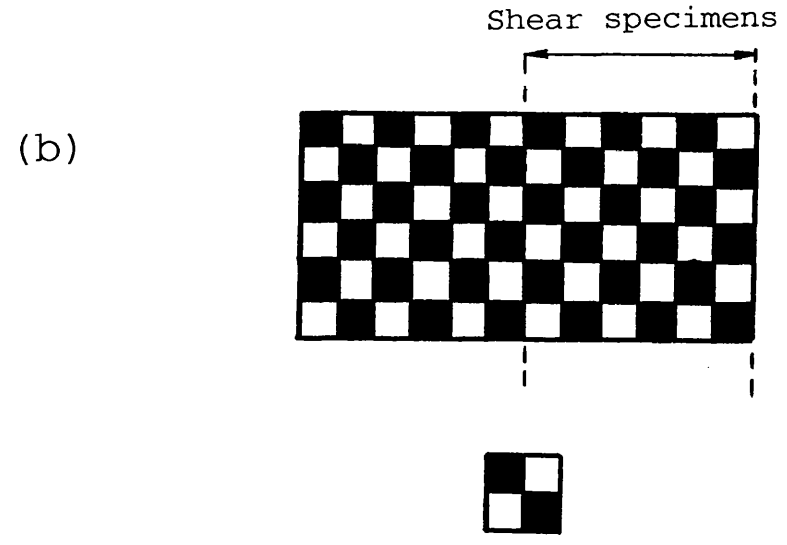

9 samples of 50% bonded area

Average: 50 ± 0 %

Fig. 4.1. Schematic diagram showing different distributions of bonded areas for one-half of a joint.
a. Bonded central region (50%), large scatter.
b. Patchy bonded areas (50%), small scatter.

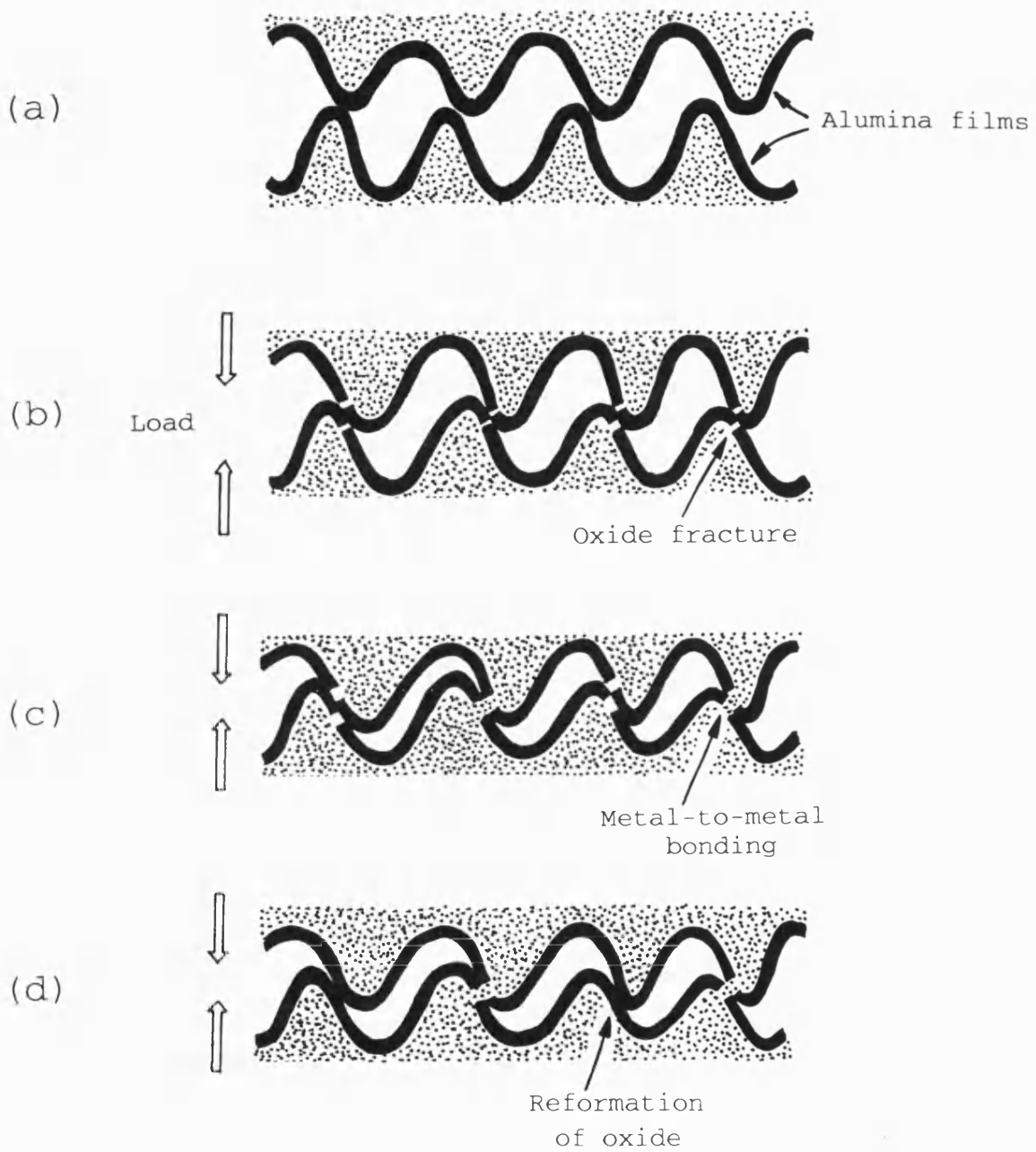

Fig. 4.2. Bonding mechanism for the bonding of aluminium.
a. Contacting surfaces, 500°C.
b. Load applied, fracture of alumina film.
c. Limited metal-to-metal bonding.
d. Reformation of alumina film.

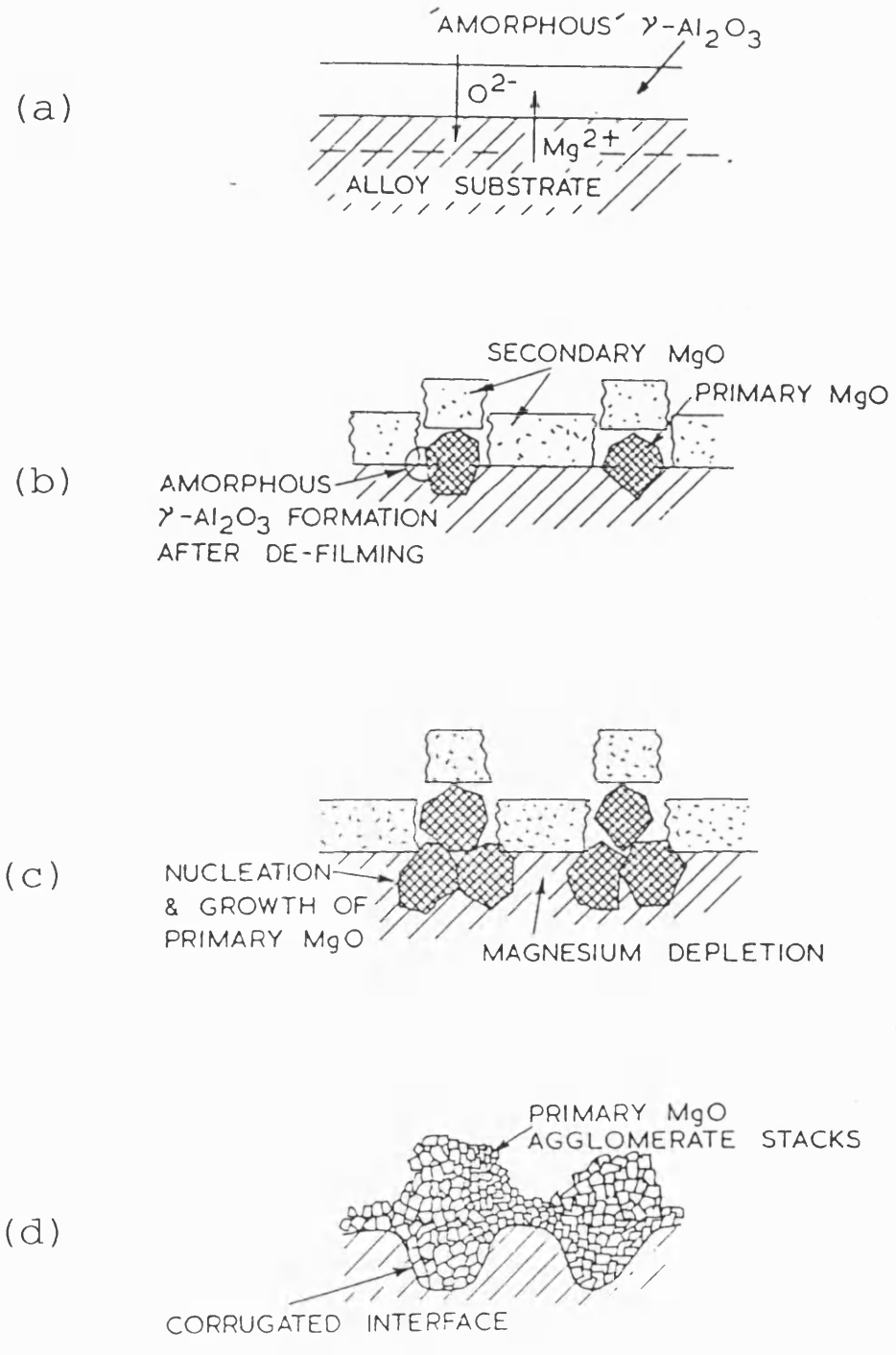

Fig. 4.3. Oxidation of an Al-Mg alloy at 400°C [159].
a. Absorption of Mg^{2+} into alumina film.
b. Formation of primary and secondary MgO.
c. Disruption of alumina film by MgO growth.
d. Complete reduction of alumina to MgO.

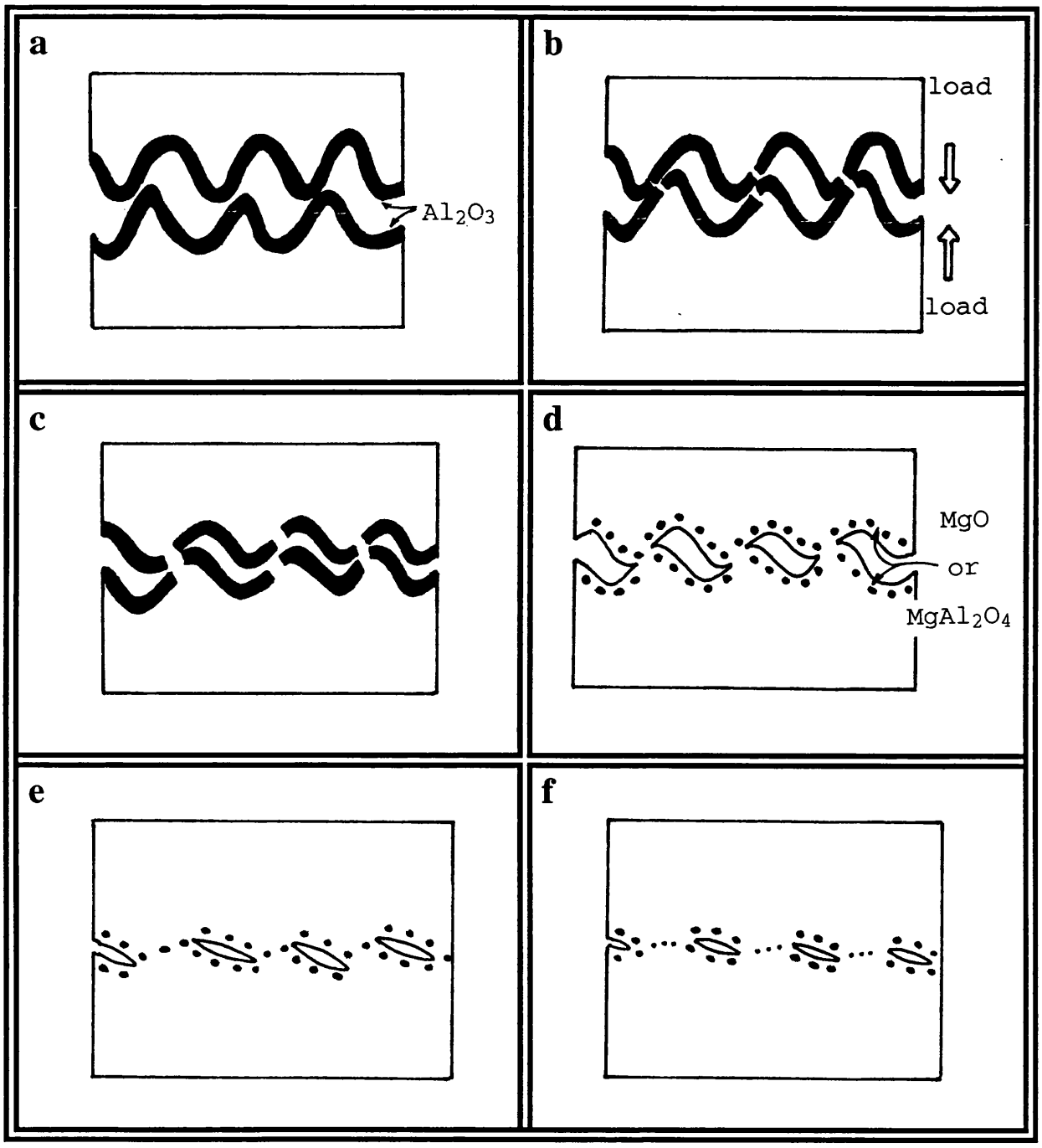

Fig. 4.4. Bonding mechanism for 2124 aluminium alloy.
a. Contacting surfaces, 500°C.
b. Load applied, fracture of alumina film.
c. Limited metal-to-metal bonding.
d. Magnesium reduction of alumina film.
e. Bulk and surface diffusion.
f. Elimination of interfacial voids.

(a)

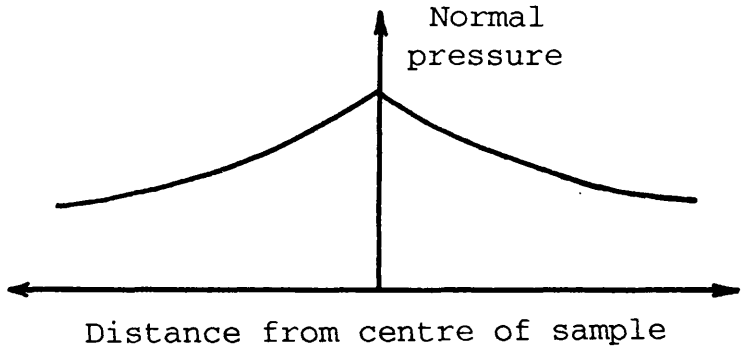

(b)

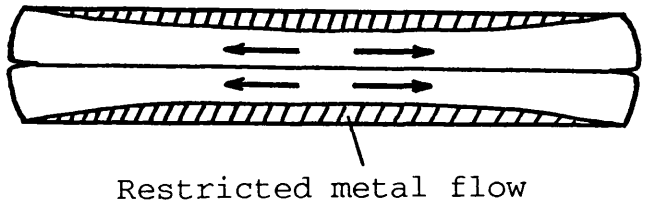

Fig. 4.5. Schematic representation a specimen during diffusion bonding [162].
a. Normal pressure distribution at interface.
b. Metal flow at interface.

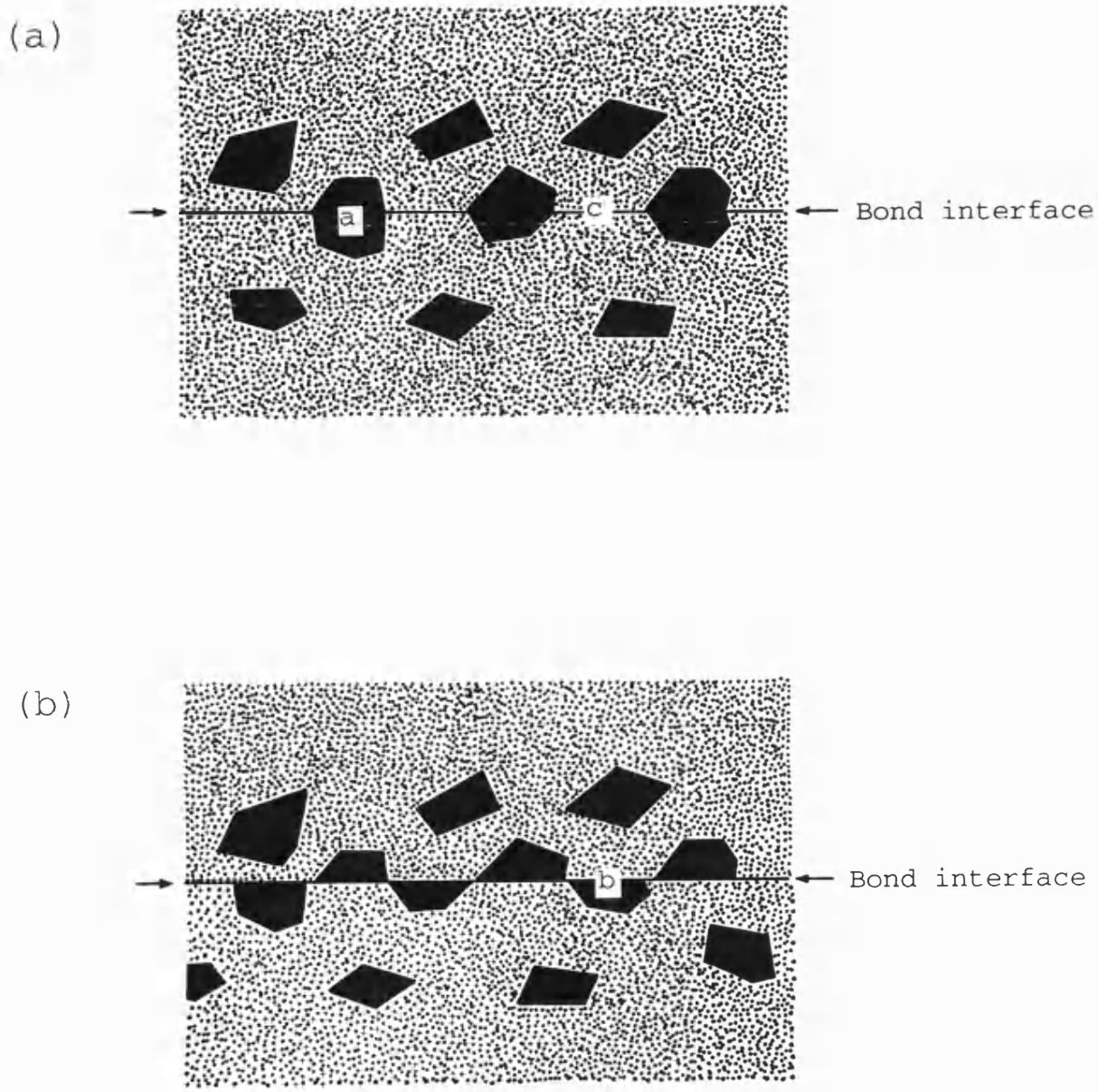

Fig. 4.6. Models used for predicting strengths of bonded 2124/P composite.
a. Upper-bound, complete SiC overlap.
b. Lower-bound, no SiC overlap.

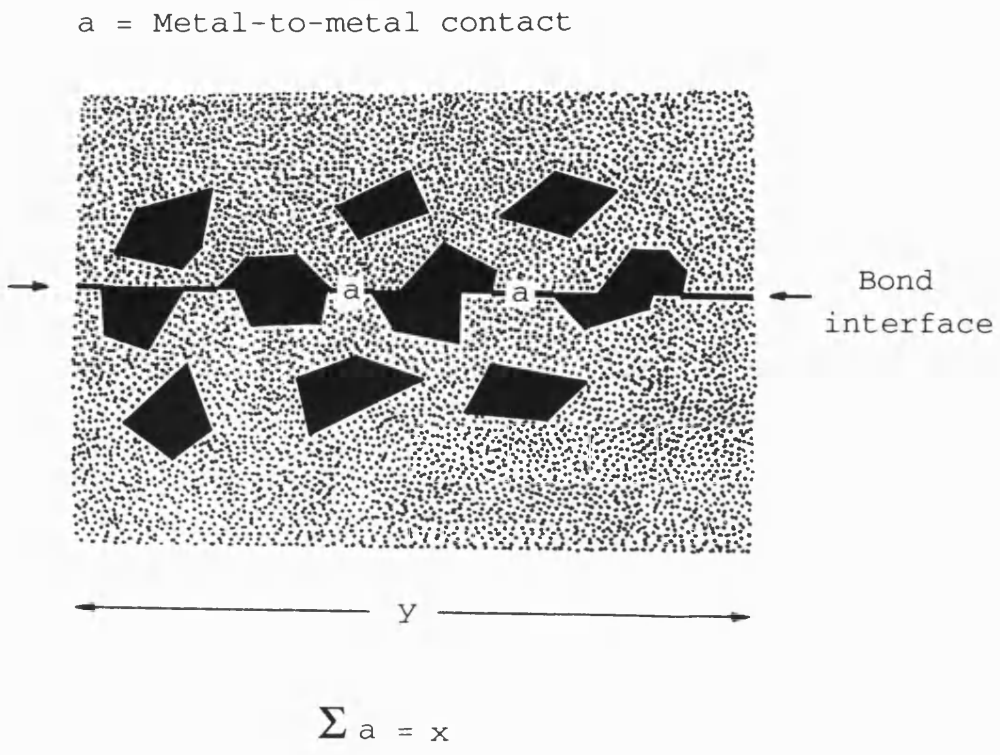

Area fraction of metal-to-metal contact ~x/y

Fig. 4.7. Estimation of metal-to-metal contact at the joint interface for diffusion-bonded 2124/P composite.

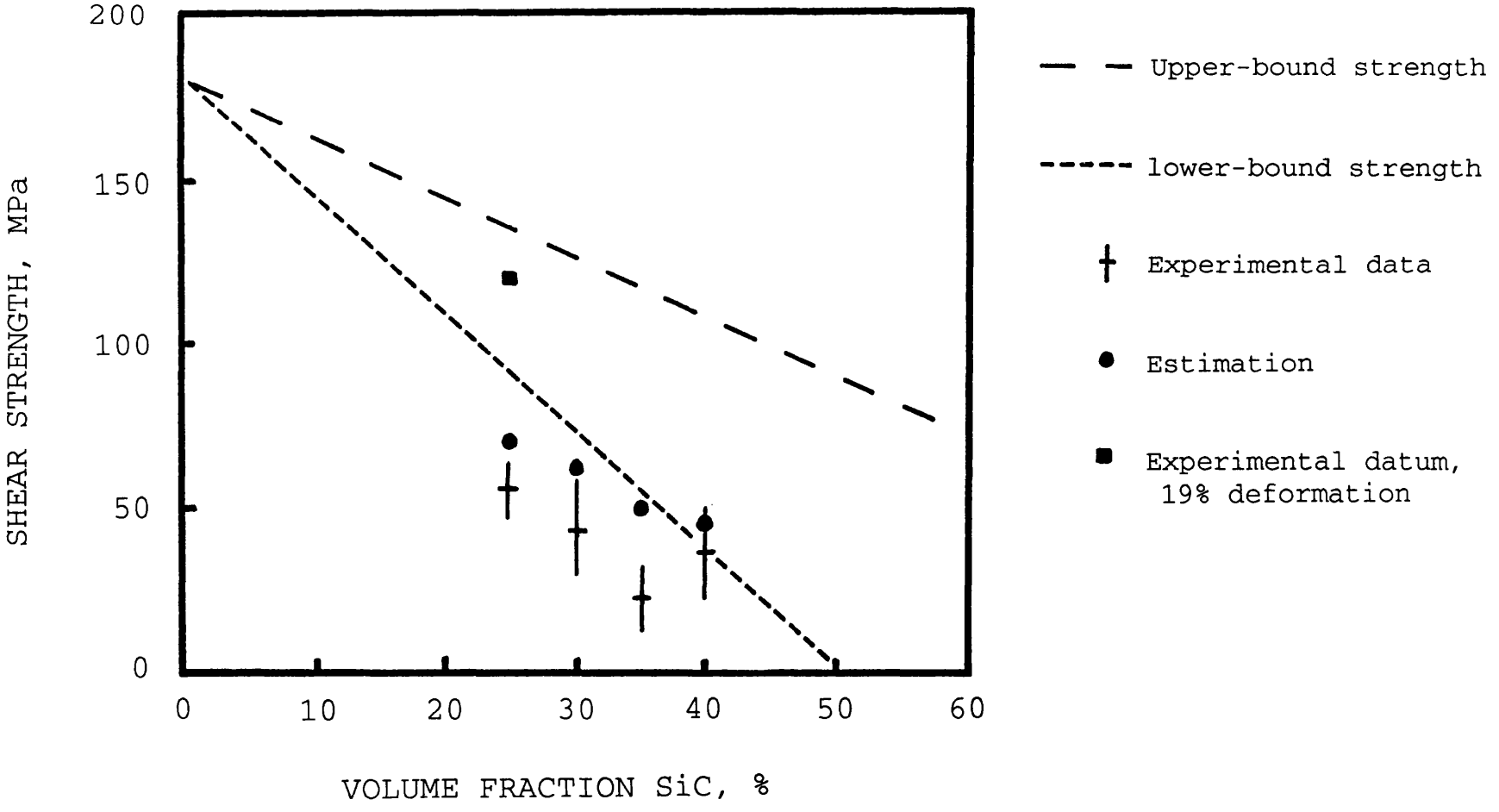

Fig. 4.8. Upper- and lower-bound estimates, experimental and predicted data for the shear strength of 2124/P composites bonded using 500°C for 240 minutes, 2% deformation.

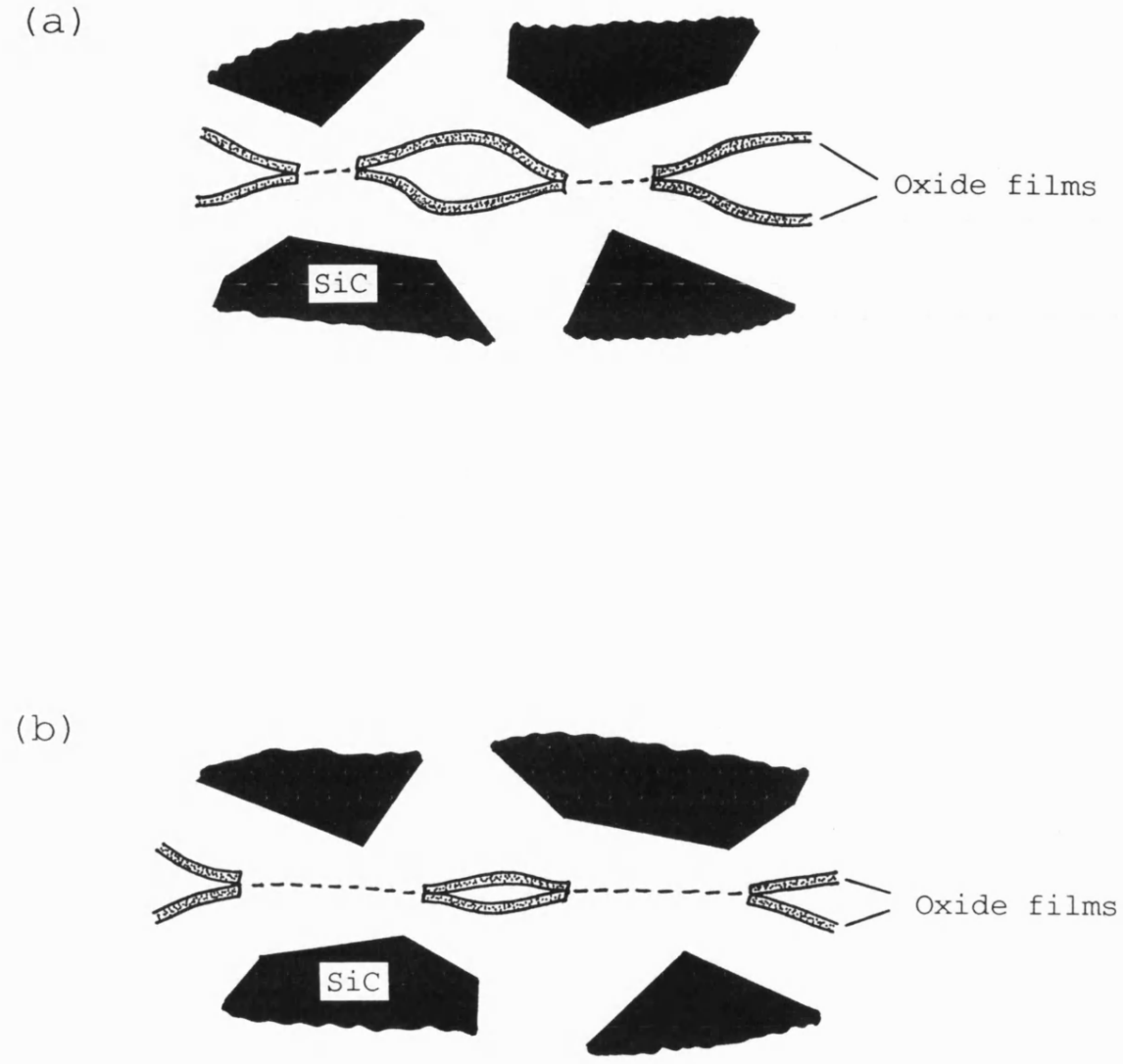

Fig. 4.9. Schematic representation of the joint interface for bonded 2124/P composite.
a. 2% deformation, low metal-to-metal contact.
b. 19% deformation, high metal-to-metal contact.

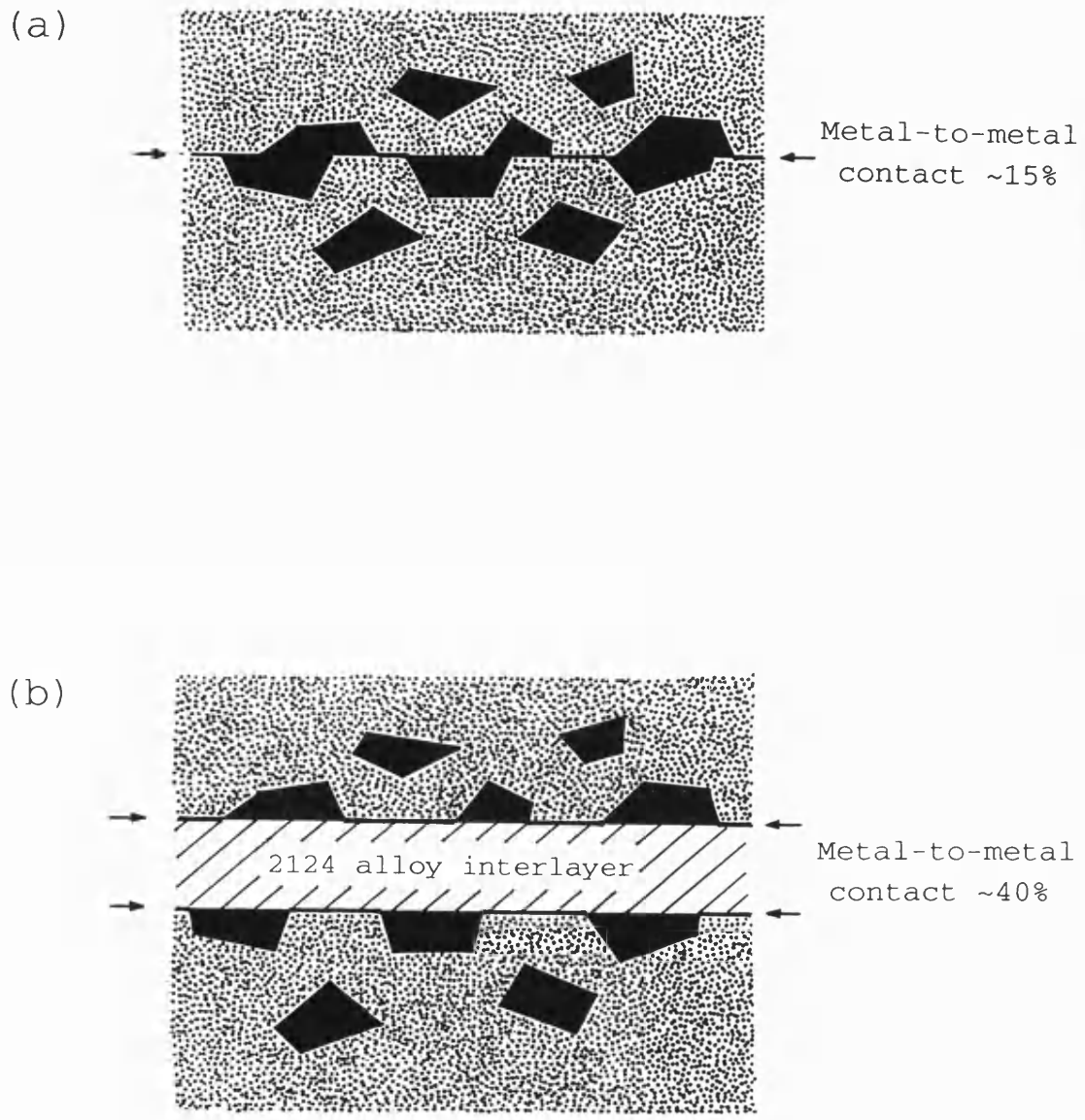

Fig. 4.10. Schematic diagram showing the effective bonded area for 2124/P composite.
a. Without an interlayer (~15%).
b. With an interlayer (~40%).

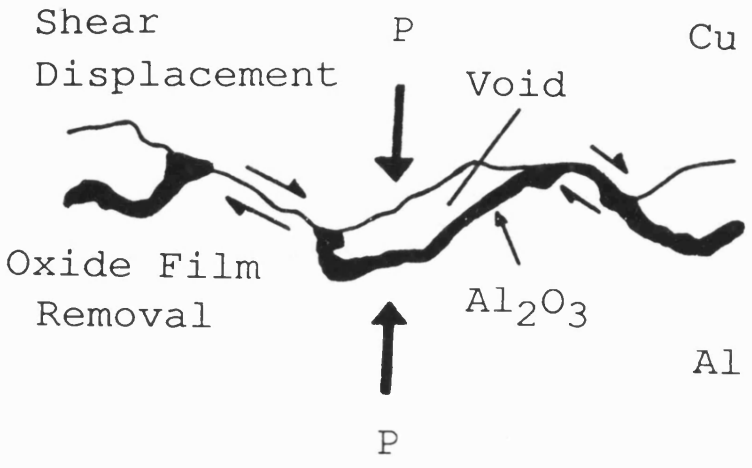

Fig. 4.11. Oxide removal at the aluminium/copper interface during the initial stages of bonding.

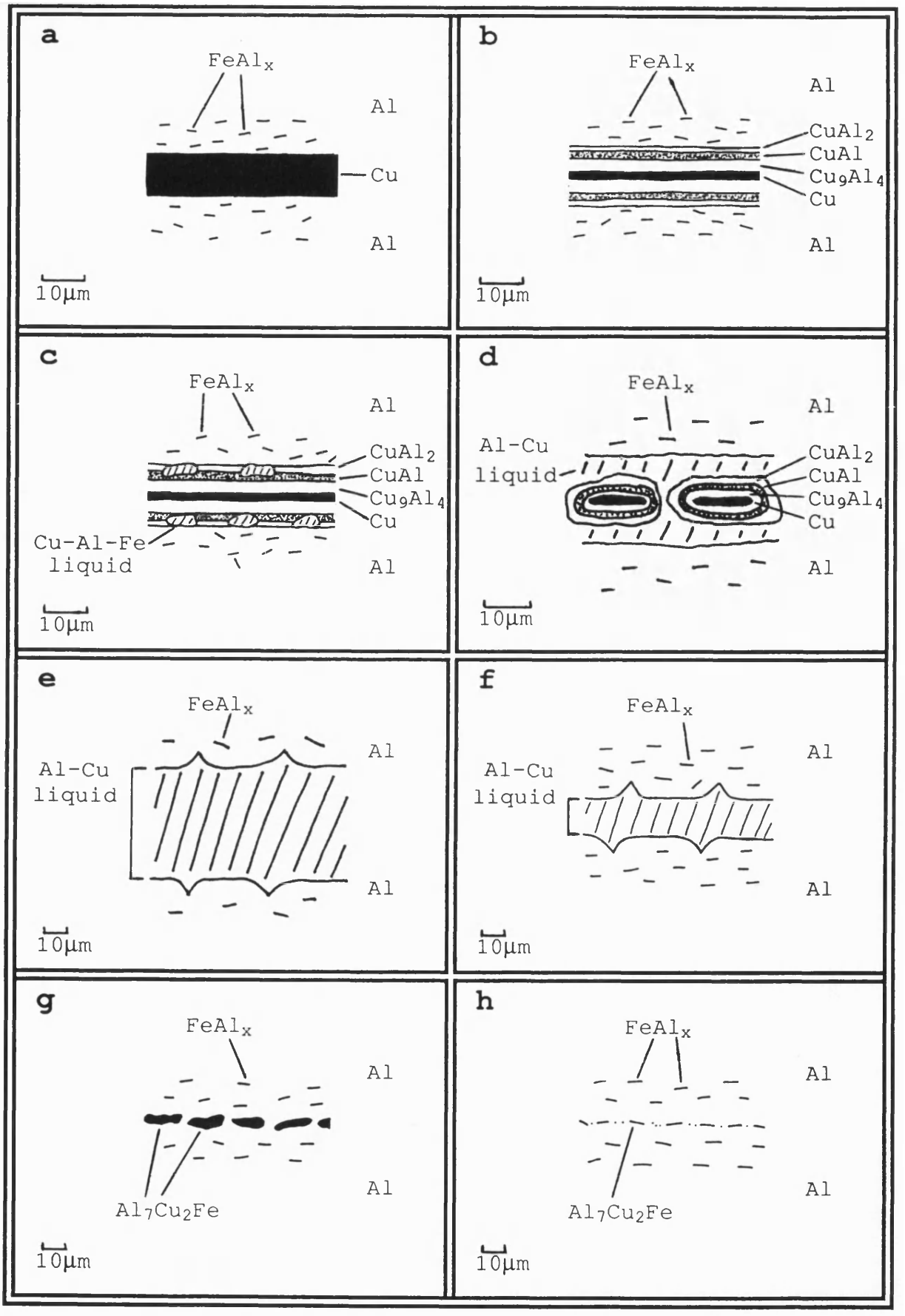

Fig. 4.12. Proposed mechanism for aluminium bonded with a copper interlayer.

a. Initial case, 0 mins, 530°C.
b. Formation of solid Al-Cu phases, 2 mins, 540°C.
c. Localised melting of Al-Cu-Fe, 3 mins, 545°C.
d. Formation of Al-Cu liquid, 4 mins, 548°C.
e. Complete melting of joint, 5 mins, 550°C.
f. Expulsion of liquid from joint, 10 mins, 550°C.
g. Isothermal solidification, 20 mins, 550°C.
h. Homogenised joint, 60 mins, 550°C.

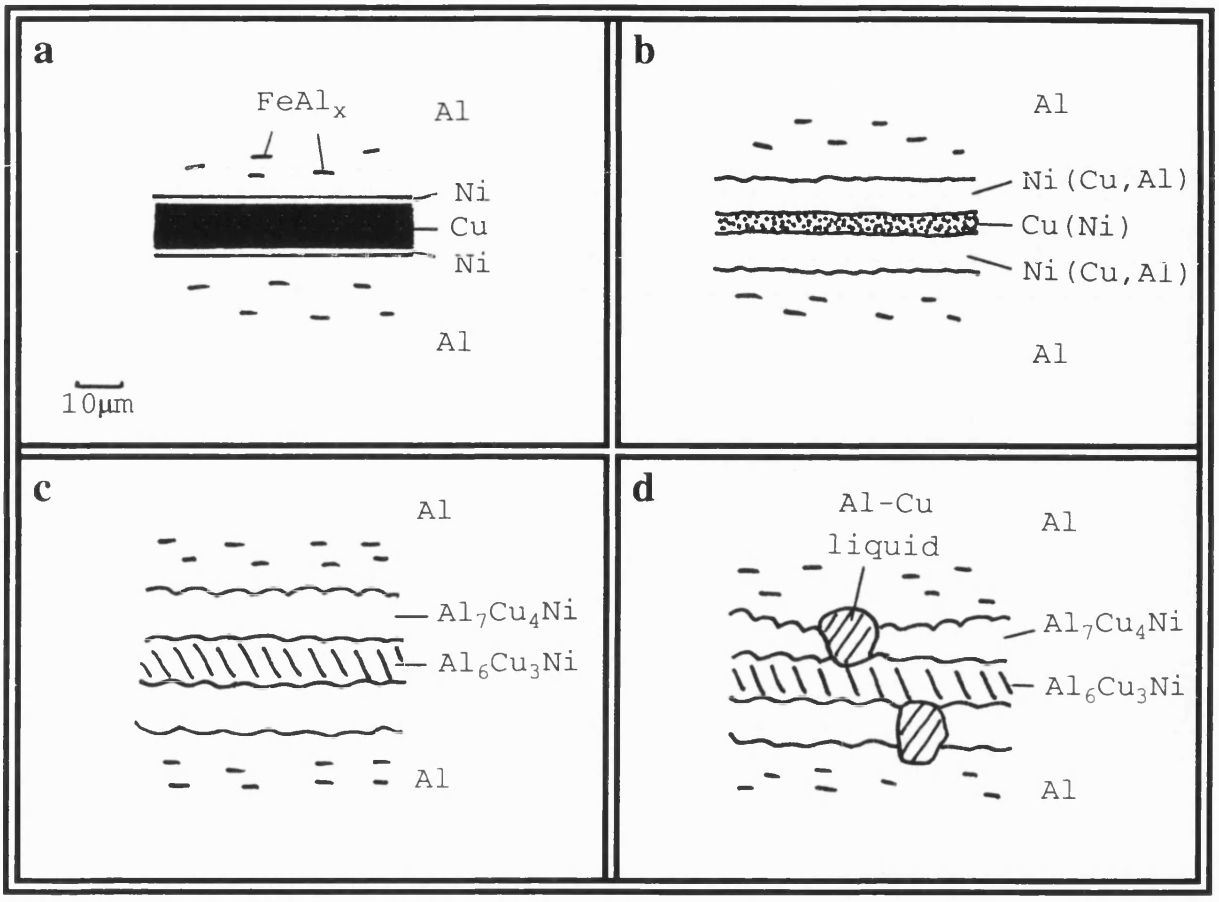

Fig. 4.13. Proposed mechanism for aluminium bonded with a nickel-coated copper interlayer.
a. Initial case, 0 mins, 530°C.
b. Interdiffusion of Cu, Ni and Al, >1 min, 535°C.
c. Formation of intermetallics, 1-5 mins, ~540°C.
d. Localised melting of Al-Cu, 548°C, 5 mins.

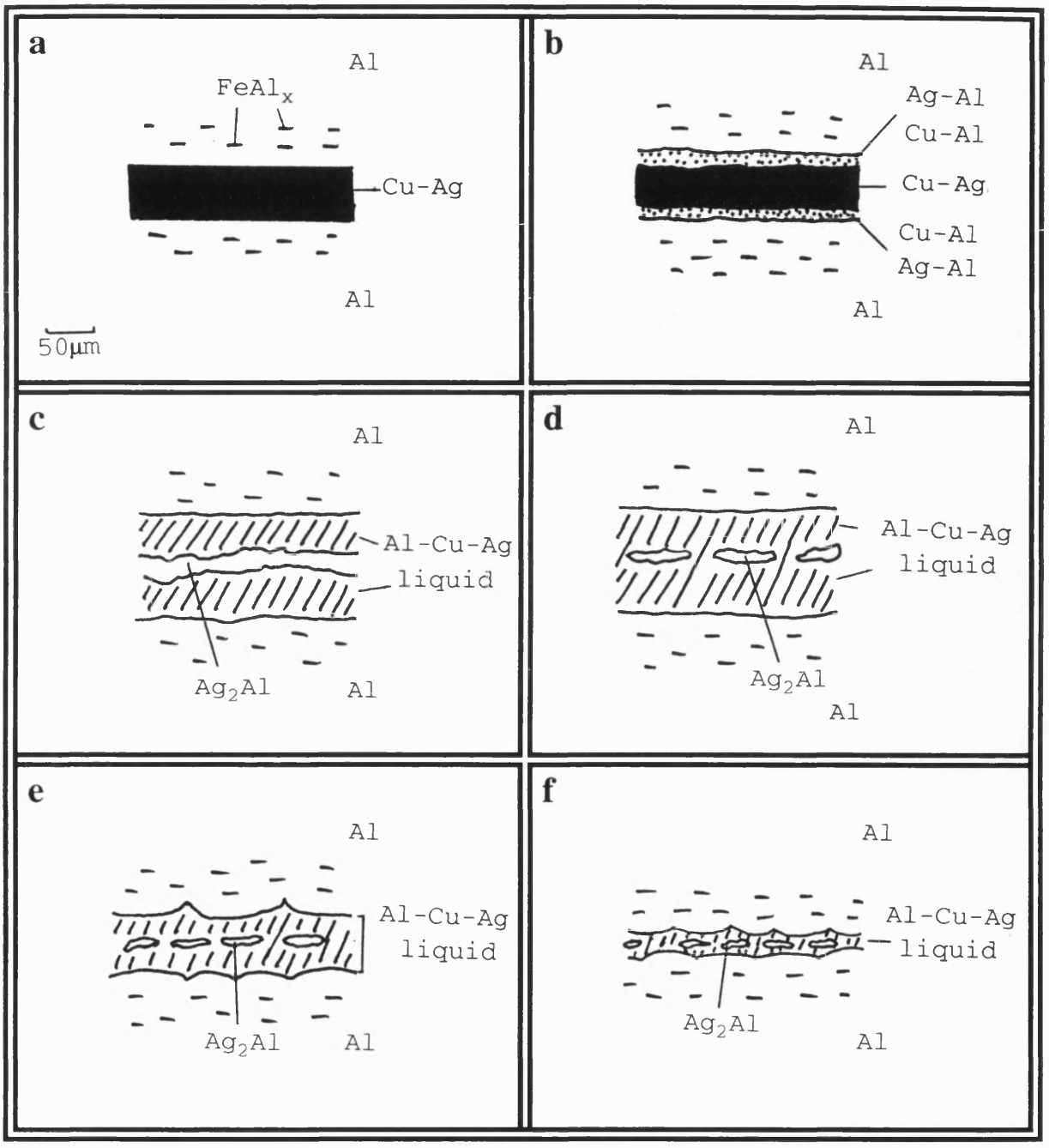

Fig. 4.14. Proposed mechanism for aluminium bonded with a copper-silver alloy interlayer.
a. Initial case, 0 mins, 490°C.
b. Solid-state interdiffusion, 2 mins, 500°C.
c. Formation of Al-Cu-Ag liquid, 3 mins, 502°C.
d. Expulsion of liquid, 5 mins, 510°C.
e. Further reaction, 5-15 mins, 510°C.
f. Isothermal solidification, ~30 mins, 510°C.